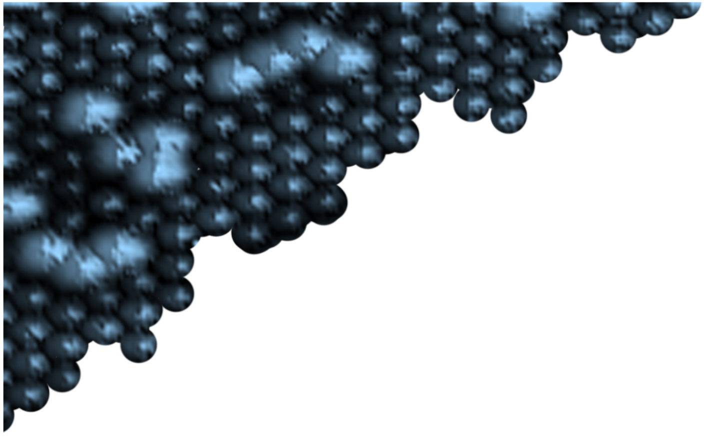

Atomic scale quantization and charging effects in topological semimetals

Raquel Sánchez Barquilla

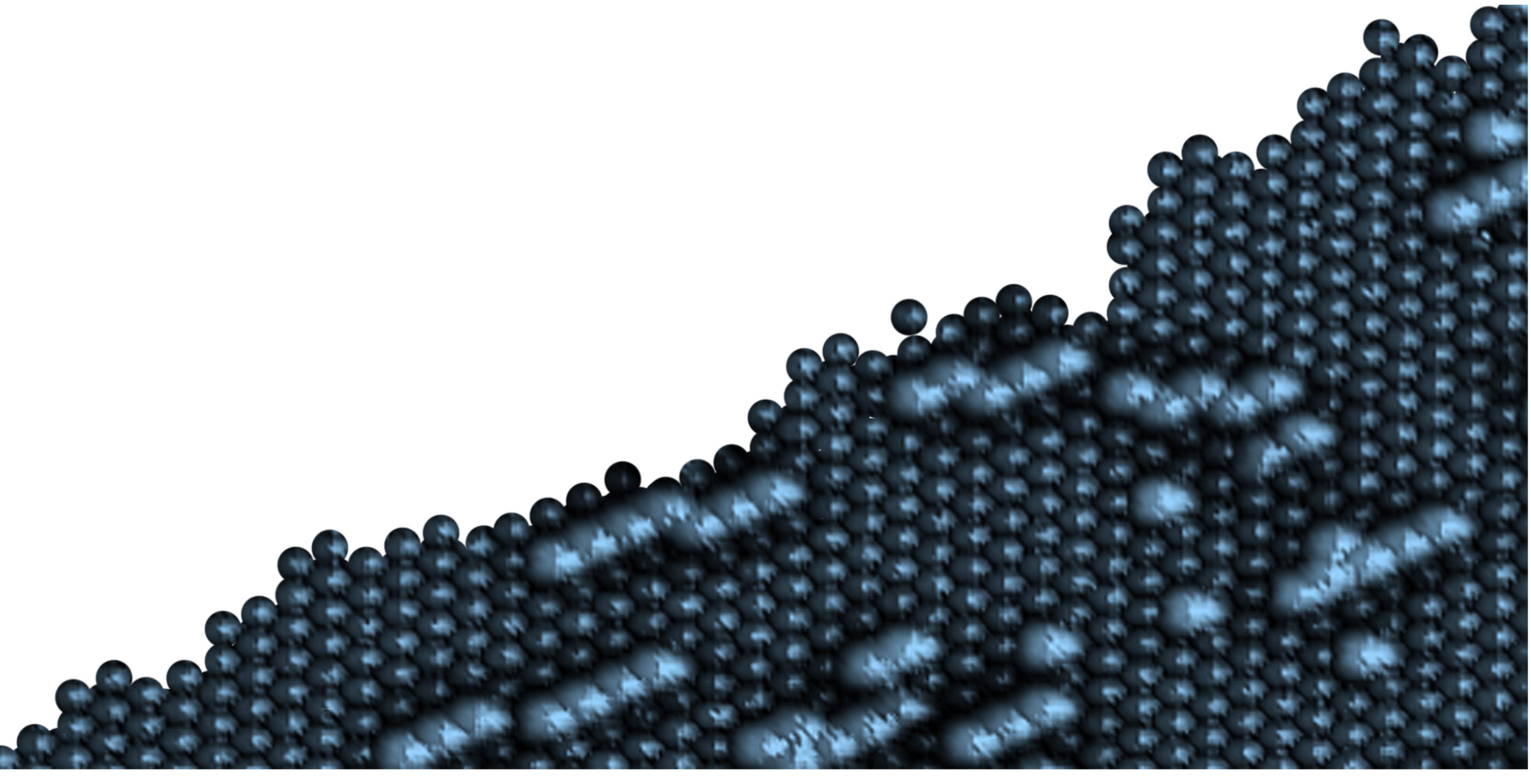

Atomic scale quantization and charging effects in topological semimetals

Dissertation submitted in partial satisfaction of the requirements for the degree of Doctor of Philosophy.

Raquel Sánchez Barquilla

Supervised by
Isabel Guillamón
Hermann Suderow

Departamento de Física de la Materia Condensada
Universidad Autónoma de Madrid
Madrid, España

January 2023

A Carlos, mi compañero.

A Jose y Mónica.

A mis padres.

Agradecimientos

En todo el proceso de escritura de la tesis, es inevitable acordarse de las personas que te han compañado durante el camino. Primero, quería dar las gracias a Isabel y Hermann, mis directores de tesis, por todo lo que me han enseñado. Por transmitirme vuestro amor por la ciencia y por estar siempre dispuestos a ayudarme. Siempre estaré orgullosa de haber iniciado mi carrera científica con vosotros. I would like also to acknowledge the members of the jury for their availability and willingness to read this thesis and travel to Madrid to attend to my defense. I would also like to acknowledge the groups of P.C. Canfield, R. Arita, J.J. Baldoví and R. Valenti for the collaboration and support related to this work.

Como no agradecer a mis predecesores en este proceso, que han pasado de ser compañeros en el laboratorio a grandes amigos. Gracias a Fran, por ayudarme tanto durante tantos años, desde que llegué en el máster. Por filosofar conmigo sobre la vida, hablar de ciencia o hablar de nada. Por ser el contrapeso necesario a mi ~~demasiado~~ entusiasmo. A Pepe, por enseñarme desde estañar cables a usar nuestro fantástico programa. Por poder hablar de cualquier tema. Todavía me debes una clase de guitarra. A Víctor, por amenizar tantos ratos y comidas, siempre con buena actitud.

Gracias también a la gente del laboratorio. Gracias a Edwin por tu buena actitud y todos tus consejos en este proceso de escritura. Eres un gran científico y una magnífica persona. A Antón, por darme los primeros consejos en el laboratorio. Muchas gracias a Chema, por las conversaciones dentro y fuera del laboratorio. Por tener siempre una solución. A Sara y Rafa por el increíble apoyo y estar siempre disponibles. A David y Beilun, por estar siempre dispuestos a ayudar. A Marta, mucho ánimo y paciencia en lo que te queda. Cómo no, muchas gracias a Jose, Pablo y Miguel, las nuevas incorporaciones. Por los maravillosos ratos en los cafés y comidas, por las discusiones sobre colormaps y los divertidos viajes a congresos. Por compartir frustaciones, pero sobretodo risas. Estoy segura de que (con o sin fugas) os irá genial.

Por supuesto, muchas gracias a todas las personas que me han acompañado fuera de la ciencia. Gracias César, Ricardo, Fabián, Juan y Paz, por hacer de la universidad un lugar mejor. A Desi, con la que he compartido cientos de horas en el tren. Muchísimas gracias por ser un rayito de luz todas las mañanas durante la carrera. Y por seguir siéndolo después para comer, cenar o ir al teatro. A Rafa, por su cariño y paciencia en nuestras incesantes conversaciones. A Alberto, porque son ya más de 10 años escuchándome. Gracias por todo tu apoyo. Qué suerte haberos conocido.

Por último, hay personas que han sido imprescindibles en este proceso, a las que les estoy AGRADECIDA. Así, en mayúsculas. A Jose, por aguantarme durante todos estos años y estar siempre dispuesto a rescatarme del desánimo y la frustración. A Mónica, por estar siempre presente y tener un hueco para mi. Por escucharme en persona, por teléfono o mensajes sin importar el día, la hora o la distancia. Eres mi gran ejemplo, y espero que estés tan orgullosa de mi como lo estoy yo de ti. A mis padres, por ser un apoyo incondicional y ponerme siempre las cosas más fáciles. Cada palabra aquí escrita es gracias a vosotros. A Carlos, mi compañero, por su infinita paciencia, por aportar luz a todas las situaciones. No existen palabras que puedan expresar todo lo que has hecho por mi. Así que, simplemente, gracias.

Contents

List of Figures

Abstract

A lot of effort has been put in the last years to study and understand the band structure of materials, especially near the Fermi level. Many recent discoveries in condensed matter physics rely on the connection of electronic structures and topology. Some materials present novel properties and topologically protected surface states that can be studied using techniques such as scanning tunneling microscopy (STM). STM can study both the bulk and surface states as a function of temperature or magnetic field. Its high spatial and energy resolution makes it an ideal technique for studying these materials. In this thesis, I addressed materials with topological properties in the band structure using STM. I studied magnetic and non-magnetic Weyl semimetals and a superconductor, all having few states at the Fermi level. From my measurements, I obtained new insight due to the peculiar properties of the band structure and the number of states close to the Fermi level in each system.

I first studied the band structure of the Weyl semimetal WTe_2. Using the Landau quantization of the bands when applying a magnetic field, we can obtain information about the bulk band structure and surface states. I studied the atomic scale Landau quantization in this material, finding evidence of two surface states related to the Weyl points in the bulk band structure, and an associated modification of the sequence of the Landau levels.

Then, I addressed the influence of the magnetic field in the magnetic Weyl semimetal $Co_3Sn_2S_2$. This is a ferromagnetic material where the bands close to the Fermi level are spin polarized, including a flat band that forms due to the arrangement of Co atoms on a kagome lattice. I have focused on studying the influence of the kagome lattice on atomic chains at the surface. I observe end states, an accumulation of electronic density at the ends of the atomic chains.

I studied the antiferromagnetic topological material $EuCd_2As_2$. The defects in this material appear significantly extended when studied with the STM, which reflects a significant reduction of screening at the surface. We have observed the formation of localized states at the defect due to both spatial confinement and the magnetic field.

Finally, I have studied the iron-based superconductor FeSe. We studied the bulk band structure and found a localized state above the Fermi level in the defects. This state reflects a change in the band structure at these points. We found a ring-like feature between the defects due to the presence of the localized state and the influence of the tip in it. This is consequence of an absence of screening due to the orbital selective correlations in this material.

Resumen

En los últimos años se han dedicado grandes esfuerzos a estudiar y comprender la estructura de bandas de los materiales, especialmente cerca del nivel de Fermi. Muchos descubrimientos recientes en física de la materia condensada se basan, precisamente, en la conexión entre la estructura electrónica y la topología. Algunos materiales presentan propiedades novedosas y estados superficiales topológicamente protegidos que pueden estudiarse mediante técnicas como la microscopía de efecto en túnel (STM por sus siglas en inglés). Mediante STM, se pueden estudiar tanto los estados de volumen como los de superficie bajo distintas condiciones, como son la temperatura o el campo magnético. Su alta resolución espacial y en energía convierten a esta técnica en una candidata ideal para estudiar estos materiales.

En la presente tesis, primero he estudiado la estructura de bandas del semimetal de Weyl WTe_2. Utilizando la cuantización de Landau de las bandas bajo la influencia de un campo magnético, podemos obtener información sobre la estructura de bandas del volumen y de los estados superficiales. Además, he estudiado la cuantización de Landau a escala atómica en este material, encontrando evidencias de dos estados superficiales relacionados con los puntos de Weyl en la estructura de bandas en el volumen, y una modificación de la secuencia de los niveles de Landau.

A continuación, he abordado la influencia del campo magnético en el semimetal de Weyl magnético $Co_3Sn_2S_2$. $Co_3Sn_2S_2$ es un material ferromagnético en el que las bandas cerca del nivel de Fermi están polarizadas en espín, incluyendo una banda plana formada por la disposición de los átomos de Co en forma de una red kagome. Me he centrado en el estudio de la influencia de la red kagome en las cadenas atómicas de la superficie, donde se observan estados de borde. Estos estados están relacionados con una acumulación de densidad electrónica en los extremos de las cadenas atómicas, debido a una diferencia considerable en las energías de los átomos de los bordes con respecto a los átomos en el interior de las cadenas. Esta diferencia se debe a la localización electrónica dentro de los hexágonos en la red kagome.

También he estudiado el material topológico antiferromagnético $EuCd_2As_2$. Los defectos en este material aparecen significativamente extendidos cuando se estudian mediante STM, lo que refleja una reducción significativa del apantallamiento en la superficie. Hemos medido la cuantización de los estados en los defectos. Cuando se aplica el campo magnético, la cuantización Landau aumenta el número de niveles.

Por último, he estudiado el superconductor de hierro FeSe. He estudiado la estructura de bandas del material y hemos encontrado un estado localizado por encima del nivel de Fermi en los defectos. Este estado refleja un cambio en la estructura de bandas en dichos puntos. Hemos encontrado una señal en forma de anillo entre los defectos debido a la presencia del estado localizado y a la influencia de la punta. Esto es consecuencia de la ausencia de apantallamiento debido a que las propiedades electrónicas dependen fuertemente del carácter orbital de las bandas.

Chapter 1

Introduction

In this work I will present studies of the electronic band structure made with Scanning Tunneling Microscope at high magnetic fields. The electronic band structure is a concept of solid state physics which is firmly established since more than a century. Experiments and calculations have agreed on the rough features of the band structure of many metals, semimetals and semiconductors for a long time. However, recent advances in calculations and techniques used to study the band structure (essentially angular resolved photoemission (ARPES), quantum oscillations and scanning tunneling microscopy (STM)) have unveiled a flurry of new physics.

As so often, the increased resolution in experiments and calculations does not just bring an increased accuracy allowing to resolve tiny structures. On the contrary, it provides a qualitatively new landscape of electronic phenomena in solids. In this PhD thesis, I have explored this new landscape, obtaining results in an iron based layered material and in semimetals.

1.1 Band structure in solids

In the free electron model, the energy levels ϵ_k can be described as a continuum[1]

$$\epsilon_k = \frac{\hbar^2}{2m}\left(k_x^2 + k_y^2 + k_z^2\right), \tag{1.1}$$

---

[1] This section follows the explanations of the solid state physics books written by Ashcroft/Mermin [1], Ibach [2], Kittel [3] and Ziman [4]

where the wave functions for free electrons are

$$\psi_k(\vec{r}) = e^{i\vec{k}\cdot\vec{r}}, \tag{1.2}$$

and the Fermi surface is a sphere of radius k_F. The free electron model is a good approximation to understand basic aspects of some properties such as the thermal and electrical conductivity, the magnetic susceptibility or the specific heat.

1.1.1 Nearly free electrons and tight binding

The electronic band structure can be obtained from two different approximations. We can start from free electrons and include a periodic potential V($\vec{r}$) to obtain Bloch functions:

$$\psi_k(\vec{r}) = \sum_K c_{\vec{k}-\vec{K}} e^{i(\vec{k}-\vec{K})\cdot\vec{r}}. \tag{1.3}$$

The corresponding band structure is shown in figure **1.1 a** in the repeated zone scheme. As we can see, we have nearly the same result as with free electrons, although Bragg scattering at the Brillouin zone boundary opens gaps in the dispersion relation.

We can also start from atomic orbitals. We take atoms periodically ordered and separated by a distance r and look at their overlap using the tight-binding approximation. For large r, the wave function overlap is small and therefore bands are narrow. When reducing r, atomic wavefunctions overlap significantly and produce large bands, as represented in figure **1.1 b**.

In this model, we can start from the Hamiltonian of one single atom $H_{at}(\vec{r}-\vec{r}_n)$ at the lattice position $\vec{r}_n$:

$$H_{at}(\vec{r}-\vec{r}_n)\varphi_i(\vec{r}-\vec{r}_n) = E_i\varphi_n(\vec{r}-\vec{r}_n), \tag{1.4}$$

where $\psi_n(\vec{r})$ is the wave function for an electron in the atomic level E_n. A term $\Delta U(\vec{r})$ can be included if the crystal Hamiltonian differs from H_{at}

$$H = H_{at} + \Delta U(\vec{r}) = -\frac{\hbar^2}{2m}\nabla^2 + V_{at}(\vec{r}) + v(\vec{r}), \tag{1.5}$$

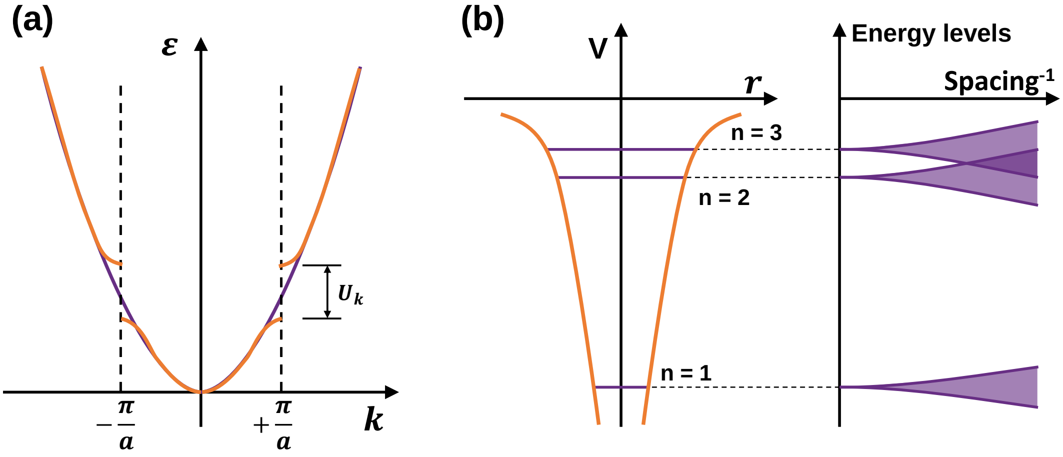

Fig. 1.1: (a) ε vs k band structure representation. Free electron parabola in one dimension is represented in purple. The parabola is distorted in the vicinity of the Bragg planes $\pm\pi/a$ due to a weak periodic potential considered in the nearly free electron model, obtaining the orange curve. (b) Schematic representation of electronic levels in an atomic potential. These levels are degenerate in a set of N independent atoms located far apart. When we reduce the spacing between atoms, discrete degenerate levels broaden into bands.

where $v(\vec{r})$ describes the perturbation to the potential V_{at} of the free atom. Thus, this perturbation can be written as a sum over the potential for all atoms apart from the atom at $\vec{r}_n$

$$v(\vec{r}-\vec{r}_n) = \sum_{m\neq n} V_{at}(\vec{r}-\vec{r}_n). \tag{1.6}$$

For the crystal Hamiltonian, the solution will be the solution to the Schrödinger equation

$$H\psi_k(\vec{r}) = E(\vec{k})\psi_k(\vec{r}), \tag{1.7}$$

where $\psi_k(\vec{r})$ are Bloch waves. Multiplying by ψ_k^* and integrating in the range where ψ_k is defined, we obtain

$$E(\vec{k}) = \frac{\langle\psi_k|H|\psi_k\rangle}{\langle\psi_k|\psi_k\rangle}, \tag{1.8}$$

where

$$\langle \psi_k | H | \psi_k \rangle = \int \psi_k^* H \psi_k d\vec{r}, \tag{1.9}$$

$$\langle \psi_k | \psi_k \rangle = \int \psi_k^* \psi_k d\vec{r}, \tag{1.10}$$

As the crystal Hamiltonian is based on the free atom Hamiltonian, we can write the crystal wave function ψ_k as a linear combination of atomic eigenfunctions ϕ_k

$$\psi_k \approx \phi_k = \sum_n a_n \varphi_n(\vec{r} - \vec{r}_n) = \sum_n e^{i\vec{k}\cdot\vec{r}_n} \varphi_i(\vec{r} - \vec{r}_n), \tag{1.11}$$

where ϕ_k are Bloch functions. Then, the coefficients are determined as $a_n = e^{i\vec{k}\cdot\vec{r}_n}$. Inserting the solution ϕ_k in Eq. 1.10 and for sufficiently localized electrons, we obtain

$$\langle \phi_k | \phi_k \rangle \simeq \sum_n \int \varphi_i^*(\vec{r} - \vec{r}_n) \varphi_i(\vec{r} - \vec{r}_n) d\vec{r} = N, \tag{1.12}$$

where N is the number of atoms in the crystal. The energy of the crystal can be obtained in terms of the energy for the free atom

$$E(\vec{k}) \approx \frac{1}{N} \sum_{n,m} e^{i\vec{k}\cdot(\vec{r}_n - \vec{r}_m)} \int \varphi_i^*(\vec{r} - \vec{r}_m) \left[E_i + v(\vec{r} - \vec{r}_n) \right] \varphi_i(\vec{r} - \vec{r}_n) d\vec{r}, \tag{1.13}$$

where E_i is the energy eigenvalue of the isolated atom. Two approximations have been made. First, in the term containing E_i, only the terms with $n = m$ have been considered. Furthermore, in the term containing the perturbation $v(\vec{r} - \vec{r}_n)$, the overlap only includes the first neighbor.

If the atomic level is not degenerate, we have an s-level and equation 1.13 reduces to a single equation. The result is an explicit expression for an s-band. For bands arising from the p-level, which is three times degenerate, equation 1.13 gives three homogeneous equations. Thus, the number of equations increases as the level of degeneration increases.

1.1.2 Semiconductors, semimetals and metals

Depending on the shape of the band structure around the Fermi level, we can classify materials as metals, semimetals, and semiconductors or insulators (see figure **1.2**).

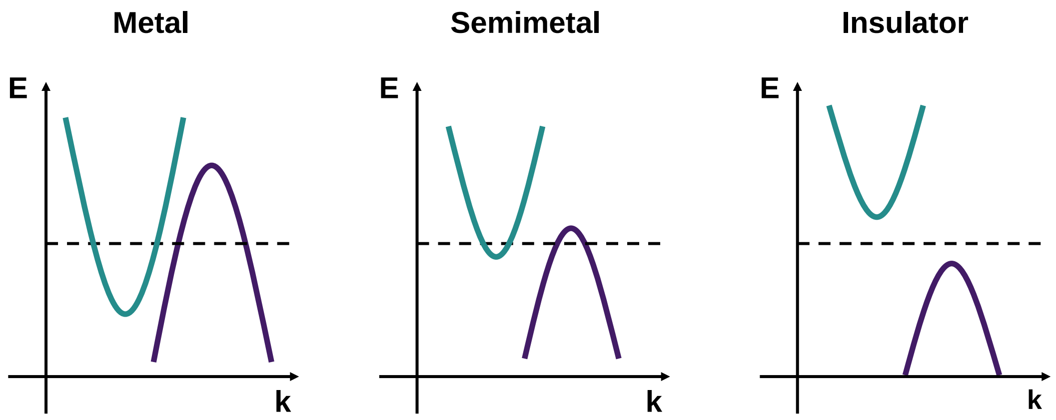

Fig. 1.2: Schematic representation of the difference between metals, semimetals and insulators. Dashed horizontal line represents E_F in metal and semimetal and the middle of the gap in the insulator or semiconductor

Of particular interest for this PhD thesis are semimetals, where the Fermi level lies very close to the top and/or bottom of the bands. To discuss our work we need to present briefly how to account for impurities in an electronic system. An atomic size impurity consisting of a defect or an impurity atom, may create charge around it. This charge is screened out in a metal but not in a semiconductor or an insulator.

Impurities create electronic states within the gap in semiconductors or insulators which can remain localized or create an additional band if the impurity density is large enough.

1.1.3 Impurities in semiconductors

Impurities are known as donors if they contribute to the carrier density of a semiconductor providing additional electrons to the conduction band. They are known as acceptors if they supply additional holes to the valence band.

For a donor impurity contributing with one extra valence electron (for example, if we dope a material with the neighbor at the right in the periodic table and ignoring the difference in size and structure between atoms), we can consider that we have the undoped material, but with electron doped centers.

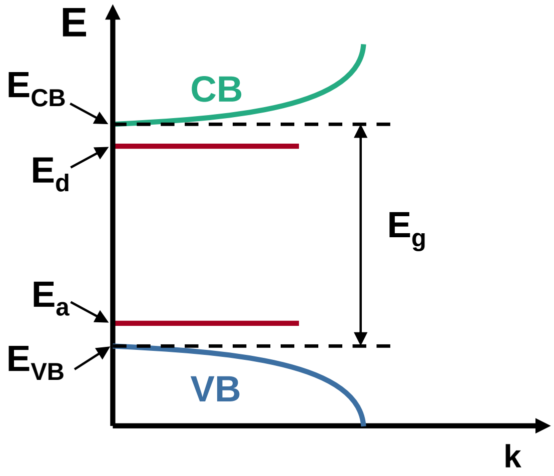

Fig. 1.3: Schematic representation of the energy levels of donors and acceptors in a semiconductor. The donor level E_d appears close to the conduction band (CB) and the acceptor level E_a, close to the valence band (VB), compared to the gap energy E_g.

The additional electron leads to an additional energy level E_d lying close to the conduction band, E_{CB}, inside the gap of the semiconductor.

When the material is doped with acceptors, we can consider the undoped material with an extra hole, and the result is an additional electronic level E_a near the top energy of the valence band E_{VB}. Figure **1.3** schematically represents the conduction and valence bands separated with a gap and the position of the donor and acceptor states in energy.

1.1.4 Lindhard function and screening

Screening is a relevant consequence of electron-electron interactions. Let us assume that a positively charged particle is placed in a fixed position in an electron gas. This particle attracts electrons, creating a charge in its neighborhood that screens its field. To describe this screening, we can introduce two potentials. ϕ^{ext}, that arises from the charged particle itself and satisfies Poisson's equation

$$-\nabla^2 \phi^{ext}(\vec{r}) = 4\pi \rho^{ext}(\vec{r}), \tag{1.14}$$

where $\rho^{ext}(\vec{r})$ is the charge density of the particle, and ϕ, which is the full potential produced by the charge and the cloud of electrons surrounding it

$$-\nabla^2\phi(\vec{r}) = 4\pi\rho(\vec{r}). \tag{1.15}$$

$\rho(\vec{r}) = \rho^{ext}(\vec{r}) + \rho^{ind}(\vec{r})$, being $\rho^{ind}(\vec{r})$ the charge density induced in the electron gas by the presence of the positive charge. Assuming that ϕ and ϕ^{ext} are linearly related and considering the Fourier transform, we can write

$$\phi(\vec{q}) = \frac{1}{\epsilon(\vec{q})}\phi^{ext}(\vec{q}). \tag{1.16}$$

where q is a wave vector and $\epsilon(\vec{q})$ is known as the dielectric constant of the material, which can be expressed as

$$\epsilon(\vec{q}) = 1 - \frac{4\pi}{q^2}\frac{\rho^{ind}(\vec{q})}{\phi(\vec{q})}. \tag{1.17}$$

In this description, the only approximation is that we considered that the applied charge is weak enough to produce a linear response in the electron gas. A more detailed description is the Lindhard approach, where we write the dielectric constant as

$$\epsilon(\vec{q}) = 1 + \frac{4\pi e^2}{q^2}\sum_k \frac{f(\vec{k}) - f(\vec{k}-\vec{q})}{\varepsilon(\vec{k}-\vec{q}) - \varepsilon(\vec{k})}, \tag{1.18}$$

where f is the Fermi function and ε the electronic energies. We sum over all available states k, to find the dielectric constant at a vector q. If we consider $\epsilon(\vec{q})$ near $\vec{q} = 0$, we can approximate

$$\varepsilon(\vec{k}+\vec{q}) - \varepsilon(\vec{k}) \approx \vec{q}\cdot\nabla_{\vec{k}}\varepsilon(\vec{k}), \tag{1.19}$$

$$f(\vec{k}) - f(\vec{k}+\vec{q}) \approx -\vec{q}\cdot\frac{\partial f}{\partial\varepsilon}\nabla_{\vec{k}}\varepsilon(\vec{k}). \tag{1.20}$$

We see that the dielectric constant is mostly influenced by the Fermi level, where $\partial f/\partial\varepsilon$ is large. When converting the sum into an integral, we find the relation

$$\epsilon(\vec{q}) \to 1 + \frac{\lambda^2}{q^2}, \quad \text{with} \quad \lambda^2 = 4\pi e^2 N(\varepsilon_F). \tag{1.21}$$

This suggests that the inverse of λ provides the distance above which the potential due to the charge is modified. Often, in metals with a large N(E$_F$), the charge is screened at small distances, whereas in semimetals with a small electronic density, the potential due to an impurity extends to larger distances.

1.1.5 Mott transition

Electronic interactions may also convert a metal into an insulator, or considerably modify the band structure. One way of seeing that is through the Mott transition. Mott considered an ordered array of monovalent atoms [5]. For small interatomic distances d, this system is a metal. But for sufficiently large d, Mott showed that such a system should be an insulator. The activation energy to form a pair of carriers is given by the ionization energy minus the energy required to add an electron (electron affinity in an insulator). The formation of electronic bound states, such as bound electron-hole pairs, is possible unless the other electrons screen the Coulomb attraction. When d decreases, the activation energy decreases. The Coulomb potential is screened as shown in Eq. 1.16. Taking $d \propto 1/q$ in Eq. 1.16, we can see that bound states no longer exist when the distance d is such that the electron density is larger than $N^{1/3}a_H \approx 0.2$ where a_H is Bohr radius.

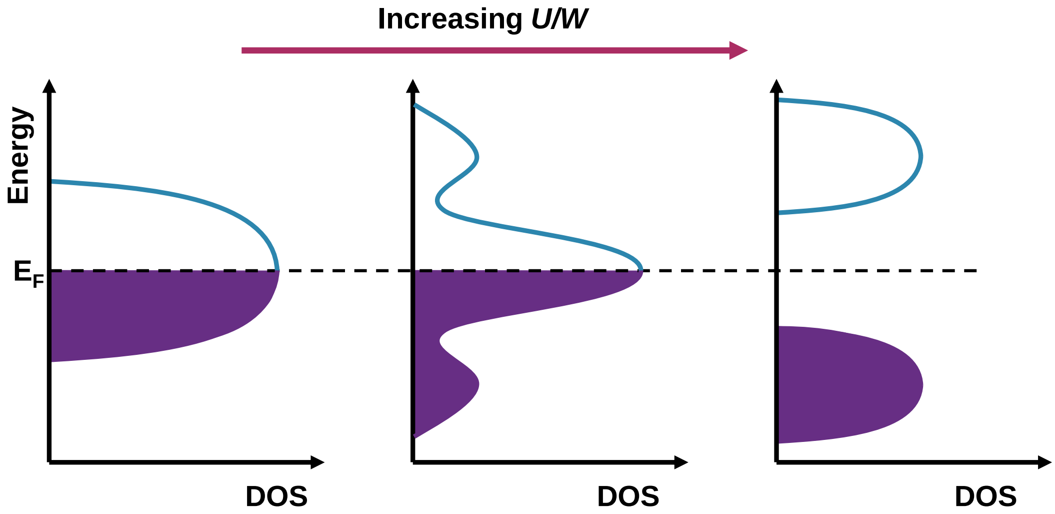

Fig. 1.4: Adapted from [6]. Schematic representation of a Mott transition. In the first case, the electrons are independent and the E$_F$ is located at the center of the band. When the ratio U/W increases, the DOS present a three peaks structure. Finally, the metal-insulator transition occurs, and the peak in the middle disappears. The final DOS consists of two bands.

Within the Hubbard model, electrons with spins $\sigma = \uparrow$ or $\downarrow$ can move between localized states at lattice positions i and j [6], and they can only interact when they are at the same position. Thus, the Hubbard Hamiltonian can be written as

$$H = \sum_{ij\sigma} t_{ij} c^{\dagger}_{i\sigma} c_{j\sigma} + U \sum_{i} n_{i\uparrow} n_{i\downarrow}, \tag{1.22}$$

where the first term is the tight-binding Hamiltonian and the second term describes the local Coulomb interaction U between two electrons in the same lattice position i. $n_{i\sigma} = c^{\dagger}_{i\sigma} c_{i\sigma}$ is the density of electrons at site i. The resulting density of states per energy can be pictured as a function of U/W, where U is given by the interaction term in Eq. 1.22 and W is the bandwidth resulting from the tight binding part of Eq. 1.22. The Mott transition occurs when the interaction is large enough [6], as represented in figure **1.4**.

1.2 Impurities and defects in semiconductors and semimetals

1.2.1 Band bending in semiconductors

Schottky and Mott first developed the band bending concept to explain the rectifying effect of metal-semiconductor contacts [7–10]. When a metal and a semiconductor are in contact, electrons flow across the interface to compensate for the difference in the work functions. If the work function of the metal (ϕ_m) is higher than the work function of the semiconductor (ϕ_s), the electrons flow from the semiconductor to the metal until the Fermi levels are aligned. Figure **1.5 a** shows a metal and a semiconductor in contact, with $\phi_m > \phi_s$. Figure **1.5 b** shows the opposite case ($\phi_m < \phi_s$). These figures describe schematically the out of equilibrium situation, in which electron flow did not yet happen.

In equilibrium, the Fermi levels of both materials align. Due to the low concentration of free carriers in the semiconductor, the electric field at the metal-semiconductor interface is not screened. This electric field results in a depletion of the carrier concentration at the surface of the semiconductor when $\phi_m > \phi_s$. Carrier concentration becomes smaller at the surface than in the bulk. In this process, a depletion layer is formed (see figure **1.5 c**). In the case where $\phi_m < \phi_s$ the electrons accumulate in the surface of the semiconductor, forming

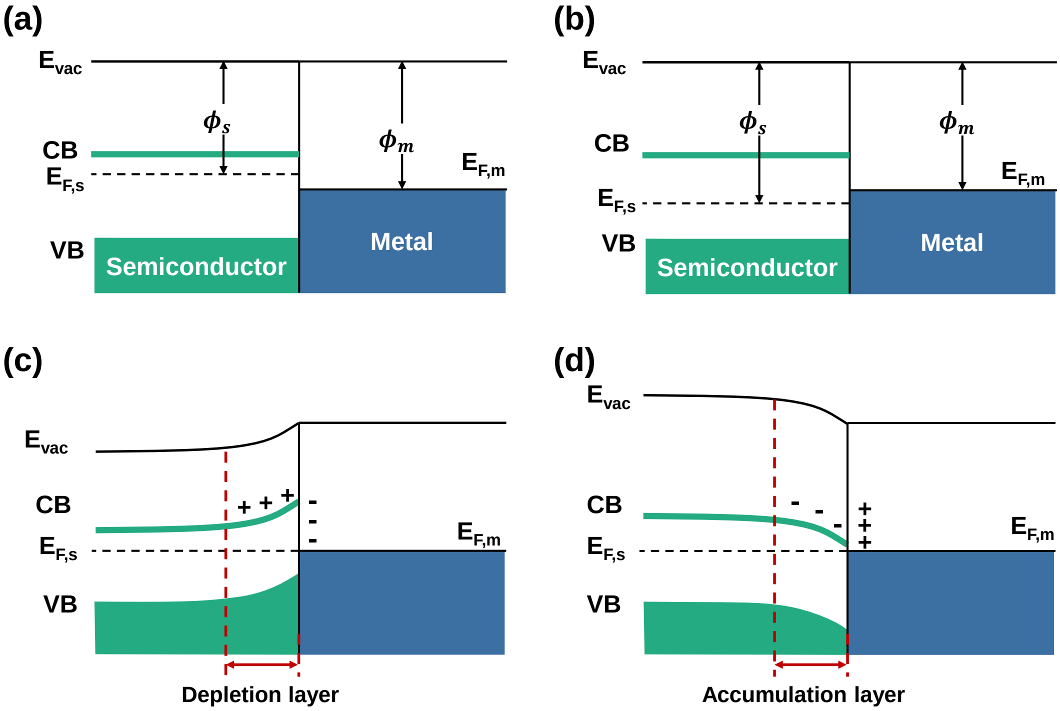

Fig. 1.5: Adapted from [11]. Metal-semiconductor contact out of the equilibrium with $\phi_m > \phi_s$ (a) and $\phi_m < \phi_s$ (d). The electrons transfer between the materials until the Fermi levels are align, causing a charge depletion (c) or accumulation (d), bending the bands in the process.

an accumulation layer (figure **1.5 d**). In the energy space, the bands shift as a function of the position due to the electric field between the semiconductor and the metal. This effect is called band bending.

An external electric field can also induce a band bending at the surface of a semiconductor which has a metal at such a small distance that electrons can tunnel between the metal and the semiconductor. To see this, let us assume for simplicity that the work functions of the metal and the semiconductor are equal (figure **1.6 a**). When a bias voltage is applied to the metal, an electric field is set up between the metal and the semiconductor. This electric field can penetrate a region near the surface of the semiconductor due to the small screening by the low concentration of carriers. Depending of the direction of the voltage applied, the band bends downwards (figure **1.6 b**) or upwards (figure **1.6 c**). When taking into account that the work function is not the same, the picture does not change qualitatively. There is just a shift in such a way that there is no band bending when the applied voltage compensates for the work function difference.

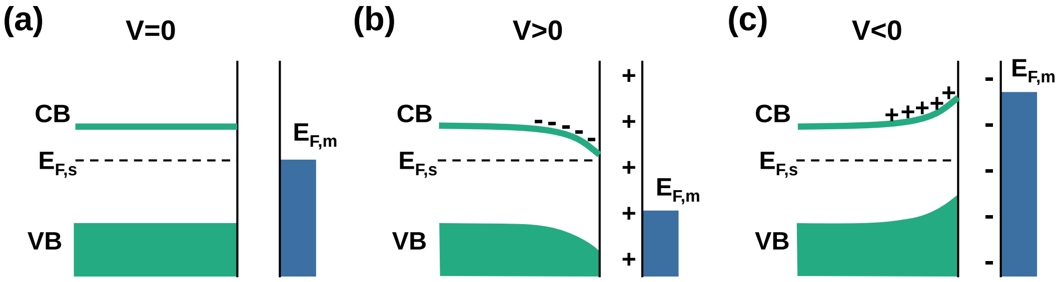

Fig. 1.6: Adapted from [11]. Band bending process of a semiconductor due to an external electric field, when $\phi_m = \phi_s$.

A direct consequence is that a metallic electrode put in connection with a semiconductor might produce a surface potential. In particular, any electrode that is used to measure a tunneling current eventually acts invasively and modifies the band structure of the semiconductor by bending the conduction and valence bands. This is important in Scanning Tunneling Microscopy (STM), where one electrode has a tip geometry which is located at tunneling distances on top of the semiconducting sample. The STM tip then can modify the band structure locally during scanning.

1.2.2 Charging by a STM tip

Figure **1.7** shows two conductance maps taken with different voltages, where a ring-like feature can be seen surrounding a defect. Note that the size of the ring changes with the voltage applied. As we shall see now, the ring like structure is a consequence of a localized state at an energy inside the semiconducting gap. The energy of the localized states is modified by the gating through the bias voltage applied to the tip [12–17].

The band bending described at the beginning of this section can also affect the donor and acceptor states created by impurities. Let's consider the case of a donor impurity, indicated with the red line in figure **1.8**. This figure schematically represents the energy variation of the top and bottom of the bands when the tip is nearby, as a function of the bias voltage. When the

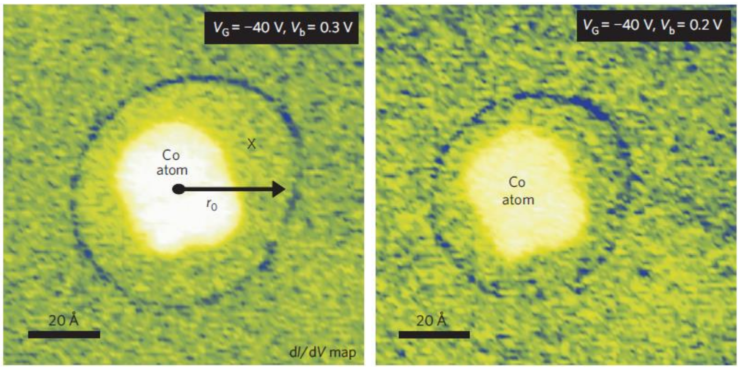

Fig. 1.7: Adapted from [12]. Conductance maps showing a ring-like shape around a cobalt adatom on a graphene surface. The size of the ring changes with the applied voltage, indicating a tip-induced effect.

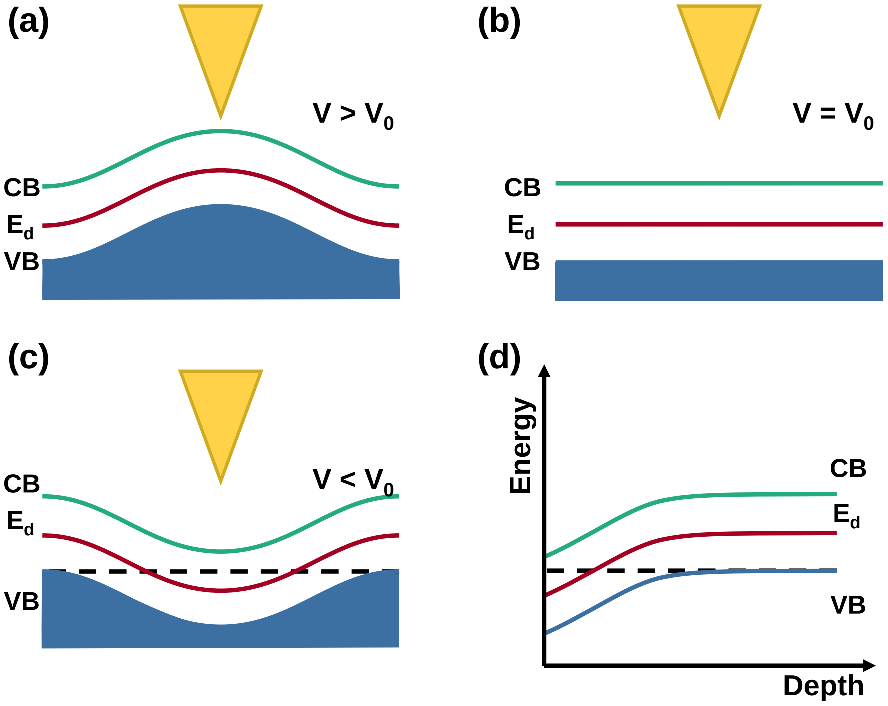

Fig. 1.8: Band bending process of a valence band (VB), a conduction band (CB) and a donor state (E_d). (a-c) The form of the bands depends on the applied voltage V in relation to the voltage necessary to compensate the work functions of the semiconductor and the tip, V_0. (d) Schematic representation of the band bending process as a function of the depth.

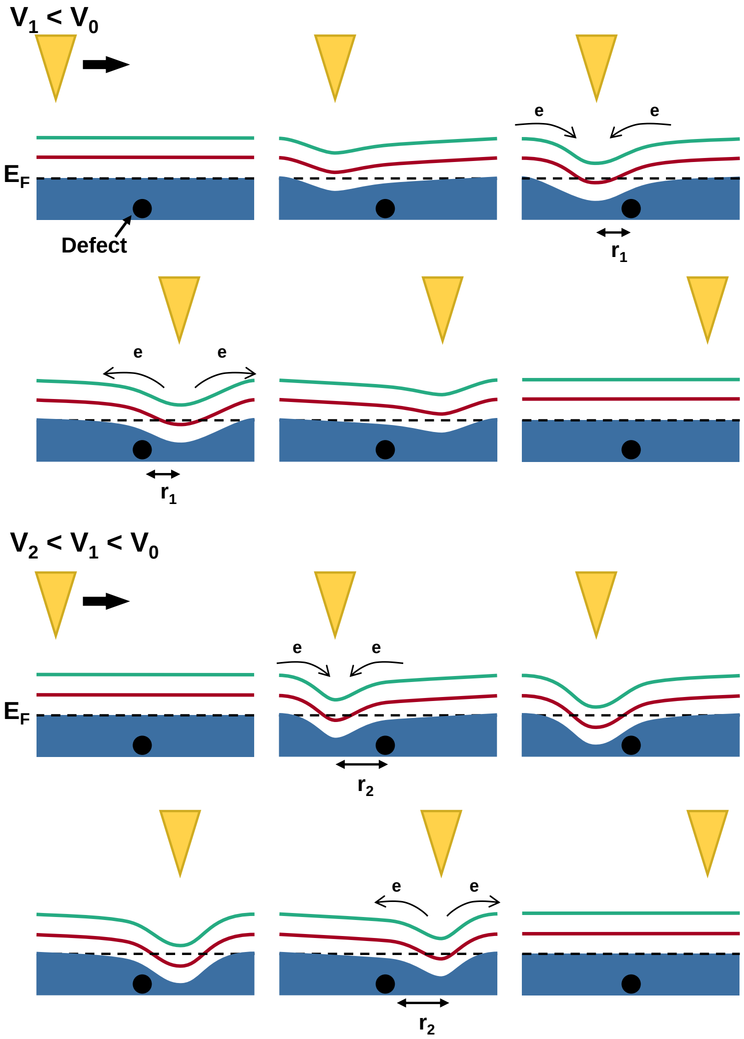

Fig. 1.9: Ring-like feature formation due to tip effects. The movement of the tip bends the bands and the donor state, creating a ring-like feature that depends on the voltage applied.

bias voltage applied is larger than the voltage V_0 necessary to compensate the work function difference between the tip and the semiconductor, the bands bend upwards (figure **1.8 a**). When both voltages are equal, the bands are flat (figure **1.8 b**). In both cases, no particular feature is expected in the conductance. However, when the voltage is low enough that the bands bend downwards, the donor state E_d crosses the Fermi level (figure **1.8 c**). Electrons must then fill the state, resulting in a sharp change in the tunneling current. Figure **1.8 d** shows the variation of the position of the bands in energy as a function of the depth in the material, in analogy to figure **1.6**. This means that this effect is only visible in defects at the surface or near the surface.

To see the formation of the ring-like signal formed during this process, we can picture the band bending process as a function of the tip position with respect to the defect. First, we consider a certain $V_1 < V_0$ where the bands bend downwards. When the tip is far enough, the bands at the position where the donor state appears do not bend. When the tip gets closer to the defect (at the center), the bands bend until the donor state E_d lies below the Fermi level. At this moment, electrons "jump" at E_d, filling the state. This is measured by the tip as a sharp signal in the conductance. The tip continues to move and the electrons empty E_d when this level is about to move above the Fermi level, leading to the same sharp feature than before. This process is schematically represented in figure **1.9** and occurs in all directions surrounding the area where E_d exists, creating the ring-like feature. For a smaller voltage $V_2 < V_1 < V_0$, the bands bend more, and E_d crosses E_F for larger distances from the defect, making the ring feature to have a bigger radius, as represented in figure **1.9**.

1.3 Band inversion and topological features of semimetals

Topology is a branch of mathematics that studies the materials under continuous deformations, such as distortion, but not breaking. A typical example of two topologically different objects is the comparison between a cylindrical loop and the Moebius loop, presented in figure **1.10**. In a normal cylindrical loop, there are two surfaces and two edges. A Moebius loop, however, has only one surface and one edge. It can be easily seen that it is impossible to change between these two loops using continuous deformations: if we want to obtain one starting from the other one, we need to break the loop, twist it, and glue it again. This means they have different topologies.

In analogy to this example, topological materials are those whose electronic structures have some features that do not change without breaking the nature of the material.

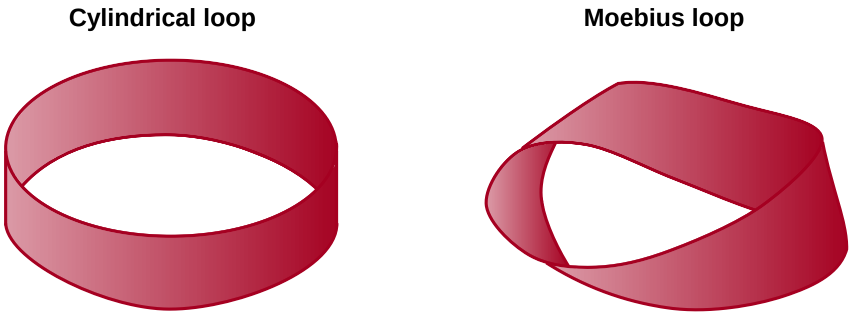

Fig. 1.10: A cylindrical loop and a Moebius loop. These two objects have different topologies, and it is impossible to obtain one from the other only by continuous deformations.

The first experimental example of a topological state was the integer quantum Hall effect [18] in 1980 by Klaus von Klitzing, who won the Nobel Prize in 1985 [19]. He discovered that, when measuring the Hall effect in a 2D electron gas at high magnetic fields, the result was a quantized conductivity. This is the result of gapless states at the sample edge that form chiral channels. But the classification of materials according to their topology started with the discovery of topological insulators that, analog to the quantum Hall effects, possess conducting states only at their edges.

1.3.1 Band inversion and topological surface states

In semiconducting and ionic materials, the conduction band is usually formed by the s electrons, while the p and d electrons form the valence band. In materials containing heavy elements, s-orbitals can experience an attractive potential until they lie lower in energy than the p or d bands. Thus, these materials have an inverted orbital band character. Band inversion was predicted in HgTe quantum wells in CdTe [20]. The CdTe band structure is represented in figure **1.11 a**, and consists of s states (blue) above the p-type band (red). However, in HgTe, the band character is inverted: the s-type band lies below the p bands (see figure **1.11 b**). The band inversion leads to topologically protected edge states and spin quantum Hall effect.

The band inversion can involve any pair of orbital characters. Figure **1.12 a** represents two bands with different orbital character crossing at the Fermi

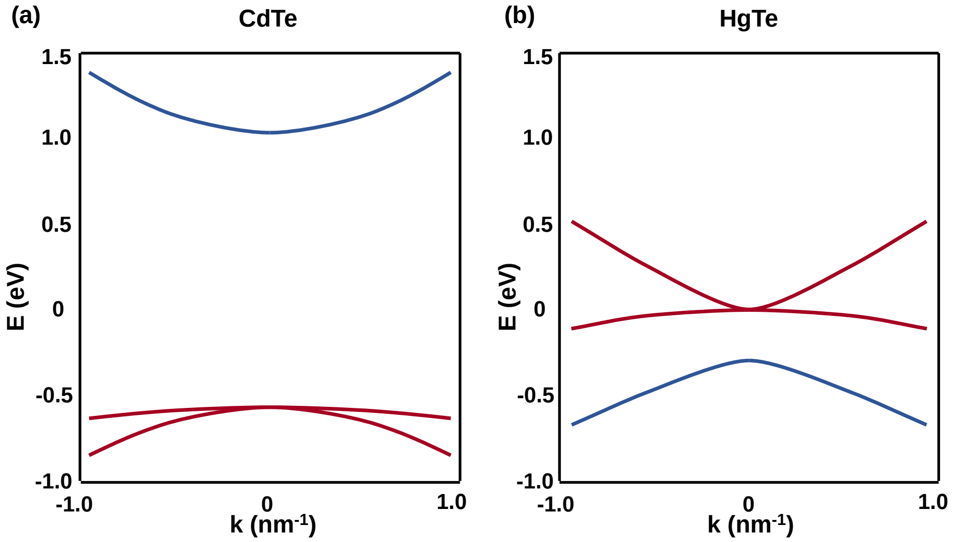

Fig. 1.11: Adapted from [20]. (a) Band structure calculations for CdTe, where the band with orbital character s (blue) is above the bands with orbital character p (red). (b) Bandstructure calculations for HgTe, where the orbital character is inverted.

level. Spin orbit coupling (SOC) opens a gap at the band crossing, leading to a band inversion. Band inversion implies surface states imposed by topology. Because the parity must be maintained in vacuum, there must be a parity transformation at the surface where band inversion is lost. Eventually, the upper s-type band crosses zero energy at the surface and becomes a lower lying s-type band in the vacuum close to the surface. Conversely, the lower p-type band crosses zero at the surface and becomes the usual upper p-type band in the vacuum [21]. This leads to surface zero energy states which are topologically protected. When the gap is completely opened, we have a Dirac cone at the surface (figure **1.12 b**). When the gap is not open, we have an arc connecting band crossing points of the bulk where the parity is inverted (figure **1.12 c**).

Topological insulators

When the SOC completely gaps the band structure of the material, the result would be an insulator. However, in topological insulators (TI), the surface is metallic due to the presence of surface states, represented by the dotted lines in figure **1.12 b**. These surface states are topologically protected

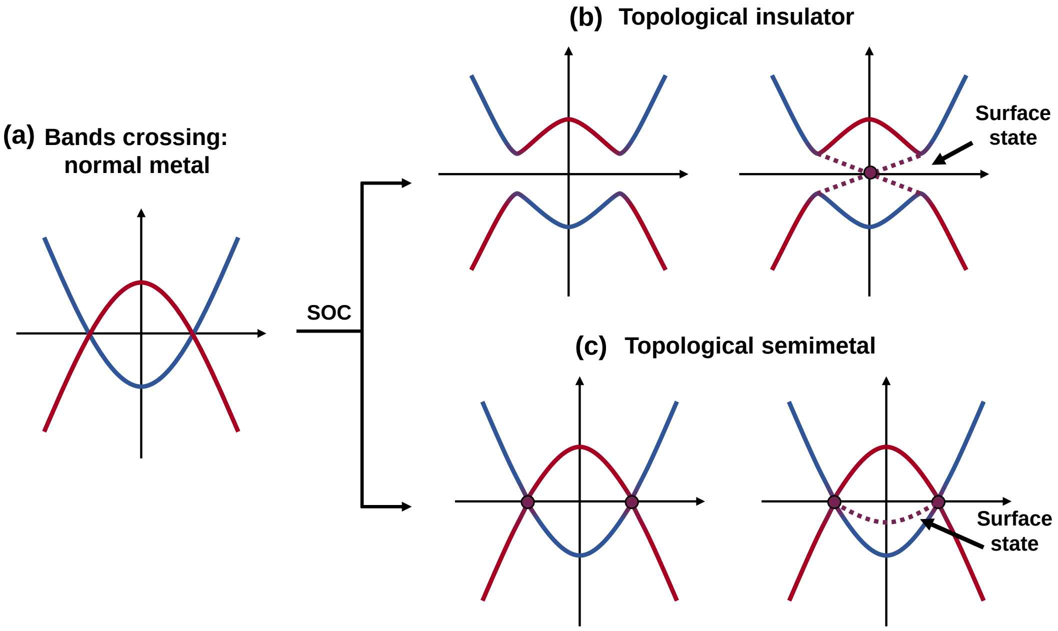

Fig. 1.12: Adapted from [22]. Gap opening due to spin-orbit coupling and formation of surface states. (a) Two bands with different orbital character cross at the Fermi level at some point in the Brillouin zone. The two bands are gapped due to strong spin-orbit coupling (SOC), leading to topological insulators (b) or topological semimetals (c).

and contain 2D Dirac points [23]. Dirac points are named as such because they are formed by electrons that can be described using the Dirac Hamiltonian for massless electrons. Thus, the energy dispersion around these points is linear. Topological protected surface states have been measured in many topological insulator materials [24–27].

Topological semimetals

When there are some points in the Brillouin zone where the bands touch, the material is a topological semimetal (figure **1.12 c**). The bulk crossing points in these materials are topologically protected and can be described using the Dirac or Weyl Hamiltonians for massless fermions [28]. Weyl points always appear in pairs with opposite Chern number corresponding to the two forms of the Weyl Hamiltonian and they can be defined as Berry curvature monopoles that act as a sink and a source [29]. Dirac points are the sum of two Weyl points with opposite Chern number at the same point in the band structure, making their topological number zero. The difference between Weyl and Dirac semimetals comes from symmetry [23]. Under inversion symmetry and time-reversal symmetry, every state in the Brillouin zone is degenerate. Thus, the linear crossing points can only be Dirac points. In crystals without an inversion center, in magnetic crystals and when applying a magnetic field, the Dirac points turn into Weyl nodes and we say that the material is a Weyl semimetal [30].

Some Weyl materials have been experimentally confirmed, such as the TaAs family [31–34], or predicted to be Weyl semimetals, such as $MoTe_2$ [35–37], $YbMnBi_2$ [38] and LaAlGe [39].

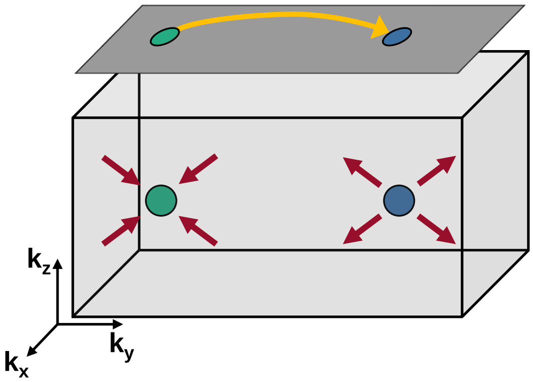

Fig. 1.13: Schematic representation of a Fermi arc (yellow) connecting the protections of two Weyl points (green and blue). Different colors in the Weyl points represent opposite Chern numbers. Red arrows indicate the Berry flux direction.

One manifestation of a Weyl semimetal is the presence of surface states known as Fermi arcs, that connect the projections of the Weyl points at the surface (see figure **1.12 b**). Fermi arcs can be measured using different surface-sensitive experimental techniques, such as ARPES [33, 36, 40–42] and quasi-particle interference (QPI) [36, 43, 44].

Fermi arcs appear as an open contour in the surface Fermi surface, with its edges located at the projections of the Weyl points in the surface [45]. Open contours such as the Fermi arcs show some characteristic features in the QPI maps, that will be discussed in chapter 2.4.1. Figure **1.13** represents two Weyl points of opposite Chern number as a green and blue dot in the momentum space. As mentioned before, they act as a source and a sink of the Berry curvature, represented by the red arrows. The Fermi arc is represented in yellow on surface Fermi surface, and connects the projection of both Weyl points.

1.4 Superconductors

Superconducting materials[2] are those whose resistance is exactly zero below a characteristic temperature, called critical temperature, T_c. Superconductivity was observed for the first time by Heike Kamerlingh Onnes in 1911. After being able to liquefy Helium for the first time in 1908, he measured the resistance of solid mercury at cryogenic temperatures. Around 4.2 K (the temperature of liquid He), the resistance of Hg abruptly vanished [49]. In 1913, Onnes received the Nobel prize for his investigations on the properties of matter at low temperatures [50]. In the next decades, superconductivity was observed in many materials.

Superconducting materials can be classified in two types. Type I superconductors present the Meissner effect[3] until the magnetic field is large enough and the material is not longer in the superconducting phase. The evolution of the critical magnetic field with the temperature follows the representation in figure **1.14**. Type II superconductors present Meissner phase until a first critical magnetic field of H_{c1}. When H exceeds this value, the superconductor enters the mixed phase and has regions where the magnetic field can penetrate the material. In these regions the material is normal, while in the rest is superconducting. This phase is known as mixed or Shubnikov phase [51] and the areas where the magnetic field can penetrate are known as vortices. Type II superconductors enter the normal phase when the magnetic field increases above a second critical field H_{c2}. Critical magnetic field *versus* temperature is represented in figure **1.14**.

---

[2] This section follows the explanations of the superconductivity books written by Schmidt [46], Tinkham [47] and Annett [48].

[3] The Meissner effect is the expulsion of the magnetic field from the interior of a superconducting material below T_c.

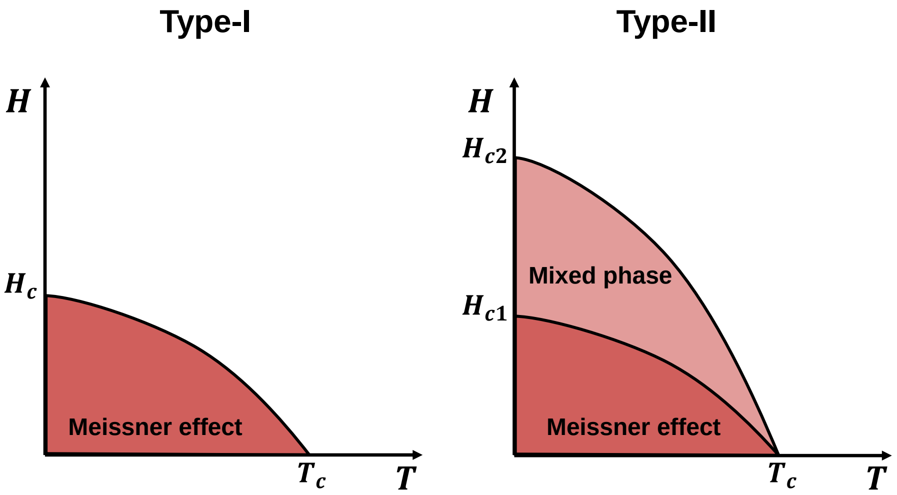

Fig. 1.14: Magnetic field *versus* temperature diagram for type-I (left) and type-II (right) superconductors. For both types of superconducting materials, the Meissner effect is present until a critical magnetic field. For higher magnetic fields, type I superconductors enter the normal phase, while in type II vortices appear in the so-called mixed phase. This phase has also a critical field where the superconducting state disappears.

The vortices in type II superconductors are quantized. The quantization is such that the magnetic flux through each vortex is a quantum of flux

$$\Phi_0 = \frac{\hbar}{2e} = 20.7 \times 10^{-15}\ Wb, \tag{1.23}$$

where h is the Planck constant. These vortices have a normal core of radius of the order of the coherence length, ξ, where the order parameter Ψ is zero. Around the vortex core, the superconducting electrons form supercurrents that circulates in an area of the order of the penetration length, λ, around the core. A schematic representation of an isolated vortex and its characteristics lengths is shown in figure **1.15 a**.

The interaction between vortices is repulsive, and they arrange forming a triangular lattice, as represented in figure **1.15 b**. As the magnetic field rises, the density of vortices in the material increases and the intervortex distance decreases, until, for $H \geq H_{c2}$, the material enters the normal phase.

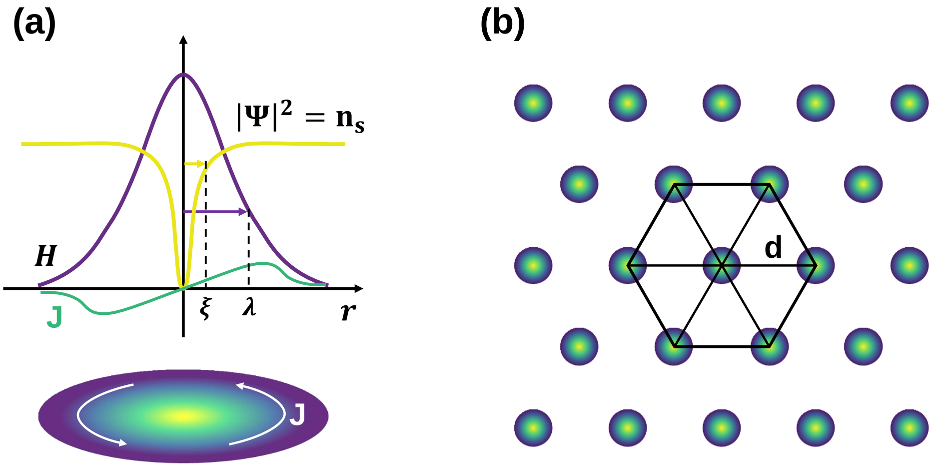

Fig. 1.15: (a) Schematic representation of an isolated vortex. Variation of the order parameter (yellow), magnetic field (purple) and the superconducting current (green) in the vortex are represented. (b) Schematic representation of the top view of an Abrikosov vortex lattice.

1.4.1 Electron-electron attraction and BCS theory

The microscopic mechanism of the superconductivity was proposed to be originated by phonon-mediated electron-electron interaction. This mechanism is represented in figure **1.16**. We consider two electrons (red) moving through a crystal. The negative charge of the electrons attracts positive ions in the crystal (blue). This enhances the positive charge and excites a phonon (see figure **1.16 a**). A second electron traveling trough this area is attracted by the positive charge accumulation, absorbing the phonon (see figure **1.16 b**). A pair of electrons can have a bound state if there is an attractive force stronger than the Coulomb repulsion [52]. The energy of this bound state is smaller than E_F, and they are known as Cooper pair. The BCS theory extends the Cooper pair formation for all conduction electrons.

1.4.2 Superconducting gap, magnitude and T dependence

In the BCS theory, the fundamental state of the superconducting material is described by a macroscopic wave function that keeps the coherence in a distance of the order of ξ. This distance can be related to the spatial extension

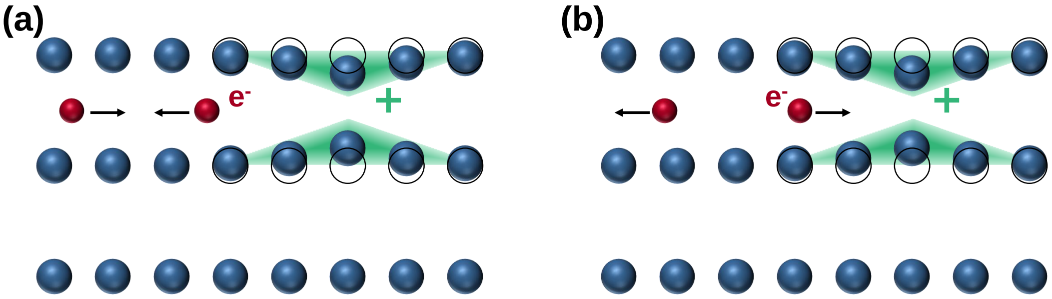

Fig. 1.16: Schematic representation of the phonon mediated electron-electorn pairing. (a) An electron traveling through the crystal attracts the positive ions in the crystal, exciting a phonon. (b) The accumulation of positive charge attracts a second electron that absorbs the phonon.

of the Cooper wave function. The BCS description of the superconducting ground state leads to the relation that describes the excited states of the system

$$E_k = \sqrt{\epsilon_k^2 + \Delta^2}, \tag{1.24}$$

where $\epsilon_k = \hbar^2 k^2/2m - E_F$ is the kinetic energy respect to the Fermi level and Δ is a constant. From this equation we can see that for an arbitrary small ϵ, the energy will be Δ above E_F. Thus, Δ indicates a region in energy where no states are allowed, the superconducting gap. The BCS theory establishes a temperature dependence of this gap

$$\Delta = 1.764 k_B T_c, \tag{1.25}$$

where k_B is the Boltzman constant. Figure **1.17 a** shows the dependence of the superconducting gap as a function of the temperature. As the electrons close to the Fermi level form Cooper pairs, the energy needed to break a pair is 2Δ. For larger energies, the normal metallic band structure is recovered.

Taking into account that the density of states in the superconducting transition does not change, we have

$$N_n(\epsilon_k) d\epsilon_k = N_s(E_k) dE_k, \tag{1.26}$$

where N_n and N_s are the normal and superconducting density of states, respectively. Using Eq. 1.24, we can write

$$\frac{N_s(E)}{N_n(0)} = \begin{cases} 0, & E < \Delta \\ \frac{E}{\sqrt{E^2 - \Delta^2}}, & E > \Delta \end{cases} \tag{1.27}$$

The dependence of the superconducting density of states normalized to the normal density of states is represented in figure **1.17 b**.

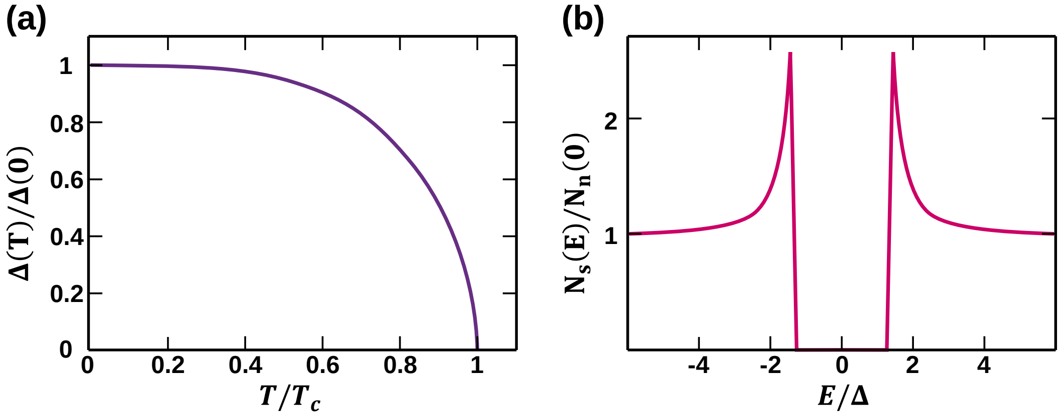

Fig. 1.17: (a) Temperature dependence of the superconducting gap normalized at $T = 0K$. (b) Superconducting density of states N_s normalized to the normal density of states N_n as a function of the energy.

Near T$_c$, Ginzburg-Landau equations can be derived from the BCS theory, and the order parameter Ψ is proportional to the superconducting gap Δ. The characteristics lengths ξ and λ can be written

$$\xi(T) = 0.74\xi_0\left(\frac{T_c}{T_c - T}\right)^{1/2}, \tag{1.28}$$

$$\lambda(T) = \frac{1}{\sqrt{2}}\lambda_L(0)\left(\frac{T_c}{T_c - T}\right)^{1/2}, \tag{1.29}$$

where $\lambda_L^2(0) = \frac{3c^2}{8\pi e^2 v_F^2 N(E_F)}$ and $\xi_0 = \frac{2\hbar v_f}{\Delta}$ from the BCS theory.

1.4.3 Two-band superconductivity

While in one band superconductors, pairing only occurs between electrons in the same band, different gaps of different sizes can appear in the Fermi surface of multiband superconductors [53] such as MgB$_2$ [54–57]. In this case, Cooper pairs might form through electron-phonon interaction within the same band (intra-band) or different bands (inter-band). The size of the gap can change

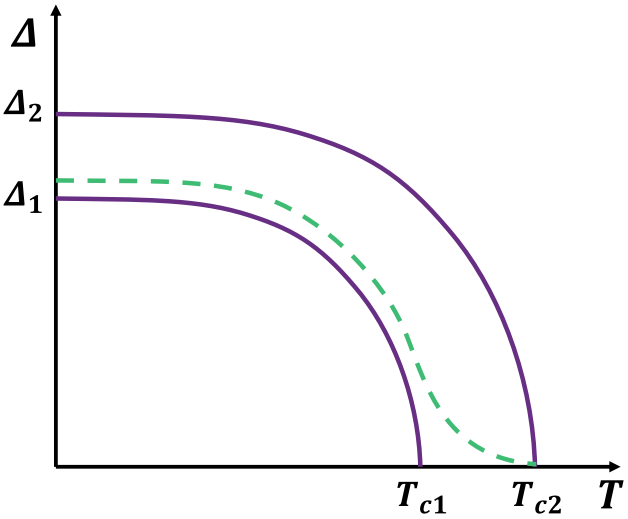

Fig. 1.18: Temperature dependence of a two gap superconductor with Δ_1 and Δ_2. Purple lines indicated the BCS dependence for the two gaps. The interband scattering modifies the T_c of the smaller gap, that deviates from the BCS theory (green dotted line).

depending on the strength of the electron-phonon interaction in different portions of the Fermi surface. This is known as multi-band superconductivity.

If we neglect interband scattering and we take the unphysical situation of two completely separate bands, there are two critical temperatures. A real material shows certainly band interactions (for example interband scattering) and has only one critical temperature. Nevertheless, the temperature dependence of the superconducting gap is influenced by the interband interactions.

1.4.4 Anisotropic superconductivity

In the BCS theory, the s-wave order parameter is isotropic for a spherical band Fermi surface and the value of the gap Δ is a constant. However, it is possible to have an anisotropy in the gap in k-space if there is anisotropy in the electron-phonon interaction. Some materials can present more complicated gap anisotropies, where the gap can even be zero at some points in the k-space. Studies on the ^{3}He superfluidity showed the possibility of pure fermion-fermion interaction forming a condensate [58–60]. In this case, the angular momentum of electrons L is different from zero, and the BCS gap equation decouples into independent paring channels for L = 0, 1, 2, ... Thus, some channels may present attractive interactions even if the fermion-fermion interaction is repulsive. Unconventional superconductivity arises when at least one of these channels presents a superconducting transition at a certain T$_c$ [61]. The Coulomb interactions are minimized due to the sign changes in the gap function, which may involve pair wavefunctions with L ≠ 0. The time scale of electronic fluctuations is comparable to the motion of the electrons, making paired electrons use space instead of time to avoid Coulomb repulsion. This results in a highly anisotropic gap function in momentum space that can even have nodes when the sign changes. For example, in cuprates L = 2, so they present a *d*-wave gap function with nodes, showing $d_{x^2-y^2}$ superconductivity [62, 63] (see figure **1.19 b**).

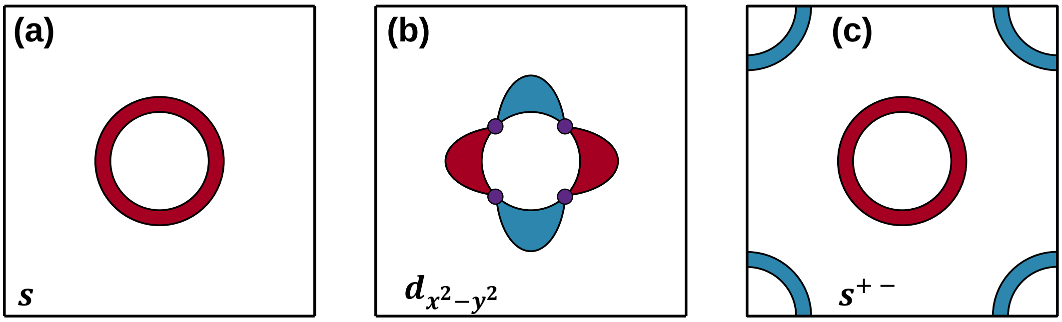

Fig. 1.19: Comparative between gaps with different symmetries. Red and blue color indicated different sign. (a) Isotropic BCS gap. (b) $d_{x^2-y^2}$ gap, where nodes are marked as purple dots. (c) s^{+-} gap.

In multiband systems such as iron-based superconductors (FeBSCs), instead of a pair wavefunction with finite angular momenta, it is assumed that the wavefunction changes sign on different sheets of the Fermi surface. In figure **1.19 c** an example of a two band model is shown. Here, the band in the center of the Brillouin zone (usually a hole pocket) and the band in the outer sheets (usually an electron pocket) are both isotropic, but they present different relative signs. This state is known as s^{+-} and, although it does not have nodes, it shares with the $d_{x^2-y^2}$ the change in sign. s^{+-} symmetry is the most accepted scenario for the majority of FeBCSs.

Furthermore, some superconducting systems share the same low energy excitation characteristics of topological insulators, presenting a topologically protected surface state. For example, spin triplet $p + ip$ wave superconductors [64].

1.5 Superconductivity and magnetism in Fe based systems

In 1986, J. G. Bednorz and K. A. Muller discovered the high critical temperature superconductivity in cuprates [65]. In these materials, the pairing mechanism is different from the conventional phonon-mediated explained by the BCS theory. Thus, they are know as unconventional superconductors. Materials in the cooper-oxide family become superconducting at critical temperatures as high as 130 K [66]. In 2006, a new family of unconventional superconductors was discovered. That year, the first iron-based superconductor discovered was LaFePO, with a $T_c = 4$ K [67]. However, the discovery of $LaO_{1-x}F_xFeAs$ in 2008 [68], with a T_c of 26 K, opened the study of iron-based superconductors, whose properties challenged the uniqueness of cuprates as high T_c superconductors [67, 68]. Fe-based materials belong to the group of unconventional superconductors, where the pairing mechanism is not the conventional BCS phonon coupling. They can have critical temperatures in bulk crystals as high as 55 K [69, 70], and critical magnetic fields that reach 60 T [71].

FeBSCs are formed when combining Fe with pnictogens (P, As) or chalcogens (S, Se, Te). They can be classified in families, depending on the stoichiometric relation between the elements: 11 (FeSe), 111 (LiFeP), 1111 (LiFePO), 122 (KFe_2As_2), etc. All of them share a layer formed by a square lattice of Fe atoms bond to the pnictogens or chalcogens. These layers have quasi-two-dimensional character and can be stacked together (for example in FeS or FeSe) or separated by one or several layers of other atoms [72, 73]. Similar to cuprate superconductors where superconductivity emerges in the CuO planes, it is thought that the superconductivity in FeBSCs originates in the iron layers.

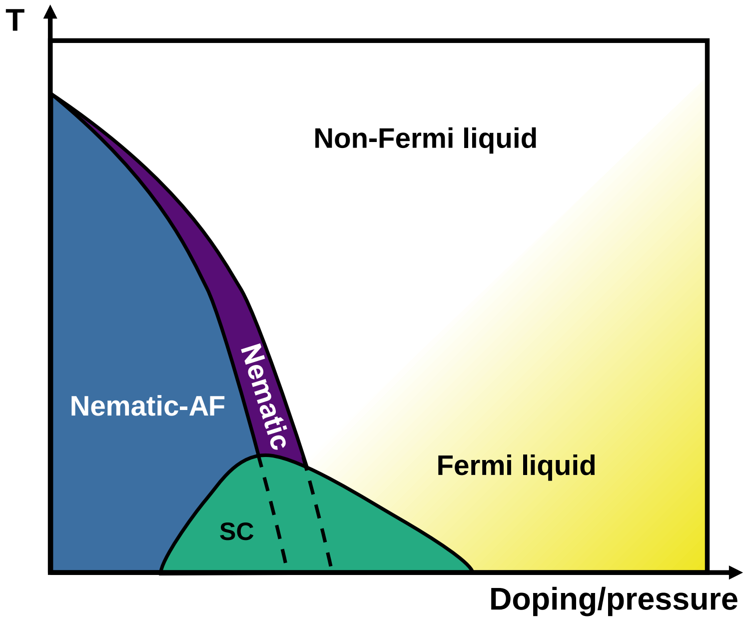

Fig. 1.20: Generic temperature vs doping/pressure diagram of Fe-based superconductors. In general, these materials have an AF phase with strong nematic properties in the stoichiometric compound. When doping or applying pressure, AF disappears first and then nematicity. When suppressing nematic and AF order, superconductivity emerges. Often, the maximum value of T_c is close to the extrapolation of the AF and nematic lines to zero temperature.

1.5.1 Phase diagram of high Tc superconductors

Most of these materials are usually antiferromagnetic (AF) in stoichiometric compounds. The magnetic phase disappears with electron or hole doping or under pressure. In the pnictides, a nematic phase appears in connection to AF. The nematic and AF transitions are often associated to a structural transition. The crystal structure changes from a high temperature in-plane symmetric (tetragonal) phase to a low temperature in-plane anisotropic orthorhombic phase. Superconductivity is found in the low temperature portion of the phase diagram. Often, the critical temperature is highest when the magnetic and nematic phase transitions vanish at zero temperature.

FeBSCs are correlated systems with multiband superconductivity, where the Cooper pair wavefunction changes its sign in different areas of the Fermi surface (see figure **1.19** in previous section). In the most accepted scenario, the superconductivity occurs thanks to spin fluctuations with the antiferromagnetic vector connecting electron and hole pockets.

Only a few stoichiometric compounds are found to be superconductors (see Table **1.1**). This is the case of the FeSe, whose superconductivity was reported only two months after the 122 systems [74]. This material attracted much attention due to its structural simplicity. Although the critical temperature is not very high, this material is a good candidate for studying the interplay between superconductivity and nematicity in absence of magnetism.

Compound	**T_c (K)**	**Reference**
FeS	5	[75]
FeSe	8.5	[74]
LiFeP	6	[76]
LiFeAs	18	[77]
LaFePO	6	[78]
KFe_2As_2	3.8	[79]
$CaKFe_4As_4$	35	[80]

Table **1.1**: Stoichiometric Fe based superconductors. Critical temperatures and references are indicated.

Some FeBSC can present topological states coexisting with the superconductivity [81]. This is the case for Fe(Te,Se), where a band with orbital character *p* appears near the Fermi level, leading to a band inversion and topological superconductivity [82].

1.5.2 Electronic properties and band structure

The main electronic properties of this family of materials at the Fermi level are derived from the Fe *d*-electron orbitals. Several bands cross the Fermi level, resulting in multi-band materials dominated by the iron d_{xy}, d_{xz} and d_{yz} orbitals [83]. The Fermi surface is usually formed by quasi-2D electron and hole cylinders. Two or three hole pockets are located at the center of the

Brillouin zone Γ. Two electron pockets are located at X point (π, 0) and Y point (0, π) positions in the tetragonal unit cell [83] (see figure **1.21 b**).

Pnictogen or chalcogen atoms in the layers above and below the Fe layer occupy non-equivalent positions in the low temperature magnetic and/or orthorhombic phase, resulting in a folding of the Brillouin zone to include two Fe atoms in the unit cell [84]. Electron pockets are set at the $\tilde{M}$ point (π, π) of the new unit cell by the folding vector (figure **1.21 c**) [83].

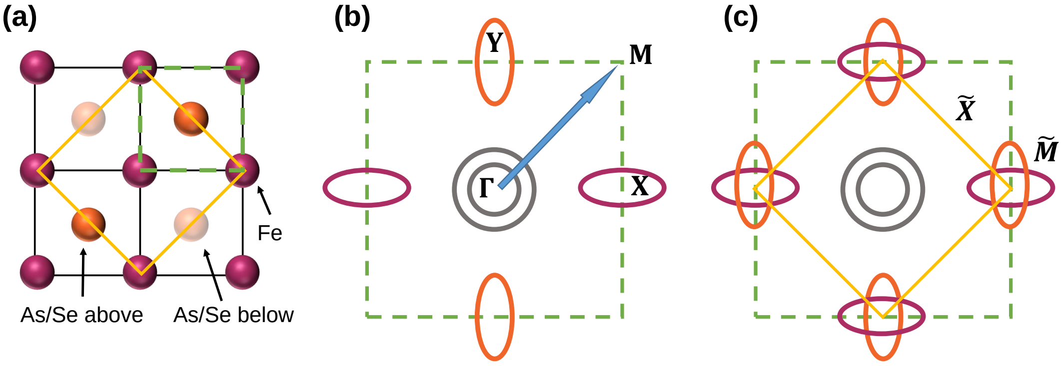

Fig. 1.21: Adapted from [83]. (a) Top view of the unit cell of an iron-based superconductor. Dashed green line and solid yellow line indicate the 1-Fe and 2-Fe unit cells, respectively. (b) Schematic Fermi surface on the 1-Fe Brillouin zone. Gray circles indicate hole pockets and purple and orange ellipses indicate electron pockets. The blue arrow indicates the AF vector along which there is a band folding in the magnetic/nematic low temperature phase. (c) Folded BZ, whose boundaries are now the yellow lines.

Superconductivity with s^{+-} symmetry requires electronic interaction to be stronger between different pockets than within them [73, 85]. Spin fluctuations have been consensually established as the main mechanism behind the inter-pocket interaction as the q vector of the spin density wave ground state coincides with the distance between electron and hole pockets in reciprocal space.

1.5.3 Nematicity

Nematic order in FeBSC breaks the rotational symmetry, while the translational symmetry remains [73, 86]. Various mechanisms can produce this transition and, in general, order parameters related with the lattice, orbital and spin order can be defined.

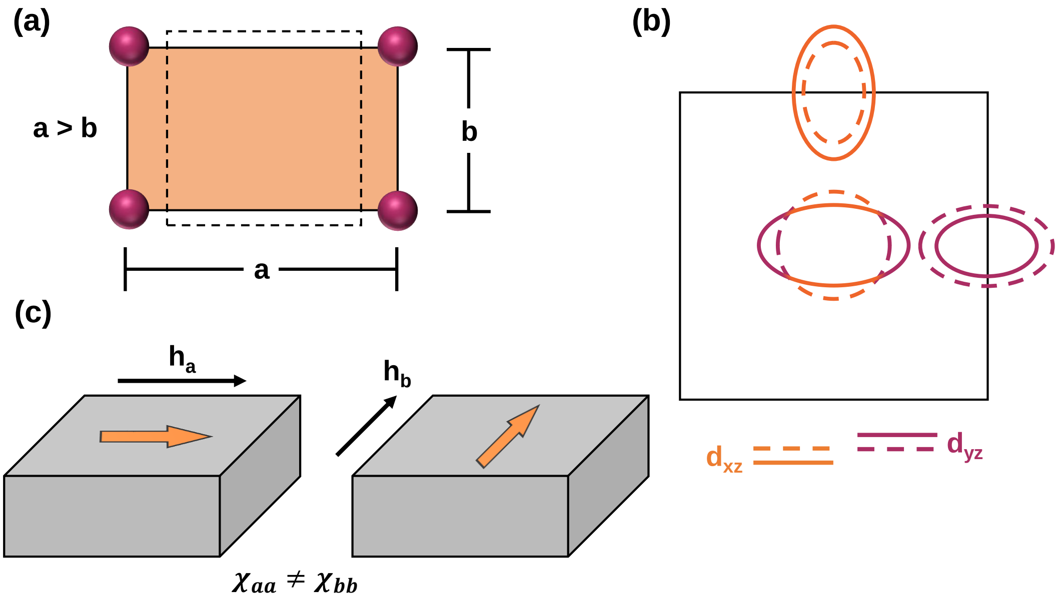

Fig. 1.22: Adapted from [86]. Breaking of the different order parameters in the nematic phase. (a) Unit cell structural distortion making $a \neq b$. (b) d_{xz} and d_{yz} orbitals splitting. (c) Uniform spin susceptibility anisotropy.

In the nematic phase, the rotational symmetry breaks by making the x and y directions non-equivalent in the Fe plane, resulting also in a tetragonal to orthorhombic transition ($a \neq b$). The difference between a and b is generally very small in FeBSC, a few 0.01 % [87, 88]. This is accompanied by a change in the orbital character that occurs when the degeneracy between d_{xz} and d_{yz} Fe-orbitals is lifted at the nematic transition, producing a two-fold distortion in the Fermi pockets. Finally, the spin order changes as the static spin susceptibility becomes different along the q_x and q_y directions of the BZ [86]. At the low temperature phase, orbital, magnetic and structural degrees of freedom are modified. We can define three order parameters, all of which have been shown to evolve inside the low temperature phase [86]. Figure **1.22** represents the order parameter change in the nematic phase for the three orders parameters.

1.6 Scope

In the following chapters, I will present the work accomplished during my PhD thesis. Many recent discoveries in condensed matter physics rely on the connection of electronic structures and topology. By using STM, I have studied magnetic and non-magnetic Weyl semimetals and a superconductor, all having few states at the Fermi level. From my measurements, I obtained new insight due to the peculiar properties of the band structure and the number of states close to the Fermi level in each system.

In chapter 3, I studied the band structure of WTe_2, a semimetal where the density of electron and hole bands is nearly exactly equal. I will show detailed measurements of the Landau quantization of the bands when a magnetic field is applied. These measurements give information about the bulk band structure and surface states.

In chapter 4, I present measurements in $Co_3Sn_2S_2$, a layered magnet with a kagome lattice that produces a flat band. I measured the effect of isolated Sn atoms on the flat band and electronic end states at chains of Sn formed at the surface.

In chapter 5, I studied the magnetic semimetal $EuCd_2As_2$, where we find an insulating surface. At this surface, impurities create discrete quantized states spanning distances of several tens of nm. Under magnetic fields, the states are further quantized due to Landau quantization.

Finally, in chapter 6, I studied the superconductor FeSe, where a transition to an orthorhombic state produces a highly anisotropic semimetal. I characterized the bulk band structure using quasiparticle interference and found a localized state on the defects. In this material, we find a behavior that is unique to semiconductors or insulators, in a good metal.

In all, this work provides a bridge from a material with practically no correlations (WTe_2) but a topologically non-trivial band structure, to a material (FeSe) where electronic correlations are dominating nearly all observables.

Correlations are also important in $EuCd_2As_2$ to explain magnetic interactions and in $Co_3Sn_2S_2$ through the geometrical properties of the kagome lattice. We thus see that the tunneling conductance at the surface addresses relevant issues in the band structure of solids, obtaining a picture that encompasses radically new electronic properties.

Chapter 2

Experimental Techniques

The Scanning Tunneling Microscope (STM) was designed and developed by Gerd Binning and Heinrich Rohrer in 1981 at IBM [89]. This powerful invention marks the beginning of the studies at the nanoscale level. The huge impact of this technique is reflected in the Nobel Prize both scientists received in 1986 [90]. Over the last 40 years, the STM has proved to be an extremely powerful and versatile tool, applied to several fields in condensed matter and applied physics.

In this chapter, I will review the principles of the Scanning Tunneling Microscopy at very low temperatures and high magnetic fields. I will describe the experimental set-up needed for measuring in such conditions. I will also explain the ^{3}He-^{4}He dilution system necessary for measuring at temperatures around 100 mK. Finally, I will describe the techniques used for measuring and the electronic system installed to improve the measurements.

2.1 Overview of the experimental setup

The experimental setup used during this PhD consists of a home-made Scanning Tunneling Microscope made of non-magnetic Shapal. Shapal is a ceramic material that avoids Joule heating produced by Foucault currents when changing the magnetic field. This STM has been developed during a previous PhD thesis in our group [91].

The STM is located in the center of a superconducting coil that can reach magnetic fields up to 17 T. This coil is placed inside a low-temperature cryostat that can reach temperatures of 2 K. A photograph of the laboratory is shown in figure **2.1 a**, where the main parts are indicated. During this work, the set-up was significantly improved by installing it on a floating floor for noise reduction. Also, a Low-Noise High-Amplification (LHA) digital electronic has been installed, improving the velocity of the measurements for the same resolution [92]. Finally, we significantly improved the temperature control, adding a heater that has allowed to perform systematic measurements as a function of the temperature from 2 K up to 60 K. The process of heating and cooling the samples is faster than in a cryostat with a dilution refrigerator.

2.1.1 Noise isolation

When measuring with an STM, isolation from mechanical noise is extremely important. As the tunneling current depends strongly on the distance between the tip and the sample (see section 2.2), the experiment is highly sensitive to mechanical vibrations. The tunneling current has an exponential dependence on the sample-tip distance: a change of 1 Å in this distance typically produces a change in the tunneling current of one order of magnitude. Thus, the design of the STM head is crucial [92]. The head can be considered as a damping oscillator with resonance frequency ω_0. The STM itself damps vibrations for $\omega < \omega_0$, with damping going as $\propto \left(\frac{\omega}{\omega_0}\right)^2$ for low frequencies [93]. We can consider $\omega_0 \approx \omega_p \approx 10^4$ Hz, where ω_p is the resonance frequency of the piezotube. The floor vibrations can be considered to decrease above 10^2 Hz. As we show below, the STM has a scanner which is often a piezotube. The piezotube has a resonance frequency close to the ω_0, $\omega_p \approx \omega_0$. Thus, if the rest of the STM is more rigid than a piezotube, floor vibrations are damped by at least 10^{-4}.

To reduce the noise vibrations, we installed the STM in a building separated from the main building with the usual activity. A photograph of the laboratory is shown in figure **2.1 a**, where the main parts are indicated. To further isolate the experiment, the cryostat is fixed to a 10 tons reinforced concrete floating floor. This floating floor is held by 16 springs and mechanically isolated from the building. The resonance frequency of the floating floor is around 1 Hz [92]. The blueprint of the laboratory is shown in figure **2.1 b**. The position of the cryostat, the springs and the center of mass are indicated. The floor

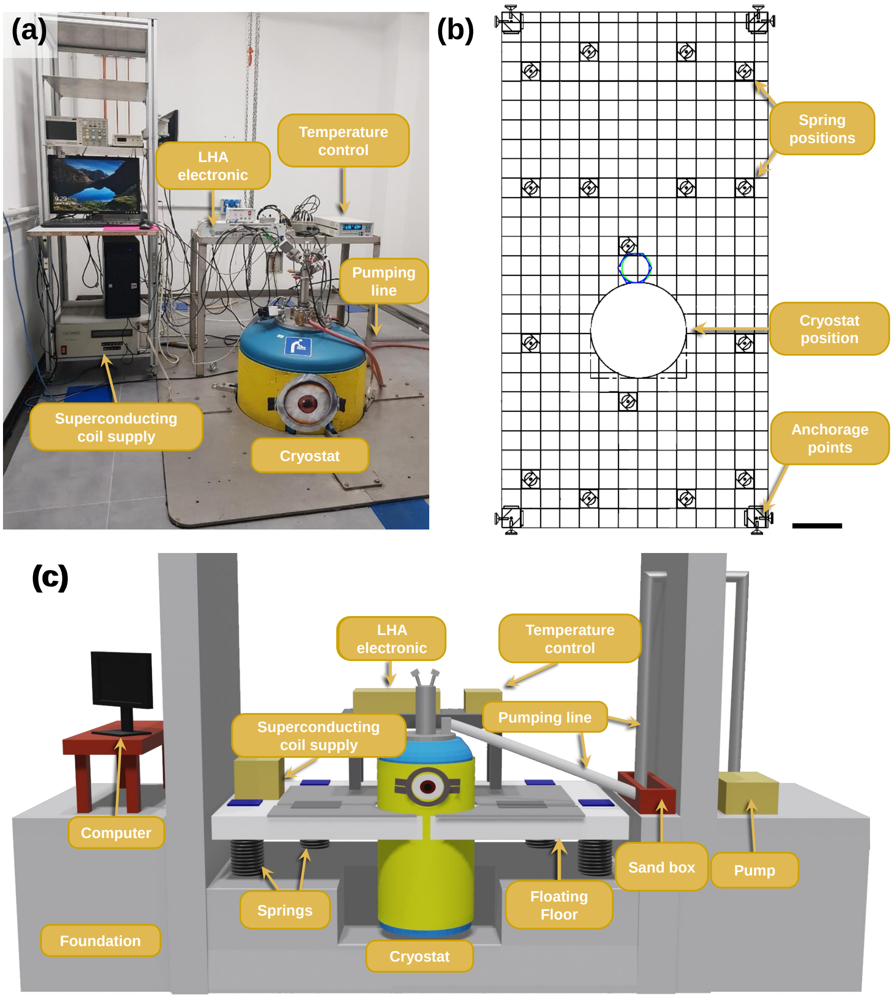

Fig. 2.1: (a) Photograph of the laboratory showing the experimental setup. (b) Blueprint of the floating floor. The position of the springs, the cryostat and the center of mass are indicated. The horizontal scale line is 50 cm long. (c) Sketch of the laboratory showing the floating floor held by springs. The floating floor is separated from the pump room and the main part of the laboratory, where the remote control system allows us to take the measurements without disturbing the experiment. The main parts are indicated.

has four anchor points at the corners that can attach the floor to the walls. The grid indicates the concrete mesh. The sketch in figure **2.1 c** shows how the floating floor is held by the springs. The pump room and the room where the experiment can be controlled remotely are separated from the experimental

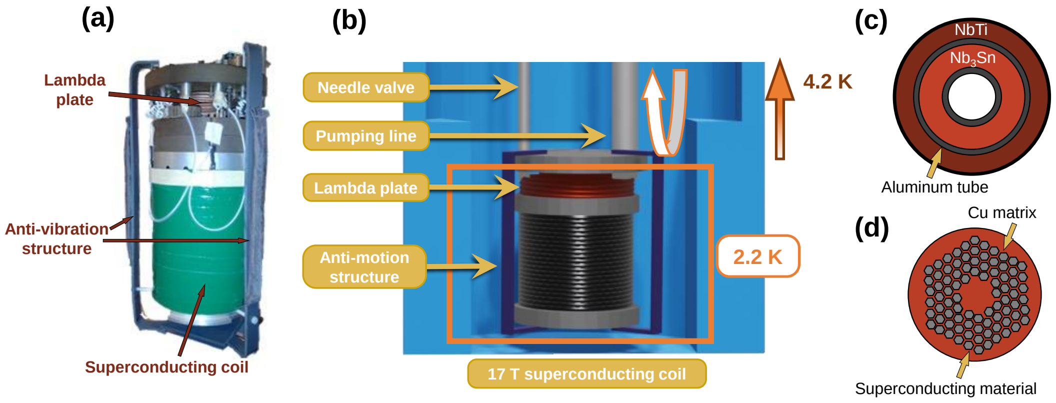

Fig. 2.2: (a) Photograph of the 17 T superconducting coil. The main parts are indicated. (b) Scheme of the superconducting coil inside the cryostat and the cooling due to the lambda plate. (c) Scheme of the two materials in the superconducting coil. (d) Scheme of the superconducting wires in a cooper matrix.

room. The remote control computer system allows us to control the experiment without disturbing the measurements. The tube that goes from the experiment to the pump goes through a sandbox to reduce the noise due to the vibrations of the pump.

2.1.2 Superconducting magnet up to 17 T

The magnet used is a superconducting coil that can reach 15 T at 4.2 K and 17 T at 2 K. A photograph of the coil is shown in figure **2.2 a**, where the lambda plate and the anti-vibration structure are indicated. This anti-vibration system is designed to clamp the coil to the inner side of the cryostat, preventing noise. The coil consists of a wound coil of superconducting wire and is operated inside a helium bath. Superconducting coils can have a persistent field. To do so, the coil is shunted by a superconducting wire with a heater, far from the high field region. The heater is switched on while charging the coil, so the shunt becomes normal and the current can flow inside. Once the current is applied, the heater is switched off, and the current remains inside the superconducting coil. Thus, the magnetic field remains applied as long as the coil temperature is under the critical temperature of the superconducting wires.

This magnet is made of two concentric coils separated by an aluminium tube, as seen in figure **2.2 c**. The outer coil is made with NbTi wires and the inner one with Nb_3Sn. These two materials have been selected by their properties, being the outer material the one with a smaller critical field and current. In figure **2.2 d** we can see a scheme of a section of a superconducting wire, where different wires of the superconducting material go inside a cooper matrix.

On the top of the coil, there is a copper serpentine called lambda plate loop, as represented in figure **2.2 b**. At one end, there is a pump line. At the other end, there is a needle valve, which controls the flow of liquid helium passing through. When we pump the helium through the lambda plate, the bath temperature below the lambda plate can decrease, reaching around 2 K. The temperature in this area is constant because the difference in helium densities, when cooled, creates convection flows. Above the coil, there is a temperature gradient such that the upper part of the bath, at ambient pressure, reaches 4.2 K. With this method, the cryostat can be refilled without heating above 2 K.

2.1.3 ^{3}He-^{4}He dilution refrigerator

By using a dilution refrigerator we can cool below 100 mK. The dilution fridge is very stable and can be running for months while refilling with He only once a week, which is an important advantage for long spectroscopy measurements.

The dilution refrigerator is based on the quantum properties of the mixture of ^{3}He and ^{4}He, that goes through different stages until reaching such low temperatures. In figure **2.3** there is a photograph and a scheme of the dilution refrigerator used in this thesis. First, the mixture is injected through a condensing line to the 1 K pot, a small container connected to the outer helium bath in the cryostat. By pumping this container with the ^{4}He pump, the temperature can go down 1.5 K. As the temperature where the mixture liquefies is below 4.2 K, the 1 K pot is a necessary stage to precooled it. Then, the mixture goes through several continuous and discrete heat exchangers, where it is cooled down using the enthalpy of the outgoing mixture. The mixture then reaches the mixing chamber, where we have the lowest temperature. In this part of the dilution refrigerator the mixture separates in two phases: we

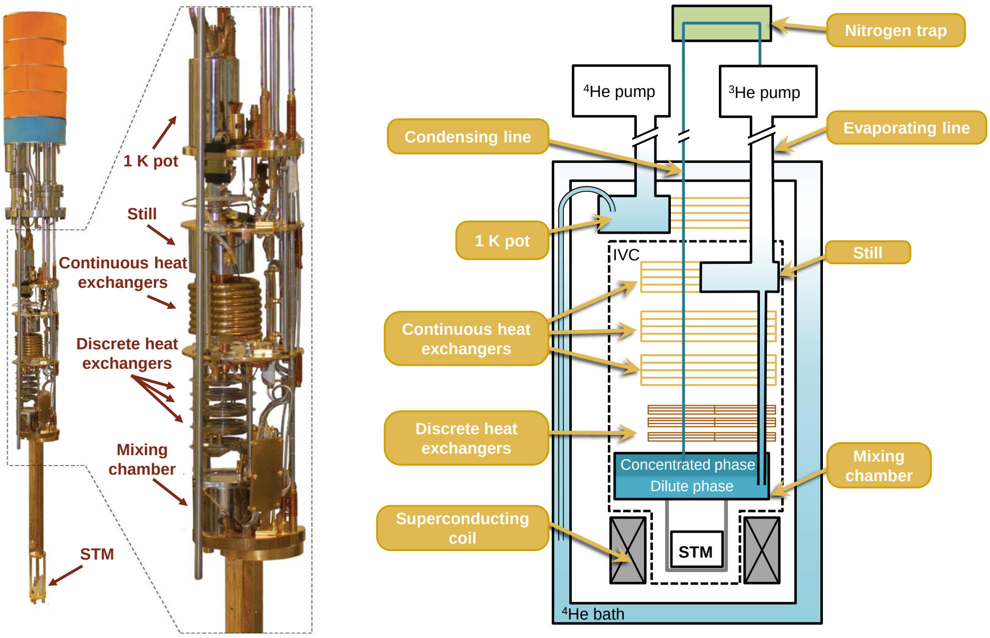

Fig. 2.3: Photograph and scheme of a dilution refrigerator, where main parts are indicated.

have the concentrated ^{3}He phase floating over the dilute ^{3}He phase. The mixing chamber is connected to the still or evaporator, going up again through the heat exchangers. By pumping the still, ^{3}He atoms in the dilute phase are constantly removed, producing an osmotic pressure gradient between the still and the mixing chamber. Then, ^{3}He atoms are forced to cross the phase boundary in the mixing chamber and going towards the still. The process of passing atoms of ^{3}He from the concentrated phase to the dilute phase provides the cooling power. Pumped ^{3}He atoms from the still are injected again, after being purified in a nitrogen trap with activated carbon filters.

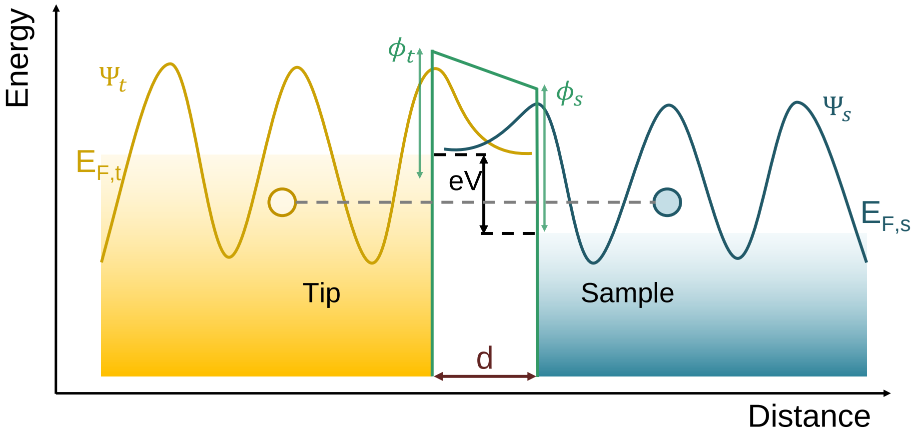

Fig. 2.4: Schematic representation of the tunneling process in a vacuum barrier of width d. The electron wave functions of the tip and sample (Ψ_t and Ψ_s) decay exponentially in the vacuum and overlap, allowing the tunneling process. In the scheme, a positive voltage eV is applied to the tip, so electrons tunnel from the tip to the sample, filling its unoccupied states.

2.2 Scanning Tunneling Microscopy

2.2.1 Operation principles

The STM operation is based on the quantum tunneling of electrons between two electrodes: the tip and the sample. When the tip is close enough to the sample, both wave functions overlap, and the electrons can travel from the sample to the tip and *vice versa*.

Using time-dependent perturbation theory, Bardeen evaluated the tunneling matrix elements to understand the tunneling junction experiments in 1961 [94]. In 1983, Tersoff and Hamann used a modified Bardeen's theory to describe the STM [95, 96] considering typical distances and sizes found in experiments, around 10 Å.

Assuming weak interaction between tip and sample and elastic tunneling, the tunneling current, I, between the tip and sample ($t \to s$) and between sample and tip ($s \to t$) are

$$I_{s\to t} = \frac{4\pi e}{\hbar}\int_{-\infty}^{\infty} |M|^2 N_s(E_s) N_t(E_t) \left[f(E_s)(1 - f(E_t))\right] dE, \tag{2.1}$$

$$I_{t\to s} = \frac{4\pi e}{\hbar}\int_{-\infty}^{\infty} |M|^2 N_s(E_s) N_t(E_t) \left[f(E_t)(1 - f(E_s))\right] dE, \tag{2.2}$$

where e is the electron charge, $\hbar$ is the Plank constant, $|M|^2$ is the tunneling matrix element described by Bardeen, N_s and N_t are the density of states (DOS) of the sample and the tip and $f(E,T)$ is the Fermi distribution function for an energy E and a temperature T

$$f(E,T) = \frac{1}{1 + e^{\frac{E-E_F}{k_B T}}}. \tag{2.3}$$

The tunneling current is the difference between them

$$I = I_{s\to t} - I_{t\to s} = \\ = \frac{4\pi e}{\hbar}\int_{-\infty}^{\infty} |M|^2 N_s(E_s) N_t(E_t) \left[f(E_s)(1 - f(E_t)) - f(E_t)(1 - f(E_s))\right]. \tag{2.4}$$

When a voltage V is applied between the tip and the sample, the Fermi levels of both electrodes are separated by eV, and we can write $E = E_t$ and $E_s = E - eV$, and the tunneling current

$$I = \frac{4\pi e}{\hbar}\int_{-\infty}^{\infty} |M|^2 N_s(E - eV) N_t(E) \left[f(E - eV) - f(E)\right] dE. \tag{2.5}$$

We can understand the electronic transport through tip and sample by modeling the junction as a barrier of width d and height ϕ, where ϕ is the average work function of the tip ϕ_t and sample ϕ_s, as represented in figure **2.4**. In the limit where $eV \ll \phi$, the matrix element $|M|$ does not have an energy dependence. We can write

$$I \propto \int_{0}^{eV} N_s(E - eV) N_t(E) \left[f(E - eV) - f(E)\right] dE. \tag{2.6}$$

In the present thesis, gold tips were used in almost all experiments at very low temperatures, so the density of states of the tip can be considered constant in the range of energies we are studying. Taking the derivative of Eq. 2.6, we obtain that the tunneling conductance is proportional to the convolution between the density of states of the sample and the derivative of the Fermi distribution function:

$$\sigma(eV) = \frac{dI}{dV} \propto \int_{-\infty}^{\infty} N_s(E)\frac{\partial f\left(E-eV\right)}{\partial V}dE. \tag{2.7}$$

The derivative of the Fermi distribution function has a bell shape whose width is given by k_BT. At low temperatures, this function tends to a Dirac delta function $\delta\left(E-eV\right)$, and the tunneling conductance can be taken as proportional to the density of states

$$\sigma(V) = \frac{dI(V)}{dV} \propto N_s(E=eV). \tag{2.8}$$

Thus, with the STM we can directly measure the density of states of our sample. The wave functions of each the tip and sample decay exponentially inside a barrier of width d:

$$\left\{ \begin{array}{l} \Psi_s \propto e^{-\kappa x} \\ \Psi_t \propto e^{-\kappa(d-x)} \end{array} \right. \quad \text{with } \kappa = \sqrt{\frac{2m_e\phi}{\hbar^2}} \approx 0.5\sqrt{\phi}\ \text{Å}^{-1} \tag{2.9}$$

where m_e is the electron mass and ϕ is the work function of the tip and the sample in eV. Using these wave functions in Bardeen's formalism, we find that

$$I \propto e^{-2\kappa d}. \tag{2.10}$$

This expression means that changes in the measured current are considerable for small changes in the distance. In this way, STM shows a very high sensitivity to the distance between the tip and the sample. Usually, $\phi \approx 5$ eV (for typical metals, such as Au and Pt), which means that changes of 1 Å in the tip-sample distance translate into changes of one order of magnitude in the current.

Although the tunneling effect is the one that gives its name to the STM, it is worth noting a second significant effect: the piezoelectric effect. Piezoelectric materials are characterized by their expansion or contraction when applying voltage. Tip displacements can be controlled at sub-nanometric scale by attaching the tip to a piezotube that deforms in the order of some nm/V. The piezotube we use has five electrodes, which allow the movement in X, Y and Z directions by applying voltages in the three pairs of electrodes. The representation of the movement of the piezotube can be seen in figure **2.5**.

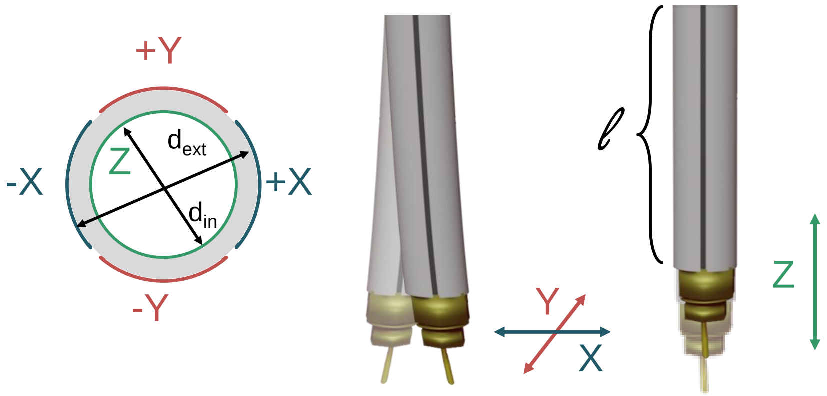

Fig. 2.5: Schematic representation of the piezotube movement in all directions. The applied voltage to the two pairs of electrodes produces its deformation in X, Y (that allows the sample scanning) and Z (that controls the tip-sample distance).

The piezotube deformation in all directions depends on its geometry, the piezoelectric coefficient of the material used, d_{31}, and the voltage applied [97]. The deformation in the three dimensions of the space can be described with

$$\begin{aligned} \Delta X = \Delta Y &= \frac{0.9 d_{13} V l^2}{d_m t}, \\ \Delta Z &= \frac{d_{13} l V}{t}, \end{aligned} \tag{2.11}$$

where l is the length of the piezotube, t is its thickness and d_m is the average value of its external and internal diameters. In the present experimental setup, d_{31} = -0.31 Å/V at 4.2 K [98], l = 12.75 mm, d_{ext} = 3.19 mm and t = 0.32mm, so we can measure a window of 1.62 μm and height differences of 0.2 μm.

To bring the tip from macroscopic separation into tunneling distance, we need a motor that can be operated in situ. The piezotube is thus attached to a prism, moved along the z-direction using a motor held to the head of the microscope. This prism is attached horizontally by a spring, doing some

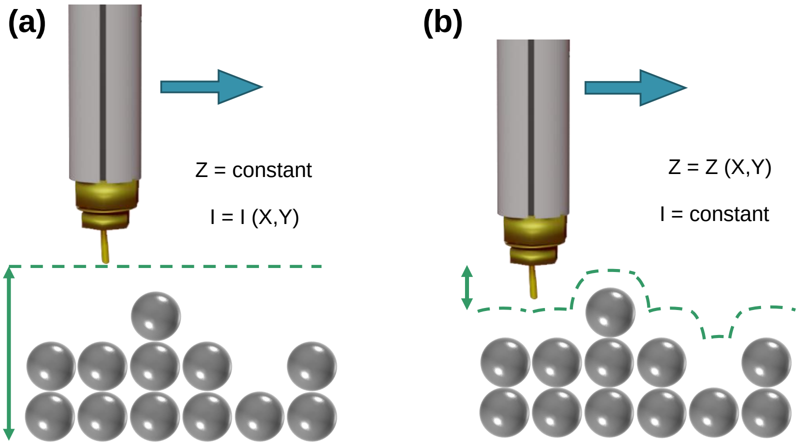

Fig. 2.6: Schematic representation of the constant height and the constant tunneling current modes. In (a), the tip height is constant during the scan and the tunneling current is recorded. In (b), the tunneling current is the same during the scan, and the piezotube height changes following the sample.

pressure to a set of stacks of shear piezos. A fast sawtooth signal is applied to these stacks. When the slow ramp is applied, the piezostacks deform up or down, sweeping along the prism with the piezotube. Once the fast ramp is applied, the piezostacks return to their original position. However, the prism slides and remains up or down. To allow this sliding, two pieces of alumina are located between the piezostacks and the prism. This movement can be of the order of several mm, so that it is possible to overcome the height difference between samples. This displacement is called Z' to distinguish from the vertical movement of the piezotube, Z.

Combining the tunneling and piezoelectric effects, we can scan the sample and obtain a surface map. To do this, two different modes can be used: constant height and constant current modes. In the constant height mode, the position of the piezotube in Z is constant, while the variations in the tunneling current are registered as a function of the position of the tip in the x-y plane, obtaining the corrugation of the sample, as represented in figure **2.6 a**. This method is limited to very flat surfaces, where the height variations should be smaller than the distance between the tip and the sample at the beginning of the measurement. In the constant current mode, the tunneling current between the tip and sample is set constant, and the variation of Z, the height of the tip, is registered while scanning the sample in the x-y plane. This scanning mode is represented in figure **2.6 b**. The constant value of the current between the tip and the sample is set using a PID feedback loop that adjusts the height of the tip at every position. All the images presented in this thesis were acquired using this method.

2.2.2 Data acquisition

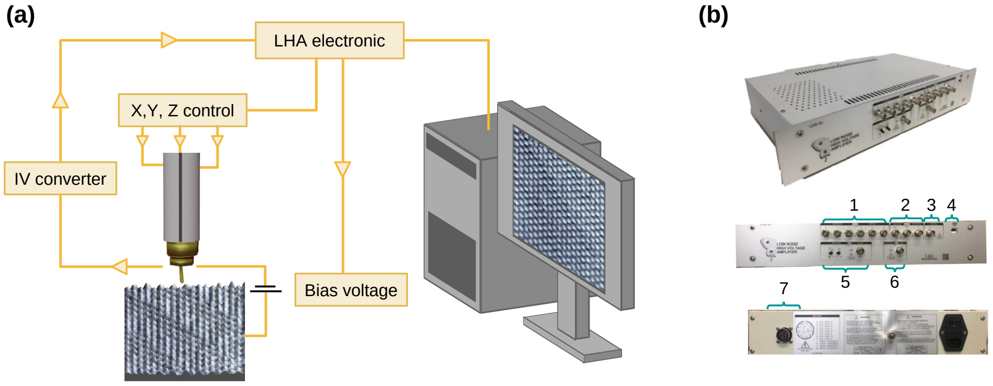

Fig. 2.7: (a) Schematic representation of the control electronics. The bias voltage forces the electrons to move from the tip to the sample or *vice versa*. The IV converter transforms the tunneling current I to a voltage with a typical conversion factor of 0.1 or 1 nA/V. (b) From top to bottom, photograph of the LHA electronics, the front panel and the back panel.

For operating the STM, we use the LHA-Digimod model, a digital electronics unit developed at the university workshop SEGAINVEX [99]. This single device contains all the signals and ports we need to measure in our system. It contains five ADCs (analog to digital) channels for reading the signals, indicated with the number 1 in figure **2.7 b** and three auxiliary DAC (digital to analog) signals. One of the ADC modules is used for reading the tunneling current signal, which goes first through a current to voltage converter with a gain that can be set between 10^5 and 10^9 V/A. The DAC modules provide signals between -10V and +10 V. The one used for the bias voltage is usually attenuated using a voltage divider. DACs' signals sent to the piezos are amplified by a factor of 14. They are sent by the connector indicated with 7 in the figure **2.7 b**. We also find a digital auxiliary output (3), a USB port for connecting the electronics to the computer (4), an input for the control Z (5) and an auxiliary input for the Z control (6).

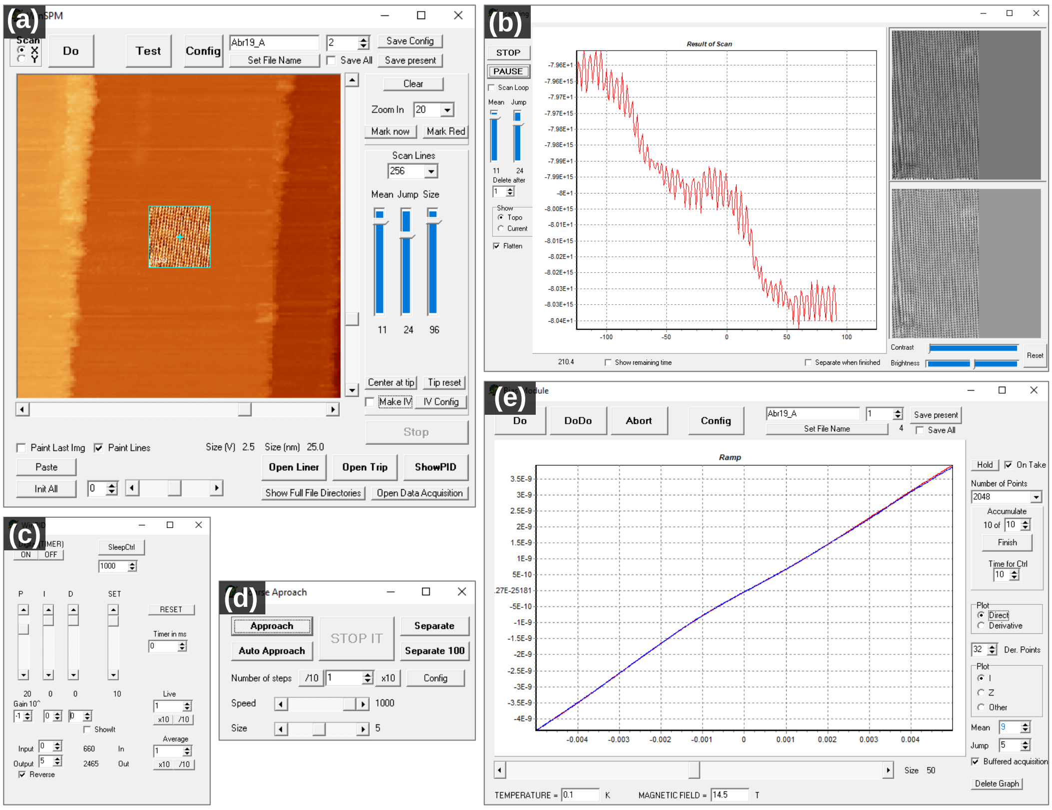

Fig. 2.8: Screenshots of the principal windows of the measuring program. (a) Scanner interface. (b) Interface for the live preview of the scan. (c) Digital PI (proportional integral) feedback interface window. (d) Coarse vertical motion (Z′) control window. (e) Curve acquisition interface.

The control electronic uses a homemade software developed in a Pascal programming environment called Delphi. It contains all the tools for scanning the sample and taking the spectroscopy curves. Screenshots of the windows of the program are shown in figure **2.8**. The program includes an interactive window (figure **2.8 a**) that controls the position of the tip in the window we can measure. This is indicated with a blue cross in the center of a blue square that marks the size of the window we want to scan. When scanning, a window with the preview of the scan appears (figure **2.8 b**). We can also control the PI (proportional integral) feedback (**c**), the macroscopic movement of the tip (**d**) and the acquisition of spectroscopy curves (**e**). We can perform scanning tunneling spectroscopy (STS) by combining the scan and spectroscopy. This technique will be described in section 2.4.

2.3 STM at very high magnetic fields

Like all the microscopes used in the low temperature laboratory of the UAM, the STM used during this thesis is a homemade design. This STM is made of non-magnetic Shapal and was built in SEGAINVEX facilities [99]. Shapal is a ceramic material based on aluminium nitride. Ceramics have interesting properties, such as the absence of Foucault currents, making them perfect candidates for experiments at high magnetic fields. Unfortunately, one of the main problems with this kind of material is its difficulty to be machined. Shapal can not only be machinable, but it presents a high thermal conductivity, a low thermal expansion and a high mechanical strength.

Material	**Density** (kg m^{-3})	**Young's Modulus** (GPa)	**Ratio** ×100
Ti Grade 5 (Ti6A14V)	4420	110	2.4
Al 7075	2700	70	2.5
Macor	2520	66	2.6
Shapal	2900	190	6.6
Sapphire (α-Al$_2$O$_3$)	3980	340	8.5
WC	15500	550	3.5

Table **2.1**: Adapted from [100], properties of typical materials used for STM.

Figure **2.9** shows a photograph and a sketch of the STM and its main parts. This design allows three different movements: the 3D movement of the piezotube with the tip, the vertical displacement of a prism holding the piezotube and the horizontal movement of the sample holder. The sample holder is located inside a track at the base of the STM. To move the sample holder, we use a thread attached to a piano wire [92]. This piano wire is

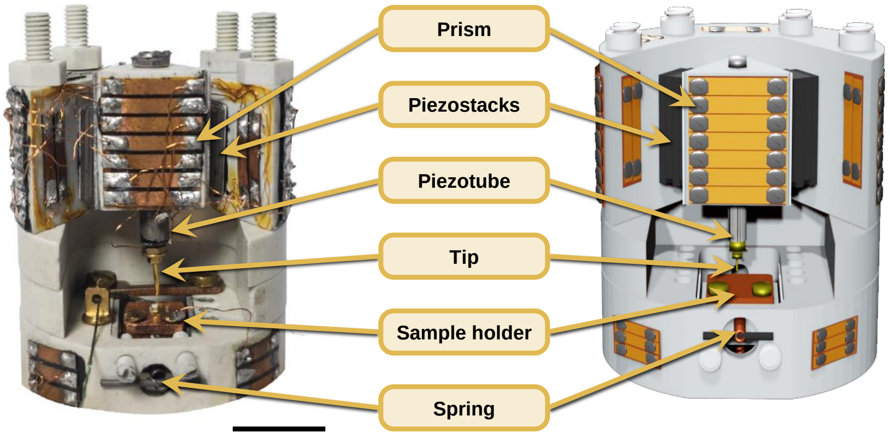

Fig. 2.9: Photograph and sketch of the STM made of Shapal. Horizontal scale bar indicates 10 mm.

soldered to a spring at the lower part of the insert and to a micro-metric screw at the top of the experiment, as represented in figure **2.11 c**. By screwing it, the piano wire pulls the sample holder backwards. A spring is attached to the front of the sample holder to move it in the reverse direction. When the sample holder is in the front part, the spring is in the equilibrium position. When the micro-meter screw is unscrewed, the piano cord relaxes its tension, and the spring pulls the sample holder to the front of the tracks. In order to keep the sample holder stable and horizontal, another spring is attached to the bottom.

This system allows a horizontal movement that can be controlled mechanically without modifying the temperature of the experiment. With it, different parts of the sample can be reached, moving macroscopically in one direction. But this displacement also allows changing the position of the tip over the sample holder. If a sample made of the same material than the tip is placed in the sample holder, the tip can also be cleaned and sharpened by a controlled nanoindentation process, as described in reference [101]. Different steps of this process are schematically represented in figure **2.10 a**. This method allows to form single atom point contacts, whose conductance is given by the quantum of conductance $G_0 = 2e^2/h$ in gold [102]. Typical curves obtained during this process at 4.2 K are showed in figure **2.10 b**. By taking thousands of these curves, we can represent the results as a normalized conductance histogram,

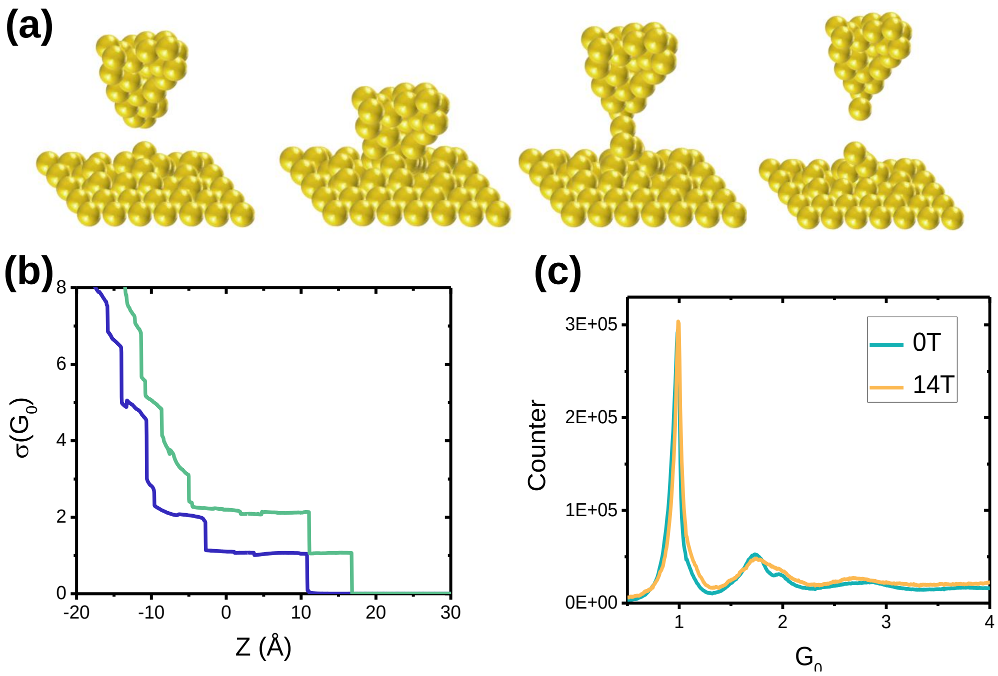

Fig. 2.10: (a) Representation of the nanoindentation process. The scheme shows different steps. When the tip crashes, it forms a single atom contact and finally separates from the sample. (b) Typical curves at 4.2 K obtained in this process, where the first step is at G_0. (c) The histograms at 0 T and 14 T were obtained by taking thousands of the previous curves.

with a huge and clear peak at G_0. In figure **2.10 c**, those histograms for 0 T and 14 T are presented. We can see that we can obtain the same results at 0 T and 14 T (small difference are found however, which we will discuss in a publication in preparation).

In addition, the movement of the sample holder also allows us to cleave the samples *in situ*. Depending on the sample, the cleaving process can be by breaking or exfoliation [103]. For cleaving the sample, a small piece of alumina is glued to the top part of the sample. This piece needs to be the same size and shape as the sample, but large enough to tower over the tracks described above. Different parts are indicated in figure **2.11 a** and **b**. When the sample holder is pushed backwards with the screw, the alumina collides with a piece fixed to the base of the STM, as represented in figure **2.11 d** and **e**. Usually, this piece is a ceramic blade or a copper bar. As the forces between layers in

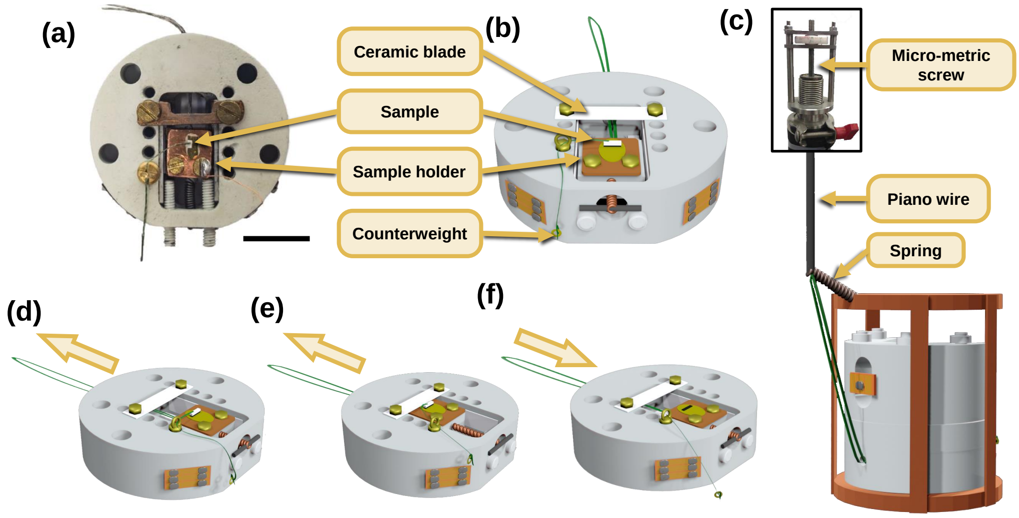

Fig. 2.11: Photograph (a) and sketch (b) of the base of the STM with a sample. The horizontal scale bar is 10 mm. (c) Representation of the pulling system. The thread and the piano wire are soldered to a string, allowing the movement of the sample holder forward and backwards. From (d) to (f), different steps of the cleaving process are represented: the sample holder is pulled backwards (d) until it hits the ceramic blade (e), where the sample exfoliates and the counterweight falls, avoiding the alumina to stay between the tip and the sample (f).

the sample are weaker than the glue used to fix the alumina, the sample is exfoliated, as represented in figure **2.11 f**. Furthermore, a thread is glued to the top of the alumina with a counterweight on its other end. Doing so, when the sample is exfoliated, the alumina and the exfoliated part of the sample fall to the bottom of the vacuum chamber, and nothing stands between the tip and the sample. Finally, to avoid sticking or hitting the tip with the exfoliated sample, a guide for the thread is screwed at one side of the track. Figure **2.12** shows photographs of all the crystals measured during this thesis before and after the cleaving process. Layered samples such as WTe_2, $NbSe_2$, $CrSiTe_3$, $TaTe_4$, FeSe or $FeSe_{0.71}S_{0.29}$ are easily cleaved using the method described before. Layered but stronger samples such as $Co_3Sn_2S_2$ or $EuCd_2As_2$ are more difficult to cleave successfully. Other samples such as $PdSb_2$ and YbAgGe are not layered, and the cleaving method needs to be modified. In these cases we need to break the sample using an alumina blade, hitting the sample directly, without a glued post.

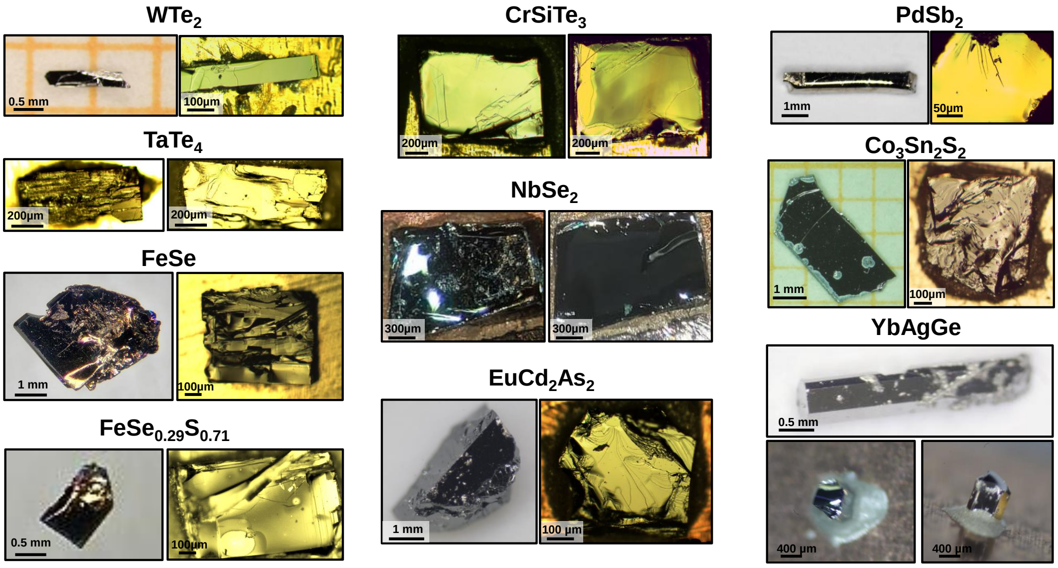

Fig. 2.12: Photographs of the samples before (left) and after (right) cleaving during this thesis.

	Material	Number of samples
Van der Waals materials	$NbSe_2$	2
	WTe_2	3
	$TaTe_4$	3
	FeSe	4
	$FeSe_{0.71}S_{0.29}$	4
	$CrSiTe_3$	5
3D crystalline materials	$PdSb_2$	5
	YbAgGe	6
	$Co_3Sn_2S_2$	6
	$EuCd_2As_2$	12

Table **2.2**: Number of times the samples have been cleaved during this thesis.

In all the cases, a careful preparation of the samples is very important. Smaller samples usually result in flat surfaces more easily than larger samples and the shape and size of the alumina glued on top need to be as similar as possible to the sample. Even then, several samples usually need to be cleaved. Table **2.2** shows the number of times the samples have been cleaved during this thesis.

2.4 Scanning Tunneling Spectroscopy

Using Scanning Tunneling Spectroscopy (STS), we can measure the local variations of the density of states in the material. While topography images give the convolution of the DOS between the Fermi energy and the applied bias voltage, STS allows measuring the energy dependence of the DOS. For doing that, the tip scans the surface of the sample as described above. Then, the tip stops at every position, and the feedback loop is opened while varying the voltage to take a current vs voltage curve. The feedback loop is reconnected, and the tip moves to the next point. Doing so, we obtain a topography image and a voltage *vs* current curve for each pixel. By numerical derivation of the voltage *vs* current curve, we obtain tunneling conductance maps as a function of the position and the voltage (see figure **2.13**). Within this PhD, we achieved a considerable gain in acquisition time, thanks to the new electronics mentioned above.

We analyze these files using software based on Matlab environment. This software includes numerous features required for data analysis, such as plotting current and conductance maps at every energy, Fourier transform spectroscopy, rotation and symmetrization of the maps, or plot current and conductance curves at any point in the image [104].

2.4.1 Quasiparticle interference imaging

With STS measurements, we can study the quasiparticle interference scattering (QPI) to get information about the band structure of the material. The relation between the measured local density of states (LDOS) and the eigenstates $\Psi(\vec{r}_k)$ is given by the expression

$$LDOS(E,r) \propto \sum_k \left|\Psi\left(\vec{r}_k\right)\right|^2 \delta\left(E-\epsilon(\vec{k})\right), \tag{2.12}$$

where $\vec{k}$ are the wavevectors and $\epsilon(\vec{k})$ is the dispersion relation of the material. When the periodicity of the crystal is broken by the presence of defects or impurities, the electrons are scattered, producing oscillations in the LDOS. This scattering processes is typically elastic. In this picture, scattering between states with $\vec{k}_i$ and $\vec{k}_f$ gives rise to a modulation with $\vec{q} = \vec{k}_f - \vec{k}_i$ in the LDOS that can be observed in the tunneling conductance with the STM. The

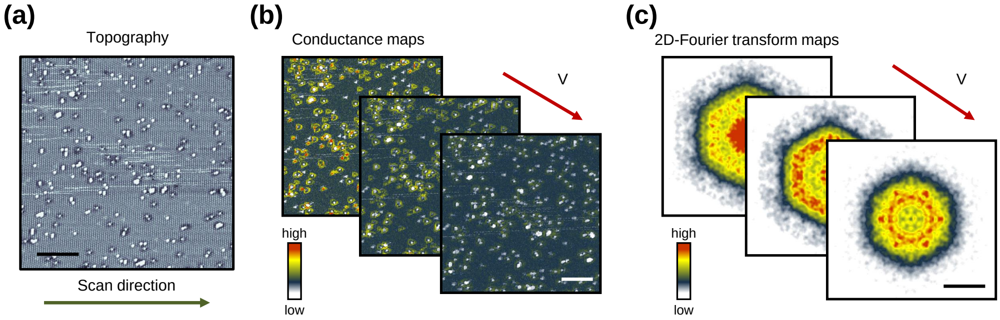

Fig. 2.13: (a) Topography image at 4.2 K of the sulfur surface in $Co_3Sn_2S_2$, taken at 100 mV and 1.6 nA. The horizontal scale bar is 13 nm. (b) Conductance maps at -20, -10 and 0 mV. The scale bar in the image is 13 nm. (c) C3 symmetrized 2D-Fourier Transform of the conductance maps. The scattering of the electrons at each energy gives different features in the FFT. Following these changes, we can obtain information about the band structure of the material. Horizontal scale bar is 0.3 nm^{-1}.

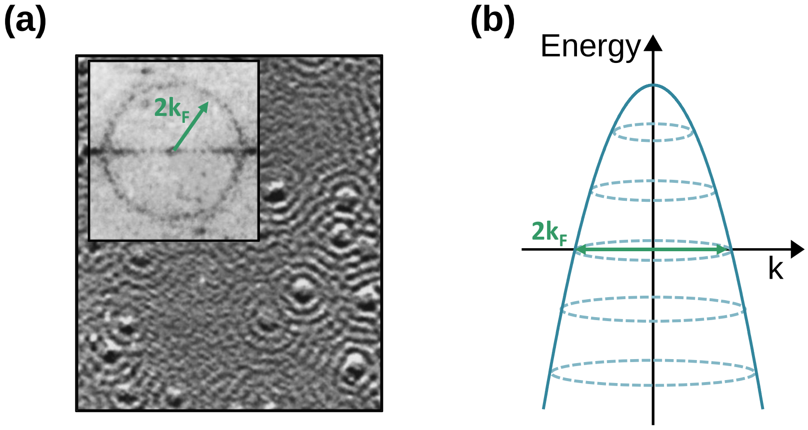

Fig. 2.14: (a) Adapted from [105]. Constant current STM image of Cu(1,1,1) at 150 mK. The point-like defects in the surface induce a modulation of the density of states. In the inset, 2D-Fourier Transform of the image. The main scattering vector is indicated. (b) Schematic parabolic band dispersion of Cu(1,1,1) that can be reconstructed from the main scattering vectors.

scattering between an initial state, i, and a final state, f, is described by the

Fermi golden rule:

$$\omega(i \rightarrow f) \propto \frac{2\pi}{\hbar} |V(\vec{q})|^2 N_i(E_i, \vec{k}_i) N_f(E_f, \vec{k}_f), \tag{2.13}$$

where $E_i = E_f$ for elastic scattering, $\vec{q} = \vec{k}_f - \vec{k}_i$ is the scattering vector, N_i and N_f are the initial and final densities of states, and $V(\vec{q})$ the scattering potential. This scattering potential can be different for different types of impurities or defects and can also be anisotropic. We can define the joint density of states (JDOS) from the momentum-resolved density of states of the sample:

$$JDOS(E, \vec{q}) = \int N(\vec{k}, E) N(\vec{k} + \vec{q}, E) d^2\vec{k}. \tag{2.14}$$

For Eq. 2.13 and Eq. 2.14 we can deduce that, in first approximation, the scattering $\vec{q}$ vectors connecting states with higher JDOS will produce a higher QPI signal. The scattering potential can be anisotropic and can enhance or reduce the scattering intensity at a given $\vec{q}$.

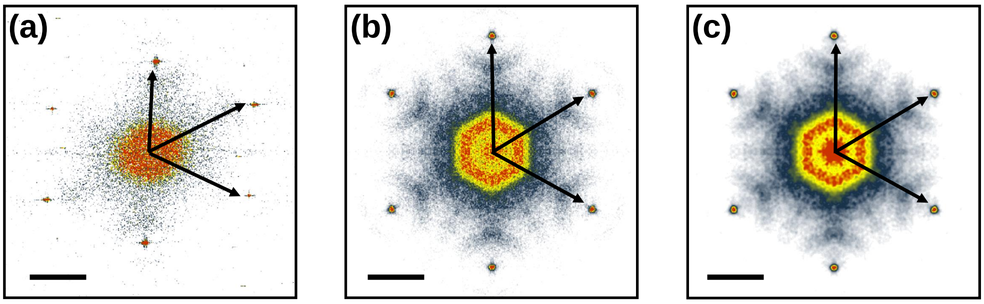

Fig. 2.15: (a) Raw 2D-Fourier transform map of the sulfur surface in $Co_3Sn_2S_2$ at -15 mV and 1.6 nA. (b) The image is rotated to align the Bragg peaks with the horizontal position. Then, we symmetrize C3 the image according to the symmetries of the crystal. (c) A Gaussian filter can be applied to improve the features of the image. The horizontal bar is 1 nm^{-1}.

The JDOS depends on the amplitudes of the density of states at initial and final scattering states and is higher at specific locations of the band structure, for example, at van Hove anomalies or when scattering occurs between flat parts of the Fermi surface. Thus, by plotting the maxima in the scattering intensity as a function of the bias voltage, we can follow the JDOS for certain $\vec{k}$ as a function of the energy. Using this information, we can reconstruct the electronic dispersion relation (as in figure **2.14**). This reconstruction is most easily obtained in those parts of the band structure that interact with defects and impurities and provide larger $V(\vec{q})$. Furthermore, STM can follow the band structure of the material for both occupied and empty states, which is a significant advantage if we compare it with techniques like angle-resolved photoemission spectroscopy (ARPES), which can only access states below the Fermi energy.

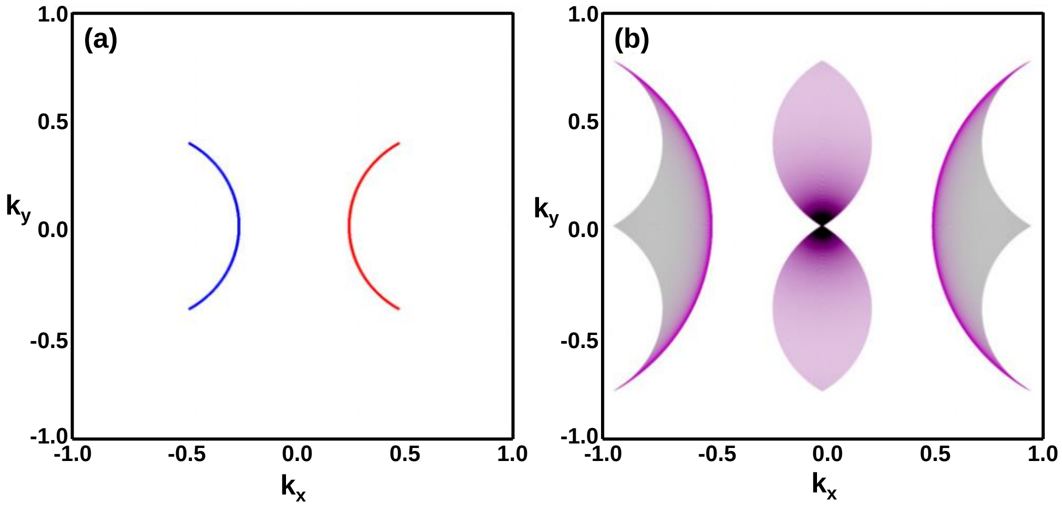

Fig. 2.16: Adapted from [106]. (a) Representation of two Fermi arcs in the $k_x - k_y$ plane and (b) the corresponding joint density of states (JDOS).

Noise reduction is essential in QPI measurements when identifying the different vectors. As can be easily understood, JDOS contains all the symmetry operations of the crystal at its surface. However, $V(\vec{q})$ includes additional components depending on the internal shape of the defects and the way these interact with the electrons of the compound. Being mostly interested in JDOS, we can use the symmetry properties of the crystal to enhance the signal to noise ratio. Figure **2.15** illustrates the symmetrization process for a case of a crystal with 3 fold symmetry. First, we need to correct the small distortion of the 2D-FFT maps, which can be caused due to thermal drift. Then, we rotate the maps to align one of the crystallographic axes with the horizontal direction, and we apply the symmetry averaging operations (figure **2.15 b**). As one would expect, the averaging processes applied will be different for crystals showing different symmetries. Once the data is symmetrized, we can follow the different $\vec{k}$ vectors with the energy to reconstruct the band structure of the material.

When there are open contours in the surface Fermi surface, such as Fermi arcs, we have some characteristic features in the QPI maps. Figure **2.16 a** shows two isolated Fermi arcs in the $k_x - k_y$ plane. The scattering probability between the Fermi arcs can be obtained by the 2D autocorrelation. The resulting map shows one feature in the center, that comes from the correlation from the arcs, plus two cross-correlation patterns corresponding to the scattering between the arcs [106] (see figure **2.16 b**). Note in particular that the features close to $k = 0$ are not observed for Fermi surfaces having a closed geometry.

Chapter 3

Landau quantization in the topological semimetal WTe_2

Recently, WTe_2 has attracted a lot of attention due to its peculiar characteristics. This material is a multiband semimetal, with a very small density of states near the Fermi level. It exhibits a huge non-saturating magnetoresistance [107], and it was the first material predicted to be a type-II Weyl semimetal [45]. These properties make WTe_2 an interesting material to measure at high magnetic fields. Other properties, such as its ultra-high mobility of carriers and layered structure, make this material a good candidate for measuring the Landau quantization of the bands near the Fermi level.

Monolayers of WTe_2 have been synthesized with molecular beam epitaxy [108–112]. Transport devices show indications for an insulating behavior inside the monolayer and edge states at the borders, at which the quantum spin Hall effect has been observed [111, 112]. The quantum spin Hall effect arises in systems with an insulating bulk and helical edge states. The helicity in the edge states provides counter propagating currents with carriers of different spin. Application of a magnetic field leads to gap opening and a reduction of edge conduction [112]. The origin of the gap opened in the single layer limit is still under debate, with indications for a charge density wave and of a Coulomb gap [108, 110]. It is thus important to better understand the band structure of WTe_2 and how it is modified by a magnetic field.

Here I will present a careful study of the magnetic field dependence of the band structure of bulk WTe_2. I will use STM, so that I will probe the surface properties. Previous work by Francisco Martin Vega [91] has made the most detailed comparison of the band structure available until now using quasiparticle interference. The comparison with DFT calculations at zero field was successful. There was however a very puzzling result, namely the apparent absence of Landau quantization when measuring spatially averaged conductance curves in a magnetic field. Here I will show that the tunneling conductance under magnetic fields varies as a function of the position in such a way that the Landau quantization is averaged to zero when making spatially averaged measurements. Using the Landau level structure, I will analyze Landau quantization at energies close to the surface states identified previously with quasiparticle interference. I will show that there is a non-trivial shift of the Landau level structure that can be related to topological surface states.

3.1 Electronic and topological properties

A non-saturating linear magnetoresistance has been found in the case of topological semimetals, like Dirac semimetals Cd_3As_2 [113], Na_3Bi [114] and Weyl semimetals NbP [115], NbAs [116] and TaAs [117]. In WTe_2, this property varies with a quadratic behavior and its value increases a 13,000,000 % at 0.53 K and 60 T, with no sign of saturation. This behavior is probably due to perfect compensation of carrier densities of electrons and holes [107].

3.1.1 Weyl semimetal

Weyl fermions are massless particles predicted in 1929 [118] that, although not yet observed among elementary particles, exist as collective excitations in so-called Weyl semimetals. Similar to Dirac semimetals, in these materials there is a linear crossing of some bands, forming the Weyl points (WPs). The massless nature of the Weyl points protects them from gapping (see chapter 1.3, note that in WTe_2 Weyl points arise as a consequence of the absence of inversion symmetry in the crystal structure).

Two types of Weyl points have been described. Let us assume for simplicity that the Fermi level is fixed at the Weyl point. In Type-I WPs, the protected

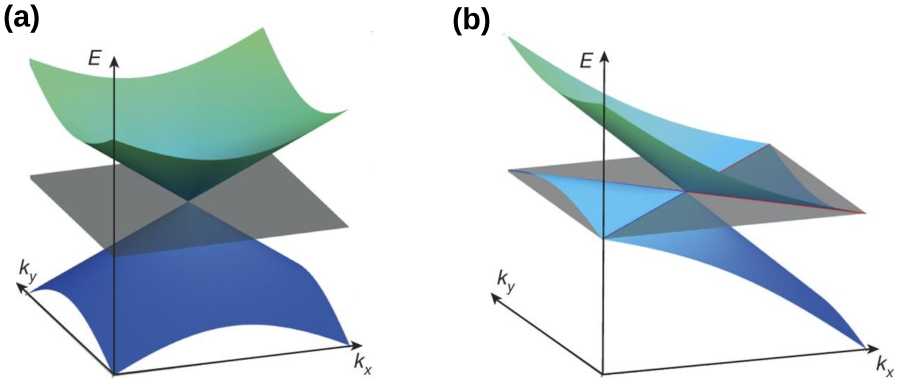

Fig. 3.1: Adapted from [45]. Schematic representation of Weyl points. (a) Type-I Weyl point, where the bands crossing is linear and the Fermi surface is point-like. (b) Type-II Weyl point, where the crossing is oblique and the Fermi surface is no longer point-like.

band crossing is perpendicular (figure **3.1 a**). Electron and hole bands only overlap at the Weyl points, and the Fermi surface is a closed point-like. Type-II WPs exist at the crossing of the oblique conduction and valence bands, and the Fermi surface is no longer point-like (figure **3.1 b**).

WPs always appear in pairs and act as a topological charge. A Fermi surface enclosing a Weyl point has a well-defined Chern number that corresponds to the topological charge of the WP. As the topological charge over all the material must be zero, Weyl points appear in pairs with opposite Chern numbers. They act one as a source and the other as a sink of the Berry curvature [45]. A non-trivial Berry phase of π is another important characteristic of Weyl semimetals. A non-zero Berry phase indicates the existence of one of these protected band crossings [29]. Weyl semimetals have surface Fermi arcs that appear as open contours in the Fermi surface. The edges of the Fermi arcs are the projections on the surface of the WPs with opposite chiral charges.

WTe$_2$ was predicted to have four pairs of Weyl points in the bulk, at 52 meV and 58 meV above the Fermi level. In figure **3.2 a** one pair of Weyl points are shown. The other three pairs can be obtained by symmetry operations [45]. WTe$_2$ was also predicted to have Fermi arcs on the (001) crystal surface. Figure **3.2 b** shows the spectral density function on this surface. The orange areas represent the bulk density of states (DOS), while the thin lines are the surface states. The yellow arrows indicate the two surface states predicted to

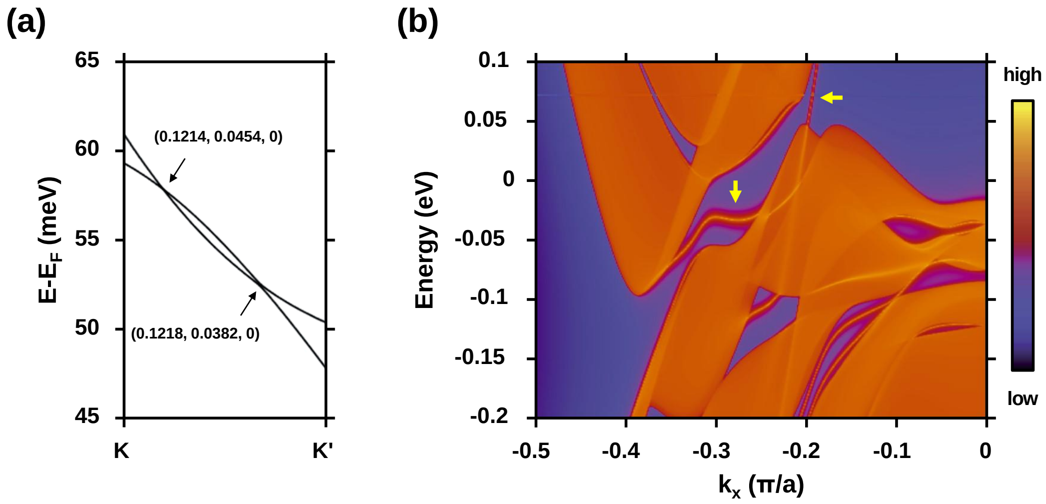

Fig. 3.2: Adapted from [45]. (a) One pair of the four pairs of Weyl points in WTe_2, along the K-K' line. The rest of the Weyl points are related by symmetries. (b) Calculated spectral density function on (001) surface. Surface estates are given by the lines connecting the orange shaded areas, that represent the bulk density of states. Yellow arrows indicate the surface states near the Fermi level.

be near the Fermi level. WTe_2 has two main energy ranges with surface states. One below the Fermi level going from about -0.05 to -0.1 meV and another one from 0.05 meV to about 0.1 meV.

To better understand the formation of Fermi arcs in presence of Weyl points, it is useful to follow the thought experiment described in ref [45]. In figure **3.3**, the evolution of the Fermi surface for a small energy range around the Weyl points is shown (following Ref. [45]). The electron pocket (solid blue line) and the hole pocket (dashed magenta line) come in pairs. Weyl points are represented as red and blue dots and have Chern numbers +1 and −1, respectively. When the Fermi energy is below 52 meV, both WPs are enclosed by the same hole pocket, and the total Chern number is zero for all the pockets. The electron and hole pockets touch at both WPs at 52 meV (figure **3.3 a**) and 58 meV (figure **3.3 c**). In between, the hole and electron pockets disconnect (figure **3.3 b**) and the hole pockets only encloses one Weyl point, with $C = \pm 1$. In figure **3.3 b**, only one hole pocket is shown, but the topology of the other hole pockets can be obtained by symmetry operations [45]. The Chern number of the pockets is the same as the WP they enclose. The electron pockets enclose

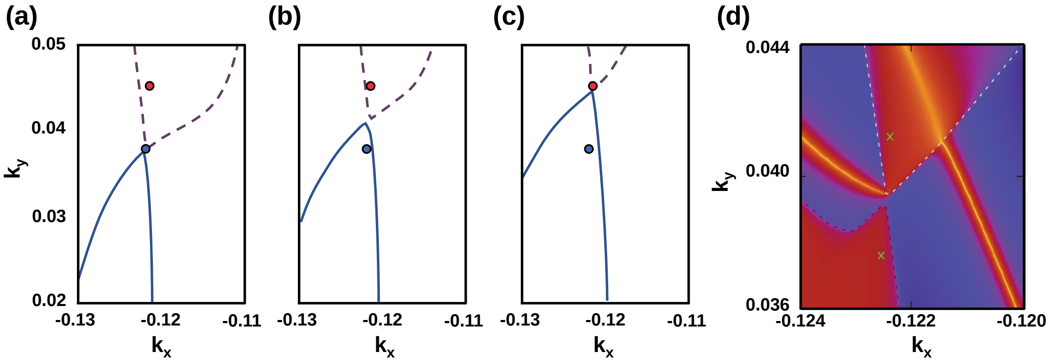

Fig. 3.3: Adapted from [45]. Part of the Brillouin zone, showing WP with Chern number $C = +1$ ($C = -1$) in red (blue). The electron pocket (blue) and the hole pocket (magenta) come in pairs. (a) At $E_F = 52$ meV, the electron and hole bands touch at the lower WP. (b) At $E_F = 55$ meV there is a gap between the electron and hole pockets. The hole pocket encloses a WP with Chern number +1. The electron pocket encloses a WP with Chern number −1, but also its mirror image (not shown). The total Chern number of this pocket is zero. (c) At $E_F = 58$ meV the electron and hole pocket touch again at the other WP. (d) Part of the Fermi surface for the (001) surface. A Fermi arc is connecting the electron and hole pocket. Green cross indicates the position of the Weyl points. The Fermi level is set to be between the WPs.

two Weyl points with different Chern numbers, so the total Chern number for all electron pockets is zero [45]. Topological surface states appear at the (001) surface because the WPs are projected to different points. Surface states connecting electron and hole pockets are shown in figure **3.3 d**.

With these interesting properties, much effort has been put into characterizing the Fermi surface and visualizing topological features of WTe$_2$. With quantum oscillations [119–121], the Fermi surface has been studied, and evidence of four pockets crossing the Fermi level has been found. ARPES measurements resolved two electrons and two hole bands below the Fermi level, and a small energy range above the Fermi level is accessible when increasing the temperature [41, 122, 123]. QPI can measure and characterize the band structure above and below the Fermi level [124–126], although only partial characterization of the band structure was done until the study by Ref. [91]. However, evidence of the non-triviality of the bands and surface states is still incomplete.

3.1.2 Landau quantization

The application of a strong magnetic field $\vec{B}$ forces the electrons to move perpendicular to the direction of the magnetic field and perpendicular to $\vec{v}(\vec{k}) = \frac{1}{\hbar}\nabla_{\vec{k}}E(\vec{k})$, which is itself perpendicular to the surface of constant energy [4].

$$\dot{k} = \frac{e}{\hbar}\vec{v} \times \vec{B}. \tag{3.1}$$

Thus, the electron describes a circular orbit defined by the intersection between a constant energy cut of the band structure and the plane perpendicular to the magnetic field. If the electron is not scattered, it makes an orbit in the period

$$\frac{2\pi}{\omega_c} = \frac{\hbar}{eB}\oint \frac{dk}{v_\perp}, \tag{3.2}$$

where $v_\perp$ is the component of $\vec{v}$ normal to $\vec{B}$ at $\vec{k}$. By geometry, we have

$$\oint \frac{dk}{v_\perp} = \frac{2\pi m}{\hbar}, \tag{3.3}$$

where m is the mass of the electron. The so-called cyclotron frequency is then

$$\omega_c = \frac{eB}{m}. \tag{3.4}$$

To obtain the values of the energy, we consider free electrons in the magnetic field

$$\frac{1}{2m}\left(\frac{\hbar}{i}\nabla - \frac{e}{c}\vec{\mathrm{A}}\right)\psi = E\psi, \tag{3.5}$$

where $\vec{\mathrm{A}}$ is the vector potential. For a magnetic field applied in the z direction, we choose the gauge $\vec{\mathrm{A}} = B_z x\hat{y}$. The movement of the electrons must satisfy the relation

$$\frac{\partial^2\psi}{\partial x^2} + \left(\frac{\partial}{\partial y} - \frac{ieB}{\hbar c}x\right)^2\psi + \frac{\partial^2\psi}{\partial z^2} + \frac{2mE}{\hbar^2}\psi = 0. \tag{3.6}$$

We find that we can separate this equation into motion along the z-axis, which follows the same energy dispersion relation as for free electrons

$$E' = E - \frac{\hbar^2}{2m}k_z^2, \tag{3.7}$$

and x-y in-plane motion, which gives

$$-\frac{\hbar^2}{2m}\frac{\partial^2 u(x)}{\partial x^2}+\frac{1}{2}m\left(\frac{eB}{mc}x-\frac{\hbar\beta}{m}\right)^2 u(x)=E'u(x). \tag{3.8}$$

This equation is equivalent to Schrödinger equation for a 1D harmonic oscillator and a wavefunction $u(x)$. The quantum-mechanical energy eigenvalues of the orbits are those of a harmonic oscillator with eigenfrequency $\omega_c = \frac{eB}{m}$. The total energy is the sum of the quantized energy levels in the x-y plane, plus the translational energy along the direction of the magnetic field

$$E_n=\left(n+\frac{1}{2}\right)\hbar\omega_c+\frac{\hbar^2 k_z^2}{2m}. \tag{3.9}$$

From Eq. 3.9 we see that a finite magnetic field induces a quantization of the continuous parabolic band into discrete states, called Landau levels, with a separation in energy $\hbar\omega_c$. The quantization of one band in k_x or k_y is represented in figure **3.4 a**. In this plane, each Landau level corresponds to one orbit, as the ones in figure **3.4 b**. However, when we look in the k_z direction, the energy levels form a set of parabolas separated by $\hbar\omega_c$, as represented in figure **3.4 c**. If we write the density of states of this set of parabolas, we find

$$N(E)=\frac{1}{4\pi^2}\left(\frac{2m}{\hbar^2}\right)^{\frac{3}{2}}\hbar\omega_c\sum_n\left[E-E_0-\left(n+\frac{1}{2}\right)\hbar\omega_c\right]^{-\frac{1}{2}}, \tag{3.10}$$

where E_0 is the Fermi energy of the band. The electronic density of states follows the inverse of a square root function for each level. When $E = \hbar\omega_c$, the DOS strongly increases, and then decays as $1/E$ until reaching the next level, as represented in figure **3.4 d**. As the total DOS when $B \neq 0$ needs to remain the same as in the case with no magnetic field applied, the degeneracy of each level also increases with the magnetic field.

A Landau level with an energy below the Fermi level is occupied with N electrons at sufficiently low temperatures. When the external magnetic field increases, the Landau levels separate in energy and shift to higher energies. When a level crosses the Fermi energy, the electrons are emptied and occupy the lower Landau levels. The system reaches the lowest energy each time a Landau level just crosses the Fermi energy. Then, the energy increases when increasing the magnetic field until the next Landau level crosses the Fermi energy. As a result, the energy oscillates with the magnetic field, and so do

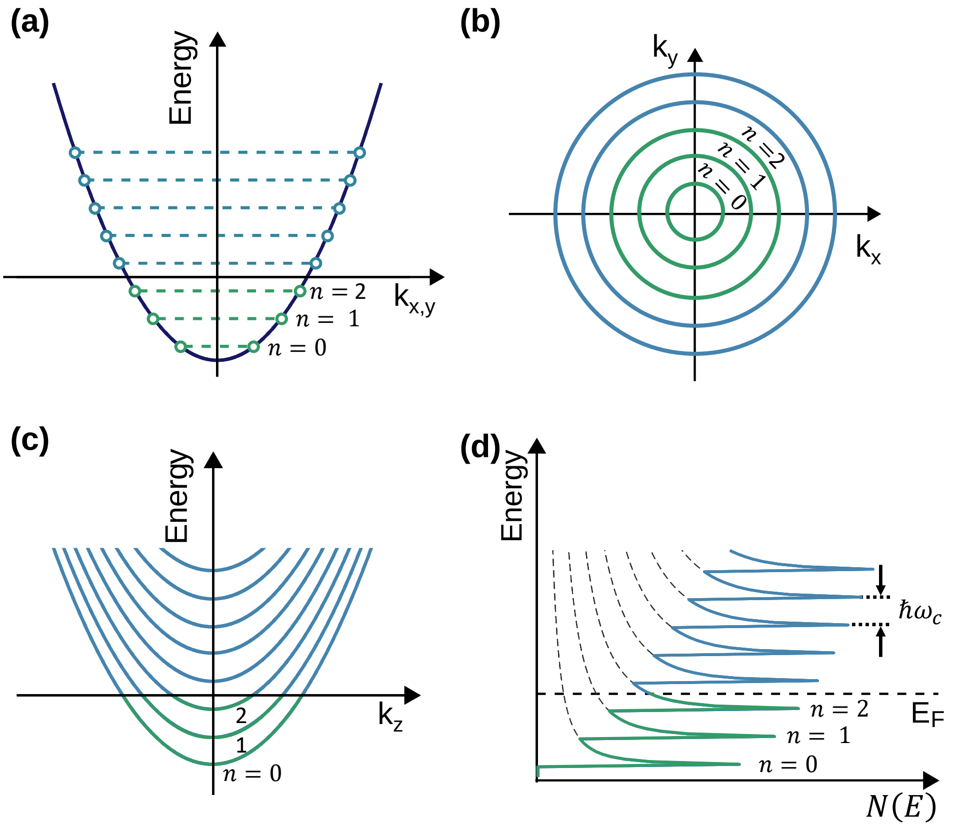

Fig. 3.4: Schematic representation of the quantization of a parabolic band in an external magnetic field. The green color indicates the occupied states and the light blue color, the empty states. (a) Representation of a parabolic band (dark blue line) along $k_{x,y}$ direction, when $B = 0$. When $B \neq 0$, the band quantized in Landau levels, represented by the dotted lines in green and light-blue. (b) Landau orbits in the plane k_x-k_y. (c) Quantization of the band in the k_z direction. In this plane, we can see a set of bands separating in energy. (d) Density of states of the band when $B \neq 0$. The separation in energy between levels is $\hbar\omega$.

the properties of the material, such as the electrical conductivity (Shubnikov-de Haas effect) or the magnetic susceptibility (de Haas-van Alphen effect). Figure **3.5** represents the separation of the Landau levels while increasing the magnetic field and a measurement of the quantum oscillations.

Quantum oscillations have been significant in the characterization of the topology of Fermi surfaces. When the measured property is plotted against

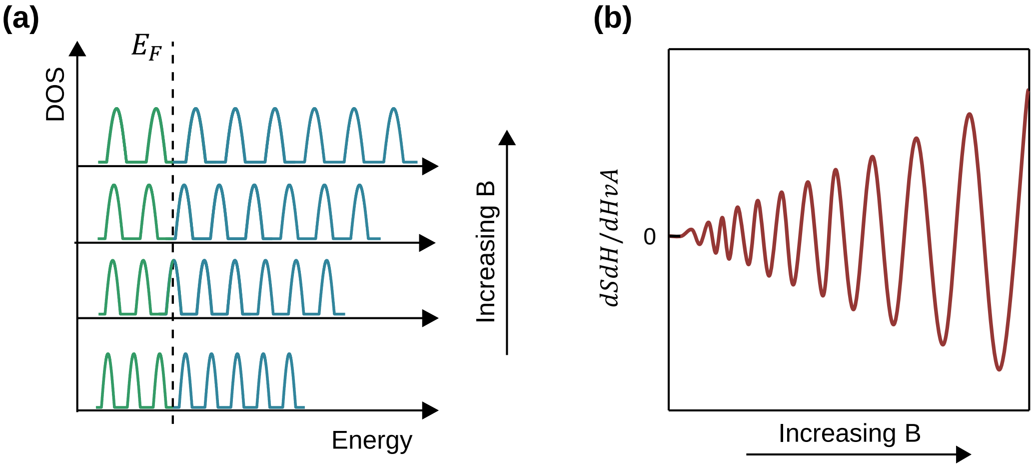

Fig. 3.5: Schematic representation of quantum oscillations. (a) Representation of the Landau levels in the DOS. When the magnetic field increases, the levels separate in energy and cross the Fermi level. In this process, the level crossing the Fermi energy empties, and the occupied levels increase its degeneracy. (b) Representation of the quantum oscillations measured at the Fermi level.

one over the magnetic field, the frequency of the oscillation is proportional to the extremal (maximum/minimum) area of the Fermi surface in the momentum space, in the plane perpendicular to the magnetic field. However, the changes in the Fermi surface with the magnetic field can complicate the determination of single frequencies in quantum oscillations. Furthermore, the states below and above the Fermi level are not accessible with this method.

3.1.3 Bulk density of states

As mentioned above, WTe$_2$ is a semimetal, with a small DOS near the Fermi level. Bulk band structure calculations predict two hole pockets and two electron pockets along Γ-X direction, with a small overlap at the Fermi level (see figure **3.6**). The electron bands have W-5p character, while the hole bands have Te-5d character.

The Fermi surface can be experimentally characterized with different techniques, like quantum oscillations. Figure **3.7 a** shows quantum oscillations measurements for WTe$_2$ at fields up to 14 T. With this method, two electron

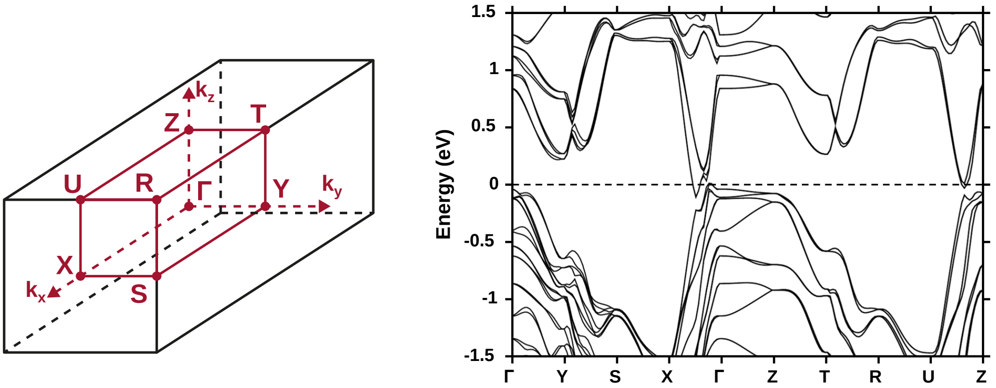

Fig. 3.6: Adapted from[45]. Diagram of the Brillouin zone of WTe_2 (left) and the calculated bulk band structure (right).

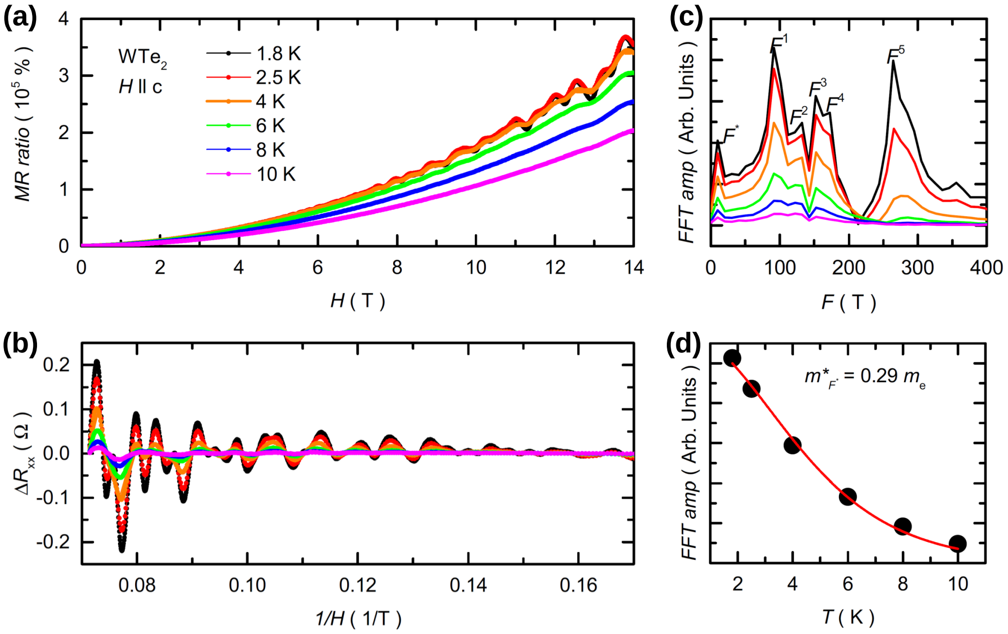

Fig. 3.7: Adapted from [119]. Quantum oscillations in WTe_2.(a) Magnetoresistance measured at T = 1.8 K, 2.5 K, 4 K, 6 K, 8 K, and 10 K. (b) Shubnikov-de Haas oscillations after subtracting the background. (c) Fast Fourier transform (FFT) analysis of quantum oscillations.(d) Temperature dependence of the oscillation amplitude as a function of the temperature for the frequency, F^*. The black points are the data, and solid line is the fitting to the Lifshitz–Kosevich formula.

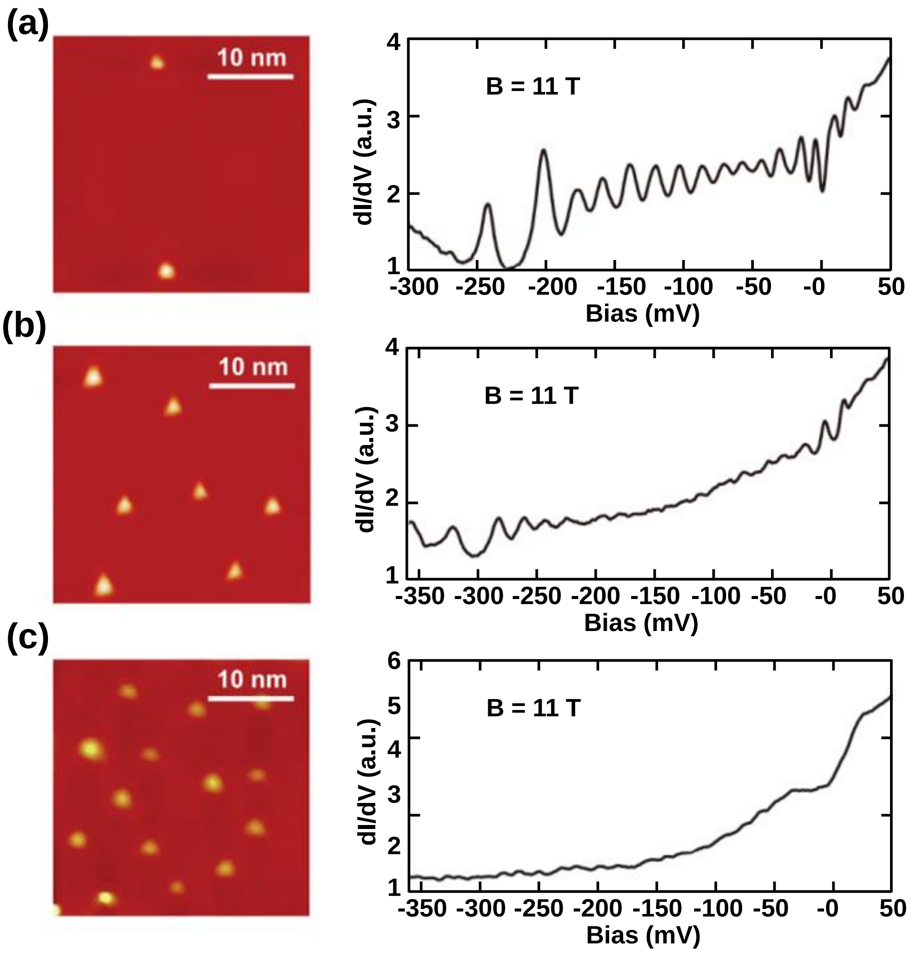

Fig. 3.8: Adapted form [127]. Suppression of the Landau Levels by defects. On the left, STM images of Bi_2Se_3 with Ag impurities (bright points). On the left, STS spectra of the Landau levels for the different areas. (a) The LL are well resolved when the coverage of the impurities is small. When increasing the impurities, the LL smooth (b) until they disappear for high coverage of impurities (c).

and two hole pockets are found, in agreement with calculations and ARPES measurements [119]. The effective masses of these bands have been found to be between $m^* \simeq 0.23\ m_e$ and $m^* \simeq 0.28\ m_e$ [120].

Using spectroscopy measurements with the STM, we can access the bands in the range of energy we are measuring, and then we can see the Landau levels above and below the Fermi level (see section 3.1.2). However, these experiments have been mostly made with success in systems with a relatively simple band structure with a single band crossing the Fermi level, such as graphene [128]. Furthermore, for the Landau levels to be visible in real space, the number of defects in the material needs to be very low. For example, in figure **3.8** we can see how the Landau levels vanish when increasing the number of defects on the surface on Bi_2Se_3 [127]. A relevant scale is the magnetic length $l_B = \sqrt{\hbar/eB}$, which is associated with radius of the cyclotron orbits $r_n = \sqrt{2n+1} l_B$. Thus, the average defect distance must be of the order or larger than l_B in order to resolve the Landau levels in the density of states. For example, in the case shown in figure **3.8**, the Landau quantization vanishes when the distance between defects is comparable to $l_B \sim 10$ nm at 11 T.

3.2 Atomic structure

WTe_2 belongs to the transition metal dichalcogenides (TMDs). TMDs are a group of materials with chemical formula MX_2, being M a transition metal atom and X a chalcogen atom (S, Se or Te). These materials often form a layered crystalline structure, with layers in which the transition metal is sandwiched between two chalcogens. Each Te-W-Te layer is separated by a van der Waals gap along the c direction of the crystal structure. We can see the atomic structure of WTe_2 in figure **3.9 a**.

In WTe_2 the W atoms form zigzag chains along the a-axis. As the distance between W atoms is significantly smaller along the a-axis than along the b or c-axes, the material exhibits rather one-dimensional electronic properties, as we shall see below. WTe_2 lattice parameters are $a = 3.477$ Å, $b = 6.249$ Å and $c = 14.018$ Å, and its unit cell is indicated with a dotted black rectangle in figure **3.9 a** and **b**. WTe_2 crystallizes in an orthorhombic structure with space group $Pmn2_1$ [129]. This space group is noncentrosymmetric, which is a requirement for the existence of Weyl fermions in a nonmagnetic system [45] (see chapter 1.3).

We measured WTe_2 single crystals from the group of Prof. Paul C. Canfield. They were grown from a Te-rich binary melt following the procedure described in references [130, 131]. The crystals were plate-like with typical dimensions of 2 mm × 0.1 mm × 0.01 mm, with the crystallographic c-axis perpendicular to the larger crystal surface. The samples were cleaved in situ in cryogenic

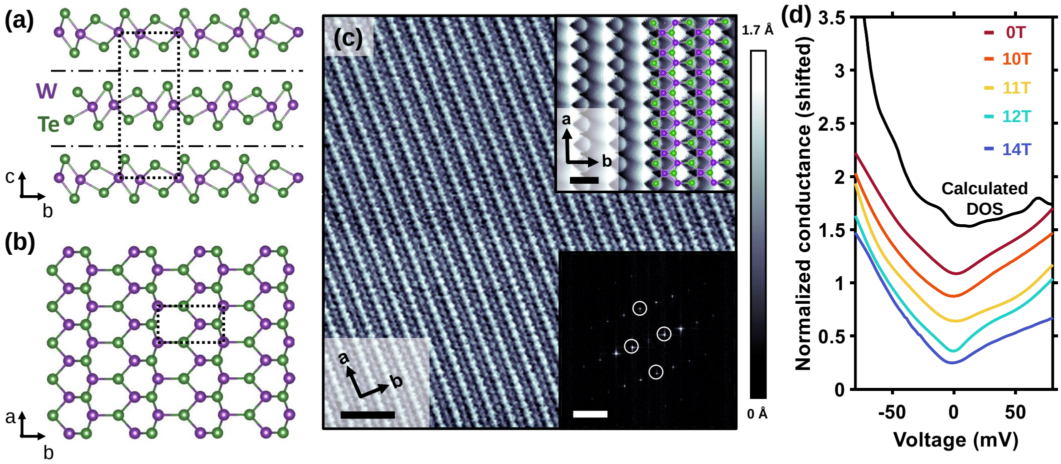

Fig. 3.9: Side view (a) and top view (b) of the atomic structure of WTe_2. W atoms are in purple and Te atoms are in green. The dotted black rectangle indicates the unit cell. Dotted lines in (a) indicate cleaving planes. (c) STM topographic image with atomic resolution at 14 T and 4.2 K. Image taken at 100 mV and 4 nA. The horizontal scale bar is 2 nm long. Fourier transform is shown in the bottom insert, where the horizontal scale bar is 3 nm^{-1} long. In the top inset, high-resolution STM topography where both rows of Te atoms are perfectly resolved. The horizontal scale bar is 5 Å long. (d) Spatially average normalized conductance curves at different magnetic fields. Calculated DOS is plot in black. Curves are shifted for clarity. Calculations by Masayuki Ochi and Ryotaro Arita.

conditions, as described in the previous chapter. This cleaving process allows us to obtain very flat and clean surfaces of Te atoms. In topography images, we can see the Te atoms forming chains along the a-axis, which is also the orientation of the underlying W zigzag chains. This pattern remains constant under the variation of magnetic fields up to 14 T, meaning that there are no substantial modifications of the electronic structure with magnetic fields (the topography pattern shows the pattern of the tunneling current, which is the integral of the density of states from zero up to the bias voltage, see chapter 2.2.1). A topography image at 14 T and 4.2 K is shown in figure **3.9 c**. Using topographies with atomic resolution in large areas, we can estimate the number of defects in the material 1.3×10^{12} cm^{-2} [91], which is very small. This means that the electron can move along ~ 350 unit cells without finding any defects, and the mean free path can be estimated as $l \sim 170$ nm. As the Landau orbits at 14 T are of the order of $r_0 \approx l_B \approx 7$ nm and $l_B < l$, this material is a good candidate for measuring Landau levels.

As mentioned before, this material is a semimetal with a small DOS at the Fermi level. In figure **3.9 d**, we plot the tunneling conductance averaged over a full field of view. This DOS is larger below the Fermi level and reaches almost zero at the Fermi level, as expected from DFT calculations and in agreement with previous measurements [91, 126, 132]. When measuring at high magnetic fields, the shape of the curve remains without change. Let us remind that the magnetoresistance of WTe_2 is of about 400,000 % at 4.5 K and 14.7 T [107]. Our measurements show that the band structure remains essentially unchanged close to the Fermi level when increasing the magnetic field. Thus, we show that the extreme magnetoresistance is not a consequence of changes in the band structure. This is in line with the explanation suggested in Ref. [107], in which the magnetoresistance is due to electron-hole compensation.

3.3 Spectroscopy at high magnetic fields

3.3.1 Landau Levels

Although this material is an excellent candidate to observe Landau quantization, the tunneling conductance under magnetic field presents no signature of Landau level formation (figure **3.9 d**). Note that these curves have been obtained after averaging over many different sites. To better understand this point, we first focused on finding, using the low temperature in-situ positioning mechanism described in Refs. [92, 104], fields of view which were far from defects and consisted mostly of defect-free areas. Furthermore, we analyzed curves taken at precise positions defined at atomic scale, not curves averaged over a certain field of view. As we can see in figure **3.10**, we could observe Landau quantization clearly in the tunneling conductance. Curves are shifted for clarity and its background has been removed (background accounts for the bias voltage dependence of the tunneling conductance, shown in figure **3.9 d**). The amplitude of the Landau levels increases with the magnetic field as it is expected (inset of figure **3.10**).

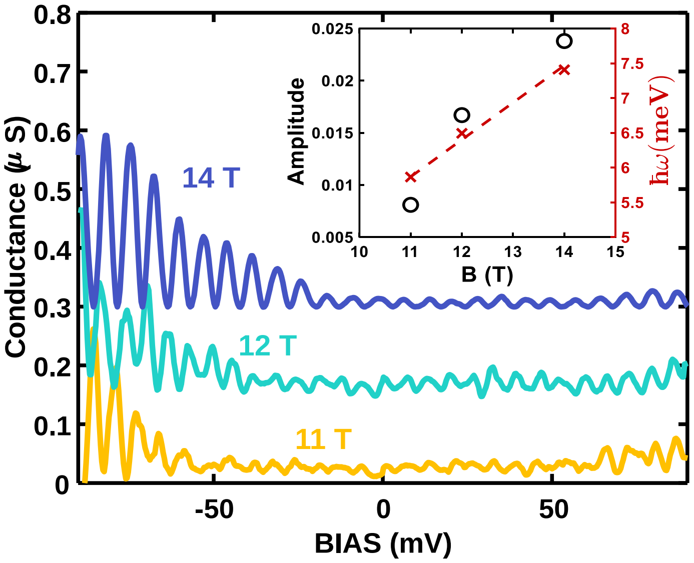

Fig. 3.10: Conductance curves at 11 T, 12 T and 14 T at one point in the sample. The background has been removed and curves are shifted for clarity. In the inset, FFT amplitude (black) and the energy separation between levels (red). Dashed red line indicates the calculated energy between levels with a mass of $m^* = 0.22\ m_e$.

From the Fourier transform we obtain a single peak, that corresponds to the separation in energy between consecutive Landau levels ΔE. Using Eq. 3.4 we obtain an effective mass $m^* \approx 0.22 m_e$. In the inset of figure **3.10** we represent as crosses the ΔE found at each magnetic field. The calculated ΔE for $m^* = 0.22 m_e e$ is shown as a red dashed line. The m^* obtained is very close to the values for the effective masses obtained from quantum oscillations (between $m^* \approx 0.23 m_e$ and $m^* \approx 0.28 m_e$ in Ref [120]).

We should note that, as all the bands have very similar values of m^*, energy difference between Landau levels does not change significantly in different bands. For example, at 14 T, a difference in the mass of 0.04 m_e results in a separation between levels of only 1.2 meV. Note that such values are also of the order of the Zeeman splitting. We find a Zeeman splitting of approximately 1.6 mV at 14 T ($E_Z = \mu_B g_L J B$, where μ_B is the Bohr magneton, g_L is the Landé g-factor, $J = S + L$ is the total angular momentum). For smaller fields, the difference is even smaller. Furthermore, levels are broad, with peaks being about 5 meV large. Thus, we see that level broadening is of the same order as differences in band mass.

3.3.2 Landau levels with atomic resolution

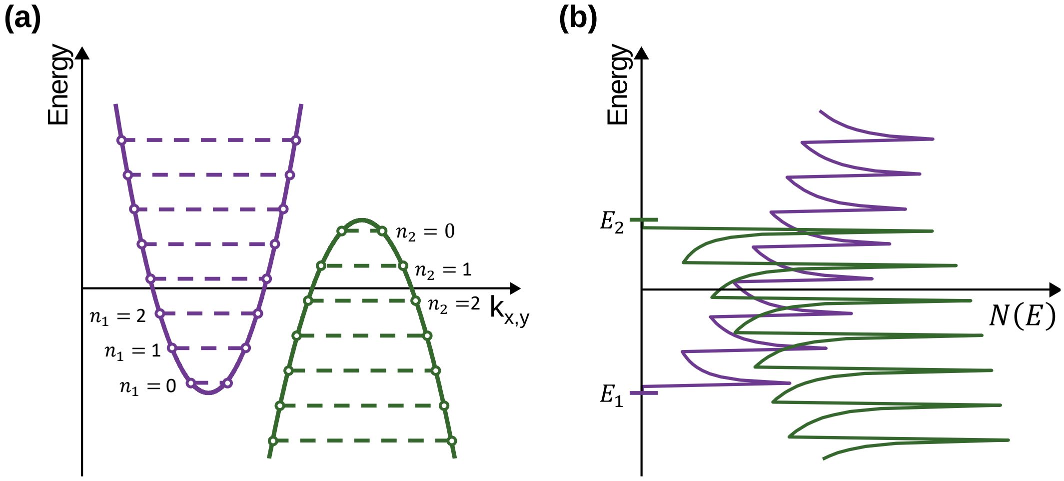

Fig. 3.11: Schematic representation of the quantization of two parabolic bands with different Fermi energy. (a) Parabolic electron band (purple) and hole band (green). The continuous lines represent the bands at $B = 0$. When $B \neq 0$, both bands are quantized in Landau levels. (b) Electronic density of states of each band when $B \neq 0$.

Let us now try to understand how the Landau level structure is washed out in spatially averaged measurements. Figure **3.11 a** schematically illustrates the situation when we have several bands. One electron band (green) and one hole band (purple) with the same effective mass are quantized when applying a magnetic field. The electronic DOS can be obtained by applying Eq. 3.10 for each band. Hence, the final $N(E)$ is the superposition of Landau levels for both of them (figure **3.11 b**). As the bottom and top of the bands are different, the levels are located at different positions in energy. Small changes in the top or bottom of the bands produce considerable changes in the level scheme. Contrary to the dispersion in values of the effective mass, the difference in the position of the bands can be of the order of the level broadening or larger.

As we have seen above, when taking atomically resolved tunneling conductance curves, we observe Landau oscillations, but these are absent in spatially averaged tunneling conductance curves. This suggests that the contribution of a certain set of bands to the tunneling conductance slightly changes as a function of the atomic position.

To account for the contribution of different bands to the spatial changes in the tunneling conductance, we can add an oscillatory term to the DOS Eq. 3.10. We probe at a single position a given band structure, and the probed band structure changes at the next position.

$$N(E,x) = \frac{1}{4\pi^2}\left(\frac{2m^*}{\hbar^2}\right)^{\frac{3}{2}} \hbar\omega_c \sum_n \left[E - E_0 - \left(n + \frac{1}{2}\right)\hbar\omega_c + Acos(qx)\right]^{-\frac{1}{2}}, \tag{3.11}$$

where A is the amplitude of the oscillatory term, q indicates the periodicity of the oscillation, and x is the distance. This oscillatory term only modifies the top and bottom of the band periodically, changing the position of the Landau levels in energy without modifying their energy separation $\Delta E = \hbar\omega_c$.

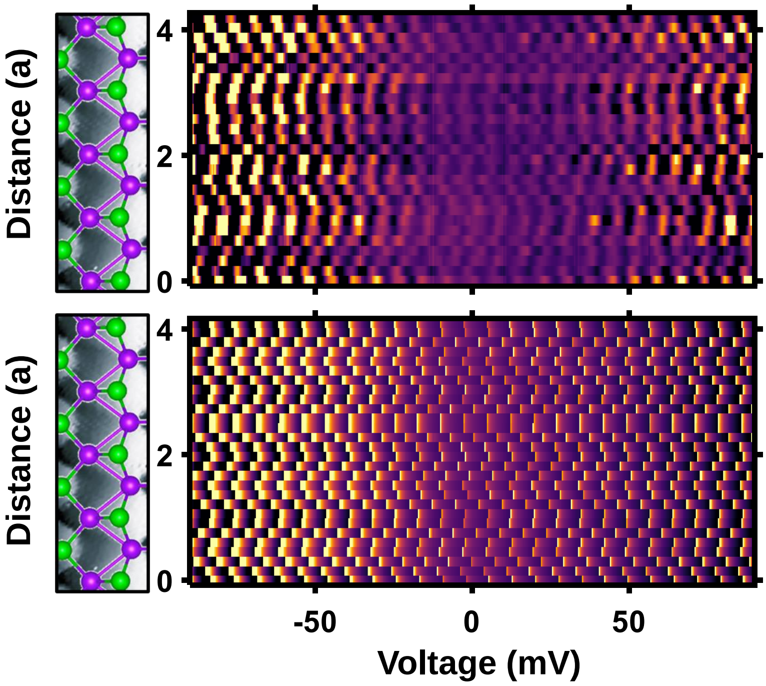

Fig. 3.12: Experimental (top) and calculated (bottom) conductance maps for a profile on top of Te atoms at 14T. The position of the atoms are indicated with the topography on the left. The map was calculated using the Eq. 3.11 with parameters A = 4.2 mV and $q = 2\ \pi a$, and using the experimental parameters of number of points and the obtain $\hbar\omega_c$ at 14 T.

Using Eq. 3.11, we can simulate patterns of the density of states. We use $A = 4.2$ mV and $q = 2\pi a$, where a is the unit cell parameter in the direction of the Te chains. Note that A is larger than $\hbar\omega_c/2$. Thus, the pattern is not a simple cosine wave. Instead, it is an intricate set of maxima and minima. Figure **3.12** shows the comparison between a profile along one of the Te chains at 14 T and a simulation of Eq. 3.11. The simulation was made with an effective mass $m^* = 0.22m_e$ at 14 T. The average curve of the STS measurement was added to Eq. 3.11 to obtain the background.

Thus, we see that when we scan the surface of the sample, we are tunneling into different atomic positions. Depending on the atomic position, a certain contribution to the tunneling conductance from different parts of the band structure is dominating. From the analysis made here we can understand that the structure of the bands contributing at each atomic position to the tunneling current is slightly different. The overall behavior is well reproduced by Eq. 3.11, as shown in figure **3.12**. For example, let us consider the two Te derived hole bands close to the Γ point. When tunneling on top of a Te atom or in between, we can expect a different tunneling wavefunction overlap between tip and sample. This can be parametrized into a different tunneling matrix element, when there is just a single band and gives just a prefactor to the tunneling current. But in a system with two close-lying bands, the wavefunction overlap does not need to be the same everywhere on atomically resolved positions. We can see this by taking a $N_{local}(E)$ composed of different portions of the band structure, whose relative weight changes depending on the atomic position. The same effect should be more pronounced when taking into account the W-derived electron bands and the Te-derived hole bands (figure **3.11**).

3.3.3 Surface states in Landau level spectroscopy

Previous QPI measurements [91] demonstrate two surface states in WTe_2. Figure **3.13 a** shows bulk bandstructure DFT calculations in the $\Gamma - X$ high symmetry line, in the range of energies we are measuring. Electron bands have W-5d character and are represented in purple. Hole bands have Te-5p character and are represented in green. Surface calculations predict two arc-like surface states, at −50 mV and +75 mV (see figure **3.2**) [91]. In figure **3.13 b** and **c**, the calculated spectral density maps are represented for both energies (calculations by Masayuki Ochi and Ryotaro Arita). Surface states are indicated with yellow arrows. The autocorrelation of the isolated Fermi arcs are represented in figure **3.13 d** and **e** (see chapter 2.4.1).

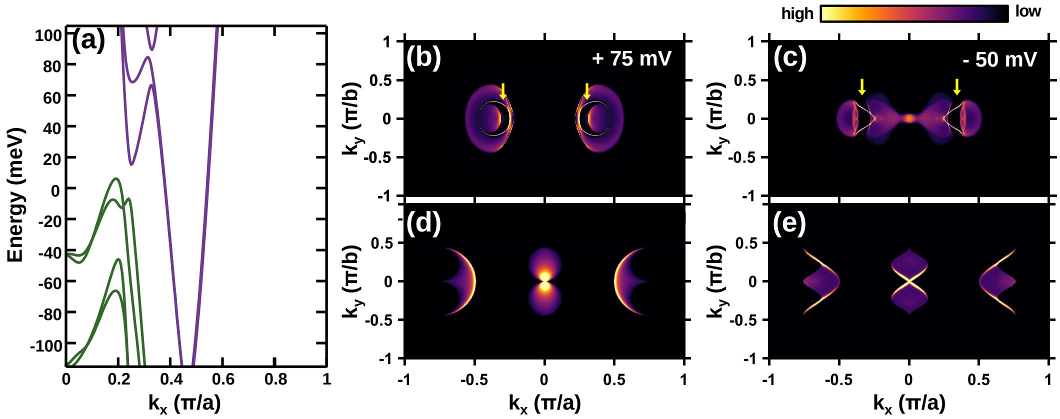

Fig. 3.13: Adapted from [91]. (a) Calculated bulk density of states in $\Gamma - X$ direction by Masayuki Ochi and Ryotaro Arita. Purple and green color of the bands indicates the orbital character of each of them: electron bands have a predominant W-5d character, while hole bands have Te-5p character. (b) and (c) are the calculated spectral density function on (001) surface at +75 mV and −50 mV. Yellow arrows mark the surface states. (d) and (e) JDOS associated with the surface state in (b) and (c), respectively.

Evidence of these two surface states can be found when looking at the amplitude of the Landau levels in the conductance curves taken at certain positions. In particular, we can expect enhanced Landau oscillations when surface states contribute to the tunneling conductance, due to the increased contribution of two-dimensional surface states to the density of states measured by STM. For the conductance curves taken on top of the Te atoms (green arrow in figure **3.14 a**), the amplitude of the oscillations increases at energies below −50 mV. Figure **3.14 b** shows the curves taken on top of four consecutive Te atoms. The gray shadow indicates the energy range where we observe an enhanced tunneling conductance. For the curves in between the Te atoms (purple arrow in figure **3.14 a**), the conductance curves show a similar enhancement for energies below −50 mV, but also above +75 mV. This increase in the signal intensity can be related to the presence of surface states below -50 mV and

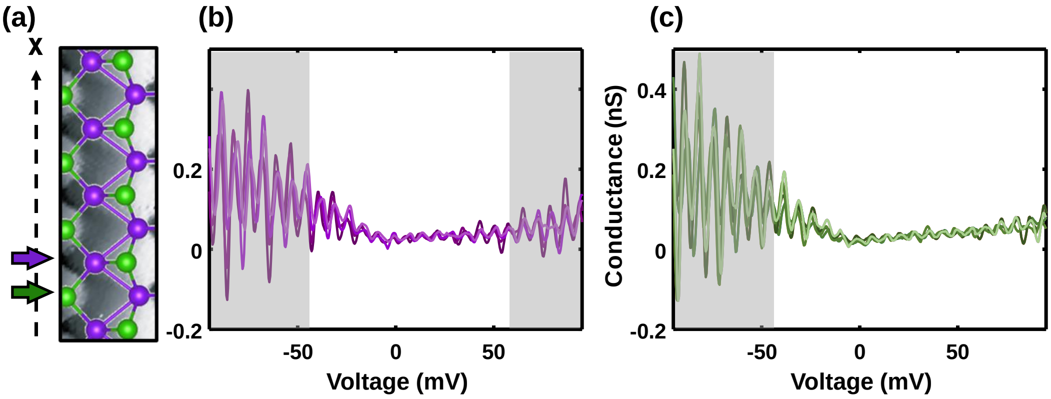

Fig. 3.14: (a) High resolution atomic topography with the position of the atoms indicated. Purple and green arrows indicate the first position where the conductance curves for (b) and (c) are taken, respectively. (b) Conductance curves taken on top of four W atoms. (c) Conductance curves taken on top of Te atoms. The gray shadow indicate the energy ranges where the conductance is enhanced.

above 75 mV, as also found in the calculations presented in figure **3.13**. Figure **3.14 c** shows curves taken in between Te atoms for four consecutive Te positions. As the surface states around −50 mV connect one electron and one hole band, each with a different orbital character, it can be resolved for both atomic positions. However, the surface state above +75 mV has only W-5*d* character. Hence, it can only be resolved in the positions where the W atoms lay below the surface. This supports the description made above, in which atomically different positions contribute differently to the tunneling conductance.

3.3.4 Phase accumulation in Landau levels

To see if there are any deviations in the position of the Landau levels close to the surface state energies, we take one conductance curve (figure **3.15 a**) and assign arbitrary values of the LL index n, starting at $+100$ mV. We plot the position of this value *versus* the position of the level in energy as dots in the inset in figure **3.15 a**. It is easy to see from Eq. 3.9 that the result for one band should be a straight line. The resulting curve is indeed very close to a straight line. However, there is a tiny but relevant change. The line obtained taking the points at large negative and positive bias voltages have the same

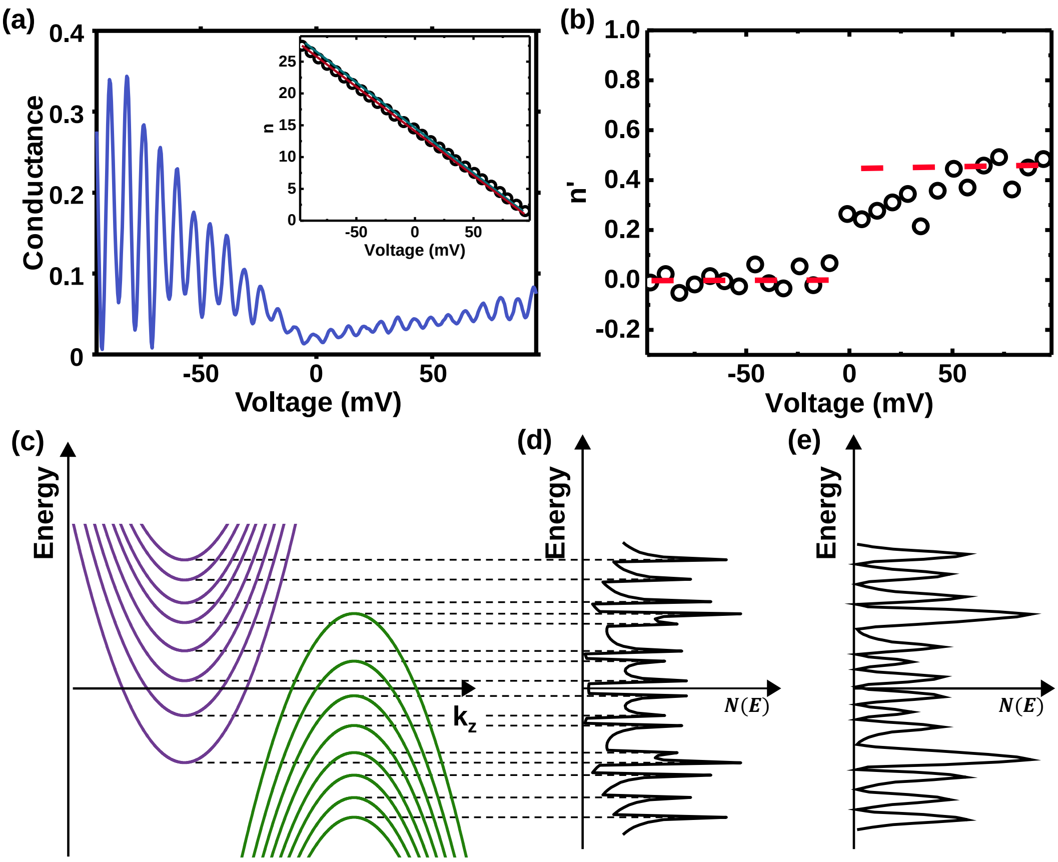

Fig. 3.15: (a) Conductance curve at 14 T. In the inset, Landau index as a function of the voltage. Points near 100 mV have been fit to the blue line, and points near -100 mV, to the red line. (b) Difference between the red line and the Landau index from the inset in (a). Red dashed line indicates the result using a model in (c-e) (see main text). (c) Schematic representation of the Landau level quantization of two bands with Dirac dispersion. (d) Total density of states of the two bands. (e) Broadening of the levels due to the resolution.

slope but are shifted with respect to each other (red and blue lines). The shift is of $\delta = \frac{1}{2}$ in n. This means that, at some point along the line, there is a difference between levels of $\frac{1}{2}n$. This behavior is the same for different atomic positions in figure **3.12**. When the fitted line is subtracted to the experimental data, we find the energy variation of the Landau level index shown in figure **3.15 b**. When the magnetic field is reduced, the Landau levels approach in energy and more levels are measured in the same energy range. Then, the linear dispersion is harder to differentiate from the quadratic dispersion and it is more difficult to examine the difference from the experimental data.

To better understand the Landau level structure, let us consider the situation depicted in figure **3.15 c**. Here, we represent two bands quantized by the influence of the magnetic field. These bands disperse linearly in the plane $k_x - k_y$. Thus, when we represent the sub-bands in k_z, the separation between them follows the Dirac quantization

$$E_n = E_0 \pm \sqrt{2e\hbar v_F^2 |n| B}, \tag{3.12}$$

where v_F is the Fermi velocity. These two bands contribute with peaks to the total density of states $N(E)$, and the levels mix in the energy range where the two bands superpose (see figure **3.15 d**). The resolution of the experiment can lead to the level broadening, giving a single peak for the levels that are near in energy. A broadening of ~ 5 mV is represented in figure **3.15 e**. Analog to the experiment, we can represent the Landau level position as a function of the energy, obtaining a similar result that in the experimental data. The Landau levels from this model can also be fitted to two straight lines with the same slope, but whose difference in position is $\sim \frac{1}{2}n$. With this model and using the experimental parameters, we obtain the dashed red line depicted in figure **3.15 b** when one of the lines is subtracted.

For the model above, we supposed that the band disperses linearly in the $k_x - k_y$ plane. But let us discuss the quantization of two parabolic bands with the same m^* (see figure **3.16**) and see if it is possible to obtain a change in the Landau level sequence. The total DOS is described by the equation

$$N_T(E) \propto \sum_n \left[(E - E_1) - \left(n + \frac{1}{2} \right) \hbar\omega_c \right]^{-\frac{1}{2}} + \sum_m \left[(E_2 - E) - \left(m + \frac{1}{2} \right) \hbar\omega_c \right]^{-\frac{1}{2}}, \tag{3.13}$$

where E_1 and E_2 are the top and bottom of the bands. Having the distribution of Landau levels in figure **3.16** would mean that the top and bottom of the bands are related as

$$E_1 = E_2 \pm n\hbar\omega_c. \tag{3.14}$$

It can be seen in the DOS resulting from these bands (figure **3.16 b**) that the result of this configuration would be a straight line when representing n *vs* energy. However, this is not what we observe. Alternatively, the Eq.

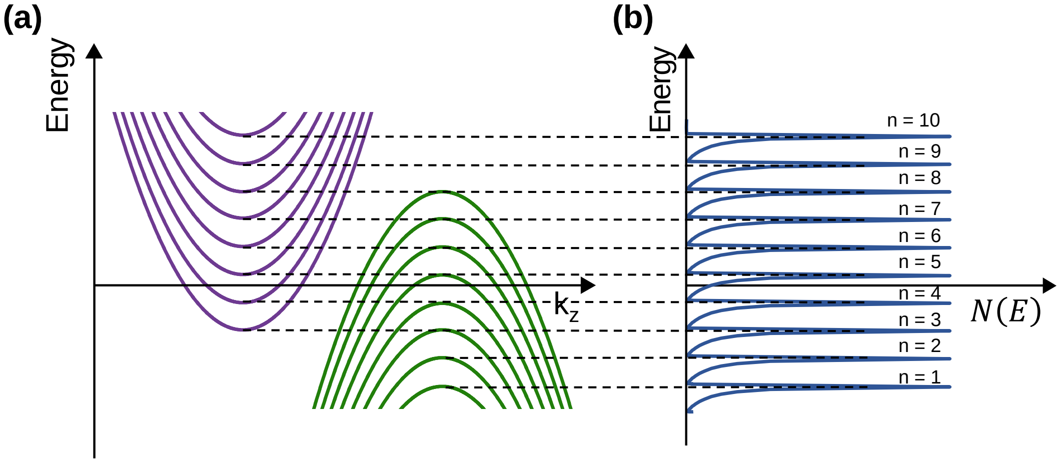

Fig. 3.16: (a) Adapted form [45]. Electron and hole bands, quantized by the presence of a magnetic field B ≠ 0. We represent a situation in which positions of top and bottom of bands are aligned. This leads, of course, to alignment of the Landau levels too. (b) Density of states of the two bands, where n = 1,2, ... are the arbitrary count of the levels, analog to the counting made in figure **3.10 a**. The top and bottom of the bands are related by the Eq. 3.14.

3.14 might not be fulfilled, in which case, the Landau level sequence is not linear. However, this would also imply that Landau level smearing (figure **3.11**) eliminates the difference.

3.4 Conclusion

In summary, we performed high resolution topography images on atomically flat surfaces, measuring the Te chains. This pattern remains the same with the magnetic field, indicating no significant modifications in the band structure. In agreement with the topography images, the spatially averaged DOS remains very similar at high magnetic fields, demonstrating that the huge magnetoresistance in the material is not a consequence of a variation in the band structure. Although WTe$_2$ gathers lots of conditions favorable to Landau levels to be measurable (2D layered structure, a small density of defects, small effective mass,...), no oscillations were found in the spatially averaged tunneling conductance curves.

We performed very high resolution spectroscopy maps at high magnetic fields to find the Landau levels. Doing so, we resolve Landau quantization of the density of states under magnetic field with associated effective mass m^* = 0.22 m_e. Following the conductance curves along the Te chains, a change in the position of the Landau levels is visible. We can reproduce the distance dependence by parametrizing the Landau level DOS as a function of the atomic position, evidencing a new form of atomic size quantum oscillations. This can now be applied to many other systems showing multiple bands crossing the Fermi level.

By representing the conductance curves on top of the Te atoms and between them (corresponding to the positions of the W below the surface), we found evidence of the surface states previously found with QPI measurements. An enhancement of the amplitude of the oscillations below −50 meV is observed for both positions. The surface state at this energy connects both the electron (with W-5*d* character) and hole bands (with Te-5*p* character). Similarly, an enhancement is found above 75 meV, for a surface state connecting the electrons bands.

Equipped with the knowledge that we can observe Landau quantization by taking a look on atomically defined conductance curves, we have analyzed the Landau level structure and unveiled a significant modification when changing the bias voltage. We show that this implies a change in the Landau level structure due to a non-parabolic band dispersion in the studied energy range. Thus, we have shown that the surface states unveiled in Ref [91] are probably topologically non-trivial and lead to a Landau quantization scheme characteristic of a linear dispersion.

Chapter 4

Kagome lattice induced end states in one dimensional atomic chains

MATERIALS with flat bands have emerged as novel materials to study electronic correlations, magnetism and topological properties [133–137]. Defects excitation such as vacancies or adatoms can reveal new physical properties on this kind of materials [138–140].

In this chapter, I present measurements on the magnetic Weyl semimetal $Co_3Sn_2S_2$. We used high resolution topographies to characterize the surface, finding signatures of a flat band on the S layer [141]. Sn atoms on the empty triangles of the kagome lattice produce a modification of the magnetic order. We found end states on Sn chains related to the flat-band breaking.

4.1 Band structure in the kagome lattice

A non-trivial band structure can be created by proper design of the lattice structures. For example, Dirac bands with linear dispersion can be created in the honeycomb lattice [142, 143]. In contrast with this linear Dirac band hosting massless particles, specific atomic configurations produce a destructive quantum phase interference of Bloch wave functions, leading to electronic confinement and flat bands [144]. Several lattices have been proposed to generate flat bands, such as twisted bilayer graphene [143, 145, 146], kagome [147–151], side centered square [152], checkerboard [153], Lieb lattice [154] or Dice lattice [155].

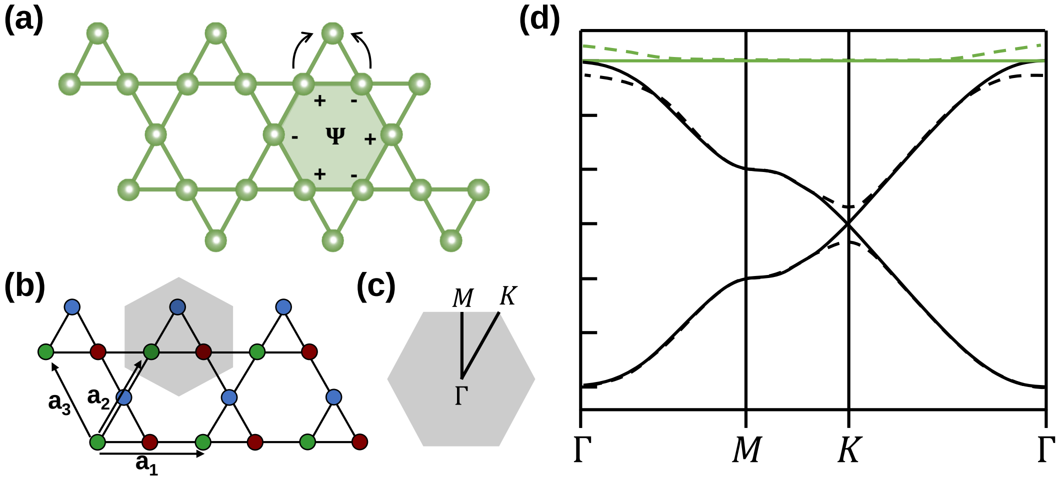

Fig. 4.1: (a) Atomic structure of a kagome lattice. Plus and minus signs indicate the phase of the eigenstate at neighboring sublattices. Colored green hexagon indicates the electron confinement in the lattice. Any hoppings outside the hexagon (indicated with black arrows) are cancelled by destructive quantum interferences. (b) Inequivalent atomic positions in the kagome unit cell (gray hexagon) are indicated with different colors. $\vec{a}_{1,2,3}$ are the shortest lattice vectors. (c) Brillouin zone of the kagome lattice. (d) Tight-binding band structure of kagome lattice featuring flat band (solid green line) and two Dirac bands with linear crossing at K (solid black lines). Inclusion of spin–orbit coupling gaps both Dirac crossing and quadratic touching between the flat band and the Dirac bands (dotted lines).

In the simplest nearest-neighbor electronic hopping model, the tight-binding Hamiltonian can be written as

$$H_t = -t \sum_{\langle ij \rangle} c_i^{\dagger} c_j + h.c. \tag{4.1}$$

where i, j denote the sites of the kagome lattice, $\langle ij \rangle$ denotes nearest-neighbor pairs of sites, the operators $c_i (c_i^{\dagger})$ annihilate (create) a fermion on site i and t is the hopping parameter. The kagome lattice is composed of interlaced triangles where each lattice point interconnects two neighboring hexagons, as shown in figure **4.1 a**. One can construct real-space eigenfunctions with alternating phases at the neighboring corners of the hexagon. This electronic state is geometrically confined within the single hexagon since the destructive phase interference hinders any hopping from neighboring cells. Electronic states are geometrically confined within a single hexagon (color hexagon in figure **4.1 a**) since any hopping from neighboring cells is cancelled by the destructive phase interference. This real-space electronic localization leads to the formation of eigenfunctions with no energy dispersion in the momentum space, namely flat bands.

The three inequivalent atomic positions are indicated with the colors green, red and blue in each unit cell (gray hexagon) in figure **4.1 b**. When resolving Eq. 4.1 [151, 156, 157], the resulting band structure consists of one non-dispersive band

$$\epsilon_0(\vec{q}) = 2t, \tag{4.2}$$

and two dispersive bands

$$\epsilon_{\pm} = -t\left(1 \pm \sqrt{3 + 2\Lambda(\vec{q})}\right), \tag{4.3}$$

with

$$\Lambda(\vec{q}) = cos(\vec{q} \cdot \vec{a}_1) + cos(\vec{q} \cdot \vec{a}_2) + cos(\vec{q} \cdot \vec{a}_3). \tag{4.4}$$

The vectors $\vec{a}_{1,2,3}$ are the shortest lattice vectors for the kagome lattice and are indicated in figure **4.1 b**. Its values are

$$a_1 = \hat{x}, \quad a_2 = -\frac{1}{2}\hat{x} + \frac{\sqrt{3}}{2}\hat{y}, \quad a_3 = -\frac{1}{2}\hat{x} - \frac{\sqrt{3}}{2}\hat{y}. \tag{4.5}$$

Figure **4.1 d** shows the band dispersion when resolving the Hamiltonian of Eq. 4.1. The non-dispersive band, ϵ_0, is depicted in green. The two dispersive bands, $\epsilon_{\pm}$, cross in K, forming a Dirac point. These two bands touch the flat band at Γ (solid lines), although this touching point and the Dirac point gap when including the spin-orbit coupling (dotted lines) and the bands become topologically non-trivial [153, 158, 159].

Systems with flat bands produce unconventional phenomena, such as the presence of the fractional quantum Hall effect in the absence of a magnetic field [160–162], and can host electronic states including ferromagnetism [152], superconductivity [163] and Wigner crystallization [164]. Several materials with kagome lattices and different properties have been measured, like non-magnetic CoSn [165], the superconducting family AV_3Sb_5 [163] or the ferromagnetic and Weyl semimetal $Co_3Sn_2S_2$. This later material presents exceptional topological properties due to its Co kagome lattice interplay with nontrivial surface band and has been object of the research work presented in this chapter.

4.2 Phase diagram

$Co_3Sn_2S_2$ is a ferromagnet below a Curie temperature $T_C \approx 175$ K. The temperature dependence of the magnetization and the susceptibility are shown in figure **4.2 a** and **b**. Above T_C, $Co_3Sn_2S_2$ presents a Curie-Weiss behavior, following:

$$\chi = \frac{C}{T - \Theta_P}, \tag{4.6}$$

where C is the Curie constant and Θ_P is the Weiss temperature. An effective magnetic moment ~ $0.96\mu_B$ per Co has been found in Ref. [166]. Furthermore, we see that the magnetization is anisotropic (figure **4.2 a**). Ferromagnetic behavior is found when the field is applied along the c-axis.

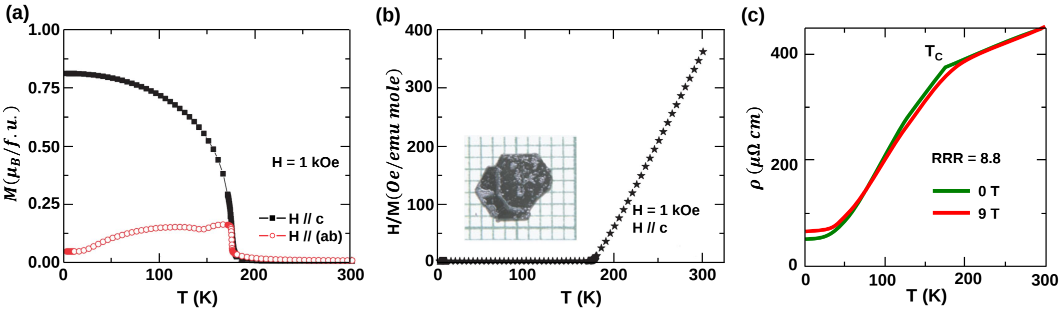

Fig. 4.2: Adapted from [166]. (a) Magnetization as a function of the temperature. (b) Inverse magnetic susceptibility as a function of the temperature. In the inset, a picture of a $Co_3Sn_2S_2$ single crystal on a millimeter grid is shown. (c) Adapted from [134]. Temperature dependence of the longitudinal electric resistivity ρ in zero-field and at 9 T.

This transition can also be seen in the resistivity (figure **4.2 c**), where a kink is visible at T_C when measured at 0 T.

4.3 Atomic and band structure

$Co_3Sn_2S_2$ has a layered crystal structure. It belongs to the space group $R\bar{3}m$ with lattice parameters a = b = 5.373 Å and c = 13.178 Å. Its structure consists of a Co_3Sn layer sandwiched between two S layers, as shown in figure **4.3**. These three layers are at the same time sandwiched between Sn layers. Cobalt atoms in the Co_3Sn layer form a kagome lattice with a Sn atom in the middle of the hexagons. The S and Sn atomic layers form a hexagonal lattice with the same lattice parameter (figure **4.3**). The solid black line in figure **4.3** indicates the unit cell. The dashed lines mark the different planes and their distance with the bottom of the unit cell is indicated. In this material, the magnetic properties arise from the cobalt planes, whose magnetic moments align ferromagnetically out of plain below T_C ~ 175 K, as indicated by the arrows in figure **4.3**.

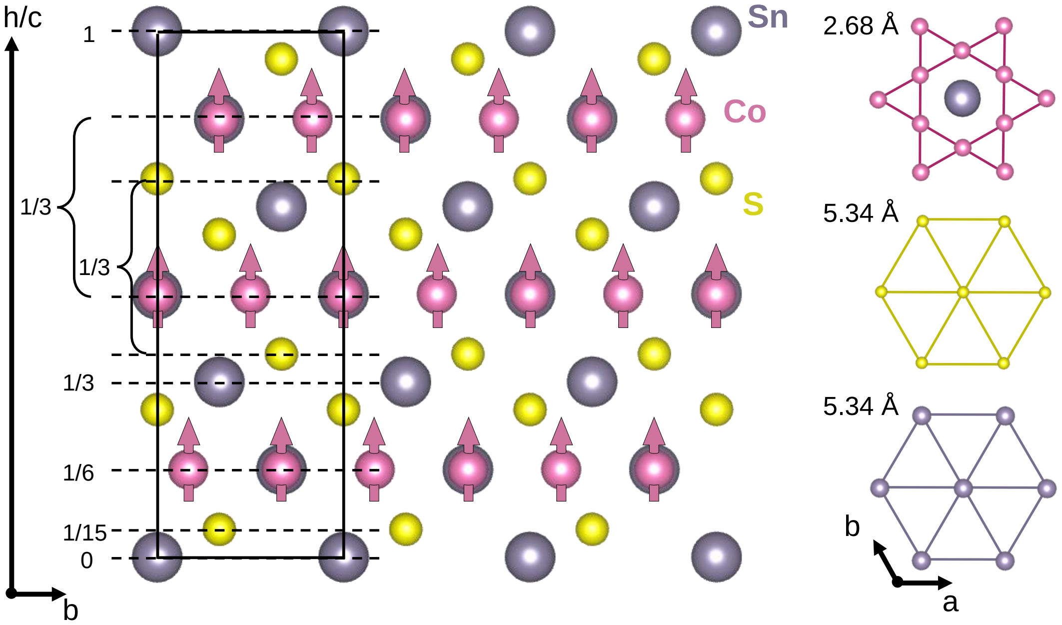

Fig. 4.3: Side view of $Co_3Sn_2S_2$ atomic structure. Solid black rectangle indicates the unit cell. Dashed lines show the different planes, where the distance from the bottom of the unit cell is indicated in units of c. The Co atoms form a kagome lattice with a Sn atom at the middle of the hexagon, forming a Co_3Sn layer. The S and Sn atom form hexagonal lattices with the same atomic distance.

Near the Fermi level, the main contribution to the bands is from the $3d$ Co orbitals. The calculated band structure provides spin polarized bands when the spin orbit coupling (SOC) is not included (figure **4.4 a**). In this case, all the bands crossing the Fermi level are polarized with spin up (in blue in figure **4.4 a**), while the bands polarized with spin down for a gap of ~ 0.4 V (in green) [134, 167]. Without SOC, there is band inversion at the L point between the valence and conduction bands (figure **4.4 a**). They form a nodal ring that is protected by the mirror symmetry in the (010) plane. The nodal line joins the crossing points along the $U-L$ and $L-\Gamma$ directions, marked with the red circles in figure **4.4 a**. When the SOC is included in the calculations, the nodal line opens in all the directions of the Brillouin zone except at the Weyl points [134, 167]. Three pairs of Weyl points are formed by the opening of the nodal lines [168] related by the C_3 rotation and inversion symmetry. The Weyl points are shown in purple and red in the Brillouin zone in figure **4.4 b**, where the color difference indicates opposite chirality. Note that the Weyl points do not appear in the high symmetry directions of the Brillouin zone. The Fermi surface at the (001) surface and the projection of the Weyl points is also shown, where two extra Weyl point outside from the first Brillouin zone are also depicted. Surface states connecting the Weyl points have been measured at this surface [44].

The surface band structure shows a nearly flat band (figure **4.4 c**) with an electron-like bottom close to the zone center. When the SOC is included, further hybridization between the two bands opens a small gap (figure **4.4 d**) [141]. Although the band structure in Ref. [141] has been calculated using first principles calculations, the flat band has also been obtained using a first neighbors tight-binding model (see section 4.1 and Ref. [141]). Under the influence of the magnetic field, this flat band has been shown to shift in an opposite direction as expected for the bulk bands [141].

In this thesis, we measured $Co_3Sn_2S_2$ single crystals grown by the group of Prof. Paul C. Canfield. They were grown from a ternary melt following the procedure in [166]. The samples were plate-like with the c-axis perpendicular to the largest crystal surface (see picture in figure **4.2**). The samples were cleaved in-situ in cryogenic conditions in the a-b plane. We performed scanning tunneling measurements at 4.2 K and magnetic fields up to 14 T using the experimental setup described in chapter 2.

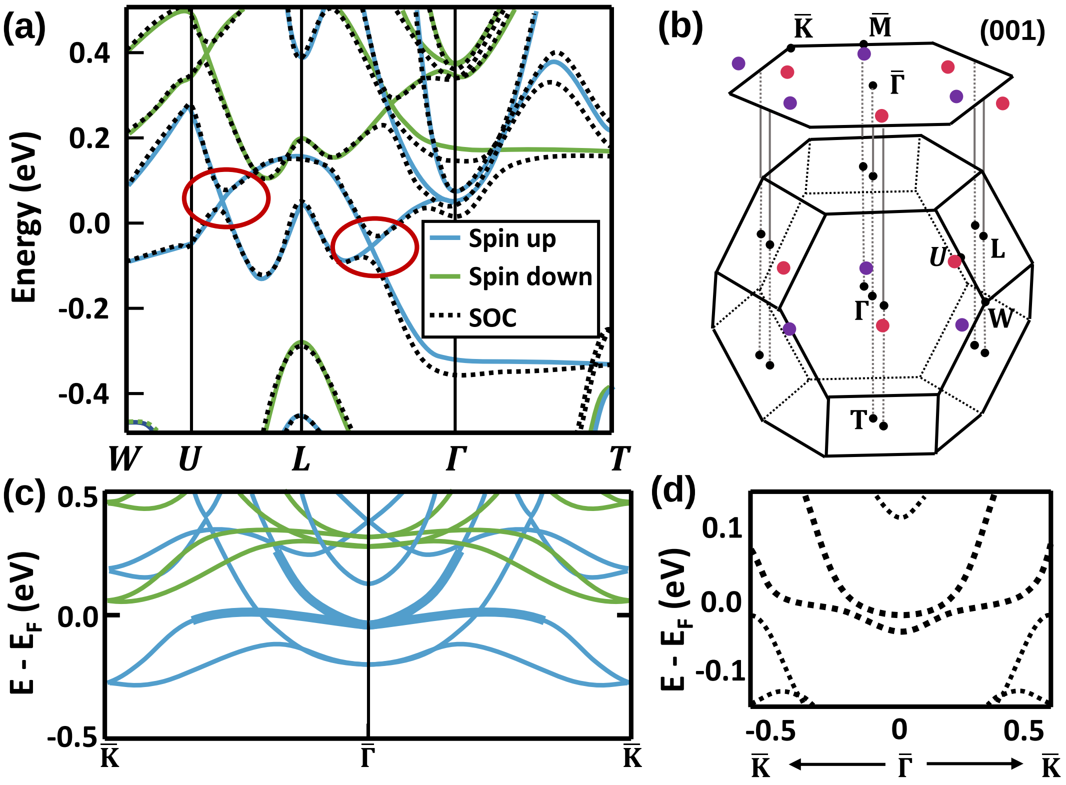

Fig. 4.4: (a) Adapted from [167]. First principles calculated band structure without the spin-orbit coupling and with SOC. Colors indicate the polarization of the bands. Red circles mark the crossing points of the nodal line. Dotted black line include the SOC. (b) Adapted from [44]. Brillouin zone and the projection on the (001) surface. The Weyl points are depicted in purple and red, indicating opposite chirality. (c) and (d) Adapted from [141]. First principles calculation surface band structure using in the $\Gamma - K$ direction without SOC (c) and with SOC (d).

4.4 Surface characterization

We present several fields of view found over the surface in figures **4.5**, **4.6**, **4.7** and **4.8**. Note first that the structure of $Co_3Sn_2S_2$ is relatively simple, there are always hexagons on the surface. There are three possible terminations, all providing a hexagonal surface. One of Sn, one of S and another one combined Co-Sn.

In figures **4.5** and **4.6** we find surfaces with very different tunneling conductance(figures **4.5 c** and **4.6 c**). The height histograms (insets of figures **4.5 a** and **4.6 a**) provide in both cases step sizes of 1/3 the c-axis unit cell. The lattice parameter is identical in both surfaces. These conditions are met by the three different possibilities mentioned before.

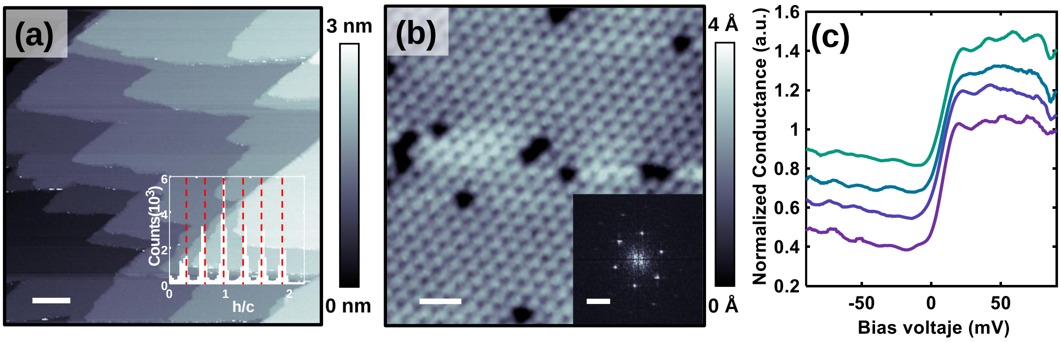

Fig. 4.5: (a) STM topographic image of Sn steps. Horizontal scale bar is 15 nm long. Inset shows the height histogram of the image, where we can see the steps are separated c/3. Red lines indicate the c/3 separation. (b) High resolution atomic topographic image at 100 mV and 1.2 nA in these steps. Horizontal scale bar is 1.5 nm. Inset on the right shows the FFT. Horizontal scale bar is 2 nm^{-1}. (c) Normalized conductance curves are taken at different steps and are shifted vertically for clarity.

Exposing the Co_3Sn surface requires breaking the Co-S bonds. This has been considered as highly unlikely [44, 141, 169], because of the large difference between the bond energy of Co-S and of S-Sn (the latter being much smaller). Thus, the observed surfaces are likely Sn or S surfaces.

Now let us consider the images shown in figures **4.7** and **4.8**. In figure **4.7** we see a large field of view, in which there is a clear gradient in the density of atoms that have been left on top of a full layer. In figure **4.8** we see that such atoms can form, with enough density, triangular structures and cover the whole surface. From the height histogram in the inset of figure **4.7 a** we obtain that the height difference obtained after covering the surface is of 1/15 the c-axis unit cell. The covered surface is equivalent to the surface shown in figure **4.6 b** and the atomic layer covering the said surface equivalent to figure **4.5 b**, from the tunneling conductance curves obtained at each place.

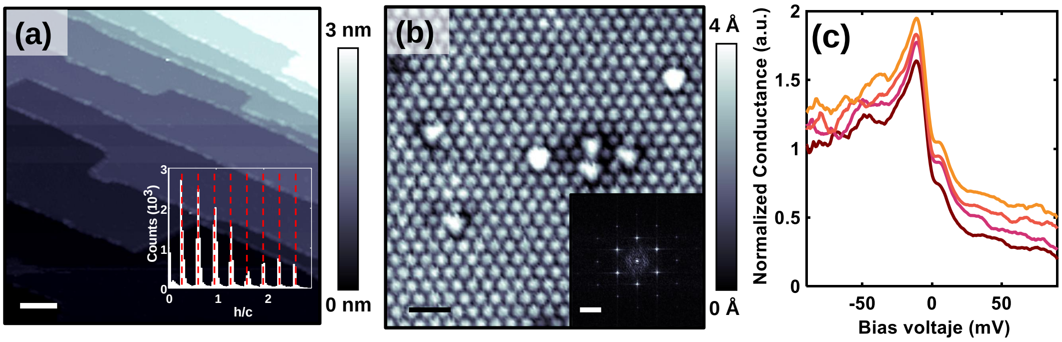

Fig. 4.6: (a) STM topographic image of S steps. Horizontal scale bar is 40 nm long. Inset shows the height histogram of the image, where we can see the steps are separated c/3. (b) High resolution atomic topographic image at 100 mV and 1.2 nA in these steps. Horizontal scale bar is 1.5 nm. Inset on the right shows the FFT. Horizontal scale bar is 2 nm^{-1}. (c) Normalized conductance curves are taken at different steps. Curves are shifted vertically for clarity.

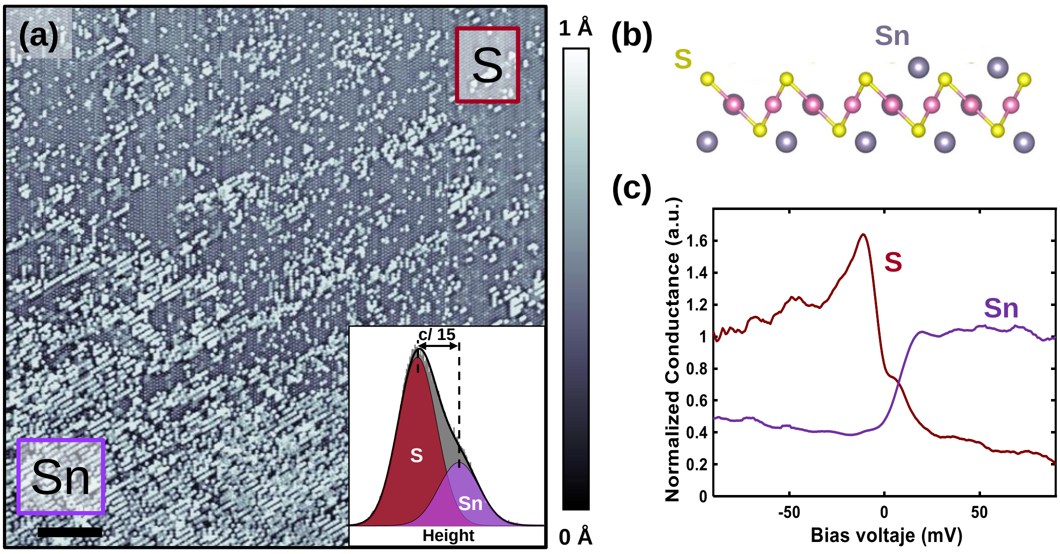

Fig. 4.7: (a) High resolution atomic topographic image, with 100 mV bias voltage and 3.2 nA set point. In this image, the transition between consecutive layers can be seen. Horizontal scale bar is 10 nm long. In the inset, height histogram of the image fitted with two Gaussian curves separated c/15. (b) Side view of the crystal structure when the sample is cleaved and the two possible surfaces are visible. (c) Normalized density of states of both surfaces.

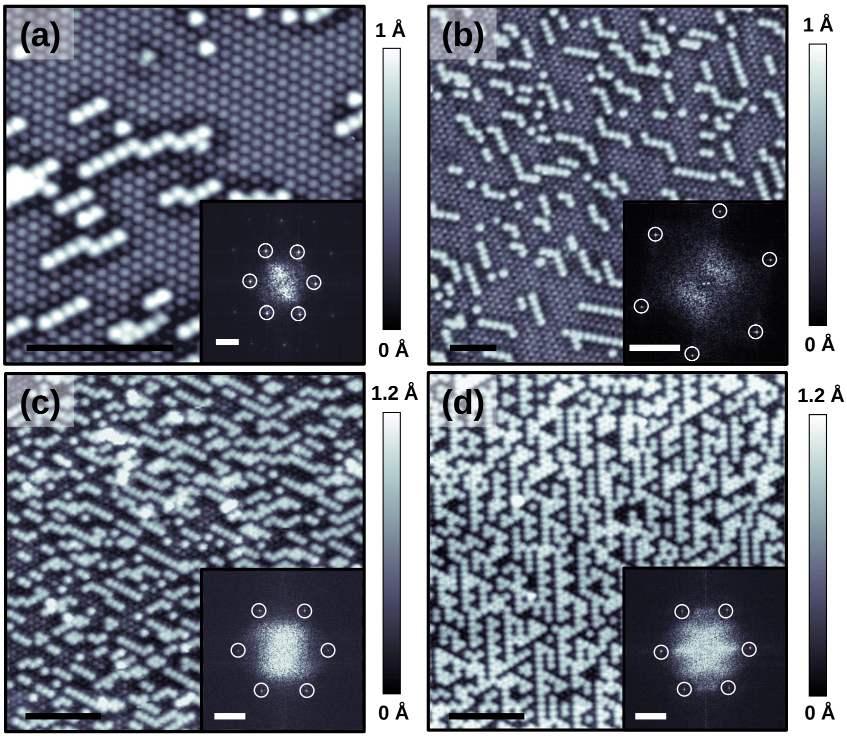

Fig. 4.8: Atomic resolution topographic images at taken using 100 mV bias voltage and 3.2 nA set point. Two different surfaces are visible with different coverage of the top layer. Horizontal scale bar in all the images is 6 nm. Both surfaces are hexagonal with the same lattice parameter, as we can see in the Fourier transform maps, where white circles indicate the Bragg peaks. Horizontal scale bar in all the FFT images is 1.5 nm^{-1}.

Thus, the two surfaces we observe can only be either S or Sn on the S-Sn atomic layers that separate Co_3Sn-S groups. This confirms the strong bond between Co_3Sn-S and shows that the light S-Sn bonds can be used to obtain surfaces covered arbitrarily just by searching for different fields of view on the sample. But how can we separate S from Sn?

To do so, we have to consider the possible situation of each layer. If we are looking on a S layer belonging to the Co_3Sn-S groups, we should likely observe features of the kagome flat band in the tunneling conductance. A Sn layer not belonging to the Co_3Sn layers is unlikely presenting such features, as it lies one atomic layer above the Co_3Sn-S groups. We see from figure **4.7 c** that the top partially filled atomic layer presents no flat band features, whereas the bottom layer presents a clear peak at the same energy at which the flat band is observed (~ -10 mV) (see figure **4.4 d**) [141]. Furthermore, the bottom layer provides a neat hexagonal shape, which is compatible with the atomic surrounding of S atoms belonging to the Co_3Sn-S groups.

Thus, in figure **4.5** we are observing a Sn layer and in figure **4.6** we observe a S layer of atoms belonging to the Co_3Sn-S groups. This assignment of surfaces is in agreement with ab initio calculations of the bonding strength and on the assignments made in Refs. [141, 170].

At the same time, we see that we can obtain images with very different Sn coverages. From isolated single atoms up to full layers, passing through situations in which we find Sn chains. Since the S and Sn layers have atomic distances that are very close, their bonding can compete with the in-plane Sn-Sn bonds [141].

We now turn our attention to the behavior around Sn atoms on top of the S surface belonging to the Co_3Sn-S groups.

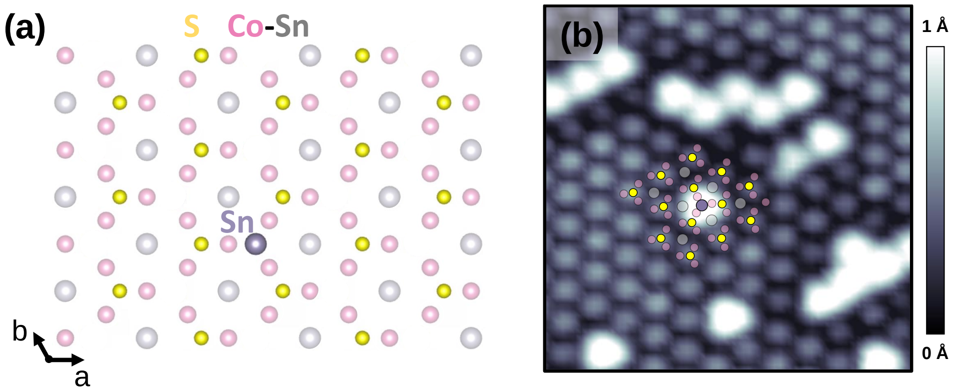

Fig. 4.9: (a) Top view of the atomic structure of the Co_3Sn (magenta and gray) and S (yellow) layers, with a Sn atom from the layer on top. (b) Very high atomic resolution image with the atomic lattice on top.

To this end, let us analyze the atomic position of isolated Sn atoms. In figure **4.9** we show a Sn atom and compare atomic positions (figure **4.9 a**) with the structure observed at the surface (figure **4.9 b**). Note that Sn atoms are located on top of the triangles of the Co kagome lattice, not at the hexagons. The Sn lying on the same layer as the Co is located within the hexagon. The Sn can be located on three possible triangles, as the other triangles are occupied by

S. This builds up the corresponding hexagonal Sn lattice, intertwined with a S lattice of the same lattice constant. A single atomic Sn on top of the S lattice thus has a characteristic triangular shape, indicative of the triangular atomic surroundings of Sn (figure **4.9 a**). As the Sn lattice has hexagonal symmetry, it is filled along lines with kinks of 60 degree each.

4.5 Sn on top of the S surface

4.5.1 Isolated Sn atoms

An impurity provides a different electron count than the atomic constituents of a solid. This leads to a positive or negative charge located at the impurity site and often to atomic size changes in the electronic density. Similar effects can happen on atoms located as an additional atom on top of a flat surface. The modified charge density is screened in metals by the conduction electrons, as discussed in chapter 1. Screening occurs in the bulk as well as at the surface. Generally, screening is much less efficient in semiconductors, and an impurity level might be found within the gap between valence and conduction bands. In a metal, screening is efficient both in the bulk and at the surface. At the surface, two-dimensional electronic states are built within the gaps of the bulk energy dispersion relation. Charge at the impurities can be efficiently screened by the two-dimensional surface electrons, as well as by bulk electrons. $Co_3Sn_2S_2$ presents several surface states within bulk band gaps [44]. The consequence of screening far from the impurity site, due to the nature of the Lindhard function, is the appearance of oscillations at a wavevector k_F of the surface states (chapter 2.4.1). These oscillations have been observed and studied in detail in Ref. [44] and are mostly due to defects within each of the possible atomic termination layers. Here however we focus on the Sn atoms located on top of the S surface. As we shall see below, the charge screening around these atoms is very interesting. It has been shown that screening considerably modifies the local band structure, for instance in presence of a flat band in graphene [171] or on impurities located on top of black phosphorus [172]. It is thus of interest to analyze in detail the shape of the charge distribution around Sn atoms on top of the S surfaces belonging to the Co_3Sn-S groups, in which Co forms a kagome lattice.

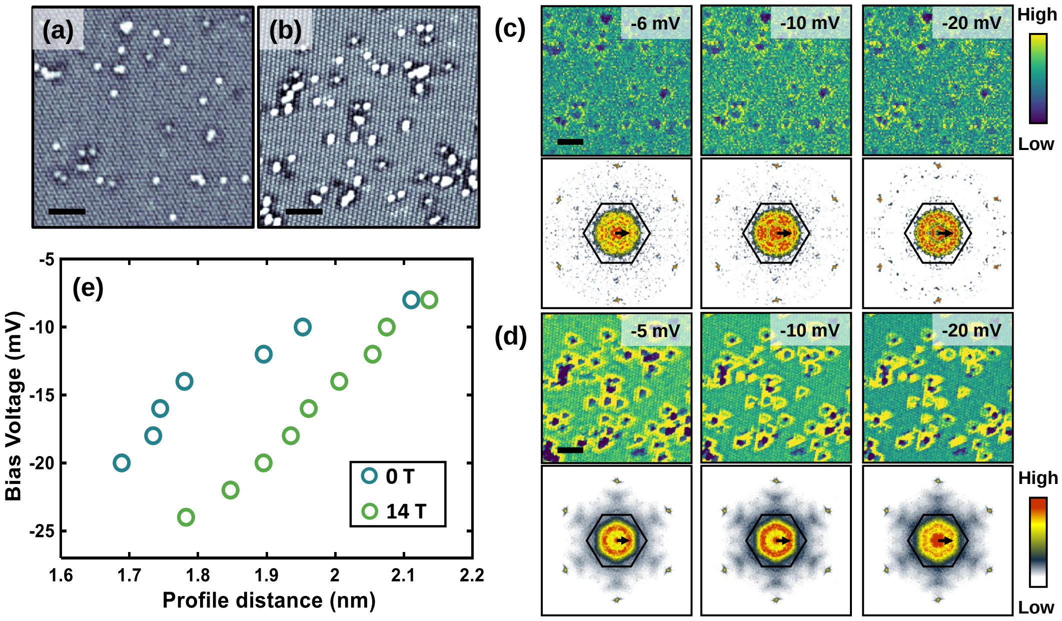

Fig. 4.10: Sn defects on the S layer. Topographic images of an area of 30 × 30 nm measured at 100 mV and 3.2 nA at (a) 0T and (b) 14 T. Conductance maps and their C3 symmetryzed Fourier Transform maps for different energies at 0T (c) and 14 T (d). All horizontal scale bars are 5 nm long. Black hexagon in the FFT maps indicates the Brillouin zone. (e) Bias voltage *vs* real space size of the hexagons indicated with the black arrow in the FFT maps.

We focus now on large surfaces full of isolated atoms on the surface at zero magnetic field (figure **4.10 a** and **c**) and at 14 T (figure **4.10 b** and **d**). We see in the topographies (figure **4.10 a** and **b**) that, in both cases, the atoms on the surface consist of a bright spot with a dark shadow around them. These are single atoms of Sn on top of the S surface. As schematically described in figure **4.9**, their location at the center of the triangles of the kagome lattice suggests that we can expect a strong interaction between the flat band and the Sn atoms.

Note that Sn atoms at the surface are different than the defects leading to quasiparticle interference scattering and discussed in Ref. [44]. The Sn atoms produce a much larger distortion of the local density of states and no visible oscillations, at least not when there are a large number of close lying Sn atoms.

Indeed, when taking full tunneling conductance maps (figure **4.10 c**) we observe a considerable energy dependence of the shape of the density of states around Sn atoms as a function of the bias voltages, with only a small amount of quasiparticle oscillations. For voltages above the flat band (~ -9.5 mV), Sn atoms provide a dip in the tunneling conductance which is localized around the atom site and essentially independent on the bias voltage. When approaching the flat band, Sn atoms start building up a corona of charge around them. The radius of this corona increases when decreasing the bias voltage in a narrow energy range below the flat band.

At 14 T (figure **4.10 e**) we observe qualitatively the same behavior, with coronas having more pronounced borders.

The coronas have a triangular shape and are oriented randomly along one of the six possible orientations of the structure shown in figure **4.9**. To account for the behavior on a large number of isolated atoms, we make a C3 symmetrized Fourier transform and study its evolution with energy. Due to the triangular coronas, we find a hexagonal structure located around $k = 0$ (see black hexagon in the FFT maps of figures **4.10 c** and **d**). The hexagon increases in size when reducing the bias voltage, both at zero field and at 14 T. The bias dependence of the size of the hexagon is marked with the black arrows in the FFT maps in figure **4.10 c** and **d** for 0 and 14 T, respectively. By inverting the wavevector, we can find the bias dependence of the average size of the triangles in real space (figure **4.10 e**). We see that the lateral size of the corona shape increases when increasing the bias voltage towards the position in energy of the flat band.

We can interpret the data considering the generic shape of the electronic density of states. Remember from the bulk band structure description above that there are only spin up bands crossing the Fermi surface in absence of SOC. We can hypothesize that the Sn produces a modification of magnetic order, in which case there are few states to screen the charge in a range of about 100 meV above the Fermi level. So that the charge on the Sn atoms on the surface remains essentially unscreened, with small dips in the tunneling conductance at the Sn sites (blue areas in figure **4.10 c** and **d**). The dips confirm that the Sn atom provides positive charges, or a reduction of the electron density. When reaching the flat band, screening builds up, with an enhanced charge density around the Sn atoms. This is at first sight puzzling, as the magnetic polarization of the bulk bands and the said absence of screening at higher energies points out an opposite magnetic polarization around Sn than for the bulk electrons at the Fermi level and the macroscopic magnetization. However, the flat band has an opposite spin polarization as the bulk [170], so that it should be oriented along a similar direction than the spins on Sn, for which the flat band can screen the charge of Sn.

The screening leads to a corona of charge around the Sn atoms. The size of the corona is of approximately five Sn interatomic distances or ten Co distances, suggesting partial screening due to the flat band. When decreasing the bias voltage away from the flat band, the coronas close leading to triangles with a large charge accumulation. The size of the triangles decreases down to about three S interatomic distances. This suggests that charge screening builds up around the Sn impurity. The magnetic field leads to a slightly steeper dependence of the size of the triangles, suggesting less efficient screening with the decrease of inverse polarization on the flat band with the applied magnetic field (see Ref. [141]).

4.5.2 Sn atomic chains

In the previous section we have studied isolated Sn atoms which lead to a triangular shape of the density of states around them. This leads to the corona described above. However, as we can see in figure **4.8**, we can also find fields of view in the sample where there is an accumulation of Sn atoms along chains. This changes the interaction from 0-D to 1-D. In presence of a flat band, the phenomenology is likely being different in a one-dimensional chain.

Figure **4.11 a** shows a topographic image at 0 T of an area with Sn atoms on top of the S surface. In order to see how the Sn adatoms change the density of states, we superimposed the largest values of the conductance measured at -90 mV on the topography (yellow color). It can be seen that these points concentrate in single atoms and chains containing only two atoms. This only occurs when the chains are not too close together. We can now discuss the full bias voltage dependence of the conductance (figure **4.11 b** and **c** right panels). We see that on a single Sn atom, the conductance at the flat band energy decreases and instead the conductance at negative bias strongly increases (figure **4.11 b** right panel). For two Sn atoms, we see large conductance values on both atoms (figure **4.11 c** right panel).

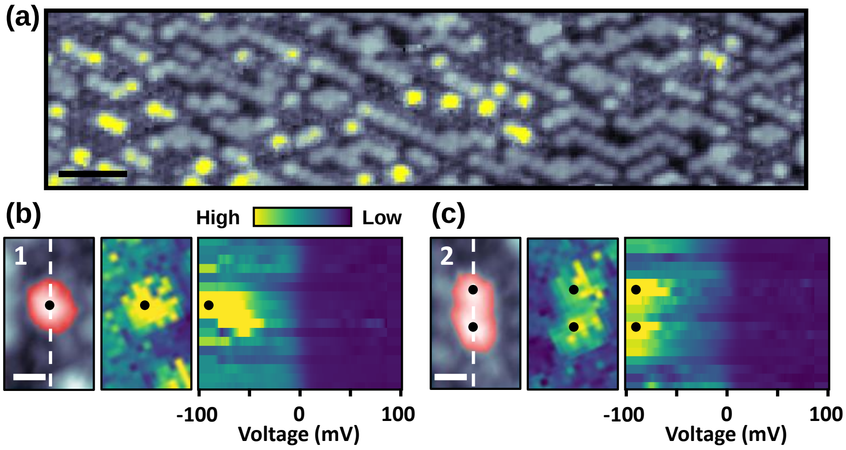

Fig. 4.11: (a) Topographic image with 100 mV bias voltage and 3.2 nA. Yellow signal superposed to the topographic image indicates the brightest points of the conductance maps at -90 mV. Horizontal scale bar is 2 nm. (b) and (c) show the changes in the conductance for one single atom and a chain formed by two atoms, respectively. The left panels show a zoom up of the topography shown in (a) with the Sn atoms highlighted in red. The middle panels show a conductance map at -90 mV and the right panel the conductance along the dashed white line as a function of the distance and bias voltage. Black points indicate the center of the atoms. Horizontal scale bar in the topographies is 5 Å.

It becomes more intriguing when we take a look on longer chains (figure **4.12 b**). For three Sn atoms, we observe just two peaks at the end atoms. For four Sn atoms, also only the two atoms at the ends of the chain have large conductance at negative bias. For up to six atoms, we observe the same effect: only the edge atoms have a large conductance at negative bias. In between, the tunneling conductance remains small. The conductance curves at the end of the chains are independent of their length, as can be seen in figure **4.12 c**.

This suggests that, similar to the case discussed before for isolated atoms, the spin state of the chain follows the spin of the kagome flat band. But it also shows that the atoms at the edges have a very peculiar position.

End states have been previously considered in chains of Au on top of Si(553) [173]. Such states are a consequence of the modified tight binding relation of an atomic chain when the binding energy of the Au end atoms is lower than

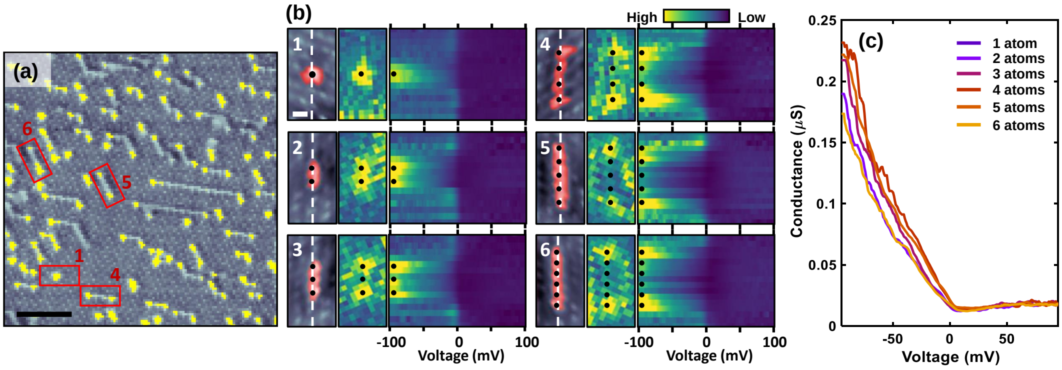

Fig. 4.12: (a) Topographic image with 100 mV and 3.2 nA. Yellow colored areas superposed to the topographic image indicated the the points with the largest conductance values at - 90 mV. Horizontal scale bar is 10 nm. (b) show the changes in the conductance for one single atom until chains formed by six atoms. The left panels show a zoom up of the topography shown in (a) with the Sn atoms highlighted in red. The middle panels show a conductance map at -90 mV and the right panel the conductance along the dashed white line as a function of the distance and bias voltage. Black points indicate the center of the atoms. Horizontal scale bar in the topographies is 5 Å. (c) Conductance curves taken at the edge of the atomic chains.

those Au atoms within the chain by an amount which is comparable to the gaps opened in the tight binding scheme used to describe the Au chains.

Here, however, we can consider another possibility, represented in figure **4.13**. There we plot the atomic Sn positions on a chain. We see that the atoms inside the chain all break the destructive interference phenomenon which occurs on the triangles of the kagome lattice. However, the atoms at the ends of the chain have a triangle where the localization condition is satisfied again. This can lead to a build up of charge at the ends of the chain.

We see that in our case, the chains, independent of their length (number of atoms), show all end states. The end states decay very rapidly towards the kagome lattice, but rather slowly towards the chain. The latter decay presents a certain dependence as a function of the chain length. To analyze this dependence, we have plotted the curves obtained on top of atomic sites, divided by r^{β} as a function of the bias voltage (figure **4.14 a-e**). We show in figure **4.14 f** and **g** the dependence of α and β on the chain length. We see

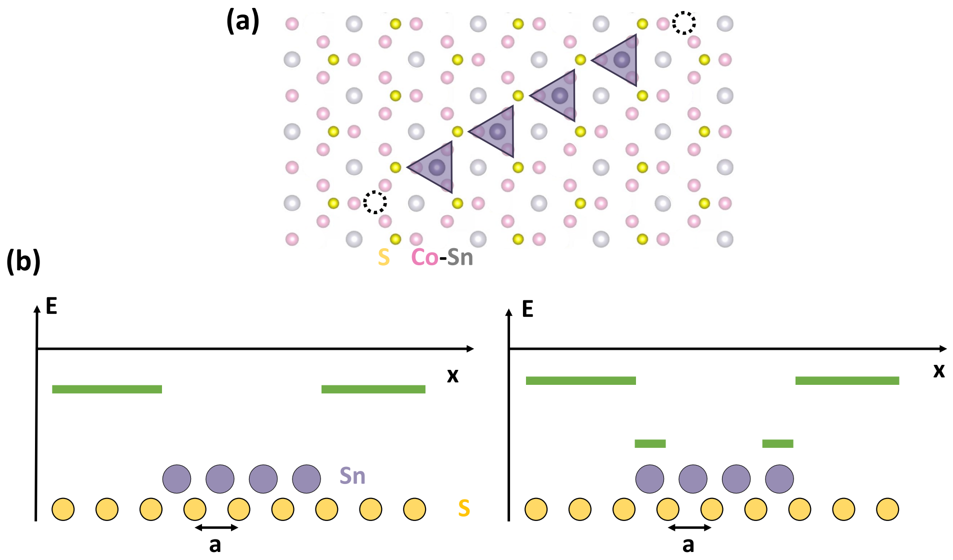

Fig. 4.13: (a) Schematic representation of the Co$_3$Sn atomic layer with the S layer on top. Above the S, a chain of Sn atoms occupies the positions in the triangles of the kagome lattice. Dark triangles indicate the shape of the Sn atoms in the topographies and the dashed circles, the position of the first missing Sn atoms. (b) Schematic representation of the flat band as a function of the position on the chain. The expected behavior is that the flat band (green line) disappears on the chain (left). However, we find two localized states at the edges of the chain, as indicated by the green lines at smaller energies (right).

that shorter chains of a couple of atoms have practically no spatial dependence and that the decay becomes close to r^{-1} for four atom long chains and then decreases again for longer chains. At the same time, α is reduced, giving less energy dependent features for large chain lengths.

For well separated end states, we can expect an exponential decrease. The observed power law behavior, which essentially flattens in energy and space for longer chains, suggests the presence of correlations between the end states.

Let us finally note that the end states appear in chains with a kink (figure **4.12 a**). This situation is schematically represented in figure **4.15 a**, where the Sn atoms are arranged in a chain with a kink. Thus, the charge is again located at the end of the chains (figure **4.15 b**).

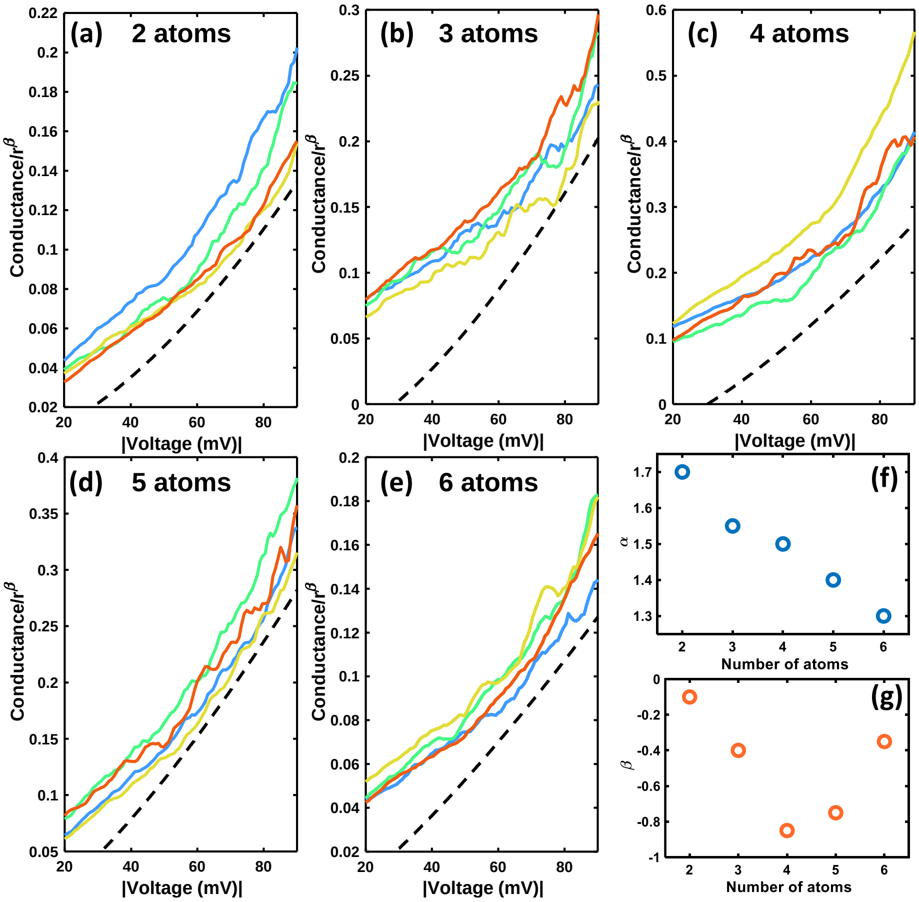

Fig. 4.14: (a-e) Representation of the conductance curves taken from the edge to the center of the chain for chains with different length. Curves are scaled to r^β, where r is the distance from the edge. Black line indicates the slope far from the Fermi level, which follows the dependence with V^α. α (f) and β (g) as a function of the chain length.

4.5.3 Edge state

We have also studied the presence of edge states in steps of the S surface. Figure **4.16 a** shows a topographic image of a 55 nm × 30 nm area with four steps where the S layer is exposed. As can be seen in this image, the step edge is not uniform. As explained before, in the cleaving process, the S layer is exposed by breaking the atomic bond between this atom and the Sn layer on top. This process can result in non-uniform step edges with different atomic terminations or reconstructions. As we see from the height profile in figure

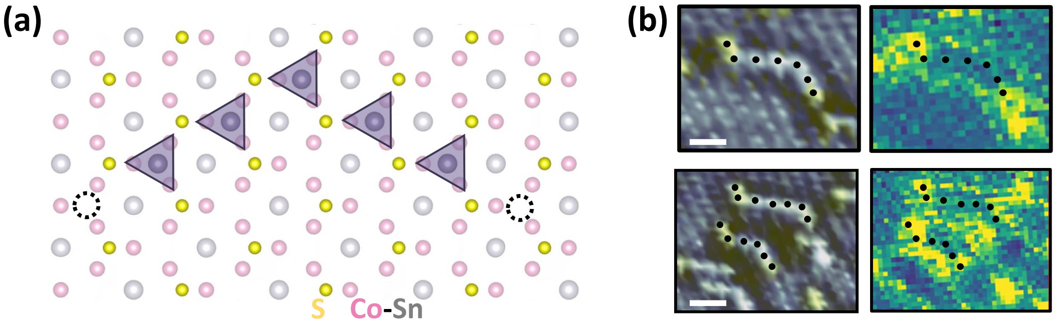

Fig. 4.15: (a) Schematic representation of the Co_3Sn atomic layer with the S layer on top. Above the S, a chain of Sn atoms occupies the positions in the triangles of the kagome lattice, forming a kink. Dashed circles indicate the position of the next missing Sn atoms. (b) Topographic images with 100 mV bias voltage and 3.2 nA set-point and conductance maps at -90 mV. Black dots mark the position of the atoms of the chain. Horizontal scale lines are 1 nm long.

4.16 c, the steps are not just heaviside functions. There is an increase just before the step. We attribute this increase to a small amount of Sn atoms lying on the S layer. We can then discuss the tunneling conductance curves at the positions indicated in **4.16 d** by the colored circles.

The conductance maps in figure **4.16 d-i** show a state localized along the edge of the steps with one-dimensional behavior at small bias voltage, analog to the states found at the chain ends. Figure **4.16 j** shows the conductance curves at different positions near the step edge. The conductance curve taken at the Sn edge (red dot in **4.16 d**) has the same shape and value than the curves at the edge of the chains from the cases discussed above. Thus, we clearly see that the build up of a large density of states at negative bias is related to the Sn position on top of the kagome lattice of the Co-S blocks. Schematic representation of the step edge is depicted in figure **4.16 k**.

4.6 Conclusions

In summary, we performed high resolution topography images and found two different possible surfaces. In this material, the three possible surface terminations (Co_3Sn, S and Sn) provide a hexagonal surface. The strong bond

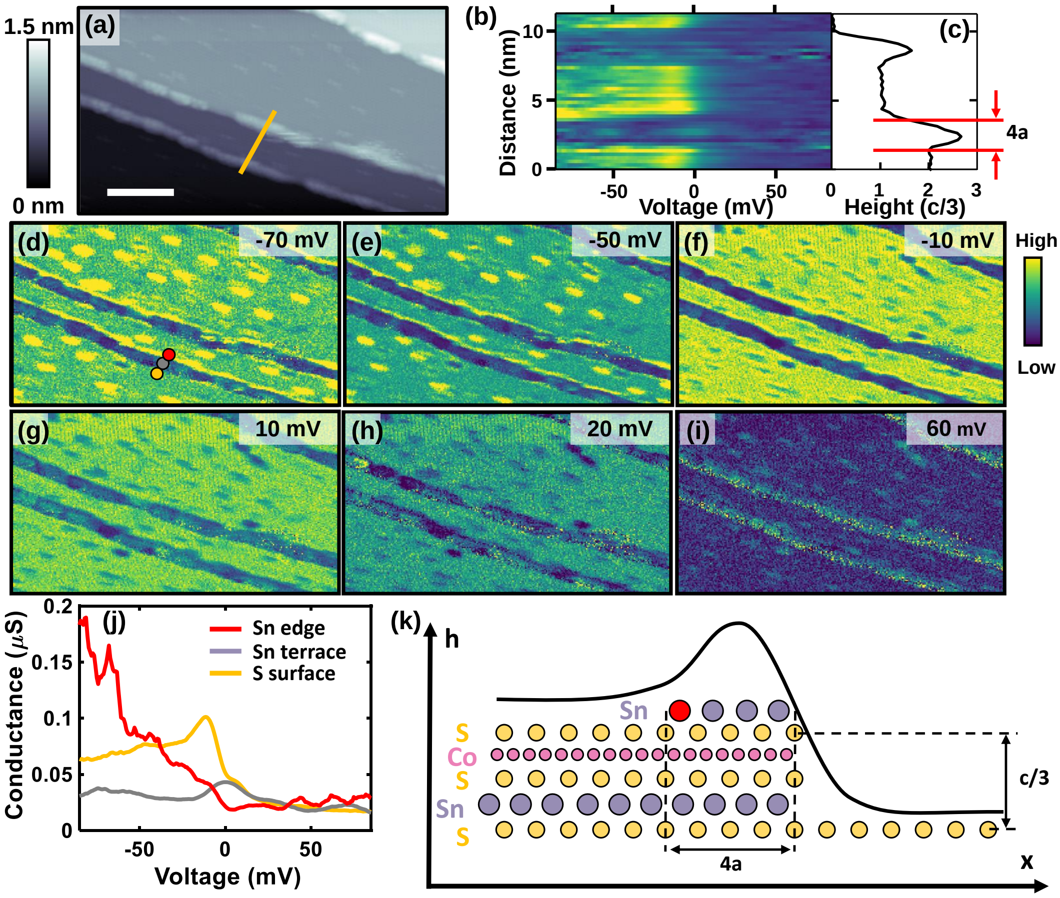

Fig. 4.16: (a) Topography in steps exposing the Sn layer, taken at 100 mV and 3.2 nA set point. Horizontal scale line is 10 nm long. The yellow line indicates where the conductance (b) and height (c) profiles are taken. (d-i) Conductance maps at different bias voltages. (j) Conductance curves in the positions indicated by the colored dots in (d). (k) Schematic representation of the step edge, where the red atom indicates the first Sn atom at the edge. The black line indicates the height profile at the step.

between the Co_3Sn and the S layers layer in comparison with the weaker S-Sn bond, makes most likely to find S and Sn surfaces in this material. We identified these two surfaces, both with the same lattice parameter. Conductance curves measured in both surfaces are very different. In particular, in the S layer we find a peak at the energy of the flat band due to the kagome lattice [141].

Sn atoms remain on top of the S surface, forming isolated atoms or atomic chains. A careful characterization of the isolated Sn atoms on top of the S surface shows that they are located at the center of the Co kagome triangles, while the Sn atoms in the Co_3Sn layer are located at the center of the hexagons of the kagome lattice. Thus, the location of the Sn atoms can have a strong influence in the kagome flat band.

To study this effect, we performed high resolution spectroscopy maps at large S surfaces full of isolated Sn atoms on top, at 0 T and 14 T. We hypothesize that the Sn atoms produced a modification of the magnetic order. As all the bands crossing the Fermi level are polarized with spin up, for energies above the flat band the Sn atoms remains unscreened. The flat band however, has a negative magnetization [141]. Then, when the energies are below the energy of the flat band, the screening around the Sn atoms is possible, and a corona shape appears surrounding the Sn atoms in the conductance maps.

There are areas on the S surface where the Sn atoms form atomic chains, changing the iteration from 0-D to 1-D. We performed spectroscopy maps in these surfaces, finding a large conductance at negative bias voltages for single atoms and the end atoms of the chains. In the atoms at the middle of the chain the conductance is small, and no signature of the flat band is observed. End states have been considered in other materials [173] as a consequence of the different binding properties at chain ends. In this material, however, the location of the Sn atoms breaks the flat band formation condition, that is satisfied again at the edge of the chains. This can explain the increasing conductance at the edges.

Finally, we performed spectroscopy measurements on steps of the S surface, finding a similar phenomenon. At the edge of the steps, several Sn atoms remain. The same increase of the conductance than in the chain edges can be measured at the first Sn atom (the one closer to the S surface, where the flat band appears), while a decrease of the conductance is measured in the rest of the Sn terrace. This result further evidences that the conductance enhancement is related to the position of the Sn atoms on top of the kagome lattice.

Chapter 5

Quantum confinement and Landau levels of localized states in the magnetic Weyl semimetal $EuCd_2As_2$

THE semimetal $EuCd_2As_2$ shares the chemical formula with iron based superconductors. It presents magnetism which is highly dependent on the arrangement of bands close to the Fermi surface. The predicted band crossings [174, 175] provide an interesting system where Weyl points can appear as a consequence of magnetism (and not of absence of inversion symmetry as in WTe_2).

Here, I present STM measurements at the surface of $EuCd_2As_2$. We found a shift of the valence bands that produce a gap. Localized electrons confined at the defects appear within the gap, giving a set of states due to lateral quantization. With the magnetic field, the states further quantize in Landau levels.

5.1 Atomic structure and magnetic configuration

$EuCd_2As_2$ is a layered material that belongs to the centrosymmetric space group $P\bar{3}m1$ and has lattice parameters $a = b = 4.45$ Å and $c = 7.38$ Å. The material orders in the *c* axis with two layer of Eu enclosing As-Cd-Cd-As layers, as shown in the lateral view of figure **5.1 a**. The magnetism lies in the Eu layers. When looking at the *ab* plane, all the layers have a hexagonal atomic arrangement with the same lattice parameter (see figure **5.1 b**).

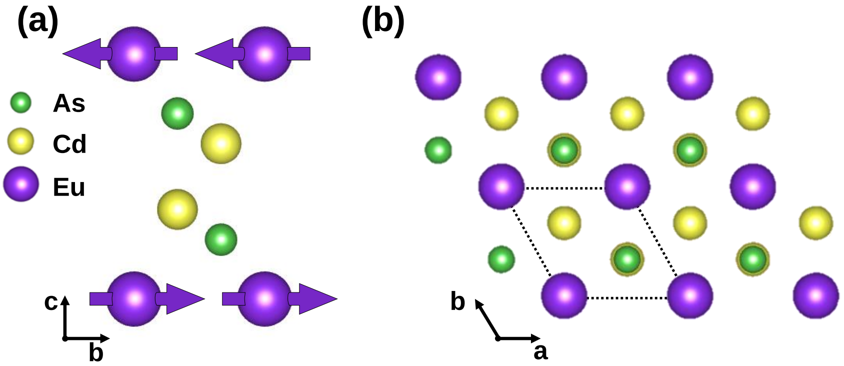

Fig. 5.1: (a) Lateral and top (b) view of the $EuCd_2As_2$ atomic structure. Dotted line in (b) marks the unit cell. The magnetic moment of the Eu atoms is indicated with the arrows in (a).

One of the most remarkable aspects of $EuCd_2As_2$ is that the magnetic properties are strongly interlinked with the electronic band structure [176, 177]. As it is a semimetal, small changes in the band structure lead to considerable modifications of the magnetic properties. It has been shown [178] that magnetism can be manipulated using different single crystal growth methods, going from an antiferromagnet with $T_N \approx 9$ K to a ferromagnet with $T_C \approx 26$ K. The modifications have been associated to changes in the electronic structure and the Eu^{2+} content.

Band structure calculations are shown in figure **5.2** [174]. We see (figure **5.2 a**) that there is a large gap nearly everywhere on the Brillouin zone. Valence and conduction bands only approach near Γ. Valence bands have a As-p character and conduction bands Cd-s character. The overlap between bands occurs just in a few meV around the Fermi level, which explains the sensitivity of the physical properties of this system to small distortions.

Three magnetic phases are considered. First an AFM phase with moments along c-axis. Within this symmetry (three-fold rotational symmetry [174]), the bands cross and there is band inversion, but as the bands are protected

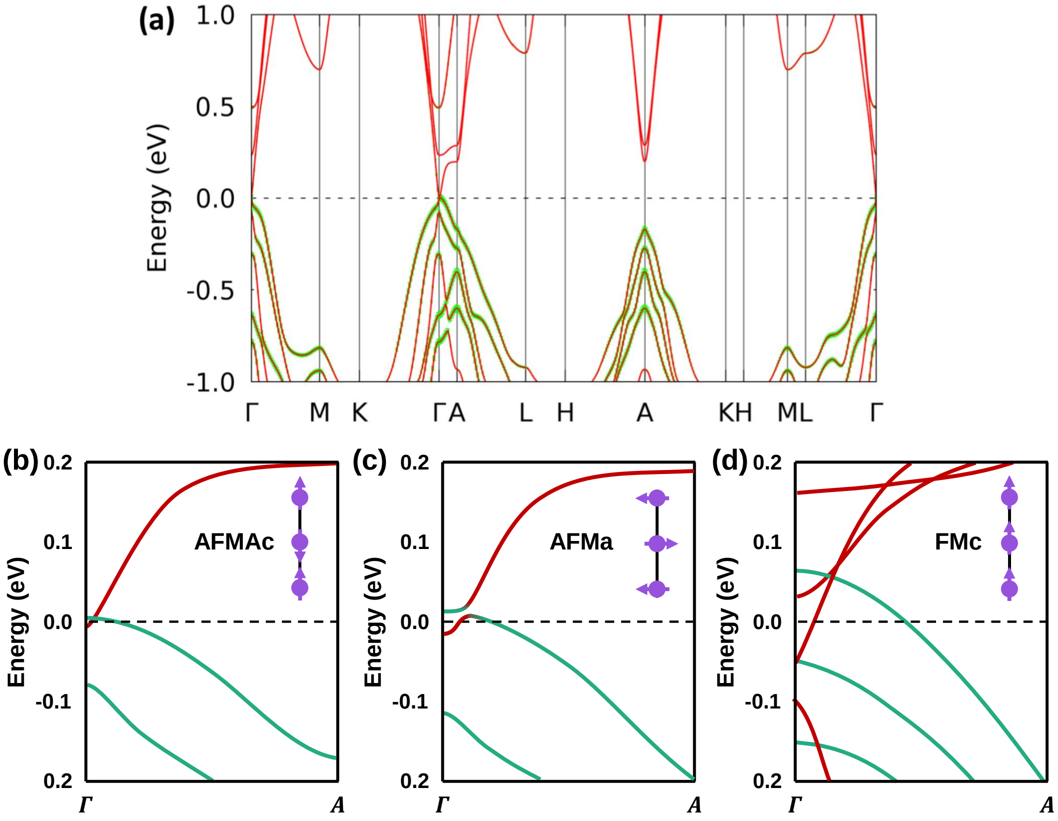

Fig. 5.2: Adapted from [174]. EuCd$_2$As$_2$ band structure calculations, depending on the magnetic configuration. (a) Band structure for A-type AFM with the spins along the c-axis. Band structure along the $\Gamma - A$ direction for (b) AFMc (c) AFMa and (d) FM configuration. The band with Cd s character are depicted in red, and the ones with As p character, in green.

by symmetry, there is no gap opening [174] (figure **5.2 b**). In another magnetic phase, AFMa, the spins are in-plane forming ferromagnetic layers, but change sign on each layer. Here, the crossing point is not protected and a gap opens (figure **5.2 c**). There is a surface state which has been predicted to hold interesting topological properties [174]. The gap opening is expected to be very small, of about 10 meV. Under magnetic fields, the system becomes ferromagnetic and presents the possibly unique property [174, 175] of having a single pair of Weyl nodes (figure **5.2 d**).

Furthermore, it was recently shown that small differences in the sample growth can result in either the AFM or FM configurations, depending on the initial compositions [178]. The difference between these samples is the band filling, that can be associated with the Eu-site occupancy.

In this thesis we measured $EuCd_2As_2$ single crystals provided by the group of Prof. Paul C. Canfield, grown by excess of Sn flux following the procedure in [179]. These samples shows an A-type AFM order below $T_N = 9.5$ K, whose transition can be seen in the magnetization data [178] (figure **5.3 a**). At 2K, the sample become saturated below 10 kOe when the magnetic field is applied parallel to the c-axis (figure **5.3 b**).

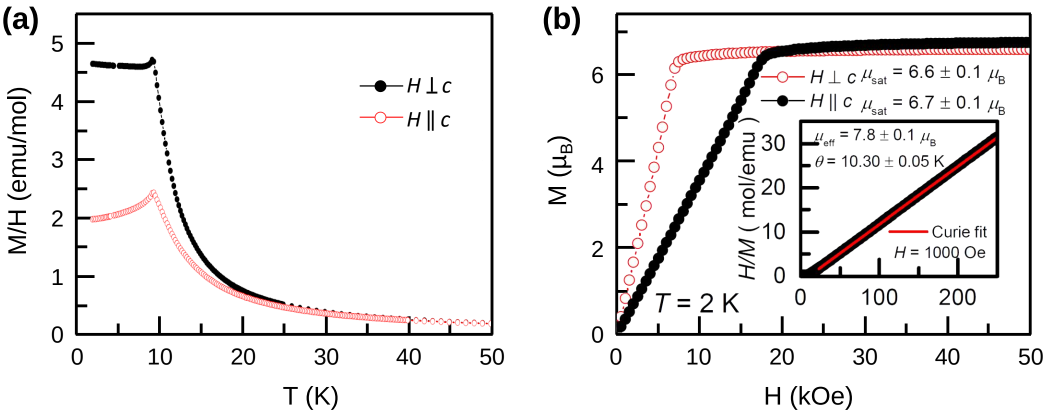

Fig. 5.3: Adapted from [178]. (a) Anisotropic magnetization at 1000 Oe with the field ∥ c and ⊥ c. (b) Magnetic field dependence magnetization at 2 K with the field ∥ c and ⊥ c. In the inset, inverse susceptibility with a Curie-Weiss fitting.

5.2 STM characterization

The samples were cleaved in the (001) plane in cryogenic conditions, as described in previous chapters, which allows to have clean and flat surfaces. We find atomic resolution presenting two well differentiated atomic arrangements.

In figure **5.4 a** we show a hexagonal lattice. The distance between Bragg peaks is of 4.5 Å, which coincides with the interatomic distances of any of the three hexagonal layers present in the crystal structure of $EuCd_2As_2$ (figure **5.1**).

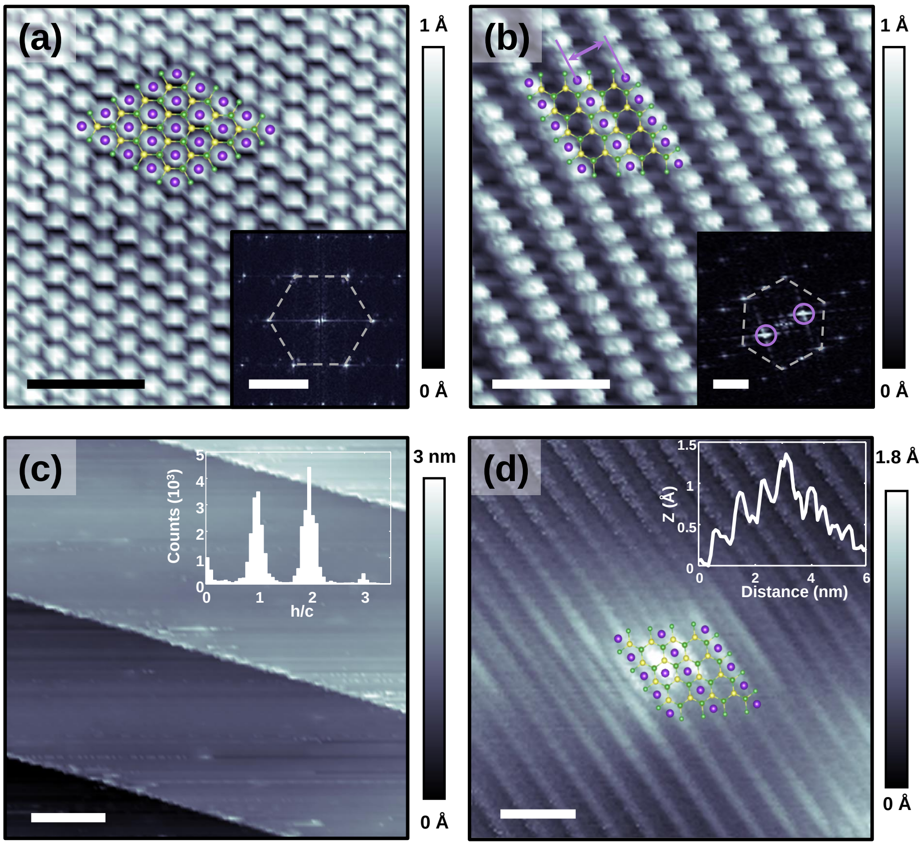

Fig. 5.4: STM topographic images measured at 100 mV and 0.4 nA current setpoint of the atomic lattice in (a) the hexagonal lattice and (b) the linear arrangement. The horizontal scale line in both images is 1 nm long. In the inset, FFT maps for both images, where the horizontal scale line is 3 nm^{-1}. The arrow represents the distance between rows and is of 7.8 Å. The circles in the inset provide the Bragg peaks due to the 2×1 surface reconstruction. (c) Topographic image of atomically flat steps measured at -100 mV voltage and 0.2 nA current setpoint. The horizontal scale line is 40 nm long. In the inset, height histogram showing that every step is separated a distance c from the next one. (d) Topographic image showing a defect in an image measured at 100 mV and 0.4 nA current setpoint. The horizontal scale bar is 3 nm long. We also provide the atomic structure superimposed to the image. In the inset, height profile on top of the defect. In (b,c), the color scale of the spheres representing atoms is the same as in figure **5.1**.

In figure **5.4 b** we show the surface on which we have focused our work. We see that there is no hexagonal arrangement. Instead, we find a linear atomic arrangement. From the Fourier transform we obtain that the distance between atoms in the same row is of 4.5 Å and that the distance between rows is of 7.8 Å ($= 2a\ cos(30)$ where $a = 4.5$ Å). This reminds one of the usual surface reconstructions found in the iron pnictides, the 2×1 reconstruction [180].

Height histograms between atomically flat surfaces show that the step size is always of c (figure **5.4 c**). Thus, the surface could be any of the three possible atomic layers: Eu, Cd or As.

Previous work on $CaFe_2As_2$ showed that the 2×1 reconstruction is formed when cleaving at low temperatures [181–183]. $CaFe_2As_2$ and similar pnictide materials crystallizes in the tetragonal structure and has strongly bonded Fe-As layers. The Ca plane is the cleaving plane in that case. The cleaving leaves approximately half of the Ca layer on each cleaved surface, forming Ca rows on the surface that arrange at 45 degrees to the underlying square As lattice. The structure of $EuCd_2As_2$ is clearly different, with hexagonal layers instead of square layers. The c-axis stacking is similar in $CaFe_2As_2$ than in $EuCd_2As_2$ in that there are Fe_2As_2 and Cd_2As_2 groups which build strong bonds (although the atomic arrangement in each group is very different [181, 182]). Thus, we can assume that the cleaved layer is the Eu layer and that the 2×1 reconstruction is due to Eu rows. Indeed, when placing atomic positions on top of our images (figure **5.4 b** and **d**) we can reproduce the images by assuming that the top layer is made of rows of Eu atoms.

In figure **5.4 d** we represent the defects that we discuss in the following. We show that the observed STM image is compatible with having a single interstitial Eu atom on the impurity site. The influence of this interstitial atom extends over large distances. For example in the defect shown in figure **5.4 d**, the topography image presents a corrugation of over 1 Å on a distance which extends above 5 nm, i.e. about 10 in-plane unit cells.

As we show below, a small amount of defects produces considerable modifications of the tunneling conductance over nearly the whole surface. Nevertheless, we always observe similar features on the tunneling conductance and of its magnetic field dependence, particularly when we are far from defects. These features are described in figure **5.5**.

We observe at zero magnetic field a small conductance for bias voltages above the Fermi level (figure **5.5**, in purple). There are a set of peaks and a gap like structure close to the Fermi level which we discuss in more detail below. For voltages below the Fermi level, we observe a large increase in the tunneling conductance. This suggests that there are few or no states above the Fermi level.

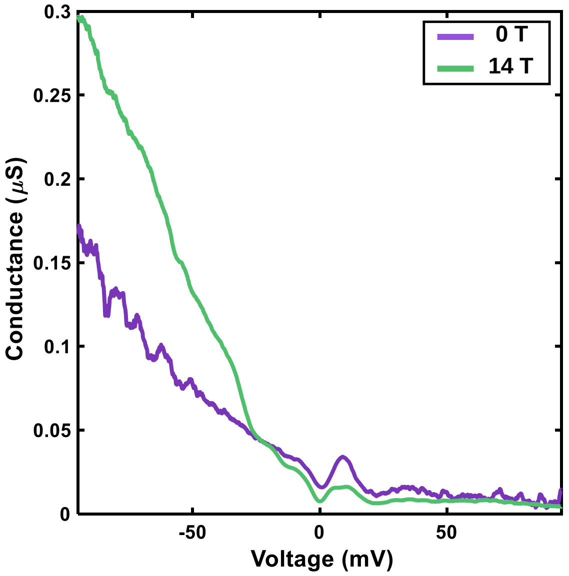

Fig. 5.5: Conductance curves at 0 T and 14 T.

When applying a magnetic field, we observe a considerable increase of the tunneling conductance below the Fermi level (figure **5.5**, green curve). This suggests considerable changes in the band structure below the Fermi level.

We can compare these results with the predicted band structure shown in figure **5.2**. Clearly, our results are incompatible with the presence of bands above the Fermi level, as indicated in the bulk calculations. This suggests that the band structure at the surface is different. Indeed, band structure calculations [184] show that a gap of several 100 meV opens up at the surface. The gap is just for states above the Fermi level. Essentially, the valence Cd-s bands are pushed upwards close to the surface. Below the Fermi level, the band structure is similar, dominated by degenerate As-p character bands.

The observed increase of the tunneling conductance when applying a magnetic field can be related to the lifted degeneracy of As-p valence and the entry of new bands into the bias voltage range analyzed in our experiment. Furthermore, we observe no changes above the Fermi level, so that the magnetic field might not be enough to shift the Cd-s conduction bands to enter the gap.

In general, we observe a decrease of the density of states for negative bias voltages when measuring on top of defects. This suggests that the bands below the Fermi level are bent close to defects, increasing the gap at the surface.

5.3 Quantum confinement

5.3.1 Spectroscopy without magnetic field

To understand the behavior on the defects, we performed spectroscopy measurements in an area with defects. In figure **5.6 a** we can see an 44 × 88 nm topographic image with several defects similar to the one described in figure **5.4 d**.

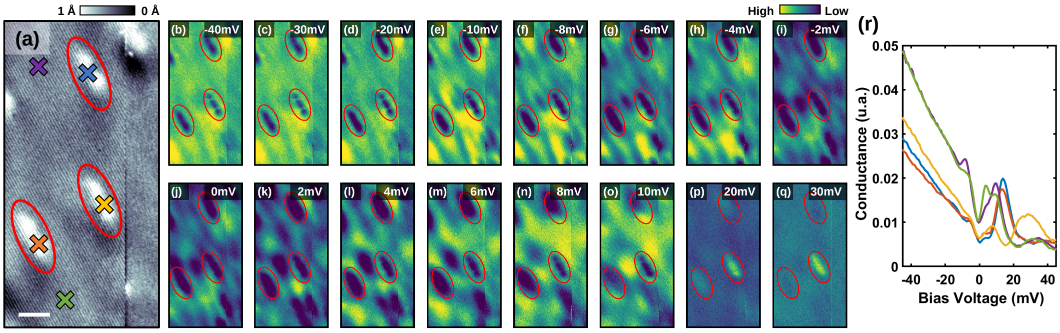

Fig. 5.6: Spectroscopy maps at 4.2 K and 0 T on $EuCd_2As_2$. (a) Topography image measured at 100 mV and 0.2 nA current setpoint. Horizontal scale line is 10 nm long. We highlight the three defects that we discussed later. (b-q) Conductance maps at different bias voltages. The three defects (r) Conductance curves on top of the colored crosses in (a). Colors of curves and crosses coincide.

From the curves shown in figure **5.6 r** we see that curves made on the center of the defects have a lower conductance for negative bias than those made far from defects. Furthermore, there are a set of peaks between about -20 mV and 40 mV which change their energy position and shape on top of defects.

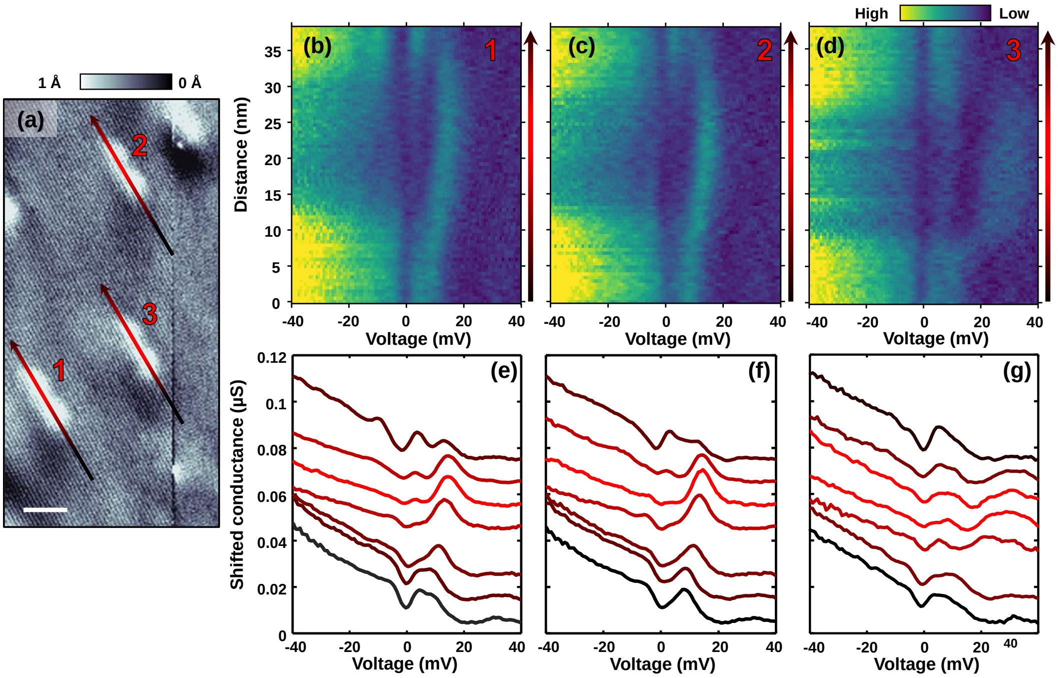

Fig. 5.7: In (a) we show the topography in the same field of view as in the previous figure. We highlight three defects. Color lines and numbers show the position where we took the profiles in (b-d and e-g). In (b-d) we show the tunneling conductance in a color scale (provided on the top of (d)). In (e-g) we show the tunneling conductance vs bias voltages on different positions. We use a color code that goes from black to red, following the color of the lines shown in (a) and in (b-d). Curves are vertically shifted for clarity. Note that the curves inside the defect are nearly flat, suggesting a strong drop of the density of states at the defects.

We can discuss the variation of these peaks *vs* distance more in detail with the data shown in figure **5.7**. As we see in the top panels (marked 1-3) of figure **5.7**, there is a clear decrease of the tunneling conductance at negative bias voltages along the position of the defects. In addition, there is a peak very close to the Fermi level which loses intensity on the defect. There is a second peak for positive bias voltages which only occurs inside the defect.

The observation of an increased gap at the defect site suggests at the same time that localized electronic states can occur at the defect sites. These states mostly occur above the Fermi level. The charging phenomena discussed in the following chapter in FeSe do not occur here, probably due to smaller screening by the tip.

On the other hand, the localized states extend over a spatial range which is several nm large, far above the atomic scale discussed in the defects of WTe_2 (chapter 3.1.2). Therefore, the screening effects are not so apparent. Instead, we can consider here lateral quantization of a discrete electronic state.

To dwell on this, let us write the quantization condition for a confined state in a one-dimensional quantum well:

$$\Delta E = \frac{\hbar^2 \pi^2}{2m^* L^2}, \tag{5.1}$$

where ΔE is the distance in energy between the states, L is the size of the quantum well and m^* is the effective mass. We can take for ΔE the difference between the states observed at positive bias voltage. We find 9.5 meV for the states in defects 1 and 2, and 20.5 mV for the state in defect 3. The extension of the defect 3, as observed in the topography STM image, is smaller than the other two defects. Taking 17 nm for 1, 2 and 11.5 nm for 3, we obtain an effective mass of 0.14 m_e in both cases.

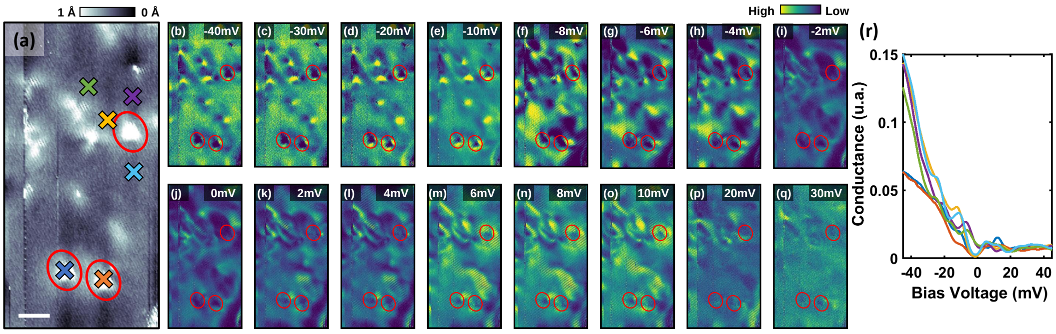

Fig. 5.8: Spectroscopy maps at 4.2 K and 14 T on $EuCd_2As_2$. (a) Topography image measured at 100 mV and 0.2 nA current setpoint. (b-q) Conductance maps at different bias voltages. Horizontal scale bar is 10 nm long. We highlight three defects we discuss later. (r) Conductance curves on top of the colored crosses in (a). Colors of curves and crosses coincide. We mark with a red circle three defects which we analyze in more detail in figure **5.9**.

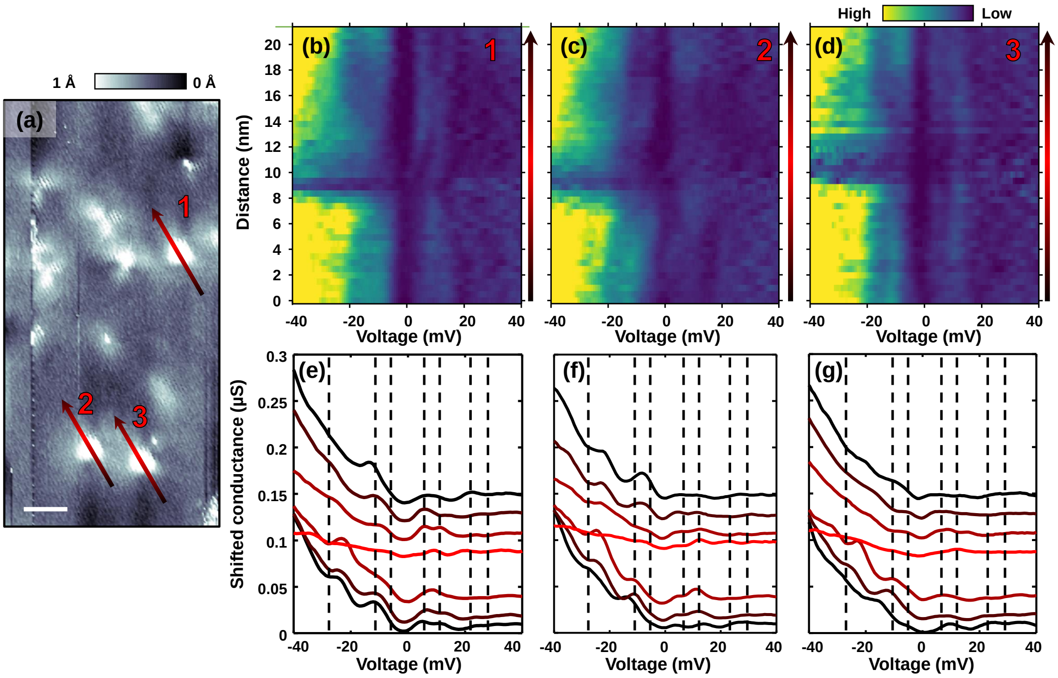

Fig. 5.9: In (a) we show the topography in the same field of view as in the previous figure. We highlight three defects. Color lines and numbers show the position where we took the profiles in (b-d and e-g). In (b-d) we show the tunneling conductance in a color scale (provided on the top of (d)). In (e-g) we show the tunneling conductance vs bias voltages on different positions. We use a color code that goes from black to red, following the color of the lines shown in (a) and in (b-d). Curves are vertically shifted for clarity. Vertical dashed lines mark the energies in table **5.1**.

This value of the effective mass is compatible with the values found previously [175]. In particular, the magnetoresistance presents oscillations under magnetic fields [175]. From these oscillations, the effective mass was estimated to be of order of 0.08 m_e, with however a large error due to the small amount of observed oscillations [175]. In the same work, ARPES measurements show the band structure below the Fermi level. From our data, we expect that the obtained effective mass value refers to bands above the Fermi level, which are pushed away at the surface but are again found on a defect.

5.3.2 Spectroscopy at high magnetic field

The observation of Landau oscillations in transport [175] suggests that the magnetic field can considerably modify the quantization pattern. Indeed, when applying a large magnetic field we observe very intricate topographic images, with tunneling conductance maps which also have a much larger variation than at zero field. We show the result in figures **5.8** and **5.9**.

We first remember that there is a generic increase of the density of states for negative bias voltages, due to the appearance of new bands in the bias voltage range studied. Also, that the density of states for positive bias voltages does not change much with the magnetic field. Furthermore, at the defects, there is an additional decrease of the density of states for negative bias voltages. Thus, we have the same overall picture as in zero magnetic field. There is a gap opened at the surface for energies above the Fermi level and defects produce an additional decrease of states available below the Fermi level.

But the quantization is much more complex under magnetic fields, as we see in figure **5.9**. The spatial range with a gap for negative bias is smaller and there are a number of states at negative bias close to the defects. At positive bias, there are generally more states too.

To analyze this, let us remind that lateral quantization under magnetic fields suffers an additional quantization due to Landau levels. For a harmonic oscillator, the level sequence is modified in a magnetic field as [185, 186]:

$$E_{l,n} = \hbar\omega_l(2l + n + 1) + \frac{\hbar\omega_c}{2}n + E_0, \tag{5.2}$$

with

$$\omega_l = \sqrt{\omega_0^2 + \frac{\omega_c^2}{4}}, \tag{5.3}$$

where E_0 is the top or bottom of the band, $\omega_c = eB/m^*$ is the cyclotron frequency, $\omega_0 = \Delta E/\hbar$ is the frequency associated with the energy of the quantum well and l and n are integers. Using the parameters obtained from the defects at 0 T we can obtain a series of levels that order in energy as shown in table **5.1**. These energies are marked as vertical dashed lines in figure **5.9 e-f**. Note that small changes in the defect size produce a significant change in the levels values.

l	n	Energy (mV)
0	0	-28
0	1	-11.1
1	0	-5.7
0	2	-6
1	1	11.2
0	3	22.7
1	2	28.1

Table **5.1**: Energies obtained using Eq. 5.2.

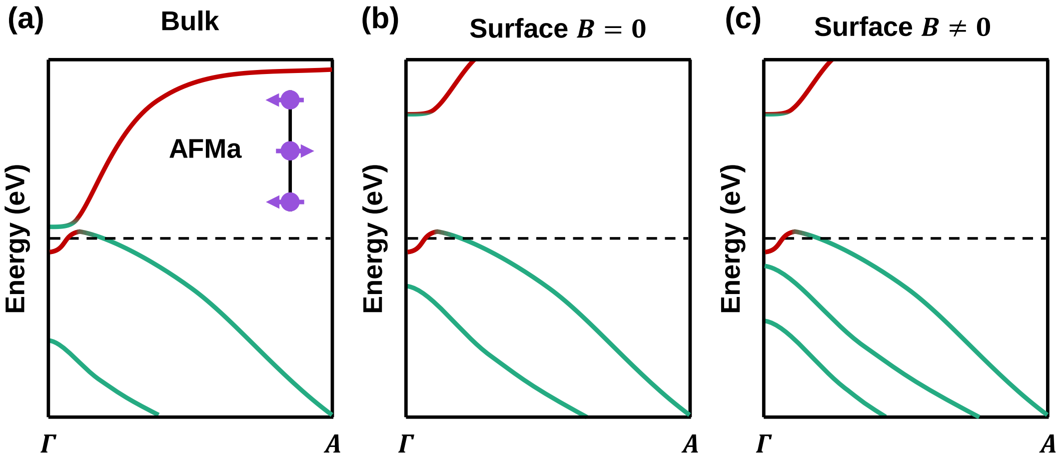

Fig. 5.10: (a) Bulk band structure at the AFMa configuration. (b) Band structure at the surface without magnetic field. (c) Band structure at the surface when a magnetic field is applied. Red and green colors indicate the Cd s and As p character, respectively.

We can summarize our observations with the band schemes shown in figures **5.10** and **5.11**.

In figure **5.10 a** we show the bulk band structure. At the surface, with zero magnetic field (figure **5.10 b**), we see that the conduction bands are pushed up, with features remaining close to the Fermi level. We hypothesize that these features remain similar as in the bulk, although this requires a careful calculation. In any event, the surface reconstruction eliminates the Weyl points, as the C3 symmetry is lost. When we apply a magnetic field, new bands appear within the bias range studied in our experiment (figure **5.10 c**).

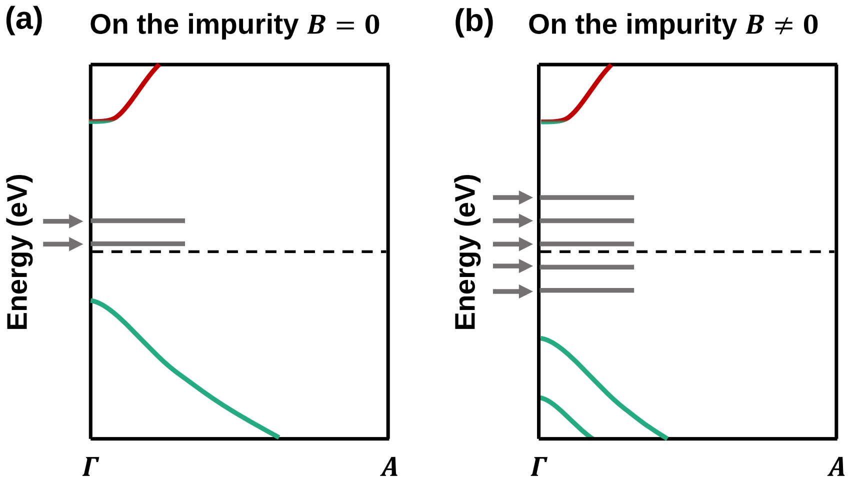

Fig. 5.11: Band structure at the defects (a) without magnetic field and (b) with magnetic field. Red and green colors indicate the Cd s and As p character, respectively. Quantized states are depicted in gray.

On the impurity at zero magnetic field (figure **5.11 a**), we observe a shift in the valence bands. At the same time, there are localized electrons within the gap. The orbital properties of these electrons are, in absence of calculations, unknown, although these might well be related to the bulk band structure. These electrons suffer lateral quantization, producing a set of discrete states. When applying a magnetic field, the set of discrete states suffers additionally Landau quantization (figure **5.11 b**).

Thus, we have a topological system presenting a highly non trivial set of quantized states at the surface. The observation of Landau quantization is different than the one in WTe_2. Here, we have localized electrons whose wavefunctions describe complex patterns in real space following Landau orbits. This provides the patterns shown by the conductance images under magnetic fields.

5.3.3 Localization properties analyzed through multifractality

Multifractal analysis gives information about the localized states. It can be applied to images to study the distribution and changes in the length scale, such as the vortex distribution in superconductors [187, 188] or the Landau level quantization [189, 190].

Using this analysis, we can assign a set of fractal dimensions that, analog to the usual concept of dimension, describe the patterns related to the field of view analyzed. One of the functions that can be used to characterize multifractality is the multifractality spectrum $f(\alpha)$. It provides the dimensions α found in a given field of view. The function is a point centred in the fractal dimension for a monofractal image. For an entirely random image, the function $f(\alpha)$ consists of a point centred at $\alpha = 2$. Multifractality effects broaden the function $f(\alpha)$ and change the position of the maximum in $f(\alpha)$ from $\alpha = 2$. Another function usually used to characterize the multifractality is the generalized dimension D_q. This parameter is analogous to the usual dimension. For a random map is $D_q = 2$ for all values of q, giving a straight line. q are a set of scaling exponents that distort the image, highlighting different areas with different heights of pixels. For a multifractal image, its values depend on q, resulting in a sigmoidal curve. We use the box counting method described in ref. [191] to calculate these parameters.

For the conductance maps at 0 T, the function $f(\alpha)$ broadens for energies above the Fermi level (figure **5.12 a**). We can see that the maximum value of this function is always near $\alpha = 2$ but moves towards larger values of alpha at the energies where $f(\alpha)$ broadens (figure **5.12 b**). The values of α_{max} deviate from 2 for the energies where the localized states appear in the conductance maps (figure **5.6**), finding the largest increase for the values where the peaks related to the defects appear. A similar behavior is observed for the generalized dimension D_q (figure **5.12 c**), which deviates from a straight line for the same energies.

The conductance maps deviate from the Gaussian distribution for the same values where the multifractality appears. Figure **5.12 d** shows the normalized conductance histograms for the energies indicated with bigger circles in **5.12 b**. At - 30 mV, the histogram deviates from the Gaussian distribution for values below 1 due to the defects, seen as depressions in the conductance maps (figure **5.6**). For positive energies such as 34 mV, where α is also 2, the conductance distribution does not show deviations from the Gaussian distributions. However, at the energies where the peaks in the localized states appear (figure **5.6**), and α_{max} increases, the conductance distribution is asymmetric and is not well fitted by a Gaussian distribution.

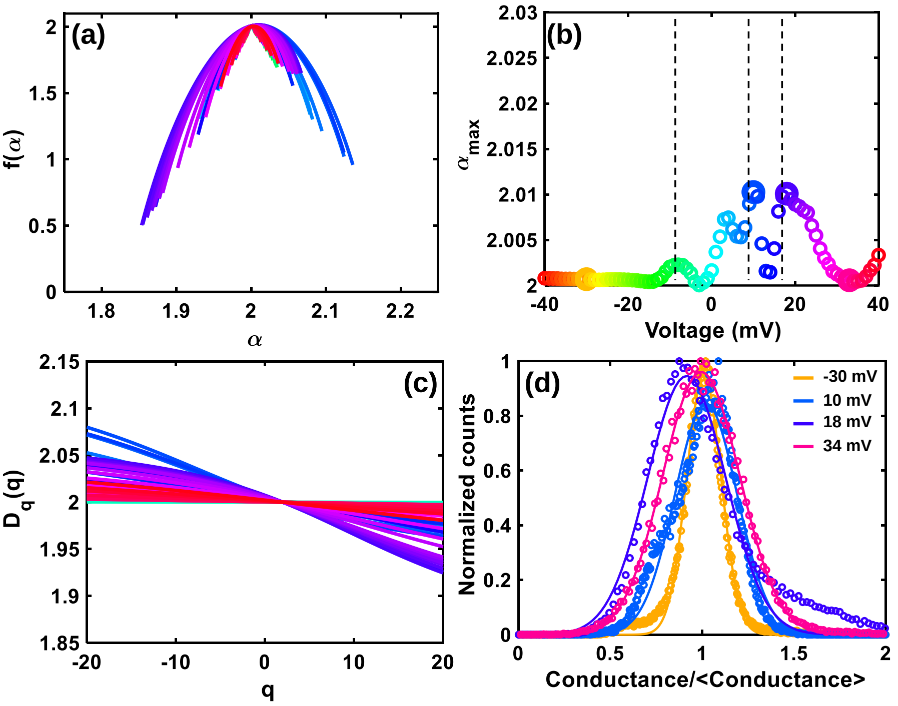

Fig. 5.12: (a) Multifractal spectrum for each conductance map between ± 40 mV for the measurement showed in **5.6**. The voltage dependence is given by the color code used in (b). (b) Value of α where we find a maximum in $f(\alpha)$ as a function of the bias voltage. Bigger dots indicate the values in (d). Dashed lines mark the energies where the localized states appear. (c) Generalized dimension D_q. (d) Normalized conductance histograms at different bias voltages. The experimental data (dots) is fitted to a Gaussian distribution (solid lines) for each map.

When doing the same analysis for the conductance maps at 14 T, we find an increase in multifractality. As discussed in the previous section, with the presence of a high magnetic field, we find that the localized states present Landau quantization. The function $f(\alpha)$ broadens more at some energies (figure **5.13 a**). The value of α_{max} increases and increases for a wider energy range (figure **5.13 b**). We can relate the changes in the α_{max} value with the energies where the localized states appear in the conductance maps (figure **5.8**). Note that the change in energy of the localized states for different defects is reflected in the multifractal analysis, making α_{max} to be $\neq 2$ even between the more prominent peaks. The same behavior is found for D_q, which deviates from a straight line at the same values where $f(\alpha)$ broadens (figure **5.13 c**).

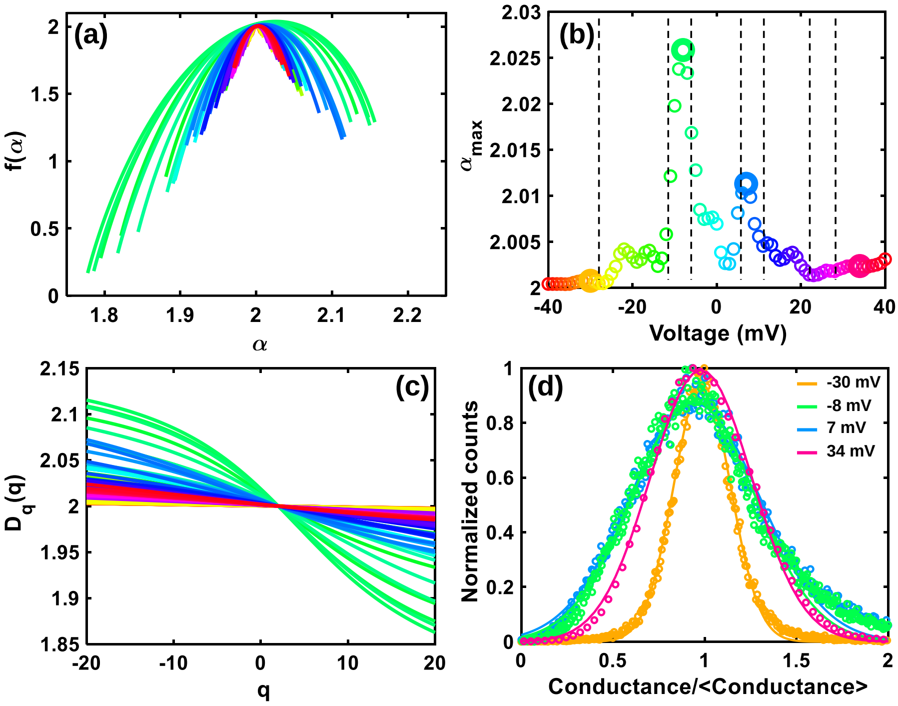

Fig. 5.13: (a) Multifractal spectrum for each conductance map. (c) Maximum value of the function f(α) from (a). Bigger dots indicate the values in (d). Dashed lines mark the energies of the quantized states from table **5.1**. (c) Generalized dimension D_q. The voltage dependence is given by the color of the curves. Bigger dots indicate the voltages chosen for the next figure. (d) Normalized conductance histograms at different bias voltages. The experimental data (dots) is fitted to a Gaussian distribution (solid lines) for each voltage.

The conductance histograms when the magnetic field is applied present similar results that in the previous case (figure **5.13 c**). Note that the conductance distribution can be fitted with a Gaussian curve for energies where α_{max} is close to 2, but deviates when the multifractality increases.

The observation of enhanced multifractal properties in the images at high magnetic fields, combined with the increased number of discrete states in the tunneling conductance, suggests a certain tendency towards localization. This could be related to quantum Hall states at the surface of EuCd$_2$As$_2$.

5.4 Conclusions

In summary, we present measurements on the surface of the magnetic semimetal $EuCd_2As_2$. Apart from the expected hexagonal lattice, we found a 2×1 surface reconstruction that reminds one of the usual reconstructions of the iron pnictides [180]. Topographies show the presence of impurities on the surface that we associate with interstitial atoms. The application of the magnetic field has an important influence on the conductance curves, producing a considerable increase in the tunneling conductance for energies below the Fermi level.

Spectroscopy maps in areas with defects show localized states that appear on the defects. On the impurity site, the valence band shifts and localized states appear in the gap. Spatial quantization produces a set of discrete states whose energy position depends on the impurity size. Using the quantization of a quantum well, we obtained an effective mass of the order of 0.14 m_e. Note that this quantization is very sensitive to the quantum well size, and small variations in the size of the defects can produce a significant shift in the position of the levels.

When a magnetic field is applied, the states also quantize in energy, producing complex variations in the spectroscopy maps. Using the formula for a harmonic oscillator quantized by the presence of a magnetic field and the parameters obtained for the zero field case, we obtain a set of levels that can be compared with our results. Multifractal analysis of the conductance maps reflects the localization of states. Multifractality increases at the energies where the localized states appear.

Chapter 6

Absence of screening in orbital selective superconductor FeSe

As explained in the introduction, high temperature superconductivity in the iron based superconductors is interwined with nematic and magnetic order [73]. FeSe is a particular example where nematicity and superconductivity arise in absence of magnetic order. Although there is no magnetic transition, as in other iron based superconductors, magnetic correlations are important and are connected to the features in orbital arrangements that occur at the nematic transition [192]. Furthermore, the carrier density is very low and the Fermi surfaces very small.

Here I present a study of stoichiometric FeSe at low temperatures, resolving its band structure using QPI. We find a localized state at the defects and a charging ring like feature that can only be explained by the opening of a semiconducting gap in a portion of the band structure which is well separated from the rest of the band structure, possibly due to orbital selectivity. The size of the ring depends on the voltage due to the electric field produced by the tip. We have also studied $FeSe_{0.71}S_{0.29}$, which is not nematic. In this system, the defects do not present the said features.

6.1 Introduction

FeSe is unique among the iron based superconductors because of the presence of strong orbitally dependent electronic correlations and small Fermi surfaces. Its crystalline structure is the simplest among the Fe-based superconductors. It consists of a layer of Fe atoms sandwiched between two layers of Se atoms and strongly bonded to them. This set of layers is stacked in the *c* direction with van der Waals forces between them, as represented in figure **6.1**.

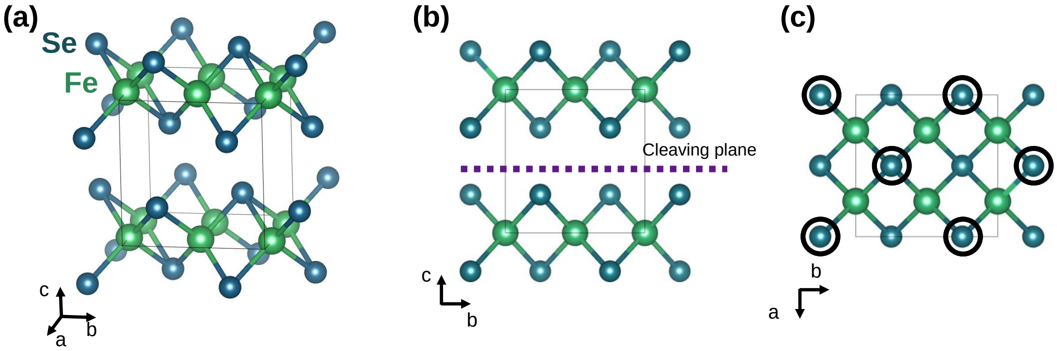

Fig. 6.1: Schematic representation of the low temperature Cmma orthorhombic atomic structure of FeSe. Fe atoms are depicted in green and Se atoms, in blue. General (a), lateral (b) and top (c) views. Light black lines delimit the unit cell. Purple dotted line in (b) indicates the cleaving plane. Black circles in (c) indicate the top Se atoms accessible with the STM tip after the cleaving process.

FeSe undergoes a tetragonal to orthorhombic transition below T_s at 90 K that stabilizes a nematic electronic state. In addition, it becomes superconducting below 8 K. Unlike most Fe-based superconductors, FeSe is not magnetic. Magnetism is believed to be connected to a high critical temperature in these materials through the spin fluctuation pairing mechanism. However, superconductivity in FeSe is remarkably tunable. Under pressure, T_c in FeSe reaches nearly 37 K [193] and in gating configurations, T_c can be boosted up to 43 K with an applied voltage [194]. In addition, superconductivity can be found up to 65 K in monolayers deposited on $SrTiO_3$, without any sign of bulk magnetism [195].

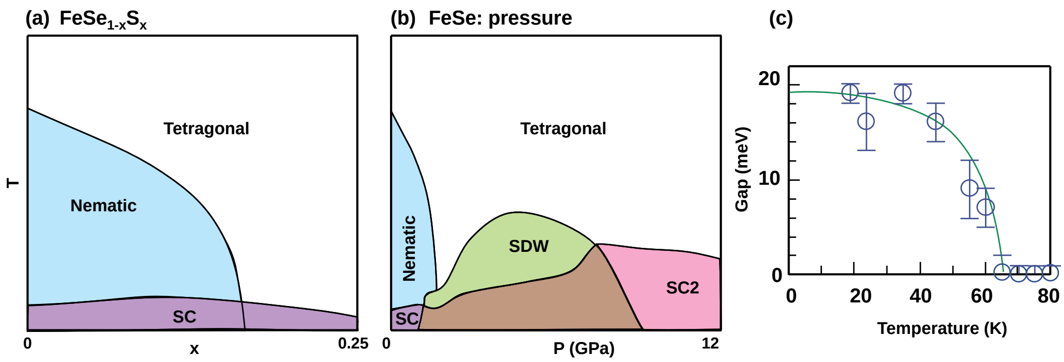

Fig. 6.2: (a) and (b) adapted from [196]. Schematic phase diagram of FeSe$_{1-x}$S$_x$and FeSe under pressure, respectively. (c) Adapted from [195]. Temperature dependence of the gap value of FeSe single layer. The green line represents the BCS gap dependence.

The fourfold symmetry breaking of the electronic properties at the nematic transition has been characterized by measurements of the in-plane anisotropy of the resistivity [197], quasiparticle interference [198] and nematic susceptibility in response to an external strain [199]. The nematic transition also manifests in strong changes in the anisotropy of the Fermi surface and of the scattering properties at low temperatures, as detailed below.

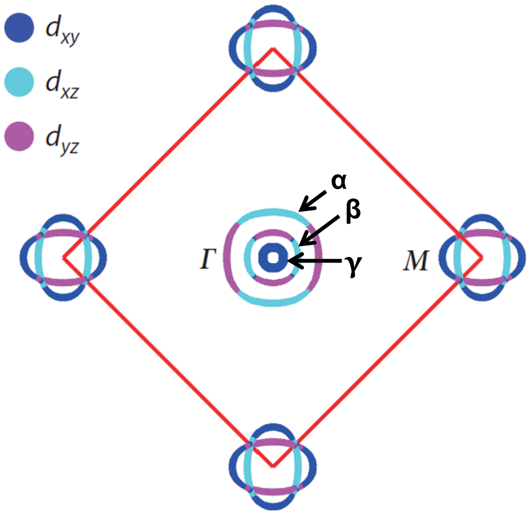

Fig. 6.3: Adapted from [196]. Calculated Fermi surface for FeSe, with three hole-pockets at Γ, and two electron-pockets at M. Colors indicate the orbital character of the pockets.

In the tetragonal phase, above T_s, DFT calculations obtain three quasi-2D hole pockets around the Γ point (α, β and γ pocket), occupying a sizeable fraction of the Brillouin zone, and two large quasi-2D electron pockets around the M-point (δ and ϵ) [199] (figure **6.3**). However, ARPES and quantum oscillation measurements have shown that the high-temperature bands have orbital-dependent band renormalizations, with respect to band structure calculations, which are particularly significant for the bands with d_{xy} character. This leads to a significant shrinkage of the Fermi surfaces (a factor of ~ 5, compared with calculations) [199, 200]. In addition, the hole pockets are shifted down such that the pockets are much smaller with rather small k_F values the Γ point, becoming larger at the Z point. The Fermi surface obtained experimentally by ARPES and quantum oscillation measurements above T_s consists of two hole pockets with d_{xz} and d_{yz} character (figure **6.4 a**): an outer quasi-2D hole pocket (α) and a small 3D inner hole pocket which just crosses the Fermi level around the Z point (β). In addition, there are two elongated electron pockets at the M_X and M_Y points with d_{xz}/d_{xy} and d_{yz}/d_{xy} character respectively (figure **6.4 a**)[199, 201].

In the nematic phase below T_S there is a strong in-plane deformation of the whole Fermi surface, becoming two-fold. The two-fold nature is only observed in detwinned samples, where there is just one domain [202, 203]. Samples showing the two possible two-fold domains provide four-fold features [199, 204]. The deformation emerges because of the lifted degeneracy between the d_{xz} and d_{yz} orbitals [86, 205] at low temperatures (figure **1.22 b**). In addition, the β hole band is pushed below the Fermi level. The α pocket elongates and becomes eliptical at low temperatures. The electron bands are made of the d_{xz} and d_{yz} orbitals that lose their degeneracy at low temperatures, with, in addition, some d_{xy} character [196]. As we show in figure **6.4**, the d_{xy} character is along the $\Gamma - M_Y$ axis and the $\Gamma - M_X$ axis. The d_{xz} and d_{yz} characters are perpendicular to both axis in each electron pocket.

The lifted degeneracy in the low temperature nematic phase is represented as in figure **6.4 b**. The d_{yz} and d_{xz} bands along the lines $\Gamma - M_X$ and $\Gamma - M_Y$ are no longer degenerate (have the same shape). The splitting eliminates the four-fold symmetry of the high temperature phase and leads to the two fold symmetry of the low temperature phase.

As the d_{yz} band shifts upwards in energy, the pocket at M_X shrinks along the $M_X - \Gamma_2$ direction. As the d_{xz} band shifts downwards in energy, the d_{xz} portion of the pocket at M_Y should become slightly larger.

The d_{xz} portion of the electron pockets in the nematic phase is not seen clearly in many ARPES measurements, except in Ref. [206], where it is shown that it vanishes below the nematic transition.

The role of the band crossing shifting between $\Gamma - M_Y$ towards $M_Y - \Gamma_2$ below the nematic transition is important. Along $\Gamma - M_Y$, the d_{xy} and d_{xz} bands have different parity and cannot mix [207, 208].

The parity here is defined with respect to the symmetry of the wavefunctions (odd/even). The symmetry of the wavefunctions is defined by the orbital character and the phase between the two inequivalent Fe sites in the nematic crystal structure [208]. Thus, the main aspect defining the symmetry is the xz mirror plane.

Along $\Gamma_2 - M_Y$ direction, the d_{xy} and d_{xz} bands have the same parity and can mix [207, 208]. This leads to a band gap opening [206]. When the gap is opened, the electron like d_{xz} band acquires d_{xy} character and the hole like d_{xy} band acquires d_{xz} character [206]. As a consequence of the hybridization, part of the d_{xz} band is pushed above the Fermi level [206].

Similar effects are observed in monolayer FeSe and in KFe_2As_2 due to an orbital selective Mott transition, in which correlations produce a modification of the spectral intensity in the bands [209, 210]. In FeSe, it is assumed that the main driving mechanism is nematicity [206], although correlations play a significant role in band renormalization too.

The nematic transition has thus a strong effect on the orbital character. The electronic properties become orbital selective in the nematic phase [211–213].

S doping suppresses the nematic order and modifies the superconducting critical temperature [214] (figure **6.2 a**). As a consequence, for S concentrations above x_c, where the tetragonal phase is recovered at low temperatures, the Fermi surface is quite similar to this in FeSe above T_s but with slightly larger FS pockets [215].

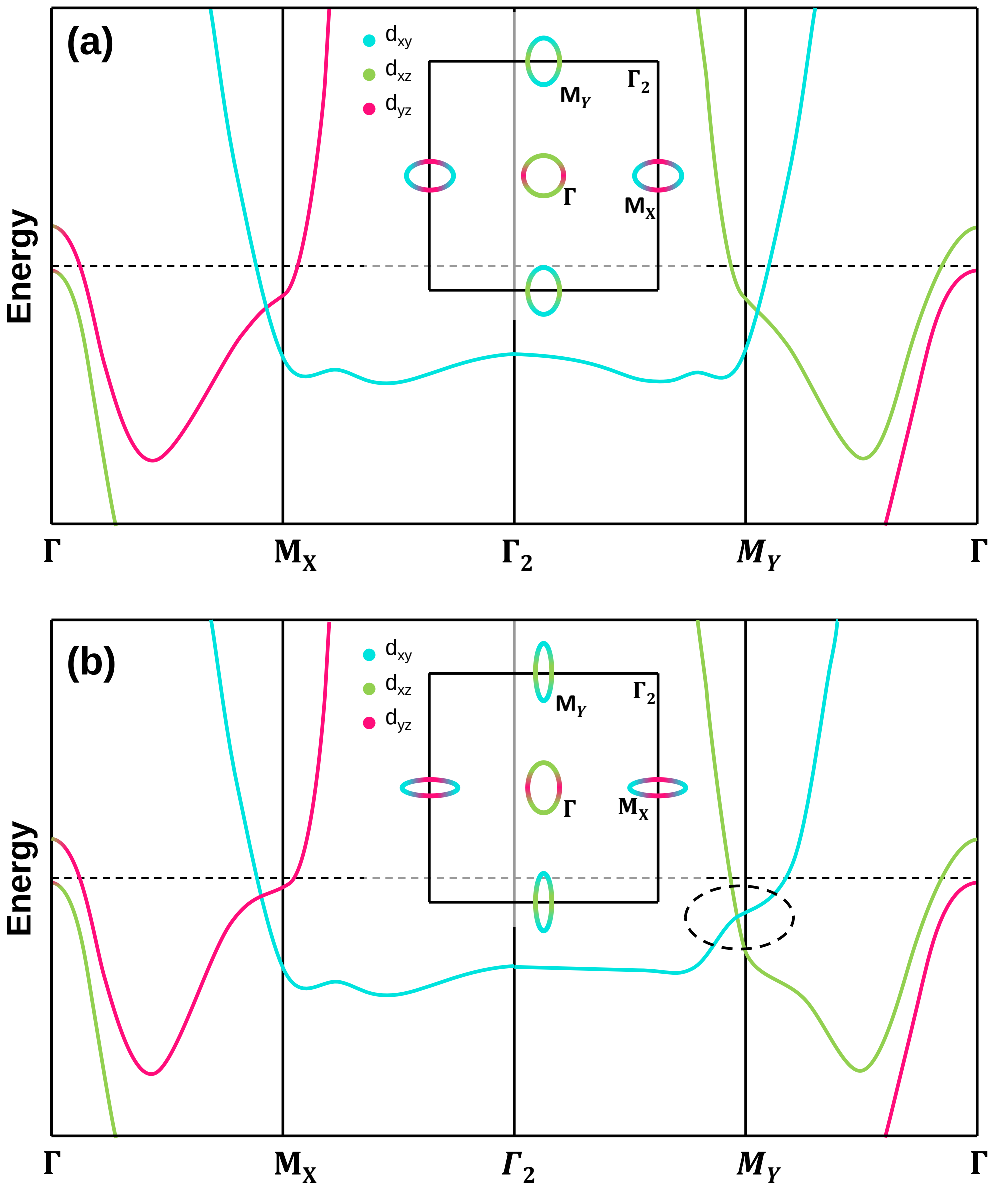

Fig. 6.4: Adapted from [206]. Band structure and Fermi surface of FeSe (a) above and (b) below the nematic transition. In the insert, the Fermi surfaces for both band structures are presented. Colors indicate the orbital character of the bands. Dashed circle indicated the point where the band crossing leads to a band gap opening.

We measured samples grown by the group of Prof. Paul C. Canfield. They were grown using chemical vapor transport as reported in [216]. Samples were plate-like with the c-axis perpendicular to the surface and typical sizes 1 mm

× 1 mm × 0.05 mm. The samples were measured at 100 mK and magnetic fields up to 17 T.

6.2 Atomic structure

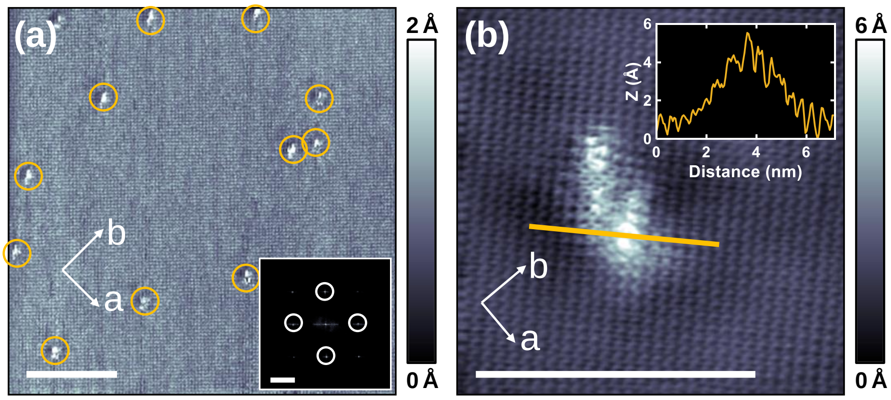

Fig. 6.5: Adapted from [91]. (a) Atomic resolution STM topographic image with several defects. In the inset, FFT of the image, where the peaks corresponding to the Se surface are observed. Horizontal scale line is 2 nm^{-1} long. (d) Zoom showing one single defect. In the insert, height profile of the yellow line over the defect. Both images were measured at 100 mK with a bias voltage of 10 mV and 4 nA current setpoint. Horizontal scale bar is 10 nm.

Samples were cleaved in cryogenic conditions with the cleaving method explained in chapter 2. At 100 mK, the samples have an orthorhombic structure with lattice parameters $a = 5.318$ Å, $b = 5.343$ Å and $c = 5.495$ Å. The layer exposed after cleaving is always formed by Se atoms due to the Van der Waals forces between Se-Fe-Se layers. Se atoms form a square lattice with lattice parameter 3.769 Å. Note that the atomic lattice visible (the Se sublattice) with STM is tilted 45° with respect to the unit cell, which follows the Fe sublattice.

The atomic Se lattice is resolved when making high resolution images (figure **6.5 a**). The Se lattice provides a square pattern in the Fourier transform (inset of figure **6.5 a**). We would like to highlight the white spots in this image. At each spot, there is a defect. When zooming into one of these areas (figure **6.5 b**) we find a large modification of the Se lattice. In particular, we see that the apparent height increases considerably above the surface and that the impurity is seen over distances which are very large, of the order of 5 nm or above. Note that the STM topography is the integral of the density of states between the Fermi level and the bias voltage. Therefore, it does not only show a structural modification or a modification of the atomic positions, but also changes in the local density of states. The observations shown in figure **6.5 b** visually represent a strong modification of the local density of states around the impurity. From the topographic images (figure **6.13 a**), we can estimate a density of defects of $7.75 \cdot \text{cm}^{-2}$. Using the crystal lattice parameters, we can assume the electrons move freely ≈ 460 unit cells and we can estimate a mean free path $l = 240$ nm. Although this is a rough approximation, the low ratio of defects is in accordance with the high residual resistivity ratio (RRR) [216]. We can also estimate this value from the resistivity. Using $\rho \sim 20 \mu\Omega$ cm [197], an effective mass $m^* = 4m_e$ [196] and a number of carriers $n = 3.58\ 10^{20}$ cm^{-2}, we obtain $l \sim 137$ nm.

6.2.1 Quasi-particle interference analysis

To explore the band structure of FeSe, we performed quasiparticle interference measurements. As explained in chapter 2.4.1, for this technique we need a surface with defects or impurities that act as scattering points. The scattering process produces oscillating patterns related to the band structure. This occurs in FeSe particularly for small size defects, marked by yellow circles in figure **6.13 a**. As shown previously in Refs [198, 217], such small size defects are mostly responsible for generating the oscillations leading to quasiparticle interference.

We performed STS measurements in a 43.5 nm × 43.5 nm area at 5 K. The conductance maps and its Fourier Transform maps (zoomed to show the Brillouin Zone) are represented for several bias voltages in figure **6.6**. The FFT maps are symmetrized according to the C_2 symmetry of the nematic phase. These directions are indicated in the real and momentum space with white arrows in figure **6.6 a**.

In the FFT maps, the scattering periodicities are seen as bright points that change with the energy. Colored dots in these maps mark the main scattering vectors we can observe in X and Y directions. The change of the scattering

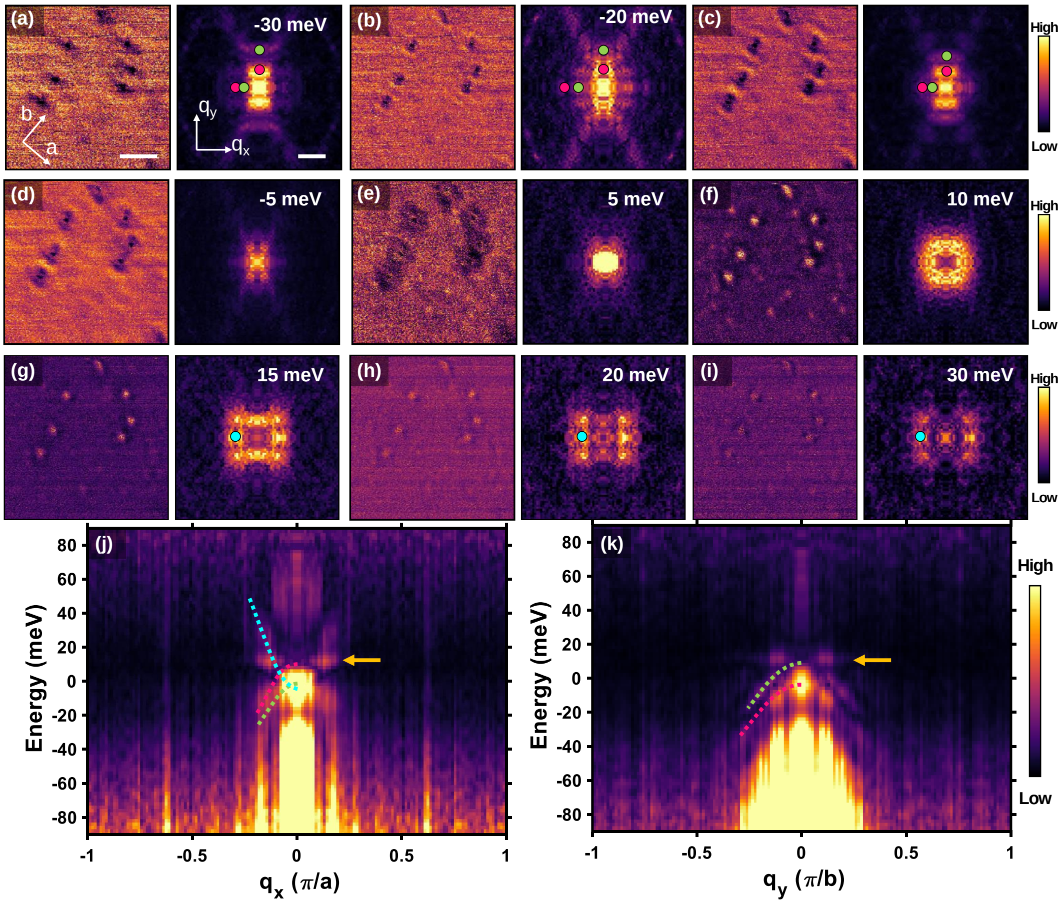

Fig. 6.6: STS measurements of an area of 43.5 × 43.5 nm^2, at 5 K. The measurements were taken between ± 100 mV with 4 nA set-point. (a-i) Conductance maps and symmetrized Fourier Transform maps at different bias voltages. Horizontal white line is 10 nm long in the conductance maps and 1 nm^{-1} in the FFT maps. Main directions are indicated with the white arrows. Blue, green and magenta dots in the FFT maps mark the main scattering points, and indicate d_{xy}, d_{xz} and d_{yz}, respectively. (j) $q_y = 0$ profile and (k) $q_x = 0$ profile showing the scattering intensities. Magenta, green and blue dotted lines indicate the dispersive signals in accordance with the dots in the FFT maps. Yellow arrows mark a non-dispersive signal around 10 mV.

signals with energy can be better seen when plotting $q_y = 0$ (figure **6.6 j**) and $q_y = 0$ (figure **6.6 k**) profiles, where the main scattering signals are indicated with dotted lines. We use the same color code for the lines and the dots in the

FFTs. Colors also indicate the orbital character of the bands in accordance with figure **6.4**.

In the $\Gamma - X$ direction, two hole bands can be seen. The magenta band crosses the Fermi level and has its top around 10 mV. The green band finishes very near the Fermi level, without crossing it [91]. These two hole-like bands are in agreement in size and position with the hole-like bands centered in Γ in figure **6.4**. Along this direction, an electron band represented with the dotted blue line can also be seen. The position of this band coincides with the electron-like band centered in X, although the size is slightly bigger than in most calculations. In the $\Gamma - Y$ direction, two hole bands are also visible. Similar to the $\Gamma - X$ direction, we see that one band crosses the Fermi level while the other does not [91]. The position in energy and size of both bands are in agreement with the bands centered in Γ in figure **6.4**. Note that the colors of the hole-like bands are different in the $\Gamma - X$ direction than in the $\Gamma - Y$ direction due to the change in the orbital character (see figure **6.4 b**). The larger band crossing the Fermi level can be associated with the hole-like α-pocket centered in Γ in the Fermi surface, and has been observed in previous QPI measurements, but only in the $\Gamma - Y$ direction [198, 217]. Note that in the $\Gamma - Y$ direction the band is wider, as expected from the ellipsoidal shape of the α-pocket, and have d_{xz} orbital character. No electron band can be seen in this direction in ours or other QPI measurements [198, 217]. Fermi energies of the hole-like and electron-like bands crossing the Fermi level are very small, as previously found.

Moreover, a non-dispersive signal around 10 mV (indicated with yellow arrows in the profiles) can be seen in both directions. The energies where this signal can be seen correspond to the energies where the defects have its maximum spatial extension in the conductance maps. The size of the q-vector associated to this signal in the FFT at 10 mV corresponds to ~ 8 nm in the real space, which is the distance between the closest defects. This feature has been observed in previous reports, but it origin has not been discussed [217].

6.2.2 Defects

To understand the origin of the non-dispersive signal discussed above, we can compare the conductance curves taken on top of the defects with conductance curves taken far from them. Figure **6.7** shows three conductance curves taken on top of three defects (purple curves) and three curves taken in an area far from the defects (yellow and orange curves). An increase of the conductance around 10 mV can be seen for the curves taken on top of the defects, indicated with the yellow arrow in figure **6.7**. Another difference between the curves in the different positions is the value of the conductance below the Fermi level. When the curves are taken on top of the defects, the conductance is smaller than in the curves taken far from defects. The inset in figure **6.7** shows the distance *versus* voltage (right) for a profile taken along the green line in the conductance map (left), on top of two defects. The yellow arrows mark the energy where there is a difference in the conductance around 10 mV.

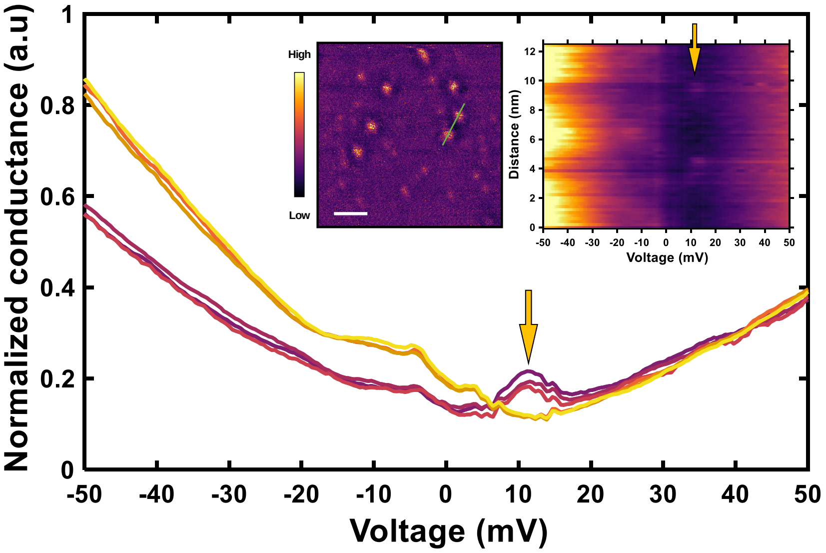

Fig. 6.7: Conductances *versus* voltage curves taken on top of the defects (purple colors) and in areas far from the defects (orange colors). The insets show the conductance map at 10 mV (left) and distance *versus* voltage (right) profile taken along the green line in the conductance map. Yellow arrows indicate the increase of the conductance at 10 mV.

This difference in the conductance curves indicated a different occupation of the bands around the defects. The hole bands are less occupied in the defects, and there is a charge concentration around 10 mV due to the presence of a localized state in the defects.

For the localized state to appear, there must be a gap opening between the electron and hole bands. Figure **6.8** schematically shows the change in the bands. The gap opens at the points where the hole and electron bands cross. As we have discussed above, in the nematic phase, the d_{xz} band is pushed upwards leading to a gap opening in ARPES [206, 208]. Similar gap openings have been also observed due to correlations [209, 210]. Thus, the charge accumulation around defects enhances the gap opening. At the same time, a localized state is built on the defects, giving the peak in the density of states shown in figure **6.7**.

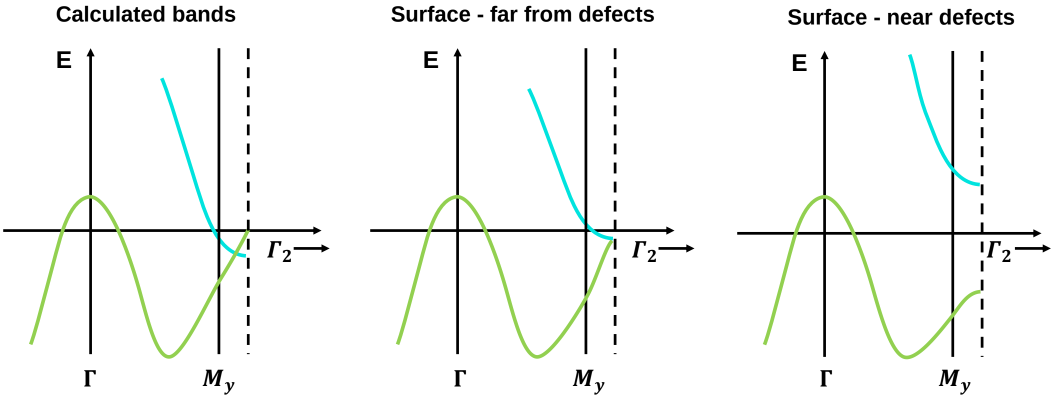

Fig. 6.8: Schematic representation of the hole and electron band that cross in the M_y–Γ_2 direction in figure **1.1**. In the surface, these two bands separate opening a small gap. Near the defects, both bands separate, opening a larger gap.

6.3 Local discharge around defects

To understand the behavior of the defects on this material, we performed spectroscopy measurements in a smaller area centered on the defects. Figure **6.9 i** shows the topography of an area of 43.5 × 43.5 nm. This measurement was taken with a superconducting Pb tip to enhance the small features in the density of states. In this case, the density of states of the tip is not constant in energy, but presents the superconducting gap and two very sharp peaks around it. The DOS of the tip can be considered as a function formed by two δ-functions centered in the positions of the quasiparticle peaks of Pb, and being exactly zero between them. At sufficiently low temperatures, the tunneling current measured with this tip is proportional to the density of states of the sample with an offset in energy equal to the Pb superconducting gap [218]. Thus, the maps represented in figure **6.9** are the current maps at different bias voltages, where the offset in energy has been corrected. In these current maps, we can see that a ring is formed between the defects. The radius of the ring increases when increasing the voltage. This was discussed in chapter 1.2.2 and is characteristic of semiconducting materials.

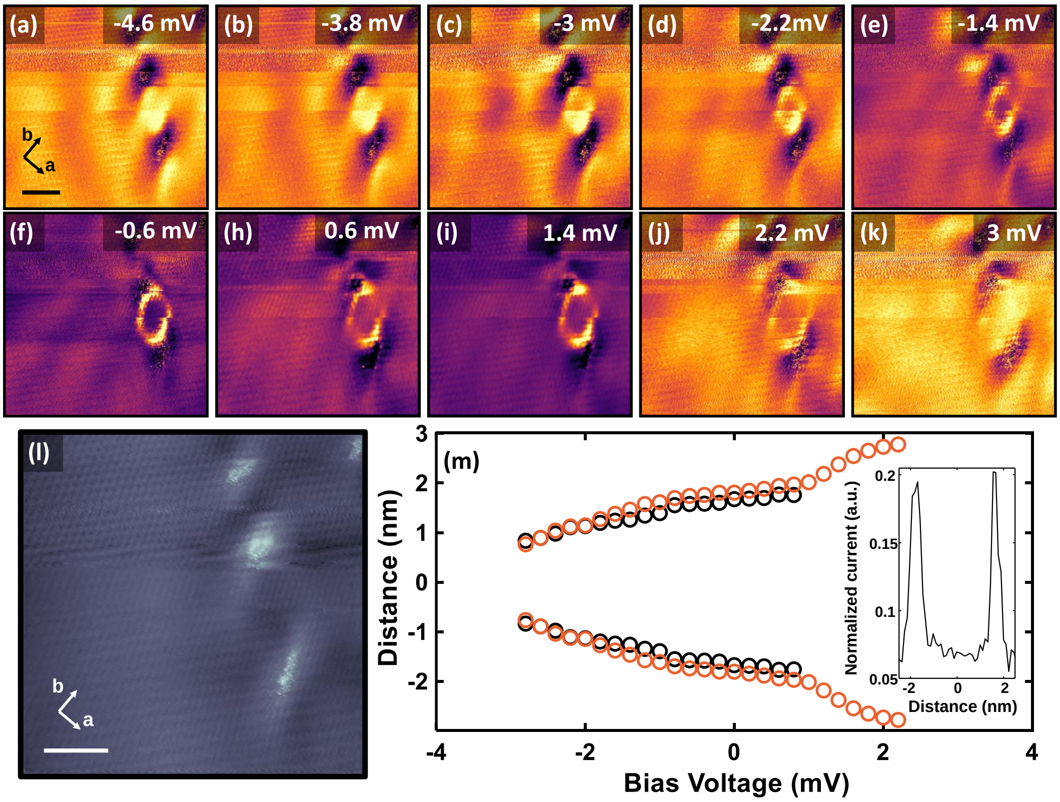

Fig. 6.9: (a-k) Current maps for different values of bias voltage, where the offset in energy due to Δ_{Pb} has been corrected. (l) Topographic image taken at the same time than the current maps, at 100 mV and 4 nA. (m) Radius of the ring *versus* voltage measured in a direction (black) and b (orange). In the inset, a current profile on the ring is shown at +2 mV.

We measured the radius of the ring for a and b directions, and represented them *versus* the bias voltage in black and red dots in figure **6.9 m**. The ring is homogeneous for small energies. However, when the ring reaches the defects at 1 mV, it can not continue increasing its size. Thus, the radius in the *a* direction can not be as large as in the *b* direction for energies above 1 mV. In the inset of this figure, a profile of the normalized current map at +2 mV is shown. The diameter of the ring can be measured as the distance between the two peaks. When fitting the radius *vs* bias voltage to a straight line (figure **6.9 m**), it extrapolated down to zero at -5.6 mV in both directions.

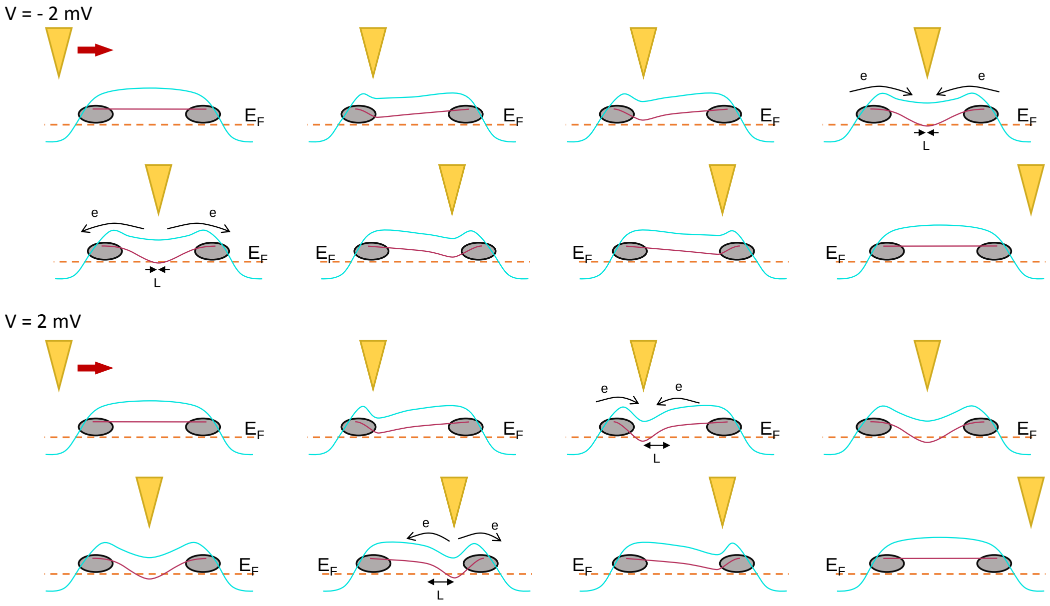

Fig. 6.10: Schematic representation of the band bending and localized state between the defects (gray circles) due to the influence of the tip (yellow). When the tip is between the defects, it bends the electron band (blue) and the localized state (magenta). Depending on the bias voltage, the localized state goes below the Fermi level at different positions, and the electrons charge the localized state (first and third rows of figures). The tip continuous moving and the electrons empty the localized state in the symmetric position between the defects, making a ring-like feature with different radius L in the current maps (see text).

Figure **6.10** represents the electron band behavior (blue) and the localized state (magenta) between the defects (gray circles) in the FeSe surface. The electron band goes from below de Fermi level (orange dotted line) to above in the defects and near them, as explained in figure **6.8**. A localized state originates in the gap between the electron and hole bands, represented by the magenta line. When the tip approaches the defects, the electron band and the localized state bend due to the electric field. The field is generated by the voltage difference between the tip and the sample. When the bending is large enough, the localized state goes below the Fermi level, and electrons fill it. This is measured in the tunneling current as a sharp signal. When the voltage is small (first two lines in figure **6.10**) the localized state only goes below the Fermi level for a small region between the defects, and the radius L is small.

For larger voltages, the band bending is larger. Thus, the localized state goes below the Fermi level for a larger lateral distance between the tip and the defect and the radius of the ring increases (see two last lines in figure **6.10**). The tip continues moving between the defects and, when it reaches the symmetrical position near the second defect, the electrons empty the localized state. This is also measured in the tunneling current as a sharp jump. This happens for all the directions around the defects, and the final feature measured has the shape of a ring whose radius increases when increasing the voltage.

6.4 FeSe-S

Isoelectronic substitution, as doping or pressure, modifies substantially the phase diagram of FeBSCs. In FeSe we can replace selenium atoms for sulfur atoms outside the iron plane, which causes an internal chemical pressure [199]. We can see in figure **6.11** that the temperature of the nematic transition T_s decreases, and it is not longer present for $x > 0.17$ [214].

Inside the nematic phase, the critical temperature T_c displays a small dome, raising from $T_c \approx 8.5$ K at $x \approx 0$ to a maximum value of $T_c \approx 10$ K at $x \approx 0.10$ (figure **6.11**). Once the nematic transition is passed, the T_c slightly decreases. The critical temperature is $T_c \approx 5$ K at $x \approx 0.29$, and hardly changes in the tetragonal phase towards FeS [75, 219].

The gap opening in the band structure of the nematic phase discussed for FeSe it is not expected for S-doped FeSe at $x > 0.17$, since it is in the tetragonal phase.

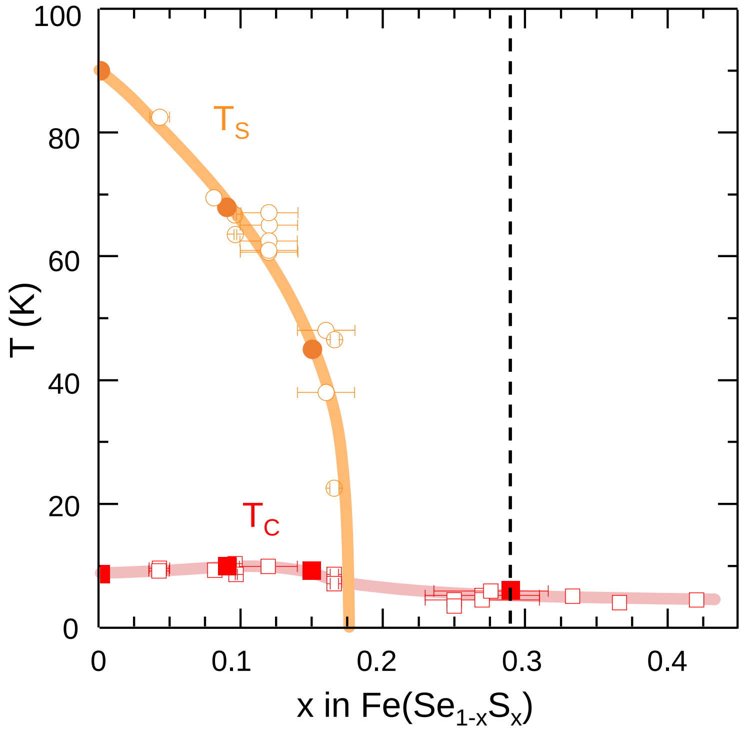

Fig. 6.11: Adapted from [214]. Phase diagram of FeSe$_{1-x}$S$_x$. The orange line and dots indicate the structural transition T$_s$. The red line and dots indicate the critical temperature of the superconducting transition T$_c$. Dashed line mark $x = 0.29$, the composition discussed in this section.

6.4.1 Atomic structure and superconducting gap

When measured in its stoichiometric form, FeSe has a V-shape double-gap structure, shown in figure **6.12 a**. These two gaps have sizes $\Delta_1 = 1.9$ meV and $\Delta_2 = 0.9$ meV, and their quasiparticle peaks are indicated in this figure with purple and green arrows, respectively. The evolution of the gaps from the deconvoluted density of states with the temperature is shown in figure **6.12 b**. The black line indicates the expected BCS evolution for a gap with T$_c$ = 8.6 K. In contrast, FeSe$_{1-x}$S$_x$ in the tetragonal phase for x $>$ 0.17 the shape of the gap change significantly and its double structure disappears.

We measured FeSe$_{1-x}$S$_x$ with $x = 0.29$, a concentration above the nematic transition at zero temperature. These crystals were grown by the group of Prof. Paul C. Canfield by chemical vapor transport, as described in [214]. Similar to

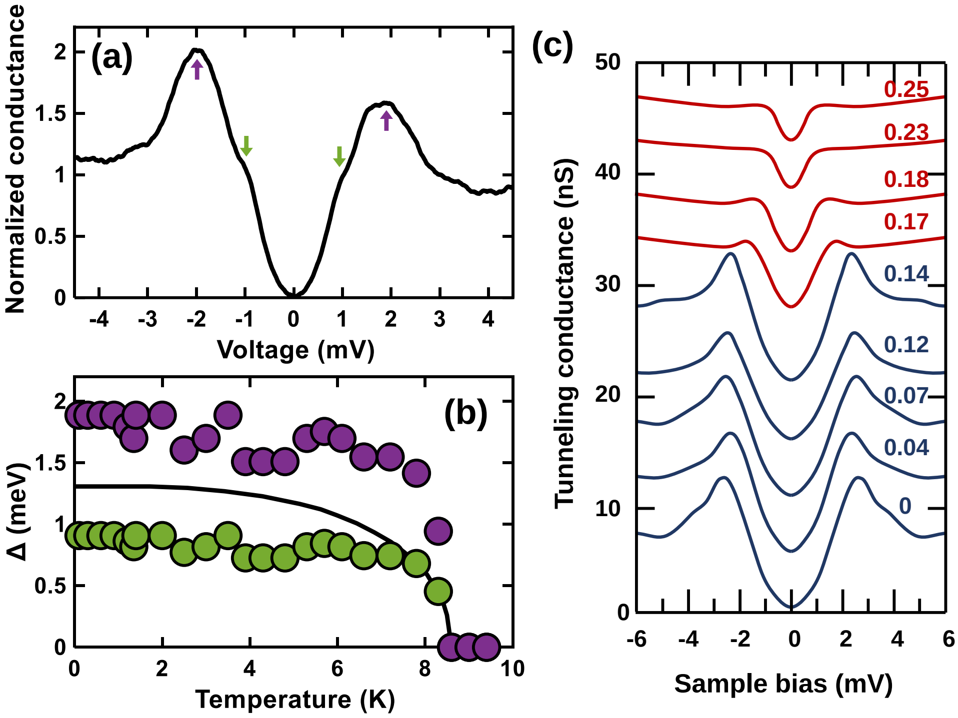

Fig. 6.12: Adapted from [91] and [217]. (a) Tunneling conductance curve versus voltage on FeSe. The two gaps are indicated with the purple and green arrows. (b) Temperature dependence of the superconducting gap. Purple and green dots indicate the variation of the two gaps. Black line represent the expected BCS temperature dependence for a gap with T_c = 8.6 K. (c) Evolution of the superconducting gap for $FeSe_{1-x}S_x$ with the doping. Curves are taken in samples with a S concentration below the structural transition (blue) and above (red). Sulfur concentration x is indicated above each curve.

FeSe, these samples were also plate-like with the c-axis perpendicular to the surface and similar typical sizes. As mentioned before, the atomic structure in this phase is tetragonal, with a lattice parameter $a = b = 5.024$ Å. As in FeSe, the atomic lattice is defined according to the Fe layer, but when cleaving, we access the Se/S layer. The crystallographic directions are rotated 45° with respect to the surface Se/S layer.

Figure **6.13 a** shows a topographic image at 150 K and 0 T, with a bias voltage of 100 mV and a set point of 2.4 nA. White arrows in the image indicate the crystallographic directions. A height profile over the defect in the image (see upper inset in **6.13 a**) shows that the defect is more than five times smaller in height than the defects in stoichiometric FeSe. Note that this image has the same size as **6.5 b**. However, there is no signature of defects that build up charge blobs as in pure FeSe. Conductance curves taken on top of the defect (red dot) and in areas far from it (blue dot) shows no presence of a localized state (see lower inset in figure **6.13 a**).

Topographic images of this compound show a small difference in the atoms that can be related to the chemical composition [217]. Gray bars in the inset in figure **6.13 b** represents the height histogram of the topography. This histogram can be adjusted using two Gaussian curves, with relative weights 0.29 (magenta Gaussian curve) and 0.71 (green Gaussian curve), which correspond to the concentration of S and Se in the sample. The magenta line in the upper inset is the sum of both Gaussian curves.

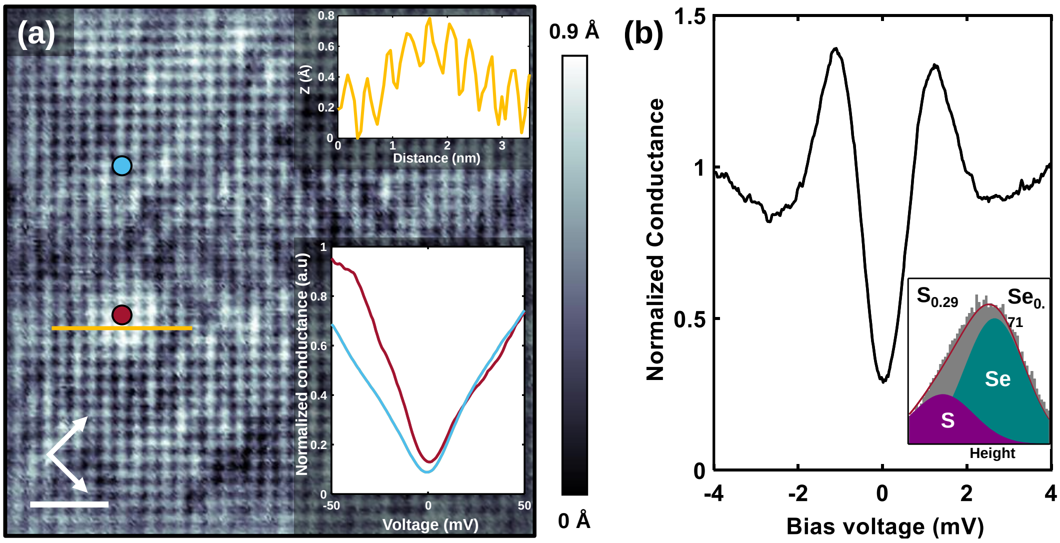

Fig. 6.13: (a) Topography image with atomic resolution in $FeSe_{0.71}S_{0.29}$ at 0 T, with bias voltage 100 mV and 1.8 nA set point. White arrows indicate the lattice direction. The horizontal scale bar is 2 nm. The upper inset shows the height profile of the yellow line over the defect. The lower inset shows the normalized conductance curves taken on top of a defect (red line) and in an area far from the defects (blue line). (b) Normalized conductance curve showing the superconducting gap at 100 mK. The inset shows the height histogram of the image in (a), which can be adjusted with a 0.29/0.71 S/Se ratio.

The normalized gap measured in this material at 100 mK is shown in figure **6.13 b**. In agreement with previous reports, we only see two quasiparticle peaks and the density of states is not zero at the Fermi level. Using the first derivative of the conductance curve, we obtain a gap size $\Delta = 0.54$ meV.

6.4.2 Vortex lattice

The vortex lattice in the stoichiometric compound FeSe has been studied with STM, even at magnetic fields close to $H_{c2} \approx 17$ T [91]. However, it has not been studied for the doped compound. Previous measurements of the vortex lattice in FeSe above 8 T [91] shows stripe-like features whose frequencies can be seen in the Fourier transform maps. Figure **6.14 b** shows the vortex lattice at 8 T of stoichiometric FeSe.

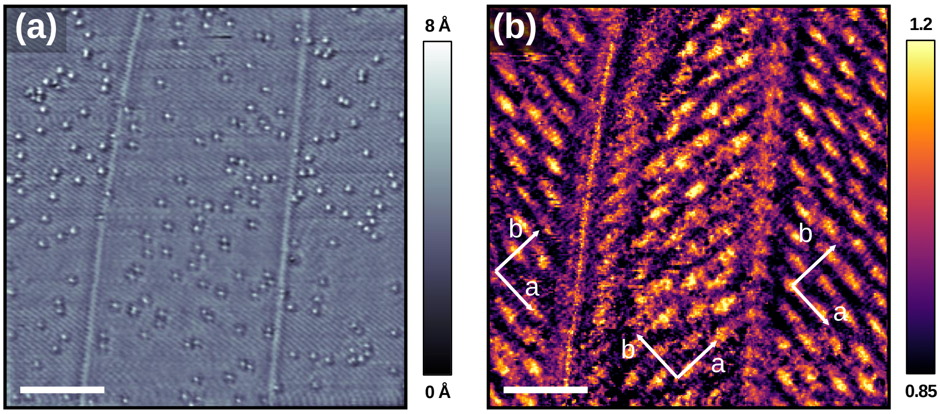

Fig. 6.14: Adapted from [91]. STM measurements of FeSe at 8 T and 100 mK, using 5 mV bias voltage and 4 nA of set point. (a) STM topographic image, with three nematic domains separated by two twin boundaries. (b) Zero bias normalized conductance map showing the vortex lattice. In the nematic regime, the vortex are elongated along a direction. For the three domains, it can be seen that the vortices rotate 90°, indicating a change in the direction of the atomic lattice. This direction is marked with the white arrows for the three domains. The vortices are also pinned by the domain boundaries. Horizontal scale line in both images is 50 nm long.

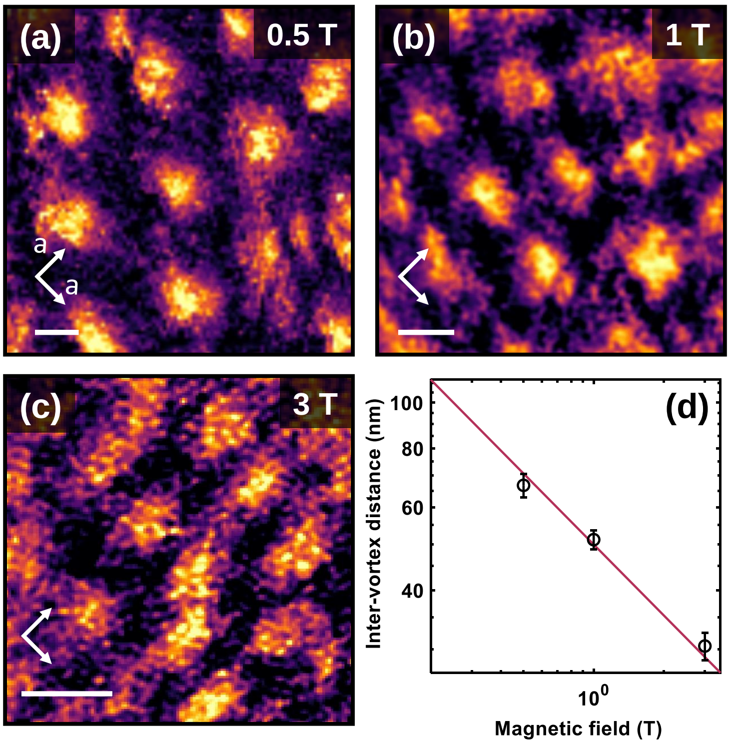

Fig. 6.15: Vortex lattice at (a) 0.5 T, (b) 1T and (c) 3T in $FeSe_{0.71}S_{0.29}$. All images were taken with 10 mV bias voltage and 3 nA. Horizontal scale bar is 30 nm. (d) Inter-vortex distance as a function of the magnetic field. Error bars indicate the deviation of the inter-core distance from the central value. Magenta line represents the relation $d(nm) = \frac{50}{\sqrt{B(T)}}$.

Vortex lattice has been previously studied in $FeSe_{1-x}S_x$ for doping values below the nematic transition. When the doping increases, the vortex core becomes more isotropic as the nematicity decreases [220].

Figure **6.15 a** to **c** shows the vortex lattice for $FeSe_{0.71}S_{0.29}$ at magnetic fields from 0.5 T to 3 T. Contrary to the vortices measured in the stoichiometric compound, where the nematicity makes the vortex core elongated in a direction (see figure **6.14 b**), the vortices cores in $FeSe_{0.71}S_{0.29}$ are isotropic. Although the vortex lattice is disordered, it tends to orient itself along the crystalline directions. The vortex density increases when increasing the magnetic field. Figure **6.15 d** shows the inter-core distance of the vortices (black dots). Error bars in the graph are calculated with the deviation in the vortex distance from the averaged value. The magenta line indicates expected variation of the intervortex distance d with the magnetic field $d(nm) = \frac{50}{\sqrt{B(T)}}$ (from Eq. 1.23), showing that the vortices form an Abrikosov lattice.

6.5 Conclusion

In summary, we performed QPI measurements of the band structure of pure FeSe, observing two hole-like bands along $\Gamma - X$ and $\Gamma - Y$ directions and one electron like band along $\Gamma - Y$ direction. We associate these bands with the expected band structure.

We focused on the behavior around defects. We observed considerable modifications of the charge distribution around defects. The charge distribution presents a ring-like feature, which evidences the appearance of charging-uncharging events when moving the tip on top of the defect.

Such events can only occur in near complete absence of screening. Given that there are many bands crossing the Fermi level in FeSe, the question is how can charging effects occur as observed in our experiment. The answer must lie in the orbital selectivity, which comes together with the nematic transition. The localized state is likely formed by an orbital whose parity is different than the parities of the orbitals forming the bands that cross the Fermi level.

The observation of a behavior characteristic of an insulator in a metal and a superconductor has far reaching consequences. It shows that FeSe is very close to a transition to an insulating state. Furthermore, it opens many new possibilities, for example the modification of the polarization around defects when gating FeSe. The interaction of vortices with charges and the possible mutual influence is another interesting line to pursue.

The behavior of S doped FeSe without a nematic transition presents no particular signatures close to defects. In this material, we have also observed atomic resolution and characterized the vortex lattice, which shows no signatures of nematicity either.

Conclusions

In summary, I have measured materials with a low density of states at the Fermi level, with different magnetic and topological properties.

In WTe_2, I resolved the Landau quantization at the atomic scale. I parametrized the Landau level DOS and reproduced the result, finding evidence of a new form of Landau oscillations. Using this atomic variation, I resolved two surface states, one associated with the electron bands, with W-5d character, and the other with hole bands, with Te-5p character. I found evidence for a non trivial topological character of the surface band structure from the observation of atomic size Landau quantization. Our measurements thus show that WTe_2 is a topological semimetal.

In $Co_3Sn_2S_2$, different surfaces with the same atomic structure can be accessed when cleaving the sample. I characterized these surfaces using atomic resolution topographies and spectroscopy curves, finding evidence of a flat band at the S surface, the one closer to the kagome lattice. The tunneling conductance close to Sn on top of a S surface suffers significant modifications in the energy range around the flat band. We find an electronic end state which is caused by the electronic correlations of the kagome lattice.

In $EuCd_2As_2$, I found a 2×1 reconstruction of the surface, as well as the hexagonal lattice expected from the lattice structure. I found defects on the surface, with a large manifestation in the topographic images. Far from the defects, the conductance curves correspond with the calculated band structure for the A-type AFM configuration. However, the spectroscopy measurements in the defects and around them show a different behavior that I could parametrize using the quantization of a 1D quantum well. With a magnetic field, the quantization pattern is enriched by Landau quantization. Multifractal analysis of the conductance maps deviates from the random distribution due to the presence of the localized states.

In FeSe, the band structure can be reproduced using QPI analysis, finding two hole bands and one electron band. I also found a resonance signal on the defects around 10 mV. This state leads to the formation of a ring-like feature due to the interaction with the tip. These kinds of features have been measured before in semiconducting materials due to the absence of screening. The nematicity and orthogonality of the bands produce an orbital selective scattering, leading to a gap opening. The low density of states cannot screen the charge and the tip induces the charge and discharge effects.

Conclusiones

En resumen, he medido materiales con una baja densidad de estados en el nivel de Fermi, con diferentes propiedades magnéticas y topológicas.

En WTe_2, he observado la cuantización de Landau a escala atómica. He medido la densidad de estados cuantizada en niveles de Landau, encontrando evidencias de una nueva forma de oscilaciones de Landau. Utilizando esta variación atómica, he identificado dos estados superficiales, uno asociado a las bandas de electrones, con carácter W-$5d$, y el otro a las bandas de huecos, con carácter Te-$5p$. Además he encontrado evidencias de la acumulación de la fase Berry en estos estados al analizar la variación de los niveles en energía. Por lo tanto, nuestras medidas demuestran que WTe_2 es un semimetal topológico.

En el $Co_3Sn_2S_2$ se puede acceder a diferentes superficies con la misma estructura atómica al clivar la muestra. He caracterizado estas superficies utilizando topografías de resolución atómica y curvas de espectroscopia, encontrando evidencias de una banda plana en la superficie de S, la más cercana a la red kagome. Los átomos de Sn sobre la superficie de S inducen que la banda plana se mueva a energías negativas alrededor de los defectos. Al aplicar un campo magnético, la banda está más cerca del nivel de Fermi y el desplazamiento alrededor de los defectos es menor. Por primera vez, se ha encontrado un estado de borde electrónico que está causado por las correlaciones electrónicas características de la red kagome.

En $EuCd_2As_2$, he encotrado una reconstrucción 2×1 de la superficie, así como la red hexagonal esperada a partir de la estructura de la red. Encontré defectos sobre la superficie, los cuales provocan deformaciones significativas en las imágenes de topografía. Lejos de los defectos, las curvas de conductancia se corresponden con la estructura de bandas calculada para la configuración AFM de tipo A. Sin embargo, las medidas de espectroscopia en los defectos y alrededor de ellos muestran un comportamiento diferente que pude describir utilizando la cuantización de un pozo cuántico 1D. Con la presencia de un campo magnético, se observa un comportamiento más rico debido a la cuantización de Landau.

En FeSe, la estructura de bandas se puede reproducir utilizando el análisis QPI, encontrando dos bandas de huecos y una de electrones. También he contrado un estado localizado en los defectos alrededor de 10 mV. Este estado conduce a la formación de un anillo alrededor del defecto debido a la influencia de la punta. Este tipo de anillos de carga se han medido antes en materiales semiconductores debido a la ausencia de apantallamiento. En primer lugar, debido a la presencia de defectos, la banda de electrones se desplaza por encima del nivel de Fermi, apareciendo entonces el estado localizado. La nematicidad y ortogonalidad de las bandas conducen a que la dispersión dependa del carácter orbital de las bandas, lo que da lugar a un gap efectivo que induce la aparición de dicho estado. La baja densidad de estados no puede apantallar la carga y la punta induce los efectos de carga y descarga.

Publications

M. Fernández-Lomana, B. Wu, F. Martín-Vega, **R. Sánchez-Barquilla**, R. Álvarez-Montoya, J.M. Castilla, J. Navarrete, J.R. Marijuán, E. Herrera, H. Suderow and I. Guillamón, *Millikelvin scanning tunneling microscope at 20/22 T with a graphite enabled stick-slip approach and an energy resolution below 8 μeV: Application to conductance quantization at 20 T in single atom point contacts of Al and Au and to the charge density wave of 2H-$NbSe_2$*, Review of Scientific Instruments **92**, 093701 (2021).

F. Martín-Vega, V. Barrena, **R. Sánchez-Barquilla**, M. Fernández-Lomana, J.Benito-Llorens, B. Wu, A. Fente, D. Perconte-Duplain, I. Horcas, R. López, J. Blanco, J.A. Higuera, S. Mañas-Valero, N.H. Jo, J. Schmidt, P. C. Canfield, G. Rubio-Bollinger, J.G. Rodrigo, E. Herrera, I. Guillamón and H. Suderow, *Simplified feedback control system for scanning tunneling microscopy*, Review of Scientific Instruments **92**, 103705 (2021).

R. Sánchez-Barquilla, E. Herrera, B. Wu, L.L. Wang, S. L Bud'ko, P.C. Canfield, H. Suderow and I. Guillamón. *End states in one dimensional atomic chains on a kagome lattice.* In preparation.

R. Sánchez-Barquilla, F. Martín Vega, B. Wu, P. García-Talavera, E. Herrera, S. Bud'ko, P. C. Canfield, H. Suderow and I. Guillamón. *Absence of screening in orbital selective superconductor FeSe.* In preparation

R. Sánchez-Barquilla, A. Valadkhani, E. Herrera, B. Kuthanazhi, S. Bud'ko, P. C. Canfield, H. Suderow and I. Guillamón, Linlin Wang, Roser Valenti. *Spatial and Landau quantization of localized states in the magnetic Weyl semimetal $EuCd_2As_2$*,

R. Sánchez-Barquilla, Francisco Martín Vega, Beilun Wu, Masayuki Ochi, Ryotaro Arita, Sergey Bud'ko, Paul C. Canfield, I. Guillamón and H. Suderow. *Landau quantization in the topological semimetal* WTe_2. In preparation

R. Sánchez-Barquilla, E. Herrera, V. Barrena, F. Mompeán, M. García-Hernández, I. Guillamón, H. Suderow and J. J. Palacios. *Surface states of nonsymmorphic* $PdSb_2$ In preparation

B. Wu, M. Fernández-Lomana, **R. Sánchez-Barquilla**, J. J. Palacios, H. Suderow and I. Guillamón. *Electronic backscattering induced by a magnetic field in atomic size contacts.* In preparation

Bibliography

[1] N. W. Achbroft and N. D. Marmin, Solid State Physics (Thomson, 1976).

[2] H. Ibach and H. Lüth, Solid-States Physics. (Springer, 2009).

[3] C. Kittel, Introduction to Solid State Physics (Wiley, 1997).

[4] J. M. Ziman, Principles of the theory of solids (Cambridge University Press, 1999).

[5] N. F. Mott, “Metal-Insulator Transition”, Rev. Mod. Phys. **40**, 677–683 (1968).

[6] G. Kotliar and D. Vollhardt, “Strongly Correlated Materials: Insights From Dynamical Mean-Field Theory”, Physics Today **57**, 53–59 (2004).

[7] W. Schottky, “Zur Halbleitertheorie der Sperrschicht und Spitzengleichrichter”, Zeitschrift für Physik **113**, 367–414 (1939).

[8] W. Schottky, “Halbleitertheorie der sperrschicht”, Naturwissenschaften **26**, 843–843 (1938).

[9] N. F. Mott and R. H. Fowler, “The collision between two electrons”, Proceedings of the Royal Society of London. Series A, Containing Papers of a Mathematical and Physical Character **126**, 259–267 (1930).

[10] N. F. Mott, “Note on the contact between a metal and an insulator or semi-conductor”, Mathematical Proceedings of the Cambridge Philosophical Society **34**, 568–572 (1938).

[11] Z. Zhang and J. T. J. Yates, “Band Bending in Semiconductors: Chemical and Physical Consequences at Surfaces and Interfaces”, Chemical Reviews **112**, Publisher: American Chemical Society, 5520–5551 (2012).

[12] V. W. Brar, R. Decker, H.-M. Solowan, Y. Wang, L. Maserati, K. T. Chan, H. Lee, a. O. Girit, A. Zettl, S. G. Louie, M. L. Cohen, and M. F. Crommie, “Gate-controlled ionization and screening of cobalt adatoms on a graphene surface”, Nature Physics **7**, 43–47 (2011).

[13] H. Li, S. Li, M. H. Naik, J. Xie, X. Li, E. Regan, D. Wang, W. Zhao, K. Yumigeta, M. Blei, T. Taniguchi, K. Watanabe, S. Tongay, A. Zettl, S. G.

Louie, M. F. Crommie, and F. Wang, “Imaging local discharge cascades for correlated electrons in WS_2/WSe_2 moiré superlattices”, Nature Physics **17**, 1114–1119 (2021).

[14]G. D. Nguyen, L. Liang, Q. Zou, M. Fu, A. D. Oyedele, B. G. Sumpter, Z. Liu, Z. Gai, K. Xiao, and A.-P. Li, “3D Imaging and Manipulation of Subsurface Selenium Vacancies in $PdSe_2$”, Phys. Rev. Lett. **121**, 086101 (2018).

[15]F. Marczinowski, J. Wiebe, F. Meier, K. Hashimoto, and R. Wiesendanger, “Effect of charge manipulation on scanning tunneling spectra of single Mn acceptors in InAs”, Phys. Rev. B **77**, 115318 (2008).

[16]C. Song, Y. Jiang, Y. Wang, Z. Li, L. Wang, K. He, X. Chen, X. Ma, and Q. Xue, “Gating the charge state of single Fe dopants in the topological insulator Bi_2Se_3 with a scanning tunneling microscope”, Phys. Rev. B **86**, 045441 (2012).

[17]K. Teichmann, M. Wenderoth, S. Loth, R. G. Ulbrich, J. K. Garleff, A. P. Wijnheijmer, and P. M. Koenraad, “Controlled Charge Switching on a Single Donor with a Scanning Tunneling Microscope”, Phys. Rev. Lett. **101**, 076103 (2008).

[18]K. v. Klitzing, G. Dorda, and M. Pepper, “New method for high-accuracy determination of the fine-structure constant based on quantized hall resistance”, Phys. Rev. Lett. **45**, 494–497 (1980).

[19]K. von Klitzing, The novel prize in physics, `https://www.nobelprize.org/prizes/physics/1985/klitzing/facts/ç`, 1985.

[20]B. A. Bernevig, T. L. Hughes, and S. Zhang, “Quantum Spin Hall Effect and Topological Phase Transition in HgTe Quantum Wells”, Science **314**, 1757–1761 (2006).

[21]A. Black-Schaffer, Topological superconductivity, `https://nanocohybri.eu/wp-content/uploads/2019/01/Black_Schaffer.pdf`, 2018.

[22]J. Xiao and B. Yan, “First-principles calculations for topological quantum materials”, Nature Reviews Physics **3**, 283–297 (2021).

[23]P. Narang, C. A. C. Garcia, and C. Felser, “The topology of electronic band structures”, Nature Materials **20**, 293–300 (2021).

[24]Y. Xia, D. Qian, D. Hsieh, L. Wray, A. Pal, H. Lin, A. Bansil, D. Grauer, Y. S. Hor, R. J. Cava, and M. Z. Hasan, “Observation of a large-gap

topological-insulator class with a single Dirac cone on the surface", Nature Physics **5**, 398–402 (2009).

[25]F. Nakamura, Y. Kousa, A. A. Taskin, Y. Takeichi, A. Nishide, A. Kakizaki, M. D'Angelo, P. Lefevre, F. Bertran, A. Taleb-Ibrahimi, F. Komori, S. Kimura, H. Kondo, Y. Ando, and I. Matsuda, "Topological transition in $\mathrm{bi}_{1--x}\mathrm{sb}_x$ studied as a function of Sb doping", Phys. Rev. B **84**, 235308 (2011).

[26]Y. Tanaka, T. Shoman, K. Nakayama, S. Souma, T. Sato, T. Takahashi, M. Novak, K. Segawa, and Y. Ando, "Two types of Dirac-cone surface states on the (111) surface of the topological crystalline insulator SnTe", Phys. Rev. B **88**, 235126 (2013).

[27]Y. Tanaka, Z. Ren, T. Sato, K. Nakayama, S. Souma, T. Takahashi, K. Segawa, and Y. Ando, "Experimental realization of a topological crystalline insulator in SnTe", Nature Physics **8**, 800–803 (2012).

[28]A. Bansil, H. Lin, and T. Das, "Colloquium: Topological band theory", Rev. Mod. Phys. **88**, 021004 (2016).

[29]D. Shin, S. A. Sato, H. Hübener, U. D. Giovannini, J. Kim, N. Park, and A. Rubio, "Unraveling materials berry curvature and chern numbers from real-time evolution of bloch states", Proceedings of the National Academy of Sciences **116**, 4135–4140 (2019).

[30]J.-Z. Ma, S. M. Nie, C. J. Yi, J. Jandke, T. Shang, M. Y. Yao, M. Naamneh, L. Q. Yan, Y. Sun, A. Chikina, V. N. Strocov, M. Medarde, M. Song, Y.-M. Xiong, G. Xu, W. Wulfhekel, J. Mesot, M. Reticcioli, C. Franchini, C. Mudry, M. Müller, Y. G. Shi, T. Qian, H. Ding, and M. Shi, "Spin fluctuation induced Weyl semimetal state in the paramagnetic phase of $\mathrm{EuCd_2As_2}$", Science Advances **5**, eaaw4718 (2019).

[31]H. Weng, C. Fang, Z. Fang, B. A. Bernevig, and X. Dai, "Weyl SemimetalPhase in Noncentrosymmetric Transition-Metal Monophosphides", Phys. Rev. X **5**, 011029 (2015).

[32]S. Huang, S. Xu, I. Belopolski, C. Lee, G. Chang, B. Wang, N. Alidoust, G. Bian, M. Neupane, C. Zhang, S. Jia, A. Bansil, H. Lin, and M. Z. Hasan, "A Weyl Fermion semimetal with surface Fermi arcs in the transition metal monopnictide TaAs class", Nature Communications **6**, 7373 (2015).

[33]S. Xu, I. Belopolski, N. Alidoust, M. Neupane, G. Bian, C. Zhang, R. Sankar, G. Chang, Z. Yuan, C. Lee, S. Huang, H. Zheng, J. Ma, D. S.

Sanchez, B. Wang, A. Bansil, F. Chou, P. P. Shibayev, H. Lin, S. Jia, and M. Z. Hasan, "Discovery of a Weyl fermion semimetal and topological Fermi arcs", Science **349**, 613–617 (2015).

[34] B. Q. Lv, H. M. Weng, B. B. Fu, X. P. Wang, H. Miao, J. Ma, P. Richard, X. C. Huang, L. X. Zhao, G. F. Chen, Z. Fang, X. Dai, T. Qian, and H. Ding, "Experimental Discovery of Weyl Semimetal TaAs", Phys. Rev. X **5**, 031013 (2015).

[35] L. Huang, T. M. McCormick, M. Ochi, Z. Zhao, M.-T. Suzuki, R. Arita, Y. Wu, D. Mou, H. Cao, J. Yan, N. Trivedi, and A. Kaminski, "Spectroscopic evidence for a type-II Weyl semimetallic state in $MoTe_2$", Nature Materials **15**, 1155–1160 (2016).

[36] K. Deng, G. Wan, P. Deng, K. Zhang, S. Ding, E. Wang, M. Yan, H. Huang, H. Zhang, Z. Xu, J. Denlinger, A. Fedorov, H. Yang, W. Duan, H. Yao, Y. Wu, S. Fan, H. Zhang, X. Chen, and S. Zhou, "Experimental observation of topological Fermi arcs in type-II Weyl semimetal $MoTe_2$", Nature Physics **12**, 1105–1110 (2016).

[37] J. Jiang, Z. Liu, Y. Sun, H. Yang, C. Rajamathi, Y. Qi, L. Yang, C. Chen, H. Peng, C. Hwang, S. Sun, S.-K. Mo, I. Vobornik, J. Fujii, S. Parkin, C. Felser, B. Yan, and Y. Chen, "Signature of type-II Weyl semimetal phase in $MoTe_2$", Nature Communications **8**, 13973 (2017).

[38] S. Borisenko, D. Evtushinsky, Q. Gibson, A. Yaresko, K. Koepernik, T. Kim, M. Ali, J. van den Brink, M. Hoesch, A. Fedorov, E. Haubold, Y. Kushnirenko, I. Soldatov, R. Schäfer, and R. J. Cava, "Time-reversal symmetry breaking type-II Weyl state in $YbMnBi_2$", Nature Communications **10**, 3424 (2019).

[39] S. Xu, N. Alidoust, G. Chang, H. Lu, B. Singh, I. Belopolski, D. S. Sanchez, X. Zhang, G. Bian, H. Zheng, M. Husanu, Y. Bian, S.-M. Huang, C. Hsu, T. Chang, H. Jeng, A. Bansil, T. Neupert, V. N. Strocov, H. Lin, S. Jia, and M. Z. Hasan, "Discovery of Lorentz-violating type II Weyl fermions in LaAlGe", Science Advances **3**, e1603266 (2017).

[40] H. Yi, Z. Wang, C. Chen, Y. Shi, Y. Feng, A. Liang, Z. Xie, S. He, J. He, Y. Peng, X. Liu, Y. Liu, L. Zhao, G. Liu, X. Dong, J. Zhang, M. Nakatake, M. Arita, K. Shimada, H. Namatame, M. Taniguchi, Z. Xu, C. Chen, X. Dai, Z. Fang, and X. J. Zhou, "Evidence of Topological Surface State in Three-Dimensional Dirac Semimetal Cd_3As_2", Scientific Reports **4**, 6106 (2014).

[41]Y. Wu, D. Mou, N. H. Jo, K. Sun, L. Huang, S. L. Bud'ko, P. C. Canfield, and A. Kaminski, "Observation of Fermi arcs in the type-II Weyl semimetal candidate WTe_2", Phys. Rev. B **94**, 121113 (2016).

[42]B. Schrunk, Y. Kushnirenko, B. Kuthanazhi, J. Ahn, L.-L. Wang, E. O'Leary, K. Lee, A. Eaton, A. Fedorov, R. Lou, V. Voroshnin, O. J. Clark, J. Sánchez-Barriga, S. L. Bud'ko, R.-J. Slager, P. C. Canfield, and A. Kaminski, "Emergence of Fermi arcs due to magnetic splitting in an antiferromagnet", Nature **603**, 610–615 (2022).

[43]P. Deng, Z. Xu, K. Deng, K. Zhang, Y. Wu, H. Zhang, S. Zhou, and X. Chen, "Revealing Fermi arcs and Weyl nodes in $MoTe_2$ by quasiparticle interference mapping", Phys. Rev. B **95**, 245110 (2017).

[44]N. Morali, R. Batabyal, P. K. Nag, E. Liu, Q. Xu, Y. Sun, B. Yan, C. Felser, N. Avraham, and H. Beidenkopf, "Fermi-arc diversity on surface terminations of the magnetic Weyl semimetal $Co_3Sn_2S_2$", Science **365**, 1286–1291 (2019).

[45]A. A. Soluyanov, D. Gresch, Z. Wang, Q. Wu, M. Troyer, X. Dai, and B. A. Bernevig, "Type-II Weyl semimetals", Nature **527**, 495–498 (2015).

[46]V. V. Schmidt, The Physics of Superconductors (Springer, 1997).

[47]M. Tinkham, Introduction to superconductivity (McGraw-Hill, 1996).

[48]J. M. Annett, Superconductivity, superfluids and condensates (Oxford University Press, 2004).

[49]H. K. Onnes, "Further experiments with liquid helium on the change of-electrical resistance of pure metals at very low temperatures, etc. vi. on thesudden change in the rate at which the resistance of mercury disappears", Comm. Phys. Lab. Univ. Leiden (1911).

[50]H. K. Onnes, The novel prize in physics, `https://www.nobelprize.org/prizes/physics/1913/summary/`, 1913.

[51]L. Shubnikov, V. Khotkevich, Y. D. Shepelev, and Y. N. Ryabinin, "Magnetic properties of superconducting metals and alloys", Zh. Eksp. Teor. Fiz **7**, 221 (1937).

[52]L. N. Cooper, "Bound Electron Pairs in a Degenerate Fermi Gas", Phys. Rev. **104**, 1189–1190 (1956).

[53]H. Suhl, B. T. Matthias, and L. R. Walker, "Bardeen-Cooper-Schrieffer Theory of Superconductivity in the Case of Overlapping Bands", Phys. Rev. Lett. **3**, 552–554 (1959).

[54]H. J. Choi, D. Roundy, H. Sun, M. L. Cohen, and S. G. Louie, “The origin of the anomalous superconducting properties of MgB_2”, Nature **418**, 758–760 (2002).

[55]S. L. Bud’ko, G. Lapertot, C. Petrovic, C. E. Cunningham, N. Anderson, and P. C. Canfield, “Boron Isotope Effect in Superconducting MgB_2”, Phys. Rev. Lett. **86**, 1877–1880 (2001).

[56]G. Rubio-Bollinger, H. Suderow, and S. Vieira, “Tunneling Spectroscopy in Small Grains of Superconducting MgB_2”, Phys. Rev. Lett. **86**, 5582–5584 (2001).

[57]P. Martinez-Samper, J. Rodrigo, G. Rubio-Bollinger, H. Suderow, S. Vieira, S. Lee, and S. Tajima, “Scanning tunneling spectroscopy in MgB_2”, Physica C: Superconductivity **385**, 233–243 (2003).

[58]K. A. Brueckner, T. Soda, P. W. Anderson, and P. Morel, “Level structure of nuclear matter and liquid He^3”, Phys. Rev. **118**, 1442–1446 (1960).

[59]V. J. Emery and A. M. Sessler, “Possible Phase Transition in Liquid He^3”, Phys. Rev. **119**, 43–49 (1960).

[60]P. W. Anderson and P. Morel, “Generalized Bardeen-Cooper-Schrieffer States and the Proposed Low-Temperature Phase of Liquid He^3”, Phys. Rev. **123**, 1911–1934 (1961).

[61]W. Kohn and J. M. Luttinger, “New mechanism for superconductivity”, Phys. Rev. Lett. **15**, 524–526 (1965).

[62]D. Scalapino, “The case for $d_{x^2-y^2}$ pairing in the cuprate superconductors”, Physics Reports **250**, 329–365 (1995).

[63]C. C. Tsuei and J. R. Kirtley, “Pairing symmetry in cuprate superconductors”, Rev. Mod. Phys. **72**, 969–1016 (2000).

[64]T. Wehling, A. Black-Schaffer, and A. Balatsky, “Dirac materials”, Advances in Physics **63**, 1–76 (2014).

[65]J. G. Bednorz and K. A. Müller, “Possible highTc superconductivity in the Ba-La-Cu-O system”, Zeitschrift für Physik B Condensed Matter **64**, 189–193 (1986).

[66]A. Schilling, M. Cantoni, J. D. Guo, and H. R. Ott, “Superconductivity above 130 K in the Hg-Ba-Ca-Cu-O system”, Nature **363**, 56–58 (1993).

[67]Y. Kamihara, H. Hiramatsu, M. Hirano, R. Kawamura, H. Yanagi, T. Kamiya, and H. Hosono, “Iron-Based Layered Superconductor: LaOFeP”, Journal of the American Chemical Society **128**, 10012–10013 (2006).

[68]Y. Kamihara, T. Watanabe, M. Hirano, and H. Hosono, “Iron-based layered superconductor La $[O_{1-x}\ F_x]$ FeAs (x= 0.05- 0.12) with T_c= 26 K”, Journal of the American Chemical Society **130**, 3296–3297 (2008).

[69]R. Zhi-An, L. Wei, Y. Jie, Y. Wei, S. Xiao-Li, Zheng-Cai, C. Guang-Can, D. Xiao-Li, S. Li-Ling, Z. Fang, and Z. Zhong-Xian, “Superconductivity at 55 K in iron-based f-doped layered quaternary compound $Sm[o_{1-x}f_x]$feas”, Chinese Physics Letters **25**, 2215 (2008).

[70]X. Wang, Q. Liu, Y. Lv, W. Gao, L. Yang, R. Yu, F. Li, and C. Jin, “The superconductivity at 18 K in LiFeAs system”, Solid State Communications **148**, 538–540 (2008).

[71]M. M. Altarawneh, K. Collar, C. H. Mielke, N. Ni, S. L. Bud’ko, and P. C. Canfield, “Determination of anisotropic H_{c2} up to 60 T in $Ba_{0.55}K_{0.45}Fe_2As_2$ single crystals”, Phys. Rev. B **78**, 220505 (2008).

[72]J. Paglione and R. L. Greene, “High-temperature superconductivity in iron-based materials”, Nature Physics **6**, 645–658 (2010).

[73]A. Chubukov and P. J. Hirschfeld, “Iron-based superconductors, seven years later”, Physics Today **68**, 46–52 (2015).

[74]F. Hsu, J. Luo, K. Yeh, T. Chen, T. Huang, P. M. Wu, Y. Lee, Y. Huang, Y. Chu, D. Yan, and M. Wu, “Superconductivity in the PbO-type structure α-FeSe”, Proceedings of the National Academy of Sciences **105**, 14262–14264 (2008).

[75]X. Lai, H. Zhang, Y. Wang, X. Wang, X. Zhang, J. Lin, and F. Huang, “Observation of Superconductivity in Tetragonal FeS”, Journal of the American Chemical Society **137**, 10148–10151 (2015).

[76]Z. Deng, X. C. Wang, Q. Q. Liu, S. J. Zhang, Y. X. Lv, J. L. Zhu, R. C. Yu, and C. Q. Jin, “A new “111” type iron pnictide superconductor LiFeP”, EPL (Europhysics Letters) **87**, 37004 (2009).

[77]X. Wang, Q. Liu, Y. Lv, W. Gao, L. Yang, R. Yu, F. Li, and C. Jin, “The superconductivity at 18 K in LiFeAs system”, Solid State Communications **148**, 538–540 (2008).

[78] J. J. Hamlin, R. E. Baumbach, D. A. Zocco, T. A. Sayles, and M. B. Maple, “Superconductivity in single crystals of LaFePO”, Journal of Physics: Condensed Matter **20**, 365220 (2008).

[79] M. Rotter, M. Pangerl, M. Tegel, and D. Johrendt, “Superconductivity and crystal structures of $(Ba_{1-x}K_x)Fe_2As_2$”, Angewandte Chemie International Edition **47**, 7949–7952 (2008).

[80] W. R. Meier, T. Kong, U. S. Kaluarachchi, V. Taufour, N. H. Jo, G. Drachuck, A. E. Böhmer, S. M. Saunders, A. Sapkota, A. Kreyssig, M. A. Tanatar, R. Prozorov, A. I. Goldman, F. F. Balakirev, A. Gurevich, S. L. Bud’ko, and P. C. Canfield, “Anisotropic thermodynamic and transport properties of single-crystalline $CaKFe_4As_4$”, Phys. Rev. B **94**, 064501 (2016).

[81] P. Zhang, Z. Wang, X. Wu, K. Yaji, Y. Ishida, Y. Kohama, G. Dai, Y. Sun, C. Bareille, K. Kuroda, T. Kondo, K. Okazaki, K. Kindo, X. Wang, C. Jin, J. Hu, R. Thomale, K. Sumida, S. Wu, K. Miyamoto, T. Okuda, H. Ding, G. D. Gu, T. Tamegai, T. Kawakami, M. Sato, and S. Shin, “Multiple topological states in iron-based superconductors”, Nature Physics **15**, 41–47 (2019).

[82] P. Zhang, K. Yaji, T. Hashimoto, Y. Ota, T. Kondo, K. Okazaki, Z. Wang, J. Wen, G. D. Gu, H. Ding, and S. Shin, “Observation of topological superconductivity on the surface of an iron-based superconductor”, Science **360**, 182–186 (2018).

[83] P. J. Hirschfeld, M. M. Korshunov, and I. I. Mazin, “Gap symmetry and structure of Fe-based superconductors”, Reports on Progress in Physics **74**, 124508 (2011).

[84] A. Chubukov, “Pairing mechanism in fe-based superconductors”, Annual Review of Condensed Matter Physics **3**, 57–92 (2012).

[85] I. I. Mazin, D. J. Singh, M. D. Johannes, and M. H. Du, “Unconventional superconductivity with a sign reversal in the order parameter of $LaFeAsO_{1-x}F_x$”, Phys. Rev. Lett. **101**, 057003 (2008).

[86] R. M. Fernandes, A. V. Chubukov, and J. Schmalian, “What drives nematic order in iron-based superconductors?”, Nature Physics **10**, 97–104 (2014).

[87] A. E. Böhmer, F. Hardy, F. Eilers, D. Ernst, P. Adelmann, P. Schweiss, T. Wolf, and C. Meingast, “Lack of coupling between superconductivity

and orthorhombic distortion in stoichiometric single-crystalline FeSe", Phys. Rev. B **87**, 180505 (2013).

[88] C. Meingast, F. Hardy, R. Heid, P. Adelmann, A. Böhmer, P. Burger, D. Ernst, R. Fromknecht, P. Schweiss, and T. Wolf, "Thermal expansion and grüneisen parameters of $(BaFe_{1-x}Co_x)_2As_2$: a thermodynamic quest for quantum criticality", Phys. Rev. Lett. **108**, 177004 (2012).

[89] G. Binnig, H. Rohrer, C. Gerber, and E. Weibel, "Tunneling through a controllable vacuum gap", Applied Physics Letters **40**, 178–180 (1982).

[90] G. Binning and H. Rohrer, The novel prize in physics, `https://www.nobelprize.org/prizes/physics/1986/summary/`, 1986.

[91] F. Martín-Vega, "Visualization of quasiparticles in quantum materials at high magnetic fields", PdH Thesis (Universidad Autónoma de Madrid, Madrid, Spain, 2021).

[92] M. Fernández-Lomana, B. Wu, F. Martín-Vega, R. Sánchez-Barquilla, R. Álvarez-Montoya, J. M. Castilla, J. Navarrete, J. R. Marijuan, E. Herrera, H. Suderow, and I. Guillamón, "Milikelvin scanning tunneling microscope at 20/22 T with a graphite enabled stick-slip approach and an energy resolution 8 μev: Application to conductance quantization at 20 T in single atom point contacts of Al and Au and to the charge density wave of 2H–$NbSe_2$", Review of Scientific Instruments **92**, 093701 (2021).

[93] B. Voigtländer, Scanning probe microscopy (Springer, 2015).

[94] J. Bardeen, "Tunnelling from a many-particle point of view", Phys. Rev. Lett. **6**, 57–59 (1961).

[95] J. Tersoff and D. R. Hamann, "Theory and application for the Scanning Tunneling Microscope", Phys. Rev. Lett. **50**, 1998–2001 (1983).

[96] J. Tersoff and D. R. Hamann, "Theory of the Scanning Tunneling Microscope", Phys. Rev. B **31**, 805–813 (1985).

[97] C. J. Chen, "Electromechanical deflections of piezoelectric tubes with quartered electrodes", Applied Physics Letters **60**, 132–134 (1992).

[98] EBL. Piezoelectric Precision, `https://eblproducts.com/`.

[99] SEGAINVEX, `https://www.uam.es/uam/segainvex`.

[100] H Suderow, I Guillamón, J. G. Rodrigo, and S Vieira, "Imaging superconducting vortex cores and lattices with a scanning tunneling microscope", Superconductor Science and Technology **27**, 063001 (2014).

[101] J. G. Rodrigo, H. Suderow, and S. Vieira, “On the use of STM superconducting tips at very low temperatures”, The European Physical Journal B - Condensed Matter and Complex Systems **40**, 483–488 (2004).

[102] A. L. Yeyati, A. Martín-Rodero, and F. Flores, “Conductance quantization and electron resonances in sharp tips and atomic-size contacts”, Phys. Rev. B **56**, 10369–10372 (1997).

[103] H. Suderow, I. Guillamon, and S. Vieira, “Compact very low temperature scanning tunneling microscope with mechanically driven horizontal linear positioning stage”, Review of Scientific Instruments **82**, 033711 (2011).

[104] F. Martín-Vega, V. Barrena, R. Sánchez-Barquilla, M. Fernández-Lomana, J. Benito Llorens, B. Wu, A. Fente, D. Perconte Duplain, I. Horcas, R. López, J. Blanco, J. A. Higuera, S. Mañas-Valero, N. H. Jo, J. Schmidt, P. C. Canfield, G. Rubio-Bollinger, J. G. Rodrigo, E. Herrera, I. Guillamón, and H. Suderow, “Simplified feedback control system for scanning tunneling microscopy”, Review of Scientific Instruments **92**, 103705 (2021).

[105] L. Petersen, P. T. Sprunger, P. Hofmann, E. Lægsgaard, B. G. Briner, M. Doering, H. Rust, A. M. Bradshaw, F. Besenbacher, and E. W. Plummer, “Direct imaging of the two-dimensional Fermi contour: Fourier-transform STM”, Phys. Rev. B **57**, 6858–6861 (1998).

[106] S. Kourtis, J. Li, Z. Wang, A. Yazdani, and B. A. Bernevig, “Universal signatures of Fermi arcs in quasiparticle interference on the surface of Weyl semimetals”, Phys. Rev. B **93**, 041109 (2016).

[107] M. N. Ali, J. Xiong, S. Flynn, J. Tao, Q. D. Gibson, L. M. Schoop, T. Liang, N. Haldolaarachchige, M. Hirschberger, N. P. Ong, and R. J. Cava, “Large, non-saturating magnetoresistance in WTe_2”, Nature **514**, 205–208 (2014).

[108] Y. Song, Z. Jia, D. Zhang, X. Zhu, Z. Shi, H. Wang, L. Zhu, Q. Yuan, H. Zhang, D. Xing, and S. Li, “Observation of coulomb gap in the quantum spin hall candidate single-layer $1T'$-WTe_2”, Nature Communications **9**, 4071 (2018).

[109] S. Tang, C. Zhang, D. Wong, Z. Pedramrazi, H. Tsai, C. Jia, B. Moritz, M. Claassen, H. Ryu, S. Kahn, J. Jiang, H. Yan, M. Hashimoto, D. Lu, R. G. Moore, C. Hwang, C. Hwang, Z. Hussain, Y. Chen, M. M. Ugeda, Z. Liu, X. Xie, T. P. Devereaux, M. F. Crommie, S. Mo, and Z. Shen, “Quantum spin hall state in monolayer $1T'$-WTe_2”, Nature Physics **13**, 683–687 (2017).

[110] Z. Jia, Y. Song, X.-B. Li, K. Ran, P. Lu, H.-J. Zheng, X. Zhu, Z. Shi, J. Sun, J. Wen, D. Xing, and S. Li, "Direct visualization of a two-dimensional topological insulator in the single-layer 1T′-WTe_2", Phys. Rev. B **96**, 041108 (2017).

[111] Z. Fei, T. Palomaki, S. Wu, W. Zhao, X. Cai, B. Sun, P. Nguyen, J. Finney, X. Xu, and D. H. Cobden, "Edge conduction in monolayer WTe_2", Nature Physics **13**, 677–682 (2017).

[112] S. Wu, V. Fatemi, Q. D. Gibson, K. Watanabe, T. Taniguchi, R. J. Cava, and P. Jarillo-Herrero, "Observation of the quantum spin Hall effect up to 100 kelvin in a monolayer crystal", Science **359**, 76–79 (2018).

[113] T. Liang, Q. Gibson, M. N. Ali, M. Liu, R. J. Cava, and N. P. Ong, "Ultrahigh mobility and giant magnetoresistance in the Dirac semimetal Cd_3As_2", Nature Materials **14**, 280–284 (2015).

[114] Z. K. Liu, B. Zhou, Y. Zhang, Z. J. Wang, H. M. Weng, D. Prabhakaran, S. K. Mo, Z. X. Shen, Z. Fang, X. Dai, Z. Hussain, and Y. L. Chen, "Discovery of a Three-Dimensional Topological Dirac Semimetal, Na_3Bi", Science **343**, 864–867 (2014).

[115] C. Shekhar, A. K. Nayak, Y. Sun, M. Schmidt, M. Nicklas, I. Leermakers, U. Zeitler, Y. Skourski, J. Wosnitza, Z. Liu, Y. Chen, W. Schnelle, H. Borrmann, Y. Grin, C. Felser, and B. Yan, "Extremely large magnetoresistance and ultrahigh mobility in the topological Weyl semimetal candidate NbP", Nature Physics **11**, 645–649 (2015).

[116] N. J. Ghimire, Y. Luo, M Neupane, D. J. Williams, E. D. Bauer, and F Ronning, "Magnetotransport of single crystalline NbAs", Journal of Physics: Condensed Matter **27**, 152201 (2015).

[117] X. Huang, L. Zhao, Y. Long, P. Wang, D. Chen, Z. Yang, H. Liang, M. Xue, H. Weng, Z. Fang, X. Dai, and G. Chen, "Observation of the Chiral-Anomaly-Induced Negative Magnetoresistance in 3D Weyl Semimetal TaAs", Phys. Rev. X **5**, 031023 (2015).

[118] H. Weyl, "Elektron und Gravitation. I", Zeitschrift für Physik **56**, 330–352 (1929).

[119] Y. Wu, N. H. Jo, D. Mou, L. Huang, S. L. Bud'ko, P. C. Canfield, and A. Kaminski, "Three-dimensionality of the bulk electronic structure in WTe_2", Phys. Rev. B **95**, 195138 (2017).

[120]N. H. Jo, L. Wang, P. P. Orth, S. L. Bud'ko, and P. C. Canfield, "Magnetoelastoresistance in WTe_2: Exploring electronic structure and extremely large magnetoresistance under strain", Proceedings of the National Academy of Sciences **116**, 25524–25529 (2019).

[121]Z. Zhu, X. Lin, J. Liu, B. Fauqué, Q. Tao, C. Yang, Y. Shi, and K. Behnia, "Quantum Oscillations, Thermoelectric Coefficients, and the Fermi Surface of Semimetallic WTe_2", Phys. Rev. Lett. **114**, 176601 (2015).

[122]F. Y. Bruno, A. Tamai, Q. S. Wu, I. Cucchi, C. Barreteau, A. de la Torre, S. McKeown Walker, S. Riccò, Z. Wang, T. K. Kim, M. Hoesch, M. Shi, N. C. Plumb, E. Giannini, A. A. Soluyanov, and F. Baumberger, "Observation of large topologically trivial Fermi arcs in the candidate type-II Weyl semimetal WTe_2", Phys. Rev. B **94**, 121112 (2016).

[123]C. Wang, Y. Zhang, J. Huang, S. Nie, G. Liu, A. Liang, Y. Zhang, B. Shen, J. Liu, C. Hu, Y. Ding, D. Liu, Y. Hu, S. He, L. Zhao, L. Yu, J. Hu, J. Wei, Z. Mao, Y. Shi, X. Jia, F. Zhang, S. Zhang, F. Yang, Z. Wang, Q. Peng, H. Weng, X. Dai, Z. Fang, Z. Xu, C. Chen, and X. J. Zhou, "Observation of Fermi arc and its connection with bulk states in the candidate type-II Weyl semimetal WTe_2", Phys. Rev. B **94**, 241119 (2016).

[124]C. Lin, R. Arafune, R. Liu, M. Yoshimura, B. Feng, K. Kawahara, Z. Ni, E. Minamitani, S. Watanabe, Y. Shi, M. Kawai, T.-C. Chiang, I. Matsuda, and N. Takagi, "Visualizing Type-II Weyl Points in Tungsten Ditelluride by Quasiparticle Interference", ACS Nano **11**, Publisher: American Chemical Society, 11459–11465 (2017).

[125]W. Zhang, Q. Wu, L. Zhang, S. Cheong, A. A. Soluyanov, and W. Wu, "Quasiparticle interference of surface states in the type-II Weyl semimetal WTe_2", Phys. Rev. B **96**, 165125 (2017).

[126]Y. Yuan, X. Yang, L. Peng, Z. Wang, J. Li, C. Yi, J. Xian, Y. Shi, and Y. Fu, "Quasiparticle interference of Fermi arc states in the type-II Weyl semimetal candidate WTe_2", Phys. Rev. B **97**, 165435 (2018).

[127]P. Cheng, C. Song, T. Zhang, Y. Zhang, Y. Wang, J. Jia, J. Wang, Y. Wang, B. Zhu, X. Chen, X. Ma, K. He, L. Wang, X. Dai, Z. Fang, X. Xie, X. Qi, C. Liu, S. Zhang, and Q. Xue, "Landau quantization of topological surface states in Bi_2Se_3", Phys. Rev. Lett. **105**, 076801 (2010).

[128]T. Matsui, H. Kambara, Y. Niimi, K. Tagami, M. Tsukada, and H. Fukuyama, "STS Observations of Landau Levels at Graphite Surfaces", Phys. Rev. Lett. **94**, 226403 (2005).

[129]P. K. Das, D. D. Sante, F Cilento, C Bigi, D Kopic, D Soranzio, A Sterzi, J. A. Krieger, I Vobornik, J Fujii, T Okuda, V. N. Strocov, M. B. H. Breese, F Parmigiani, G Rossi, S Picozzi, R Thomale, G Sangiovanni, R. J. Cava, and G Panaccione, "Electronic properties of candidate type-II Weyl semimetal WTe_2. A review perspective.", Electronic Structure **1**, 014003 (2019).

[130]P. C. Canfield and Z. Fisk, "Growth of single crystals from metallic fluxes", Philosophical Magazine B **65**, 1117–1123 (1992).

[131]Y. Wu, N. H. Jo, M. Ochi, L. Huang, D. Mou, S. L. Bud'ko, P. C. Canfield, N. Trivedi, R. Arita, and A. Kaminski, "Temperature-induced lifshitz transition in WTe_2", Phys. Rev. Lett. **115**, 166602 (2015).

[132]L. Peng, Y. Yuan, G. Li, X. Yang, J. Xian, C. Yi, Y. Shi, and Y. Fu, "Observation of topological states residing at step edges of WTe_2", Nature Communications **8**, 659 (2017).

[133]A. Noah, F. Toric, T. D. Feld, G. Zissman, A. Gutfreund, D. Tsruya, T. R. Devidas, H. Alpern, A. Vakahi, H. Steinberg, M. E. Huber, J. G. Analytis, S. Gazit, E. Lachman, and Y. Anahory, "Tunable exchange bias in the magnetic weyl semimetal $Co_3Sn_2S_2$", Phys. Rev. B **105**, 144423 (2022).

[134]E. Liu, Y. Sun, N. Kumar, L. Muechler, A. Sun, L. Jiao, S. Yang, D. Liu, A. Liang, Q. Xu, J. Kroder, V. Süß, H. Borrmann, C. Shekhar, Z. Wang, C. Xi, W. Wang, W. Schnelle, S. Wirth, Y. Chen, S. T. B. Goennenwein, and C. Felser, "Giant anomalous Hall effect in a ferromagnetic kagome-lattice semimetal", Nature Physics **14**, 1125–1131 (2018).

[135]Q. Wang, Y. Xu, R. Lou, Z. Liu, M. Li, Y. Huang, D. Shen, H. Weng, S. Wang, and H. Lei, "Large intrinsic anomalous Hall effect in half-metallic ferromagnet $Co_3Sn_2S_2$ with magnetic Weyl fermions", Nature Communications **9**, 3681 (2018).

[136]D. F. Liu, A. J. Liang, E. K. Liu, Q. N. Xu, Y. W. Li, C. Chen, D. Pei, W. J. Shi, S. K. Mo, P. Dudin, T. Kim, C. Cacho, G. Li, Y. Sun, L. X. Yang, Z. K. Liu, S. S. P. Parkin, C. Felser, and Y. L. Chen, "Magnetic Weyl semimetal phase in a kagome crystal", Science **365**, 1282–1285 (2019).

[137]L. Ye, M. Kang, J. Liu, F. von Cube, C. R. Wicker, T. Suzuki, C. Jozwiak, A. Bostwick, E. Rotenberg, D. C. Bell, L. Fu, R. Comin, and J. G. Checkelsky, "Massive dirac fermions in a ferromagnetic kagome metal", Nature **555**, 638–642 (2018).

[138] A. Pham and P. Ganesh, "Quantum material topology via defect engineering", Phys. Rev. B **100**, 241110 (2019).

[139] R. Soto-Garrido, E. Muñoz, "Dislocation defect as a bulk probe of monopole charge of multi-Weyl semimetals", Phys. Rev. Res. **2**, 012043 (2020).

[140] R. Drost, T. Ojanen, A. Harju, and P. Liljeroth, "Topological states in engineered atomic lattices", Nature Physics **13**, 668–671 (2017).

[141] J. Yin, S. S. Zhang, G. Chang, Q. Wang, S. S. Tsirkin, Z. Guguchia, B. Lian, H. Zhou, K. Jiang, I. Belopolski, N. Shumiya, D. Multer, M. Litskevich, T. A. Cochran, H. Lin, Z. Wang, T. Neupert, S. Jia, H. Lei, and M. Z. Hasan, "Negative flat band magnetism in a spin-orbit-coupled correlated kagome magnet", Nature Physics **15**, 443–448 (2019).

[142] S. Y. Zhou, G. Gweon, J. Graf, A. V. Fedorov, C. D. Spataru, R. D. Diehl, Y. Kopelevich, D. Lee, S. G. Louie, and A. Lanzara, "First direct observation of dirac fermions in graphite", Nature Physics **2**, 595–599 (2006).

[143] A. H. Castro Neto, F. Guinea, N. M. R. Peres, K. S. Novoselov, and A. K. Geim, "The electronic properties of graphene", Rev. Mod. Phys. **81**, 109–162 (2009).

[144] B. Sutherland, "Localization of electronic wave functions due to local topology", Phys. Rev. B **34**, 5208–5211 (1986).

[145] N. R. Walet and F. Guinea, "Flat bands, strains, and charge distribution in twisted bilayer h−BN", Phys. Rev. B **103**, 125427 (2021).

[146] Y. Cao, V. Fatemi, S. Fang, K. Watanabe, T. Taniguchi, E. Kaxiras, and P. Jarillo-Herrero, "Unconventional superconductivity in magic-angle graphene superlattices", Nature **556**, 43–50 (2018).

[147] A Mielke, "Ferromagnetic ground states for the hubbard model on line graphs", Journal of Physics A: Mathematical and General **24**, L73 (1991).

[148] A Mielke, "Ferromagnetism in the hubbard model on line graphs and further considerations", Journal of Physics A: Mathematical and General **24**, 3311 (1991).

[149] A Mielke, "Exact ground states for the hubbard model on the kagome lattice", Journal of Physics A: Mathematical and General **25**, 4335 (1992).

[150] B. H. Bernhard, B Canals, and C Lacroix, "The hubbard model on the kagome lattice", Journal of Physics: Condensed Matter **19**, 145258 (2007).

[151] S. D. Huber and E. Altman, “Bose condensation in flat bands”, Phys. Rev. B **82**, 184502 (2010).

[152] H. Tasaki, “Ferromagnetism in the Hubbard models with degenerate single-electron ground states”, Phys. Rev. Lett. **69**, 1608–1611 (1992).

[153] K. Sun, Z. Gu, H. Katsura, and S. Das Sarma, “Nearly flatbands with nontrivial topology”, Phys. Rev. Lett. **106**, 236803 (2011).

[154] W. Jiang, M. Kang, H. Huang, H. Xu, T. Low, and F. Liu, “Topological band evolution between Lieb and kagome lattices”, Phys. Rev. B **99**, 125131 (2019).

[155] D. Leykam, A. Andreanov, and S. Flach, “Artificial flat band systems: from lattice models to experiments”, Advances in Physics: X **3**, 1473052 (2018).

[156] D. L. Bergman, C. Wu, and L. Balents, “Band touching from real-space topology in frustrated hopping models”, Phys. Rev. B **78**, 125104 (2008).

[157] T. Bilitewski and R. Moessner, “Disordered flat bands on the kagome lattice”, Phys. Rev. B **98**, 235109 (2018).

[158] H. Guo and M. Franz, “Topological insulator on the kagome lattice”, Phys. Rev. B **80**, 113102 (2009).

[159] A. Bolens and N. Nagaosa, “Topological states on the breathing kagome lattice”, Phys. Rev. B **99**, 165141 (2019).

[160] D. Sheng, Z. Gu, K. Sun, and L. Sheng, “Fractional quantum Hall effect in the absence of Landau levels”, Nature Communications **2**, 389 (2011).

[161] Y. Wang, Z. Gu, C. Gong, and D. N. Sheng, “Fractional Quantum Hall Effect of Hard-Core Bosons in Topological Flat Bands”, Phys. Rev. Lett. **107**, 146803 (2011).

[162] T. Neupert, L. Santos, C. Chamon, and C. Mudry, “Fractional Quantum Hall States at Zero Magnetic Field”, Phys. Rev. Lett. **106**, 236804 (2011).

[163] A. T. Rømer, S. Bhattacharyya, R. Valentí, M. H. Christensen, and B. M. Andersen, “Superconductivity from repulsive interactions on the kagome lattice”, Phys. Rev. B **106**, 174514 (2022).

[164] C. Wu, D. Bergman, L. Balents, and S. Das Sarma, “Flat Bands and Wigner Crystallization in the Honeycomb Optical Lattice”, Phys. Rev. Lett. **99**, 070401 (2007).

[165] M. Kang, S. Fang, L. Ye, H. C. Po, J. Denlinger, C. Jozwiak, A. Bostwick, E. Rotenberg, E. Kaxiras, J. G. Checkelsky, and R. Comin, “Topological

flat bands in frustrated kagome lattice CoSn", Nature Communications **11**, 4004 (2020).

[166]X. Lin, S. L. Bud'ko, and P. C. Canfield, "Development of viable solutions for the synthesis of sulfur bearing single crystals", Philosophical Magazine **92**, 2436–2447 (2012).

[167]Y. Okamura, S. Minami, Y. Kato, Y. Fujishiro, Y. Kaneko, J. Ikeda, J. Muramoto, R. Kaneko, K. Ueda, V. Kocsis, N. Kanazawa, Y. Taguchi, T. Koretsune, K. Fujiwara, A. Tsukazaki, R. Arita, Y. Tokura, and Y. Takahashi, "Giant magneto-optical responses in magnetic Weyl semimetal $Co_3Sn_2S_2$", Nature Communications **11**, 4619 (2020).

[168]L. Muechler, E. Liu, J. Gayles, Q. Xu, C. Felser, and Y. Sun, "Emerging chiral edge states from the confinement of a magnetic weyl semimetal in $Co_3Sn_2S_2$", Phys. Rev. B **101**, 115106 (2020).

[169]Q. Xu, E. Liu, W. Shi, L. Muechler, J. Gayles, C. Felser, and Y. Sun, "Topological surface fermi arcs in the magnetic weyl semimetal $Co_3Sn_2S_2$", Phys. Rev. B **97**, 235416 (2018).

[170]J.-X. Yin, N. Shumiya, Y. Jiang, H. Zhou, G. Macam, H. O. M. Sura, S. S. Zhang, Z.-J. Cheng, Z. Guguchia, Y. Li, Q. Wang, M. Litskevich, I. Belopolski, X. P. Yang, T. A. Cochran, G. Chang, Q. Zhang, Z.-Q. Huang, F.-C. Chuang, H. Lin, H. Lei, B. M. Andersen, Z. Wang, S. Jia, and M. Z. Hasan, "Spin-orbit quantum impurity in a topological magnet", Nature Communications **11**, 4415 (2020).

[171]M. S. Ramzan, Z. A. Goodwin, A. A. Mostofi, A. Kuc, and J. Lischner, "Effect of Coulomb impurities on the electronic structure of magic angle twisted bilayer graphene", arXiv preprint arXiv:2211.01038 **2**, 012043 (2022).

[172]B. Kiraly, A. N. Rudenko, W. M. J. van Weerdenburg, D. Wegner, M. I. Katsnelson, and A. A. Khajetoorians, "An orbitally derived single-atom magnetic memory", Nature Communications **9**, 3904 (2018).

[173]J. N. Crain and D. T. Pierce, "End states in One-Dimensional Atom Chains", Science **307**, 703–706 (2005).

[174]L. Wang, N. H. Jo, B. Kuthanazhi, Y. Wu, R. J. McQueeney, A. Kaminski, and P. C. Canfield, "Single pair of Weyl fermions in the half-metallic semimetal $EuCd_2As_2$", Phys. Rev. B **99**, 245147 (2019).

[175]J.-R. Soh, F. de Juan, M. G. Vergniory, N. B. M. Schröter, M. C. Rahn, D. Y. Yan, J. Jiang, M. Bristow, P. Reiss, J. N. Blandy, Y. F. Guo, Y. G.

Shi, T. K. Kim, A. McCollam, S. H. Simon, Y. Chen, A. I. Coldea, and A. T. Boothroyd, “Ideal Weyl semimetal induced by magnetic exchange”, Phys. Rev. B **100**, 201102 (2019).

[176]B. Li, W. Sun, X. Zou, X. Li, B. Huang, Y. Dai, and C. Niu, “Switchable quantum anomalous and spin Hall effects in honeycomb magnet $EuCd_2As_2$”, New Journal of Physics **24**, 053038 (2022).

[177]X. Cao, J.-X. Yu, P. Leng, C. Yi, X. Chen, Y. Yang, S. Liu, L. Kong, Z. Li, X. Dong, Y. Shi, M. Bibes, R. Peng, J. Zang, and F. Xiu, “Giant nonlinear anomalous Hall effect induced by spin-dependent band structure evolution”, Phys. Rev. Res. **4**, 023100 (2022).

[178]N. H. Jo, B. Kuthanazhi, Y. Wu, E. Timmons, T. Kim, L. Zhou, L. Wang, B. G. Ueland, A. Palasyuk, D. H. Ryan, R. J. McQueeney, K. Lee, B. Schrunk, A. A. Burkov, R. Prozorov, S. L. Bud’ko, A. Kaminski, and P. C. Canfield, “Manipulating magnetism in the topological semimetal $EuCd_2As_2$”, Phys. Rev. B **101**, 140402 (2020).

[179]E. Gati, S. L. Bud’ko, L. Wang, A. Valadkhani, R. Gupta, B. Kuthanazhi, L. Xiang, J. M. Wilde, A. Sapkota, Z. Guguchia, R. Khasanov, R. Valentí, and P. C. Canfield, “Pressure-induced ferromagnetism in the topological semimetal $EuCd_2As_2$”, Phys. Rev. B **104**, 155124 (2021).

[180]Y. Yin, M. Zech, T. Williams, and J. Hoffman, “Scanning tunneling microscopy and spectroscopy on iron-pnictides”, Physica C: Superconductivity **469**, Superconductivity in Iron-Pnictides, 535–544 (2009).

[181]A. Fente, A. Correa-Orellana, A. E. Böhmer, A. Kreyssig, S. Ran, S. L. Bud’ko, P. C. Canfield, F. J. Mompean, M. García-Hernández, C. Munuera, I. Guillamón, and H. Suderow, “Direct visualization of phase separation between superconducting and nematic domains in Co-doped $CaFe_2As_2$ close to a first-order phase transition”, Phys. Rev. B **97**, 014505 (2018).

[182]T.-M. Chuang, M. P. Allan, J. Lee, Y. Xie, N. Ni, S. L. Bud’ko, G. S. Boebinger, P. C. Canfield, and J. C. Davis, “Nematic electronic structure in the "parent" State of the Iron-Based Superconductor $Ca(Fe_{1-x}Co_x)_2As_2$”, Science **327**, 181–184 (2010).

[183]M. Gao, F. Ma, Z.-Y. Lu, and T. Xiang, “Surface structures of ternary iron arsenides AFe_2As_2 (A = Ba, sr, or ca)”, Phys. Rev. B **81**, 193409 (2010).

[184] A. Valadkhani, R. Valenti, and et al., "Dislocation defect as a bulk probe of monopole charge of multi-Weyl semimetals", In preparation **2**, 012043 (2020).

[185] V. Fock, "Bemerkung zur Quantelung des harmonischen Oszillators im Magnetfeld", Zeitschrift für Physik **47**, 446–448 (1928).

[186] A. Wensauer, "Quantenpunkte im magnetfeld", PdH Thesis (Universität Regensburg, Regensburg, Germany, 2003), p. 012043.

[187] J. B. Llorens, L. Embon, A. Correa, J. D. González, E. Herrera, I. Guillamón, R. F. Luccas, J. Azpeitia, F. J. Mompeán, M. García-Hernández, C. Munuera, J. A. Sánchez, Y. Fasano, H. Suderow, and Y. Anahory, "Observation of a gel of quantum vortices in a superconductor at very low magnetic fields", Phys. Rev. Res. **2**, 013329 (2020).

[188] S. V. Postolova, A. Y. Mironov, V. Barrena, J. Benito-Llorens, J. G. Rodrigo, H. Suderow, M. R. Baklanov, T. I. Baturina, and V. M. Vinokur, "Superconductivity in a disordered metal with Coulomb interactions", Phys. Rev. Res. **2**, 033307 (2020).

[189] M. Morgenstern, J. Klijn, C. Meyer, and R. Wiesendanger, "Real-Space observation of drift states in a Two-Dimensional Electron System at High Magnetic Fields", Phys. Rev. Lett. **90**, 056804 (2003).

[190] T. Terao, T. Nakayama, and H. Aoki, "Multifractality of the quantum Hall wave functions in higher Landau levels", Phys. Rev. B **54**, 10350–10353 (1996).

[191] A. Chhabra and R. V. Jensen, "Direct determination of the f(α) singularity spectrum", Phys. Rev. Lett. **62**, 1327–1330 (1989).

[192] A. V. Chubukov, R. M. Fernandes, and J. Schmalian, "Origin of nematic order in FeSe", Phys. Rev. B **91**, 201105 (2015).

[193] S. Medvedev, T. M. McQueen, I. A. Troyan, T. Palasyuk, M. I. Eremets, R. J. Cava, S. Naghavi, F. Casper, V. Ksenofontov, G. Wortmann, and C. Felser, "Electronic and magnetic phase diagram of β-$Fe_{1.01}Se$ with superconductivity at 36.7 K under pressure", Nature Materials **8**, 630–633 (2009).

[194] B. Lei, J. H. Cui, Z. J. Xiang, C. Shang, N. Z. Wang, G. J. Ye, X. G. Luo, T. Wu, Z. Sun, and X. H. Chen, "Evolution of High-Temperature Superconductivity from a low-T_c Phase Tuned by Carrier Concentration in FeSe Thin Flakes", Phys. Rev. Lett. **116**, 077002 (2016).

[195]S. He, J. He, W. Zhang, L. Zhao, D. Liu, X. Liu, D. Mou, Y. Ou, Q. Wang, Z. Li, L. Wang, Y. Peng, Y. Liu, C. Chen, L. Yu, G. Liu, X. Dong, J. Zhang, C. Chen, Z. Xu, X. Chen, X. Ma, Q. Xue, and X. J. Zhou, “Phase diagram and electronic indication of high-temperature superconductivity at 65 K in single-layer FeSe films”, Nature Materials **12**, 605–610 (2013).

[196]A. I. Coldea and M. D. Watson, “The Key Ingredients of the Electronic Structure of FeSe”, Annual Review of Condensed Matter Physics **9**, 125–146 (2018).

[197]M. A. Tanatar, A. E. Böhmer, E. I. Timmons, M. Schütt, G. Drachuck, V. Taufour, K. Kothapalli, A. Kreyssig, S. L. Bud’ko, P. C. Canfield, R. M. Fernandes, and R. Prozorov, “Origin of the Resistivity Anisotropy in the Nematic Phase of FeSe”, Phys. Rev. Lett. **117**, 127001 (2016).

[198]S. Kasahara, T. Watashige, T. Hanaguri, Y. Kohsaka, T. Yamashita, Y. Shimoyama, Y. Mizukami, R. Endo, H. Ikeda, K. Aoyama, T. Terashima, S. Uji, T. Wolf, H. von Löhneysen, T. Shibauchi, and Y. Matsuda, “Field-induced superconducting phase of FeSe in the BCS-BEC cross-over”, Proceedings of the National Academy of Sciences **111**, 16309–16313 (2014).

[199]M. D. Watson, T. K. Kim, A. A. Haghighirad, N. R. Davies, A. McCollam, A. Narayanan, S. F. Blake, Y. L. Chen, S. Ghannadzadeh, A. J. Schofield, M. Hoesch, C. Meingast, T. Wolf, and A. I. Coldea, “Emergence of the nematic electronic state in FeSe”, Phys. Rev. B **91**, 155106 (2015).

[200]J. Maletz, V. B. Zabolotnyy, D. V. Evtushinsky, S. Thirupathaiah, A. U. B. Wolter, L. Harnagea, A. N. Yaresko, A. N. Vasiliev, D. A. Chareev, A. E. Böhmer, F. Hardy, T. Wolf, C. Meingast, E. D. L. Rienks, B. Büchner, and S. V. Borisenko, “Unusual band renormalization in the simplest iron-based superconductor FeSe_{1-x}”, Phys. Rev. B **89**, 220506 (2014).

[201]M. D. Watson, T. Yamashita, S. Kasahara, W. Knafo, M. Nardone, J. Béard, F. Hardy, A. McCollam, A. Narayanan, S. F. Blake, T. Wolf, A. A. Haghighirad, C. Meingast, A. J. Schofield, H. v. Löhneysen, Y. Matsuda, A. I. Coldea, and T. Shibauchi, “Dichotomy between the Hole and Electron Behavior in Multiband Superconductor FeSe Probed by Ultrahigh Magnetic Fields”, Phys. Rev. Lett. **115**, 027006 (2015).

[202]T. Shimojima, Y. Suzuki, T. Sonobe, A. Nakamura, M. Sakano, J. Omachi, K. Yoshioka, M. Kuwata-Gonokami, K. Ono, H. Kumigashira, A. E. Böhmer, F. Hardy, T. Wolf, C. Meingast, H. v. Löhneysen, H. Ikeda, and K.

Ishizaka, "Lifting of xz/yz orbital degeneracy at the structural transition in detwinned FeSe", Phys. Rev. B **90**, 121111 (2014).

[203]Y. Suzuki, T. Shimojima, T. Sonobe, A. Nakamura, M. Sakano, H. Tsuji, J. Omachi, K. Yoshioka, M. Kuwata-Gonokami, T. Watashige, R. Kobayashi, S. Kasahara, T. Shibauchi, Y. Matsuda, Y. Yamakawa, H. Kontani, and K. Ishizaka, "Momentum-dependent sign inversion of orbital order in superconducting FeSe", Phys. Rev. B **92**, 205117 (2015).

[204]M. D. Watson, T. K. Kim, L. C. Rhodes, M. Eschrig, M. Hoesch, A. A. Haghighirad, and A. I. Coldea, "Evidence for unidirectional nematic bond ordering in FeSe", Phys. Rev. B **94**, 201107 (2016).

[205]M. Yi, D. Lu, J.-H. Chu, J. G. Analytis, A. P. Sorini, A. F. Kemper, B. Moritz, S.-K. Mo, R. G. Moore, M. Hashimoto, W.-S. Lee, Z. Hussain, T. P. Devereaux, I. R. Fisher, and Z.-X. Shen, "Symmetry-breaking orbital anisotropy observed for detwinned $Ba(Fe_{1-x}Co_x)_2As_2$ above the spin density wave transition", Proceedings of the National Academy of Sciences **108**, 6878–6883 (2011).

[206]M. Yi, H. Pfau, Y. Zhang, Y. He, H. Wu, T. Chen, Z. R. Ye, M. Hashimoto, R. Yu, Q. Si, D. Lee, P. Dai, Z. X. Shen, D. H. Lu, and R. J. Birgeneau, "Nematic Energy Scale and the Missing Electron Pocket in FeSe", Phys. Rev. X **9**, 041049 (2019).

[207]E. M. Nica, R. Yu, and Q. Si, "Glide reflection symmetry, Brillouin zone folding, and superconducting pairing for the $P4/nmm$ space group", Phys. Rev. B **92**, 174520 (2015).

[208]V. Brouet, M. F. Jensen, P. Lin, A. Taleb-Ibrahimi, P. Le Fèvre, F. Bertran, C. Lin, W. Ku, A. Forget, and D. Colson, "Impact of the two Fe unit cell on the electronic structure measured by ARPES in iron pnictides", Phys. Rev. B **86**, 075123 (2012).

[209]M. Yi, D. H. Lu, R. Yu, S. C. Riggs, J.-H. Chu, B. Lv, Z. K. Liu, M. Lu, Y.-T. Cui, M. Hashimoto, S.-K. Mo, Z. Hussain, C. W. Chu, I. R. Fisher, Q. Si, and Z.-X. Shen, "Observation of Temperature-Induced Crossover to an Orbital-Selective Mott Phase in $A_xFe_{2-y}Se_2$ (A=K, Rb) Superconductors", Phys. Rev. Lett. **110**, 067003 (2013).

[210]M. Yi, Z.-K. Liu, Y. Zhang, R. Yu, J.-X. Zhu, J. Lee, R. Moore, F. Schmitt, W. Li, S. Riggs, J.-H. Chu, B. Lv, J. Hu, M. Hashimoto, S.-K. Mo, Z. Hussain, Z. Mao, C. Chu, I. Fisher, Q. Si, Z.-X. Shen, and D. Lu, "Observation of

universal strong orbital-dependent correlation effects in iron chalcogenides", Nature Communications **6**, 7777 (2015).

[211] A. Kostin, P. O. Sprau, A. Kreisel, Y. X. Chong, A. E. Böhmer, P. C. Canfield, P. J. Hirschfeld, B. M. Andersen, and J. C. S. Davis, "Imaging orbital-selective quasiparticles in the Hund's metal state of FeSe", Nature Materials **17**, 869–874 (2018).

[212] R. Yu, J.-X. Zhu, and Q. Si, "Orbital Selectivity Enhanced by Nematic Order in FeSe", Phys. Rev. Lett. **121**, 227003 (2018).

[213] L. Benfatto, B. Valenzuela, and L. Fanfarillo, "Nematic pairing from orbital-selective spin fluctuations in FeSe", npj Quantum Materials **3**, 56 (2018).

[214] P. Wiecki, K. Rana, A. E. Böhmer, Y. Lee, S. L. Bud'ko, P. C. Canfield, and Y. Furukawa, "Persistent correlation between superconductivity and antiferromagnetic fluctuations near a nematic quantum critical point in $\mathrm{FeSe}_{1-x}\mathrm{S}_x$", Phys. Rev. B **98**, 020507 (2018).

[215] A. I. Coldea, S. F. Blake, S. Kasahara, A. A. Haghighirad, M. D. Watson, W. Knafo, E. S. Choi, A. McCollam, P. Reiss, T. Yamashita, M. Bruma, S. C. Speller, Y. Matsuda, T. Wolf, T. Shibauchi, and A. J. Schofield, "Evolution of the low-temperature Fermi surface of superconducting $\mathrm{FeSe}_{1-x}\mathrm{S}_x$ across a nematic phase transition", npj Quantum Materials **4**, 2 (2019).

[216] A. E. Böhmer, V. Taufour, W. E. Straszheim, T. Wolf, and P. C. Canfield, "Variation of transition temperatures and residual resistivity ratio in vapor-grown FeSe", Phys. Rev. B **94**, 024526 (2016).

[217] T. Hanaguri, K. Iwaya, Y. Kohsaka, T. Machida, T. Watashige, S. Kasahara, T. Shibauchi, and Y. Matsuda, "Two distinct superconducting pairing states divided by the nematic end point in $\mathrm{FeSe}_{1-x}\mathrm{S}_x$", Science Advances **4**, eaar6419 (2018).

[218] V. Crespo, A. Maldonado, J. Galvis, P. Kulkarni, I. Guillamon, J. Rodrigo, H. Suderow, S. Vieira, S. Banerjee, and P. Rodiere, "Scanning microscopies of superconductors at very low temperatures", Physica C: Superconductivity **479**, 19–23 (2012).

[219] Z. Guo, F. Sun, Y. Chen, Y. Mao, L. Wan, X. Yan, Y. Yang, and W. Yuan, "Synthesis, structure and superconductivity of $\mathrm{FeS}_{1-x}\mathrm{Se}_x$ ($0 \leq x \leq 1$) solid solution crystals", CrystEngComm **21**, 2994–2999 (2019).

[220] S. A. Moore, J. L. Curtis, C. Di Giorgio, E. Lechner, M. Abdel-Hafiez, O. S. Volkova, A. N. Vasiliev, D. A. Chareev, G. Karapetrov, and M. Iavarone,

"Evolution of the superconducting properties in $FeSe_{1-x}S_x$", Phys. Rev. B **92**, 235113 (2015).